INVESTIGATING RESONANCE DETECTION METHODS IN DISC GALAXIES

Pouya Mahmoudi Kouch

Master of Science Thesis
Astrophysics degree
at
Department of Astronomy
Faculty of Science
University of Oulu
Finland

Supervisor: Dr. Sébastien Comerón

March 2020

Abstract

In this thesis the reliability of the Font-Beckman (FB) method in locating resonances in disc galaxies is investigated. In the first section of this thesis a general overview about galaxies is provided before moving on to the more specific topics. The literature review heavily focuses on resonance detection methods in disc galaxies, where a number them is used for comparisons with the FB method. The FB method attempts to locate resonances of a disc galaxy by finding zeros in its residual velocity map, which is a map of the galaxy's non-circular line-of-sight velocity. These zeros are then counted and averaged radially; if a radius shows a clear peak in the number of these zeros, then it is taken as a FB resonance radius. The FB method was fully re-coded for the purposes of this thesis and is put to test in various ways, resulting in a lot of findings although only the main ones are mentioned in this abstract for brevity. The FB method's reliability is tested via two approaches. The first approach is a simulation-based comparison, in which galaxies with theoretically-known resonances are simulated (using Wada simulations) and the FB method is applied to them. This allows for a direct comparison between FB and theoretical resonances. The main finding is that the FB method can reliably locate outer Lindblad resonances (success rate of 84%$\pm$16%), somewhat reliably locate inner Lindblad resonances (47%$\pm$27%) as well as inner 4:1 resonances (43%$\pm$16%), while it struggles to successfully locate the corotation resonances (17%$\pm$17%), which contradicts Font-Beckman's claim that their method can reliably find corotation resonances. The simulated galaxies were coded such that some of the galactic parameters were adjustable, which allowed us to discover that the FB method works best when the inclination of the galaxy is around 45° as well as other minor findings. The second approach is based on a number of Monte Carlo simulations, where the results from the FB method's application to real galaxies are used. A number of random resonances are generated and then compared to a number of RI (resonance indicator: a method that detects resonances) resonances. Simultaneously, the FB resonances are compared to the same RI resonances. If FB resonances correlate more closely with the RI resonances as compared to the random resonances with the RI resonances, then it is a positive sign for the reliability of the FB method. Naturally, this depends on how truly reliable the RI are themselves, which is beyond the scope of this study albeit worthy of further investigation. The RIs used are such methods as Tremaine-Weinberg, simulation-based, surface-brightness truncations, Buta-Zhang, rings, etc. In general, we find that the correlation between FB and RI resonances is weaker in barred galaxies. Furthermore, it is found that FB and RI resonances show the strongest correlation when rings are used as RI. Finally, it is concluded that although the FB method is somewhat successful, it is not perfect and further investigation is welcomed.

Contents

1 Introduction **7**

1.1 Galaxies: A general outline . . . 7

1.1.1 History of galactic study . . . 8

1.1.2 Classification of galaxies . . . 9

1.1.3 The Milky Way: Our home galaxy . . . 11

1.1.4 Stellar orbits in galaxies . . . 14

1.1.5 The Local Group: Milky Way's neighbourhood . . . 15

1.1.6 Disc galaxies . . . 17

1.1.7 Elliptical galaxies . . . 23

1.1.8 The Local Universe: Groups, Clusters, and Large-scale structures . . . 24

1.1.9 Active Galactic Nuclei . . . 26

1.2 Disc galaxies: Density-Wave Theory and Resonances . . . 28

1.2.1 Density-wave theory . . . 28

1.2.2 Resonances . . . 30

1.2.3 Resonance detection . . . 32

2 Data **41**

3 Methods **59**

3.1 Simulation application . . . 59

3.1.1 Font-Beckman phase reversal method . . . 59

3.1.2 Wada galaxy simulations . . . 64

3.2 Monte Carlo analysis . . . 66

3.2.1 Resonance indicators . . . 67

3.2.2 Units of radial measurement . . . 68

3.2.3 Monte Carlo I . . . 68

3.2.4 Monte Carlo II . . . 70

3.2.5 Monte Carlo II-i . . . 72

3.2.6 Monte Carlo III . . . 72

3.2.7 Reverse comparison . . . 74

4 Results **81**

4.1 Simulation application 81
4.2 Monte Carlo analysis 95
4.2.1 Type-II truncations as RI 95
4.2.2 Rings as RI 97
4.2.3 Final Monte Carlo comparison 98

5 Discussion **127**
5.1 Simulation application 127
5.2 Monte Carlo analysis 133
5.2.1 Type-II truncations as RI 133
5.2.2 Rings as RI 138
5.2.3 Final Monte Carlo comparison 140

6 Conclusion **143**

Bibliography **147**

Chapter 1

Introduction

In this chapter the astronomical objects of interest to this thesis, galaxies, are introduced. The related subtopics are then discussed in more detail. This chapter provides the reader with the necessary information to follow the following chapters.

1.1 Galaxies: A general outline

This section briefly introduces what galaxies are, how they are classified, how our perception of them evolved over time, how their internal elements behave, and how they shape the Universe. To keep this section as brief as possible, the specific topics that pertain to the main focus of this thesis are discussed in detail in later sections. The flow of content in this brief outlook closely follows that of the book "Galaxies in the Universe, An Introduction" by Sparke and Gallagher (2000).

Galaxies are the fundamental building blocks of the Universe. They are gravitational collections of stars as well as interstellar gas and dust, which make up the luminous portion of matter in galaxies. It is thought that galaxies also contain a large fraction of invisible matter referred to as dark matter whose presence is only detected through its immense gravitational pull. Galaxies vary in size from small to gigantic. The small ones are dwarf galaxies which may hold a few million stars or less. The large ones are giant galaxies which can hold up to around 10^{14} stars.

Galaxies vary drastically in their appearance. Some have thin rotating discs with bars or no bars while some do not have a disc structure at all. These features were used by Edwin Hubble in 1926 to classify galaxies (Hubble, 1926). That proved to be the first step for understanding what galaxies truly are. We discuss the details of this classification and further improvements made to it below.

Galaxies emit an electromagnetic spectrum that covers almost the entire wavelength range from radio to γ-rays. These various wavelengths can be used to study different aspects of galaxies. For example, in the visible part of the spectrum the colour of stars indicates what their effective temperature is. If they are bluish then they are hot, a trait usually seen in massive, young stars. On the other hand, if they are reddish then they are colder, which typically indicates that the star is old. Since galaxies are made of stars, this feature is utilized to indicate where the young or old stars reside within the galaxy. This shows where star formation is likely occurring in the galaxy.

1.1.1 History of galactic study

Unsurprisingly, the first galaxy to be discovered was the one that our Solar System resides in, the Milky Way. In 5th century BC, the ancient Greek philosopher Democritus suggested that the bright band in the night sky (the Milky Way, in Greek *milky circle*) may consist of stars. Later on in the 4th century Aristotle had come to believe that the Milky Way was caused by fiery explosions of numerous, tightly-packed, large stars in the atmosphere in line with the the heavenly motions.

The next big discovery came in the 10th century, when the Persian astronomer Abdul Rahman Sufi discovered the Andromeda galaxy (M31 or NGC224), which is the closest major galaxy to the Milky Way. In his "Book of Fixed Stars", he referred to Andromeda as *a little cloud* and there are mentions of the Large Magellanic Cloud (a satellite galaxy of the Milky Way) as well. Over the next four centuries other details regarding the nature of the Milky Way and its constituting stars were discovered by various Islamic scholars. The most notable one was the parallax measurement of the Milky Way by the Arab astronomer al-Haytham. He found no parallax for the Milky Way which meant it must be very far away from Earth, refuting Aristotle's atmosphere belief.

The next major discovery was made by the Italian polymath Galileo Galilei in 1610 when he confirmed that the Milky Way is made of numerous faint stars using a telescope. In 1750, the English astronomer Thomas Wright described the shape of the Milky Way (Wright, 1750). Shortly afterwards in 1755, the German philosopher Immanuel Kant followed up on Wright's findings and speculated that stars are held together by gravity which reside in a rotating disc forming the Milky Way. He also described the faint nebulae as separate, individual *Island Universes*, i.e. galaxies. In 1785, the German-British astronomer William Herschel performed the first observations to locate the stars within the Milky Way and mapped them (Herschel, 1785). The map is seen in Figure 1.1. In his findings the Sun is near the center of the Milky Way, which we now know to be false. Herschel's faulty observation is attributed to the presence of dust in the Milky Way plane, which obscures stars and affects the star count.

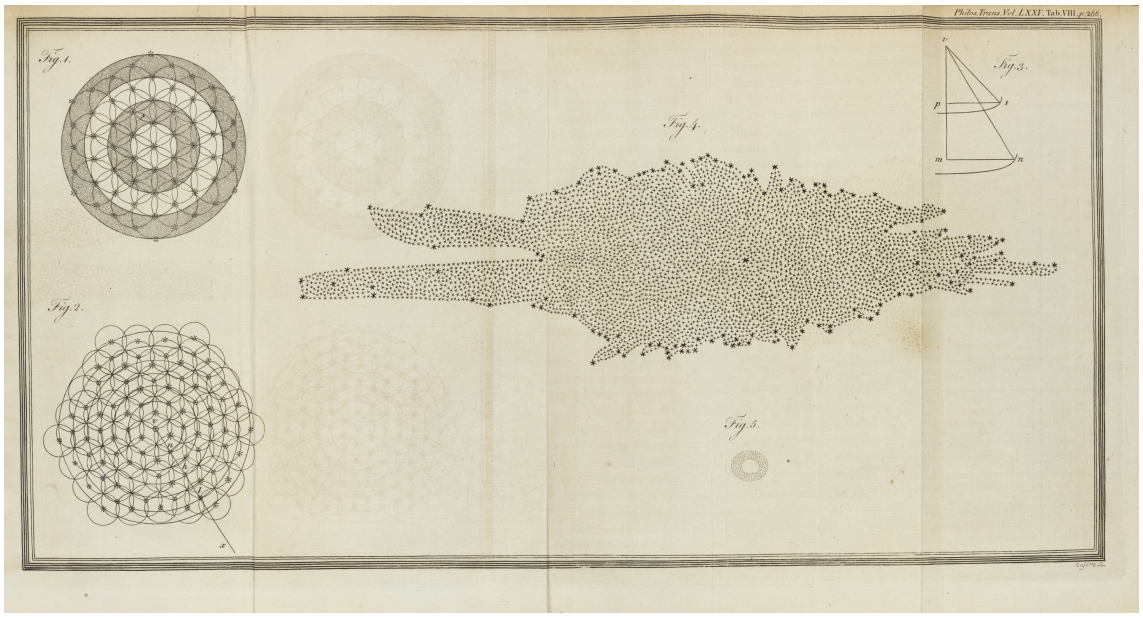

Figure 1.1: Map of the Milky Way by William Herschel in 1785. Credit: The Royal Society

Over the next century, in 1845, a spiral shape was observed in a distant "nebula" (M51 or NGC5194)

by the Anglo-Irish astronomer Lord Rosse. In 1918, the American scientist Harlow Shapley discovered that globular clusters (spherical collection of stars) are arranged in a spherical distribution around the center of the Milky Way, i.e. galactic center (Shapley, 1918). On 26th of April 1920, Harlow Shapley and a fellow American astronomer Heber Curtis engaged in a debate regarding the nature of "spiral nebulae". This is known as the Great Debate of Astronomy (Shapley-Curtis Debate). Shapley argued that Andromeda is not a separate galaxy but a section of the Milky Way which encompasses the whole Universe. On the other hand, Curtis argued for Andromeda being its own separate galaxy agreeing with Kant's *Island Universe* notion. The two sides generally had sound arguments, taking into account the limited observational data available at the time. Finally the debate was settled in 1923 when Erwin Hubble found Cepheids (a type of *standard candles*) in Andromeda enabling him to calculate the distance to the galaxy. The discovery confirmed that Andromeda and likewise other nebulae are indeed separate galaxies or as Kant would call them *Island Universes*.

1.1.2 Classification of galaxies

Three years after Erwin Hubble's crucial discovery of Cepheids in Andromeda which proved galaxies are distant collections of stars, he proposed his classification of galaxies based on their morphology (Hubble, 1926). In 1936, he expanded on this classification (Hubble, 1936). This classification is called the *Hubble Tuning Fork*; Figure 1.2 shows the reasoning behind the etymology.

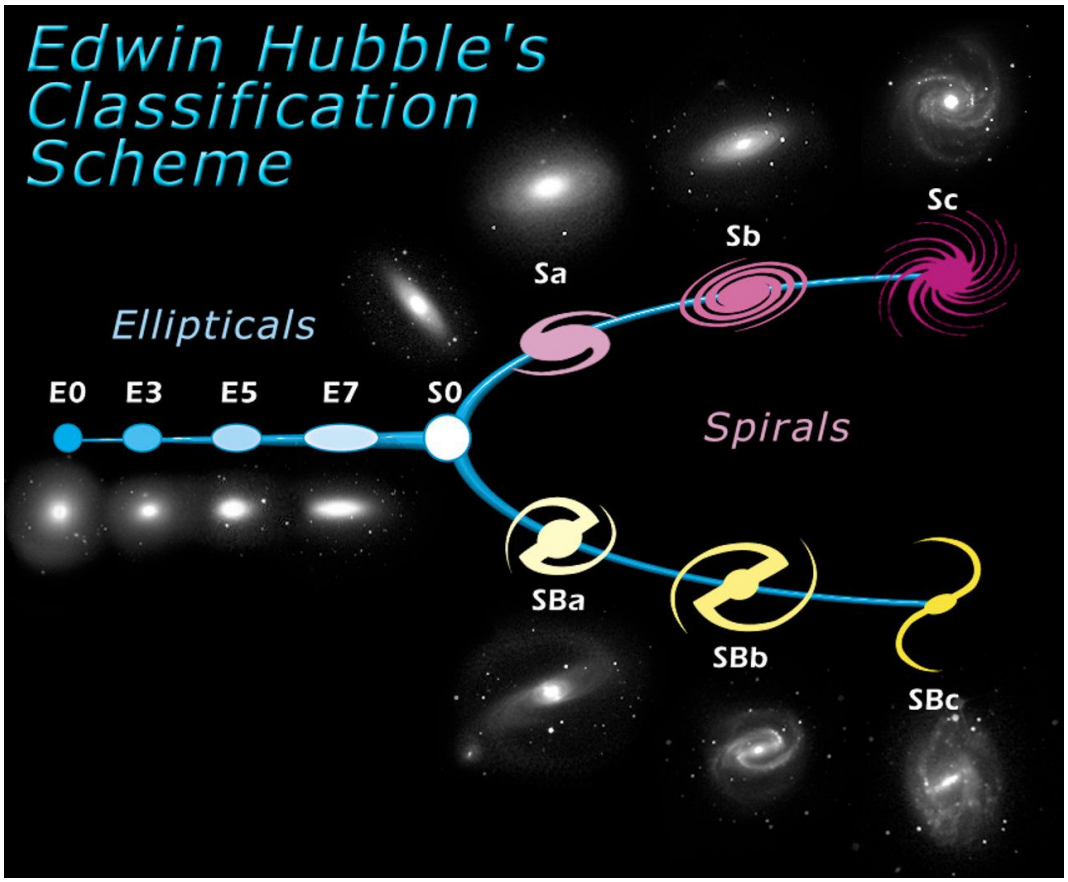

Figure 1.2: The Hubble Tuning Fork. Credit: ESA/Hubble

As it can be seen, the Hubble classification is a continuous one. The galaxies on the left, ellipticals, are

called early-type galaxies and the ones on the right, spirals, are called late-type galaxies. The early-type and late-type naming was due to Hubble's idea that the tuning fork showed the evolution of galaxies, however, nowadays this idea is not accepted.

Elliptical galaxies are reddish in colour and show no star formation signs. They have no clear visible structures and their light distribution is smooth. They are classified as E*n* where *n* is a measure of how elliptical they appear to be in observations. Spiral galaxies have an intrinsically thin disc with spiral arms where star formation is believed to occur. They may have a central mass concentration. They may or may not host a bar. Bars were first observed in 1918 by Heber Curtis (Curtis, 1918). Spiral galaxies that have bars are denoted as SB and those that do not are denoted with SA. Both barred and nonbarred spiral galaxies are ordered with increasing openness and patchiness of spiral arms as well as decreasing central mass concentration; this order is SAa, SAb, and SAc for nonbarred spirals and SBa, SBb, and SBc for barred spirals. The intermediate class between ellipticals and spirals is made of the so-called lenticular galaxies (S0) (Sandage, 1975). They possess discs without spiral arms, show almost no star formation and have a larger central mass concentration than spiral galaxies.

In 1959, the French astronomer Gérard de Vaucouleurs added some refinements and an extra parameter into the Hubble classification (de Vaucouleurs, 1959). The ellipticals are divided into E and E^+, where the latter represents a transition from E to S0 with some hint of a disc being visible. The lenticulars are ordered in a sequence of increasing definition of features, especially disc smoothness, to be $S0^-$, $S0^0$, $S0^+$, and S0/a where the latter starts to show some spiral feature. Regarding the spirals, two new stages to the a, b, and c of the Hubble classification were added which are d and m. Galaxies in these two new stages can be bulge-less and have a significant degree of asymmetries. In this classification scheme the galaxies that fall somewhere between these various stages are given an intermediary naming; for example, a galaxy may be Sab instead of Sa or Sb. The galaxies that are irregular in shape and do not fit any of the aforementioned classes are placed into *irregulars*, denoted by I.

In de Vaucouleurs classification the stages are numerically coded such that the general *shape* of a galaxy is represented by a single number. The numerals go from -5 to 10. The ellipticals' are -5 and -4, respectively for E and E^+. The lenticulars' are -3 to 0, respectively for $S0^-$,$S0^0$, $S0^+$, and S0/a. The spirals' are 1 to 9, respectively for Sa, Sab, Sb, Sbc, Sc, Scd, Sd, Sdm, and Sm. The irregulars' is 10 for I.

Note that in case of the spirals, they may be barred or unbarred. The barredness of galaxies is described by the family parameter. In case of the Hubble classification there were the SA and SB families, respectively representing unbarred and barred spirals. However, in de Vaucouleurs classification there are five bar families: SA, S<u>A</u>B, SAB, SA<u>B</u>, and SB. This is ordered with increasing bar strength, which is determined by its relative size to the galaxy as well as its surface brightness and ellipticity.

The additional parameter added by de Vaucouleur is related to existence of rings or pseudo-rings (ring-like structures that are not fully closed) at the ends of the bar or where the bar should be in case of unbarred spirals; nowadays these rings are referred to as inner rings. This determines *variety* of the galaxies. The classification is r, <u>r</u>s, rs, r<u>s</u>, and s, which goes respectively from full rings to pseudo-rings to no rings at all.

Over the years further refinements were made to de Vaucouleurs classification such that presence or absence of certain features would be noted in the classification. Some of these features are outer rings (found at two to three times the bar size) discussed by Buta and Crocker (1991), nuclear rings (found within the bar radius) discussed by Morgan (1958), inner, outer, and nuclear lenses (look like "filled"

rings) or ring-lenses discussed by Kormendy (1981). Additionally, features such as nuclear bars (bars within main bars) discussed by de Vaucouleurs (1975) and ansae ("handles" at the end of bars) are used to divide the classes further.

Despite the intricacies of the de Vaucouleurs classification scheme, there are certain galaxies that do not follow it. For example, dwarf galaxies (those smaller than the Magellanic Clouds) or galaxy mergers do not follow this classification. Furthermore, the presence of dust or orientation of a galaxy (especially, edge-on galaxies) can obscure the galaxy features such that classification becomes fallible. The dust obscuration can be bypassed by studying the galaxy at other wavelengths, especially infrared (Hackwell and Schweizer, 1983). However, it is important to note that appearance of galaxies is wavelength dependent, so a single galaxy may have multiple classifications depending on the wavelength of its image. For example, in infrared features are smoother therefore their infrared classification is biased towards early-types.

1.1.3 The Milky Way: Our home galaxy

Distances between galaxies are of the order of 10^5 to 10^6 light years. That means most galaxies are at such stupendously large distances that observations do not reveal their smallest details. As a result, astronomers look at our own galaxy, the Milky Way, to study galactic details. The more we know about the Milky Way, the more we know about galaxies in general or at least the spiral ones. Understanding the intricacies of the Milky Way is undoubtedly a crucial part of galactic astronomy.

According to the de Vaucouleurs classification the Milky Way's general class is Sbc (Gerhard, 2002), which is a spiral galaxy of somewhat loose and patchy spirals. The Milky Way's specific classification is SBbc, which means that it is a barred spiral galaxy. The true shape of the Milky Way can never be observed directly from inside it, however, using data collected from Wide-field Infrared Survey Explorer (WISE) a map of the Milky Way was created, see Figure 1.3. The features used to classify it are clearly visible in the image. This type of mapping is only possible in the infrared regime due to disruptive dust absorption that affects other electromagnetic regimes, such as optical.

To study the vertical structure of the Milky Way disc, using photometric parallaxes, stars of specific populations are selected and their perpendicular distances to the disc are calculated. It turns out that two discs of different scale-heights are needed to fit the vertical stellar distribution of the Milky Way; a thin disc (scale-height of a few 100 parsecs) and a thick disc (scale-height of about 1000 parsecs) discussed by Gilmore and Reid (1983), see Figure 1.4. The thick disc has a local relative stellar density of about 10% and it only holds about 30% of the entire disc stars. The thin disc shows a small asymmetric drift (average azimuthal drift of a star population from a perfectly circular orbit) while the thick disc shows a large asymmetric drift. The metallicity (abundance of elements larger than helium) of the thin disc is higher than that of the thick disc, implying that the thin disc is home to younger generations of stars while the thick disc contains older generations.

Generally, the greater the distance from the disc, the older the stellar population becomes. For instance, the oldest stars are found in the halo (Gilmore and Wyse, 1989). The other aforementioned properties follow the same principle. The halo has the largest scale-height and the greatest asymmetric drift; the asymmetric drift is almost as large as the Sun rotation velocity around the galactic center, which means the outer halo does not rotate and is pressure-supported by random motions of stars.

The Milky Way has many stellar clusters, even outside of the disc albeit the cluster density there is far

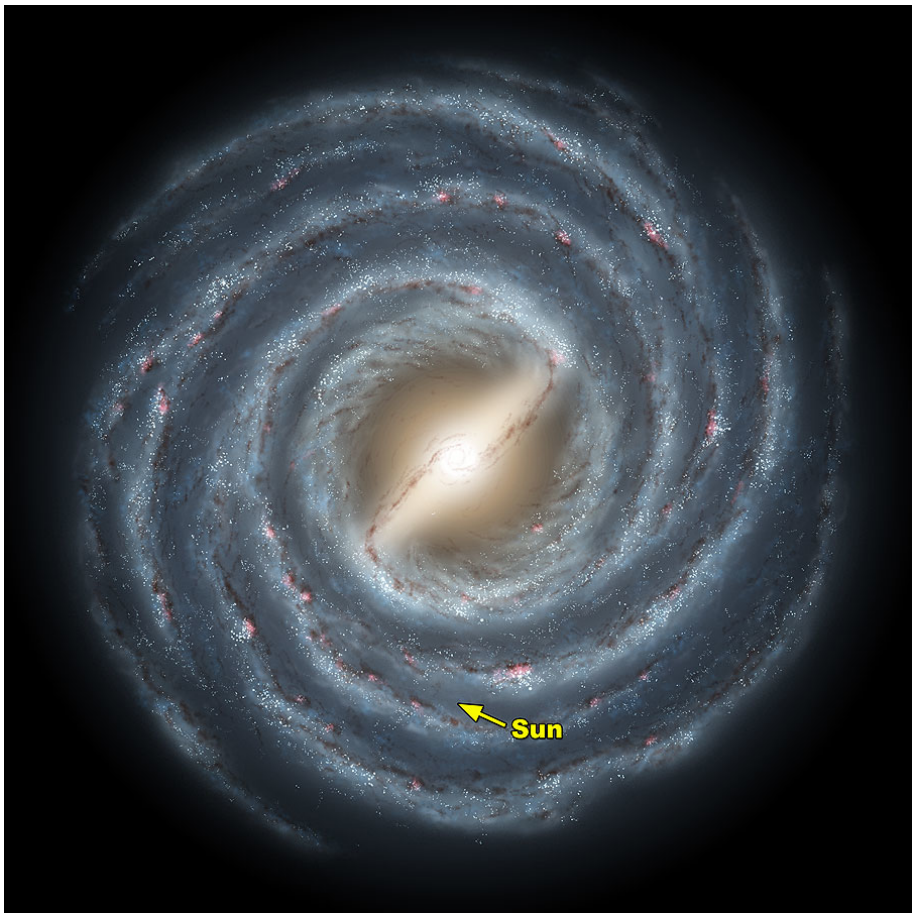

Figure 1.3: The Milky Way and the Sun's location. Credit: R. Hurt (SSC), JPL-Caltech, NASA

smaller than that in the disc, as it is noticeable in Figure 1.4. It is accepted that the Milky Way is home to more than 2000 known (only within 5 kpc) open clusters (Zasowski et al., 2013) and around 150 globular clusters (Harris, 1996). Open clusters contain up to 1000s of stars formed from the same giant molecular cloud. The stars of open clusters have small random speeds. Open clusters are found close to the disc and may still contain gas and dust as they are mostly younger than 1 Gyr. Understanding clusters is important as single stars are usually not resolved when studying other galaxies, but clusters are. Globular clusters are comparatively more massive than open clusters, as they contain up to 10^6 very tightly packed stars. The random speeds of stars in globular clusters are larger than those in open clusters. They are older (ages of several Gyr) than open clusters. Metal-rich globular clusters are found close to the bulge and the thick disc. Their orbit is similar to that of the thick disc stars. However, metal-poor globular clusters (almost as old as the Universe) show a spherical distribution around the galaxy center. Their orbits are randomly oriented and can plunge deep into the galaxy.

The Milky Way disc was generally thought to extend up to around 15 kpc from the center (Rix and Bovy, 2013), but recently the "edge" is found to be farther out at around 25 kpc from the galactic center (López-Corredoira et al., 2018). The bulge of the Milky Way has a radius of about 1 kpc and is rotating with an average speed of around 100 km/s. The nucleus of the Milky Way is a region of about 2 pc in radius with $10^6 M_\odot$ of hot gas. The structure within this extremely dense region is cluster-like, but the stars are of different generations. At the very center of this nucleus a supermassive black hole of $4 \times 10^6\, M_\odot$ resides (Schödel et al., 2002), just like for most other massive galaxies (Kormendy and Richstone, 1995).

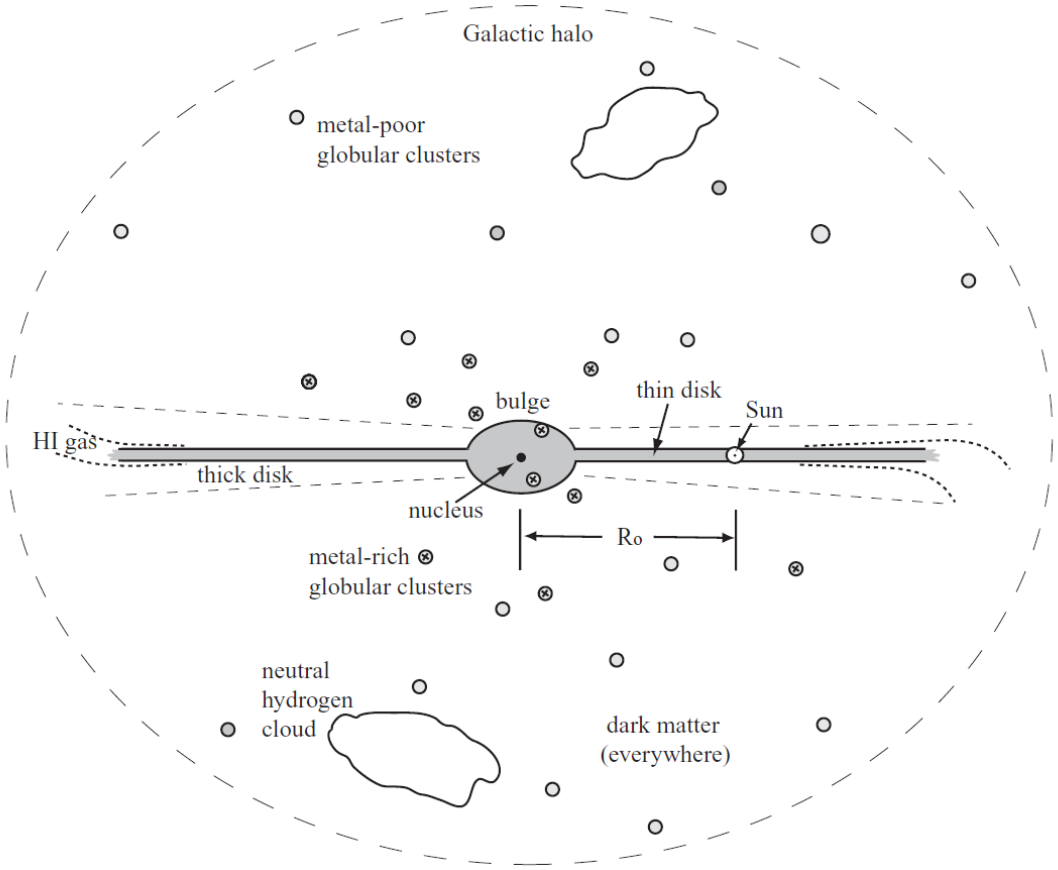

Figure 1.4: Edge-on schematic view of the Milky Way. Credit: "Galaxies in the Universe, An introduction" by Sparke and Gallagher (2000)

Using the rotation curve one can obtain the mass distribution of the Milky Way. The rotation curve of a galaxy is the orbital circular velocity as a function of the galactic radius. The rotation curve of the Milky Way is obtained by mapping the velocity of the H I gas (atomic neutral gas) via the 21 cm hyper-fine transition (Foster, 2004). It is found to be almost flat (constant orbital velocity) with radius by Bosma (1981). This goes against the nearly Keplerian rotation curve expectation at large radii if matter is heated by stars and requires more mass to be present in the disc than is observed. This invisible matter is referred to as *dark matter*. This is discussed in more details later on.

Less than 10% of the disc mass is found in gas (Sparke and Gallagher, 2000). The gas in the halo is ionized H II (hot diffuse gas), while the inner parts are atomic H I (warm diffuse gas). There also exists gas in dense molecular form H_2 (cold clumpy gas) kept within the disc (especially spiral arms), in Giant Molecular Clouds where stars are born. Apparently in-falling off-plane gas clouds exist as well. The massive ones are intergalactic in nature, while the smaller ones could be returning supernovae ejecta.

Interstellar dust absorbs around 50% of the optical and UV light emitted by stars, even though the dust particle density in interstellar medium can be 0.01 m^{-3} or less. Dust particles account for just 1% of the mass of interstellar material (Sparke and Gallagher, 2000). They are generally less than one μm in radius. They play an important role in the formation of H_2 molecules because they favor their formation through catalysis.

1.1.4 Stellar orbits in galaxies

In large disc galaxies, like the Milky Way, the driver of the particle (stellar, gas, and dust) trajectories is the smoothed potential of the galaxy. In reality, the gravitation of the individual stars perturbs the smooth potential, however this is ignored in the following general consideration of the trajectories. Using the equations of motion, conservation of energy, and Virial theorem, one obtains the results discussed below.

If a particle moves strictly on the galactic plane (it is close to the plane and its angular momentum is perpendicular to the plane), it must orbit the galaxy with an average radius called the *guiding radius*. The orbit is circular when the energy needed to complete the oscillation is minimum. However, if the energy is greater and it still possesses the same angular momentum, then the only stable scenario is its radius starting to oscillate around the guiding radius. This results in an azimuthal motion that speeds up and slows down periodically. This scenario only occurs when the angular momentum in a circular orbit increases with radius; this is true in flat rotation curve systems like the Milky Way and most other disc galaxies.

In the linear regime (small oscillation approximation), this oscillating radial value is obtained by taking the star and allowing it to orbit around a *guiding center* that itself orbits the galaxy, see the left sketch in Figure 1.5. This is known as the *epicyclic oscillation* of stars. Note that the epicycles are retrograde in nature, meaning when the star is in the inner side of the cycle it speeds up and when it is in the outer side it slows down. It turns out that in cases of a Keplerian rotation curve or a uniform sphere density the epicyclic frequency is an exact multiple of the angular speed, which results in the orbits being closed. However, in case of the flat rotation curve the orbits are not closed. This means the orbit of a star around the galaxy looks like a rosette instead of a circle or an ellipse, see the right sketch of Figure 1.5. In the flat rotation curve case, the ratio of the epicyclic frequency to the orbital frequency is $\sqrt{2} \approx 1.4$; meaning for every stellar orbit around the galaxy around 1.4 radial in-out oscillation gets completed.

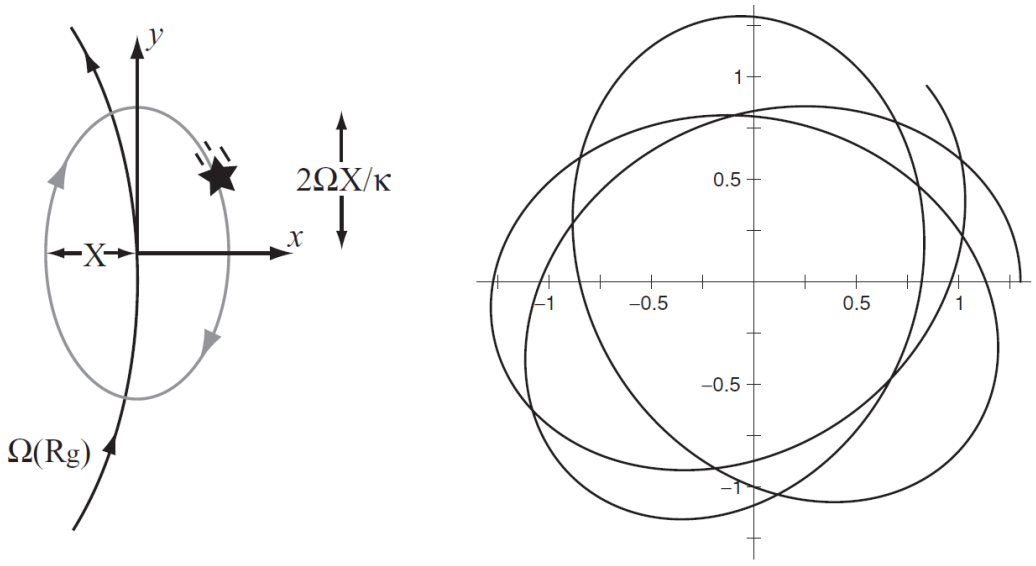

Figure 1.5: Left; orbit of a star around the guiding center. Right; path of a star viewed from above the galactic plane of a flat rotation curve galaxy. Credit: "Galaxies in the Universe, An introduction" by Sparke and Gallagher (2000)

If an individual star in the solar neighbourhood ($R_\star = R_\odot$) is selected, then its guiding center is either

closer to the galactic center than the Sun or is farther away. In case of the former the star is in its outer phase and for the latter the star is in its inner phase. Due to the retrograde nature of the epicyclic motion, the former is slower than the Sun while the latter is faster than the Sun. This is, in fact, the reason for asymmetric drift. Knowing the individual coordinates of stars is not always possible, therefore orbital speeds of stars are averaged. At any given radius, including the solar radius, there are more stars with a guiding center within the radius than outside of it (due to stellar density dropping with radius). Hence, on average more stars are in the outer phase of their epicycles, which results in a negative average azimuthal speed relative to the circular velocity – an asymmetric drift. The epicyclic oscillations grow in amplitude over time, which explains why older stellar populations have a greater asymmetric drift.

1.1.5 The Local Group: Milky Way's neighbourhood

The Milky Way belongs to a group of gravitationally bound galaxies called the *Local Group*, see Figure 1.6. This group has three main galaxies: the Milky Way, M31 (Andromeda), and M33 (Triangulum). These three are responsible for around 90% of the light output of the Local Group. The radius of this group is of the order of 1 Mpc. Of the 50 discovered Local Group galaxies, there is only one elliptical galaxy, M32, which is a satellite of M31. The rest are spirals, irregulars, and dwarfs of various types. This type composition is seen in most other galaxy groups, which are rich in late-type galaxies and poor in early-type galaxies.Note that most of the galaxies in the group are satellites of the Milky Way and M31. Galaxies within around 30 Mpc of the Milky Way are in a roughly flattened distribution called the *supergalactic plane*.

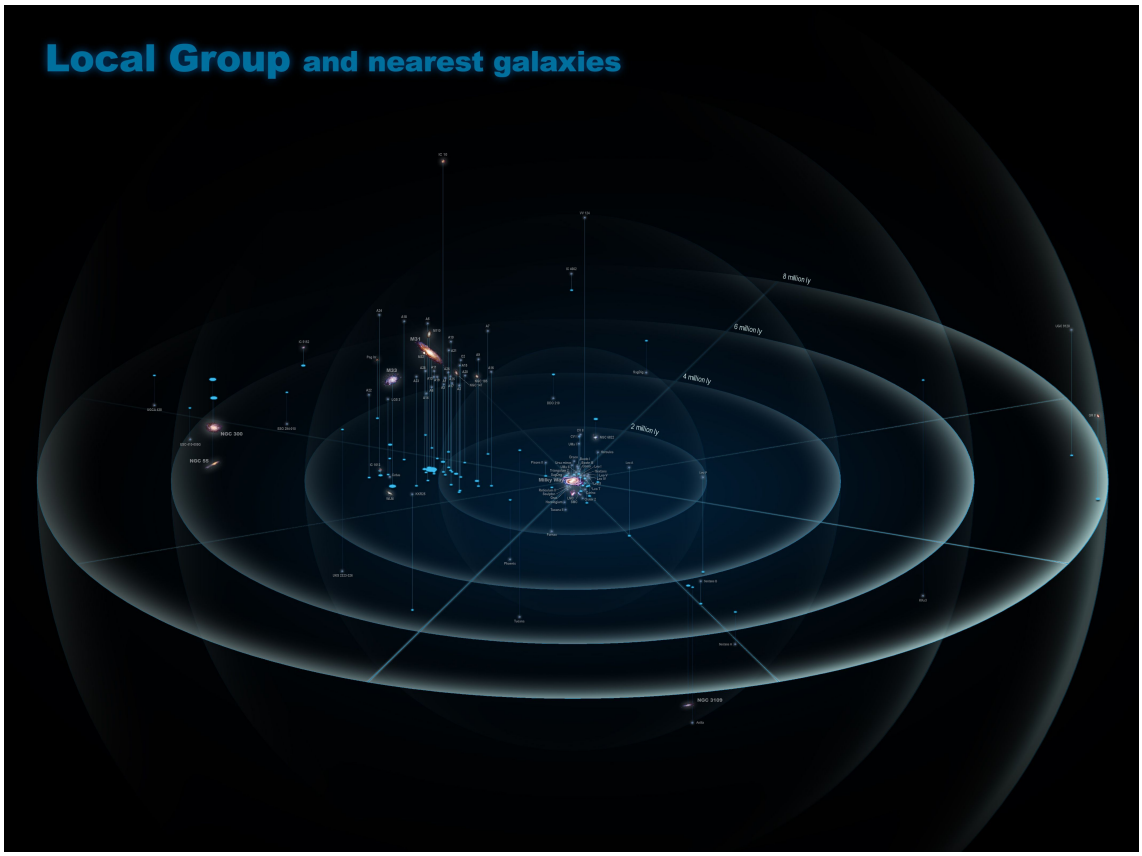

Figure 1.6: The Local Group, neighbourhood of the Milky Way. Credit: Antonio Ciccolella

The two largest Milky Way satellite galaxies are the Magellanic Clouds: Large and Small. The former is 14 kpc across and 50 kpc away from the Milky Way, while the latter is 8 kpc across and 60 kpc away. They both have low matallicity and look bluish as they are gas-rich with many young stars. The Large Magellanic Cloud is a barred single-armed spiral galaxy with an off-centered gas disc, while the Small Magellanic Cloud is an elongated irregular galaxy. The two Magellanic Clouds are in orbit around each other with a bridge of gas containing some young star clusters connecting them. Their orbit around the Milky Way has a period of 2 Gyr.

Of the other Milky Way satellite galaxies, many are dwarf spheroidals. They are considerably dimmer than the Magellanic Clouds, have no gas, are very metal-poor, and host very old (10 Gyr) stars. Their metal-enriched gas was ejected by supernovae. They have various bursts of star formation rather than a single star formation stage as globular clusters do, despite their similarities. Some of these spheroidal dwarf galaxies, like Sagittarius, are being tidally disrupted by Milky Way's gravitational field.

Of the three major galaxies in the Local Group, the biggest and the brightest is M31 (Andromeda galaxy), see the left image in Figure 1.7. Its de Vaucouleurs classification is SA(s)b, due its tightly wound spirals and large bulge. It has several satellites including the elliptical M32. Similar to the Milky Way, M31 has a central black hole in its nucleus. M31 is home to around 300 globular clusters, twice that of the Milky Way. M31's halo hosts metal-rich stars that could only have been formed in other massive galaxies; this is a sign of M31's cannibalistic past. M31 is on a collision course with the Milky Way, which is believed to occur in a few Gyr time. The end result of the collision is likely to be a larger elliptical galaxy.

The smallest of the three main galaxies in the Local Group is M33 (Triangulum galaxy); see the right image in Figure 1.7. Its de Vaucouleurs classification is SA(s)cd, as it has a tiny bulge and spiral arms that are patchy and open. M33 does not appear to have a central massive black hole, despite having a stellar nucleus. It is home to around 50 globular clusters, thrice less than that of the Milky Way. As compared to the Milky Way and M31, M33 is more gas-rich.

Figure 1.7: Left; M31 (Andromeda). Right; M33 (Triangulum).

The Local Group and the Milky Way share a similar formation history. About 3×10^5 years after the Big Bang (the beginning of the Universe around 14 billion years ago), the temperature and density became low enough for neutral gas to form as ionization fraction dropped. Regions where the density was large enough to trigger collapse, despite the cosmic expansion, became the foundation for large galaxies. These regions were usually accompanied by smaller clumps that formed the satellite galaxies. After 1 Gyr had passed since the Big Bang, stars could form in those clumps. Before matter was flattened onto a disc,

stars could form in the halo and globular clusters that explains their stars' old age. The bulge could be a result of slow inward migration of matter or a merger of two protogalactic fragments.

An important process that happens over the years in galaxies is chemical enrichment. The primordial nucleosythesis (shortly after the the Big Bang) only produced hydrogen, helium, and some lithium. Any element beyond these is created in stellar nucleosynthesis and even heavier ones in supernovae. This means that in a stellar population as time goes on the fraction of heavy elements, i.e. metallicity, generally increases. The proof of this is the presence of more metal-rich stars in regions where star formation is more abundant. As mentioned previously, young metal-rich stars (Population I) are mostly found in the thin disc (high star formation rate), whereas old metal-poor stars (Population II) are mostly in the thick disc and the halo (low star formation rate). No stars with primordial composition (Population III) are known.

1.1.6 Disc galaxies

As discussed in the classification section, disc galaxies are divided into lenticulars (S0) and spirals (S). The random motion of stars in the disc are as small as 5%, hence they are said to be *dynamically cold*. Spirals are the most common type of giant galaxies and produce the most light in the Universe. A lot of the features discussed for the Milky Way applies to other spirals.

As disc galaxies possess a thin structure and the galaxies we observe can have any orientation, it is very common to find galaxies that are not face-on. The inclination of a disc galaxy is the arc-cosine of the ratio of the observed minor and major axes. A face-on galaxy has 0° inclination, whereas an edge-on galaxy has 90° inclination. The inclination of a galaxy affects its observed surface brightness; in the absence of dust, an inclined disc (inclination of i) shines with a brightness $1/\cos i$ of its face-on brightness. Note that this rule stops working before $i = 90^\circ$ (when the disc is completely edge-on) due to the finite thickness of the disc and dust.

The *luminosity profile* is obtained when the surface brightness is averaged azimuthally for a constant radius; it is a relation between the surface brightness and the radial distance. Generally, the luminosity profile of a disc is an exponential (Freeman, 1970) or a broken exponential (Erwin et al., 2005). The different types of luminosity profiles based on the shape are Type I, Type II, and Type III (Erwin et al., 2008). Type I refers to those that only have a single exponential fit. Type II refers to those that have a down-bending (truncated) broken exponential fit. Type III refers to those that have an up-bending (antitruncated) broken exponential fit. It is possible that the luminosity profile of a galaxy has multiple truncations and/or antitruncations, in which case the type is a combination of the main types. Type II truncations often are observed to be at the end of spiral arms or near outer rings (Laine et al., 2014); such are expected regions for resonances to occur. Type II breaks are sometimes linked to resonances (Buta and Combes, 1996). Type III breaks might be related to a disc-halo transition region or in some cases the superposition of a thin disc and a thick disc (Comerón et al., 2012). An extended classification scheme for luminosity profiles are presented by Erwin et al. (Erwin et al., 2008); see Figure 1.8.

Edge-on disc galaxies do not reveal features such as bars or rings when observed, but they are valuable for allowing other features to be seen that could not have been seen if they were face-on. Many edge-on galaxies show a dust lane that is thinner than the stellar disc. Seeing a galaxy edge-on allows a clear distinction between thin and thick discs to be made (Comerón et al., 2012).

As more disc galaxies were observed, it became apparent that there are several kinds of bulges (central

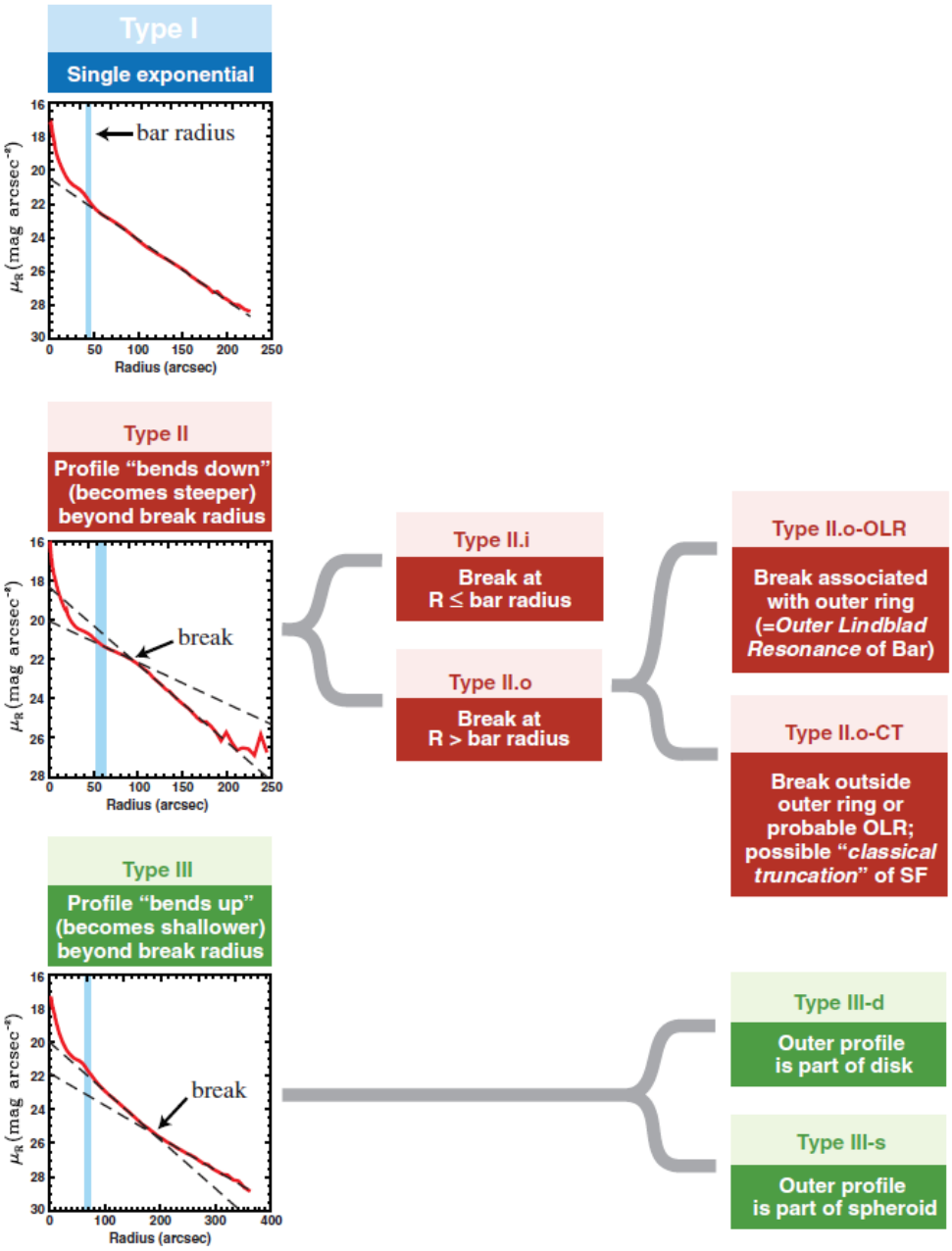

Figure 1.8: This is a general outline of the luminosity profile classification scheme used by Erwin et al. (2008). Credit: Erwin et al. (2008)

mass concentration). Nowadays, we call "classical bulges" the ones that have a clear ellipsoidal shape. The ones that are discs with a scaleheight larger and a scalelength shorter than the main disc are called "pseudobulges". A third category exists that contains edge-on bulges that appear boxy or peanut-like in appearance; these are called "boxy/peanut bulges" (Athanassoula, 2005). Boxy/peanut bulges are in fact bar-lenses (lens-like stellar structures found embedded in bars) that appear that way when seen edge-on (Laurikainen et al., 2014). Classical bulges resemble elliptical galaxies located in the middle of a disc (Kormendy, 2016). However, pseudobulges appear to be a disc within a disc, often with substructures such as spiral arms, rings, or nuclear bars (Kormendy, 1993). There are also bulge-less spiral galaxies (Salo et al., 2015). Interestingly, there are individual galaxies that include multiple superposed bulges of

various types (Peletier et al., 2007).

In general, bulges are redder than the disc as they are more metal-rich and gas-poor. The size of the bulge is measured by its *effective radius*. This is the radius within which half of the light from the bulge is contained. Disc galaxies as a whole become bluer and fainter when going from early-type to late-type galaxies. Early-type disc galaxies are generally more centrally concentrated with a large central bulge. They are also smoother as they lack the star formation patchiness induced in late-type disc galaxies.

Using multi-wavelength observations of disc galaxies one can confirm that the hottest stars (tracers for young star populations) are found in the arms and rings where star formation occurs. These hot stars are well seen in UV images, while the bar is almost invisible as it mostly contains older star populations. To see these older regions clearly infrared images are used (Eskridge et al., 2000).

The gas content of spiral galaxies is similar to that discussed in the case of the Milky Way. It is known that the average H I density in the main disc is around the same for all spiral galaxies. This is due to self-shielding. H I is made when H_2 gets photodissociated, so if there is too much H I then it will shield H_2 from getting ionized and it self-regulates its production rate to a constant density. However, the density of H I in the extended disc and H_2 may vary depending on the galaxy.

Rotation and transfer of angular momentum is how the discs are supported in disc galaxies (Lynden-Bell and Pringle, 1974), unlike elliptical galaxies (spherical systems in general) where random motion and outward transfer of energy supports the system (Lynden-Bell and Wood, 1968). By the Newtonian principles mentioned in the Milky Way section one obtains the relation for the rotation curve and disc mass within a specific radius, which is $V^2(R) \approx \frac{GM(<R)}{R}$ (essentially the Newtonian orbital velocity formula). This is where the gas (H_I) in the outskirts of the galaxy comes in handy, as it has very little random motion and asymmetric drift making its orbit almost perfectly circular. This means that by knowing the outskirt gas rotation curve, one can study the mass distribution up until the outer regions of the galaxy.

To find the rotation curve of the galaxy the systematic motion of the galaxy mainly due the Hubble-Lemaître flow (Lemaître, 1927; Hubble, 1929) must be subtracted, as this universal expansion affects any galaxy's velocity map. The rotation curve is then obtained as contours of constant velocity at a specific radius and azimuthal angle. The result is a "spider diagram", see the right image of Figure 1.9. The etymology is due to velocity contours forming features that look like spider webs. The left image of Figure 1.9 shows the gas distribution for a nearby galaxy of Circinus (LEDA 50779), while the right one shows its velocity field. The contours close on themselves due to the velocity reaching a maximum at a given radius and then dropping in value at larger radii. The systematic receding velocity of Circinus galaxy is around 440 km/s while its rotational velocity is around 200 km/s, which results in the velocity field seen in the right image of Figure 1.9.

Studying the velocity field of disc galaxies typically gives a fast climb in rotational speed for the inner 1 to 2 kpc, after which the rotation curve remains flat. This means that the rotational velocity at any given radius is a roughly constant value V. This means the angular velocity ($\Omega = V/R$) drops with radius, which explains the *differential rotation* of matter in the discs (Lindblad, 1927; Oort, 1927). Differential rotation means that the orbital period in the inner regions of the galaxy is shorter than the outer regions; i.e. the orbital period lengthens with radius.

As mentioned previously, a flat rotation curve is impossible if one only considers the gravity of visible (baryonic) matter (Bosma, 1981). According to Newtonian physics, there needs to exist an invisible source of gravity (dark matter) for galaxies to remain intact with such large observed orbital velocities.

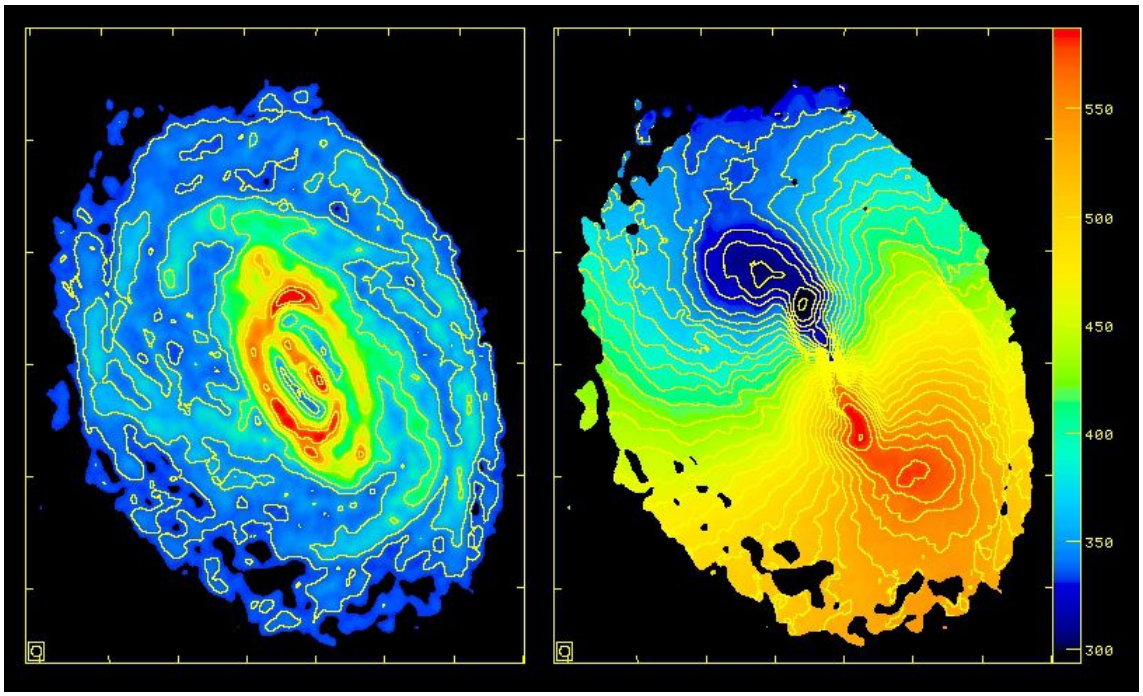

Figure 1.9: Left; H I gas distribution in Circinus galaxy. Right; velocity field of H I gas in Circinus galaxy. Credit: B. Koribalski (ATNF, CSIRO), K. Jones, M. Elmouttie (University of Queensland), and R. Haynes (ATNF, CSIRO)

Observations show that generally larger galaxies (mainly early-type Sa & Sb) rotate faster than smaller ones. Rotation curves of early-type galaxies grow more steeply as compared to late-type ones when it comes to central regions, as the early-type ones have denser central mass concentrations of baryonic and/or dark matter. Overall, it is believed that around 50% of the mass of early-type spirals is dark matter, while this fraction increases to 90% in case of late-type spirals.

An important relation that comes up when studying galaxy rotation curves is called the *Tully-Fisher relation* (Tully and Fisher, 1977). This is a relation between the luminosity of a galaxy and its maximum orbital velocity; $L \propto V_{\text{max}}^{\alpha}$ where α is around 4. Note that luminosity is determined by the galaxy's baryonic content, while the maximum orbital velocity is mainly determined by the amount of dark matter present. This mysteriously suggests that a dark matter halo of a given mass knows how much baryonic matter needs to be stored in it! Using single-dish radio-telescopes it is possible to easily obtain the maximum orbital velocity without having to map the entire rotation curve of the gas. This makes the Tully-Fisher relation very helpful in easily finding the luminosity of galaxies.

The spiral arms of spiral galaxies are visually divided into two categories: grand-design and flocculent (Elmegreen and Elmegreen, 1989). Grand-design spiral arms are continuous and traceable over lengthy twists while flocculent spiral arms consist of many short discontinuous arm-segments. Around 20% of spirals are grand-design as opposed to 50% being flocculent; the other 30% are multi-armed (Buta et al., 2015). Grand-design spirals are more often seen in early-type galaxies whereas flocculent ones are more often found in late-type galaxies (Elmegreen and Elmegreen, 1985). If the spiral galaxy is barred, the spiral arms usually start at the end of the bar. Spirals usually have tips that go to the opposite direction of disc rotation, meaning they are trailing. Spiral arms are rich in hot gas and dust which makes them great star furnaces (Schweizer, 1976).

One way that spiral arms can be formed is due to the differential rotation that exists in the disc of spiral galaxies. A region may start to have higher rates of star formation, which causes even more star formation as the surrounding clouds are disrupted and poised to collapse more often. This way a region of higher stellar density is maintained within the disc. The differential rotation then stretches this region into a winding spiral; see Figure 1.10. This does not explain why some spirals are so long lasting, as in this explanation all spirals should eventually disappear as they are wound tighter and tighter.

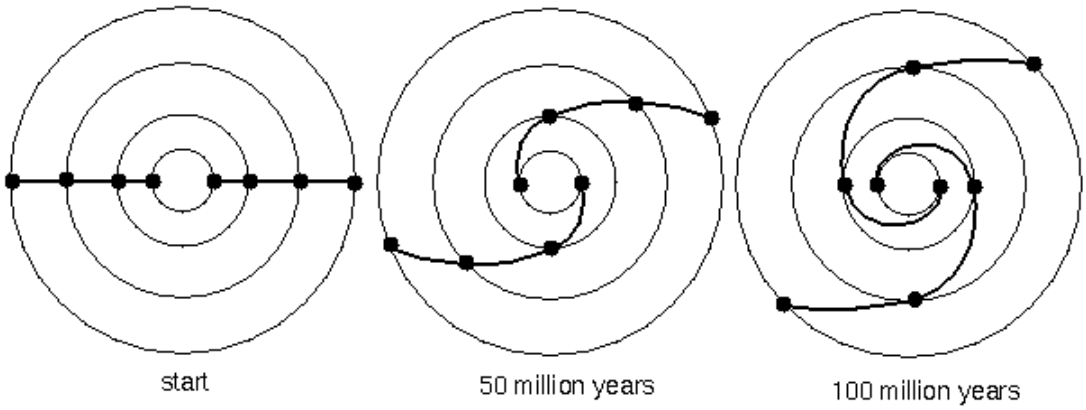

Figure 1.10: How a straight feature in the disc can get wounded into a spiral (i.e. differential rotation spirals). Credit: Nick Strobel

Another explanation uses the presence of epicycles. It was previously discussed that stars follow orbits which are not strictly circular and their radius oscillates as they go around the galaxy. Additionally, we argued that their orbits are not circles or ellipses but rosettes. If a population of stars with a certain guiding center at a single moment in time is considered, their nested epicyclic orbits form a density wave with a specific orientation; see Figure 1.11. At a later time stamp, these stars will have moved in their rosette orbits and the density wave that they make would shift its orientation. The rate at which this density wave, i.e. spiral arm, moves is called the *pattern speed*. Note that the pattern speed is slower than the orbital speed, which means when stars complete an actual orbit around the galaxy the spiral arms have not yet completed a full cycle. It is possible to create multiple arms in the disc if the epicyclic parameters are set appropriately. This type of spiral would also get tighter over time, although at a rate much slower than the differential rotation spirals. These kind of spirals are called *kinematic* spirals. In reality the galactic spiral arms are explained using density-wave theory, which utilizes the kinematic spiral model and combines it with the self-gravity of the disc material. The addition of self-gravity into the mix reinforces the spiral pattern and prevents spiral arms from winding indefinitely. Using density-wave theory, one obtains that an m-armed spiral can only exist between the Inner and Outer Lindblad resonances, which occur at radii determined by the pattern frequency and the epicyclic frequency. The density-wave theory and resonances are discussed in more detail later.

Another feature that most (50% to 60% of) disc galaxies have is the bar (Knapen et al., 2002). They can be as bright as up to 30% of the entire host galaxy's brightness. They are almost as flat as the disc itself, except for the peanut-like bulges. They have a pattern speed, similar to spiral arms, but they are not density waves. A bar has a firm structure of trapped stars and matter, which have elongated (rather than close to circular) orbits contained within the bar. The maximum possible extent of bars is determined

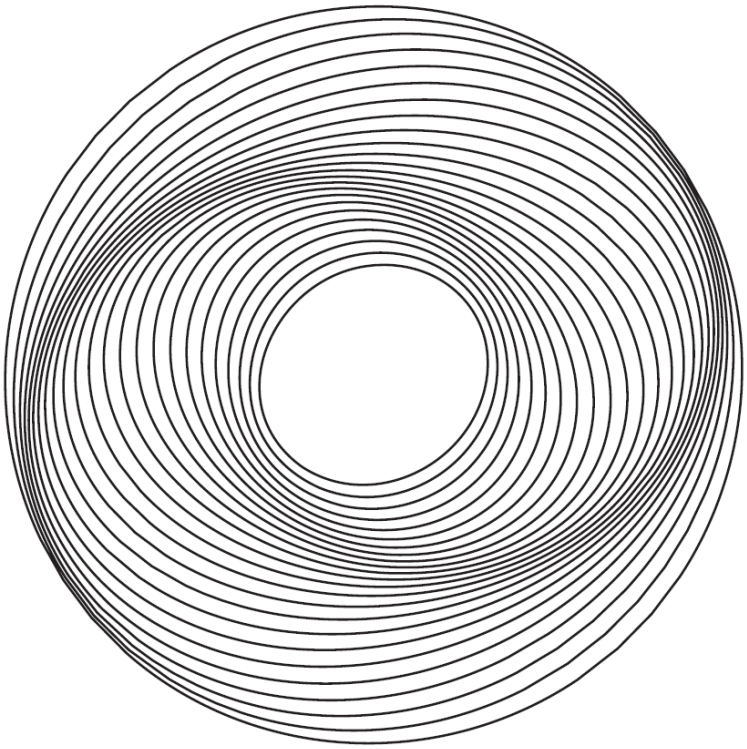

Figure 1.11: How some nested epicyclic stellar orbits can form a density wave pattern (i.e. kinematic spirals); this is a two-arm density wave formation. This shows the epicyclic orbits in the pattern speed frame of reference, which is why the orbits close unlike what was seen in Figure 1.5. Credit: "Galaxies in the Universe, An introduction" by Sparke and Gallagher (2000)

by their pattern speed; it is the radius where stellar orbits have the same orbital frequency as the bar pattern speed. Simulations show that resonances induced by the bar pattern speed push stellar matter beyond the corotation to outer radii, causing the stellar density and thickness of the outer disc to grow (Schwarz, 1984); it also pushes gas inwards from CR to the inner 4:1 resonance (I41) where inner rings are formed. For example, the inner 4:1 resonance creates inner rings near end of the bar; these resonances are discussed later. It is vital to note that spiral arms and bars do not necessarily have the same pattern speed, most notably in late-type galaxies. There exist a distinction between bars in early-type and late-type galaxies; early-type (bulge-dominated) bars are longer and show a luminosity profile that is flat, whereas late-type (disc-dominated) bars are shorter and show a luminosity profile that is exponential (Erwin et al., 2005; Kim et al., 2015). The strength of a bar is determined either by obtaining the ratio of the tangential force it exerts to the mean radial force field (Combes and Sanders, 1981) or by getting its intrinsic axial ratio photometrically (Laurikainen and Salo, 2002).

In the very core of disc galaxies the structure is very rigid with an angular velocity that is almost constant, which means differential rotation is almost absent. This creates ideal conditions for in-falling gas clouds (due to loss of angular momentum in the bar) to collapse and form stars. This explains why some galaxies show signs of intense star-burst in their cores and have nuclear star clusters (seen in the Milky Way); the star-burst process is short-lived as the quantity of gas available for such activities is limited.

1.1.7 Elliptical galaxies

Elliptical galaxies have a wide range of masses, thus both the brightest and the dimmest galaxies in the Universe are ellipticals. They can be classified based on the luminosity as luminous ellipticals, midsize ellipticals, and dwarf ellipticals. Unlike spirals, in case of ellipticals by knowing their luminosity we can know almost everything about their other properties. Their shapes are almost perfectly elliptical, as the name suggests, so their degree of ellipticity is used in the Hubble classification scheme, which was discussed previously. In the outer regions of elliptical galaxies one often observes *shells*, which are arc-like structures that might be remnants of gravitationally disrupted small galaxies.

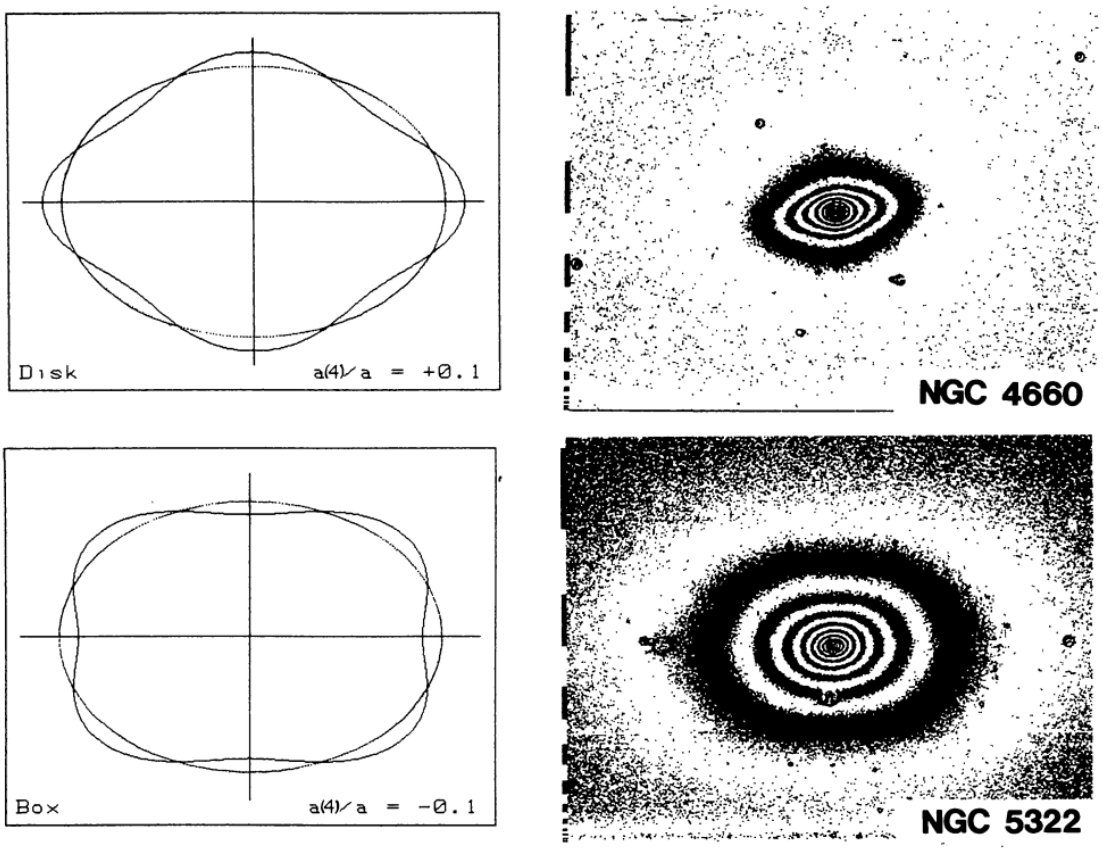

Figure 1.12: Disky (top) and boxy (bottom) isophotes in luminosity profiles of elliptical galaxies. Credit: Bender et al. (1988)

Generally, luminosity profiles of elliptical galaxies are studied in a similar way to those of bulges (of disc galaxies). In the case of luminous and midsize ellipticals, there exists an inverse co-relation between the total luminosity and the central surface brightness, i.e. the brighter the galaxy, the lower its central surface brightness is. Using the high-resolution luminosity profiles obtained from Hubble Space Telescope's observations, it is usually found that midsize ellipticals have a central cusp, whereas luminous ellipticals have a central core (a region where luminosity profile is flat). In general one finds that the dimmer an elliptical galaxy is, the more flattened it is.

Isophotes are contours of constant surface brightness in a luminosity profile. These are the features used to measure the ellipticity of an elliptical galaxy (Bender et al., 1988). Isophotes of elliptical galaxies are divided into two groups: boxy and disky (Lauer, 1985); see Figure 1.12. It is clear that the key difference is in the general roundness of the two; boxy isophotes have extended corners while disky ones

have extended tips. Sometimes the ellipticity (ratio of the major axes) changes with radius in an elliptical galaxy (Peng et al., 2002). It is also possible that a twisting in the isophotes is observed, in other words, the orientation of the observed major axes of the isophotes varies as one moves outwards along the nested isophotes. Twisted isophotes are more commonly observed in boxy-isophote ellipticals.

In disc galaxies the velocity map is produced by looking at 21cm line of H I gas, this is not possible for elliptical galaxies because, although they contain copious amounts of hot (ionized) gas, they contain very little cool (atomic) gas. Midsize and luminous ellipticals contain so little atomic gas that in less 10% of them cool gas is detected at all. For ellipticals, velocity map stellar absorption lines are studied which require high signal-to-noise ratio observations. The general oblateness of ellipticals means that, regardless of orientation, there is always a large number of stars that fall along the line-of-sight. So for each observed pixel, the line-of-sight velocity is an average of many stellar values, which significantly tarnishes the usefulness of these velocity maps to study detailed stellar kinematics.

In case of elliptical galaxies, there exist a relation between central velocity dispersion and luminosity, which is known as the *Faber-Jackson* relation (Faber and Jackson, 1976). This is the elliptical equivalent of disc galaxies' Tully-Fisher relation, albeit it is not as useful due to the challenges of correctly measuring the luminosity of elliptical galaxies. A better relation for ellipticals is the *fundamental plane* relation, which relates effective radius of an elliptical galaxy with its central velocity dispersion and the surface brightness at the effective radius.

It is observed that elliptical galaxies lack young stars (blue and highly luminous). Additionally, spectra of elliptical galaxies indicate that at least for the past 1 to 2 Gyr they have not experienced any significant star formation. The luminosity of these galaxies is mainly from solar mass stars in their red giant phase. This makes them comparable to bulges of disc galaxies; both are red and metal-rich. In general, luminous ellipticals are redder and more metal-rich than midsize ones, i.e. redness increases with luminosity. On average elliptical galaxies contain twice as much globular clusters than a disc galaxy of the same luminosity.

To obtain the mass of an elliptical galaxy the H I velocity measurements can only rarely be used, as mentioned above, so Virial theorem and globular cluster systems are used to study the mass profile of ellipticals. It is believed that, while the centers are mainly dominated by baryonic matter, the outskirts are filled with dark matter. Elliptical galaxies, just like disc galaxies, host massive black holes in their nuclear region. Generally in galaxies where the velocity dispersion is larger, the nuclear black hole is more massive.

1.1.8 The Local Universe: Groups, Clusters, and Large-scale structures

Around 50% of galaxies in the Local Universe (region of 1 Gly in radius) are in groups or clusters. Galaxy *clusters* are collections of at least 50 luminous galaxies typically a few Mpc across, whose mass is dominated by lenticulars and ellipticals. Up to 10% of luminous galaxies are found in clusters. Galaxy *groups* are smaller collections of only a handful of bright galaxies, for example the Local Group (discussed previously) only contains three major galaxies. A group's mass fraction is dominated by spirals and irregulars. Dynamically, groups exist in two distinct types: sparse and compact. Groups and clusters are gravitationally stable against the cosmic flow. They are young structures unlike the galaxies that make them up, as galaxy orbital periods within these gigantic structures are much longer than stellar periods within galaxies. Furthermore, similar to galaxies, most of the matter in galaxy groups and clusters is dark.

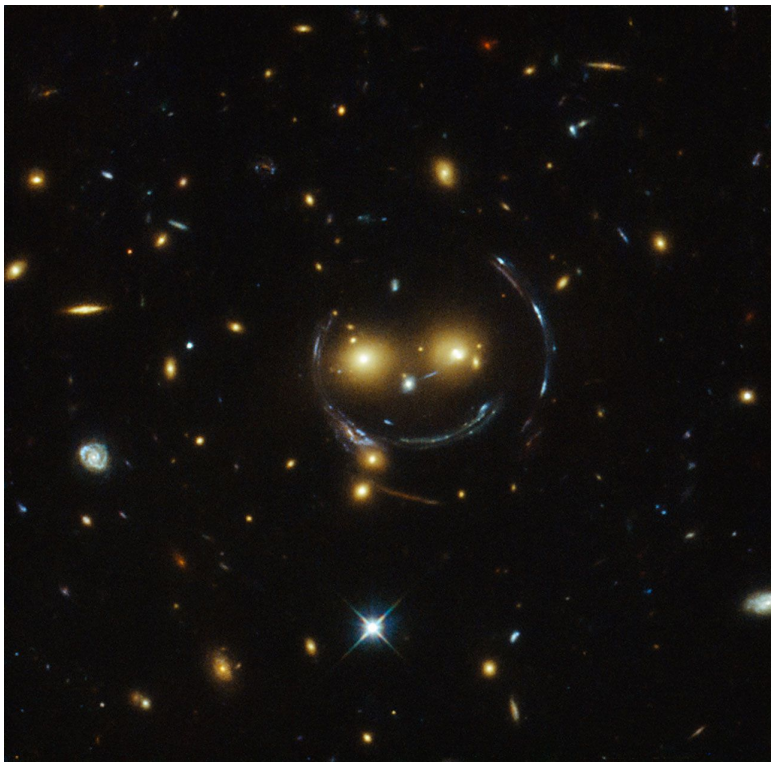

Figure 1.13: Gravitational lensing observed for the galaxy cluster SDSS J1038+4849. Credit: NASA/ESA Hubble Space Telescope

Galaxies in a group or a cluster get decelerated by a mechanism called *dynamical friction*, which is exerted by randomly moving surrounding matter on the moving body (Chandrasekhar, 1943); in this case the moving body is a galaxy and the randomly moving surrounding matter are stars and dark matter particles of another galaxy. This friction is greater on bodies that move slower. Additionally, massive bodies are slowed down faster than light ones. Note that the dark matter halo of a large galaxy can dynamically decelerate its satellite galaxies and cause them to spiral inwards as their orbits decay overtime. In groups, especially for two closely-bound galaxies, dynamical friction can slow down the pair enough for them to fall into each other and merge, creating tidal tails and intense starbursts in case of gas-rich galaxies (Moore et al., 1998). Dynamical friction can also affect the features of galaxies such as spiral arms or bars.

The *morphology-density* relation states that ellipticals are more plentiful in cluster cores while spirals are mainly found in the outskirts. This is because in the core merger events and other interactions are more common. The end result of mergers is either lenticulars or disky ellipticals if the original galaxies were rich in cold gas ("wet merger"), otherwise the end result is boxy ellipticals ("dry mergers"). Hence, mergers destroy spiral galaxies and replace them by nonspirals. This explains the morphology-density relation as cluster cores slowly transform spirals into ellipticals. During mergers and galactic encounters many stars and gas are ejected into the intergalactic space such that this space is filled with stars and gas. It is estimated that as much as 10% to 20% of stars in a galaxy cluster are found in the space between galaxies. The extreme mass of clusters also allows them to accumulate further intergalactic gas, which is kept hot due to constant feedback by supernovae and AGN (explained in the next subsection) winds. Since the gas is hot it cannot collapse into stars, which explains how the intergalactic space can always

host such massive amounts of gas.

Gravitational *lensing* allows for a precise mass measurement of clusters, based on the principles of Einstein's General Relativity (Einstein, 1916). This makes it a great tool for estimating dark matter content (Mandelbaum et al., 2006; Gavazzi et al., 2007). It happens as a mass clump (in this case a cluster) warps the space-time around it, causing the light coming from behind it to follow a bent path. This means the surrounding image is distorted (magnified and stretched), see Figure 1.13. This is a much more reliable method of mass measurement as compared to Virial Theorem that requires a number of assumptions regarding galaxy clusters.

Redshift surveys of the sky reveal the receding velocity of even the most distant of galaxies. Then using the Hubble-Lemaître law the distance to such distant objects is found. Combining the distance information with the angular positions one can map the observed distant objects around the Milky Way. In the near-by regions (small redshifts), the 3D map reveals an overdense supergalactic plane containing several clusters. While at greater redshifts, a large-scale structure of galaxy clusters united by filaments and walls of galaxies creating voids (low galactic density) of around 50 Mpc in size appears to exist.

1.1.9 Active Galactic Nuclei

The main forms of emission seen from galaxies are the stellar emissions and hot gas emissions. A third form of emission is observed when radiation is detected from the galactic core. These nonstellar and nongaseous central galactic emissions are called *Active Galactic Nuclei* (AGN) emissions. AGN emissions may range from radio to gamma rays. They can be so powerful that they outshine their entire host galaxy.

AGNs are linked to emissions from matter accreting onto a central supermassive black hole (Peterson and Wandel, 1999). The source of the matter is thought to come from the disc as the bar is expected to create a continuous inflow of cold gas towards the nuclear region, but this is not a sufficient explanation for the observational data and remains an unsettled topic (Wada, 2004). The AGN spectra show matter reaching velocities of up to 10^4 km/s. The size of the active region is on the order of the Solar system (some light-weeks across). For matter to reach such velocities at such small radii the central mass must be of the order of $10^8 M_\odot$, which is expected for supermassive black holes.

Seyfert galaxies are those that show AGN activity with a luminosity smaller than $10^{11} L_\odot$. They may show jets of highly polarized emissions in radio images, despite looking "normal" in optical images. These jets are linked to synchrotron radiation of relativistic electrons being accelerated by strong, rotating magnetic fields. The Seyfert galaxy spectra show some lines that could only exist if there were extremely energetic photons present in the AGN; these photons are so energetic that their origin cannot be stellar. Such energies are achieved when matter free-falls onto an extremely compact body (e.g. supermassive black hole) as discussed by Peterson and Wandel (1999). The kinetic energy of the free-falling matter increases and due to its angular momentum it forms a disc around the compact body. As more matter accretes, due to friction, the kinetic energy is converted into heat. The hot matter then radiates, just as a star would, via black-body radiation. It can reach a maximum luminosity of the order of the Eddington luminosity, which is a general limit for the black-body radiation of matter (greater luminosities begin to push matter away as radiation pressure starts to exceed the gravitational force); for instance see Prialnik (2000). This is a very efficient process of releasing energy as around 10% of the in-falling mass is converted into pure energy. This energy ionizes the matter to create plasma in the vicinity of the compact body. This region generally has extremely strong magnetic fields and rotates extremely fast, so it directs

the plasma into two jets along rotation axis. Note that throughout this process various forms of radiation are released. The hot accretion disc itself shines in optical, UV, and X-ray, while the synchrotron emission of the jets is detected in radio and infrared as well as a detection gamma rays when photons get scattered by the jets. Seyfert nuclei are usually found in disc galaxies and around 1% of them host a Seyfert AGN.

Low-Ionization Nuclear Emission Regions (LINER) galaxies are usually classified as AGN galaxies. They are less bright than Seyfert galaxies and do not show such high energies. LINER galaxies are seen in around 30% of nondwarf galaxies.

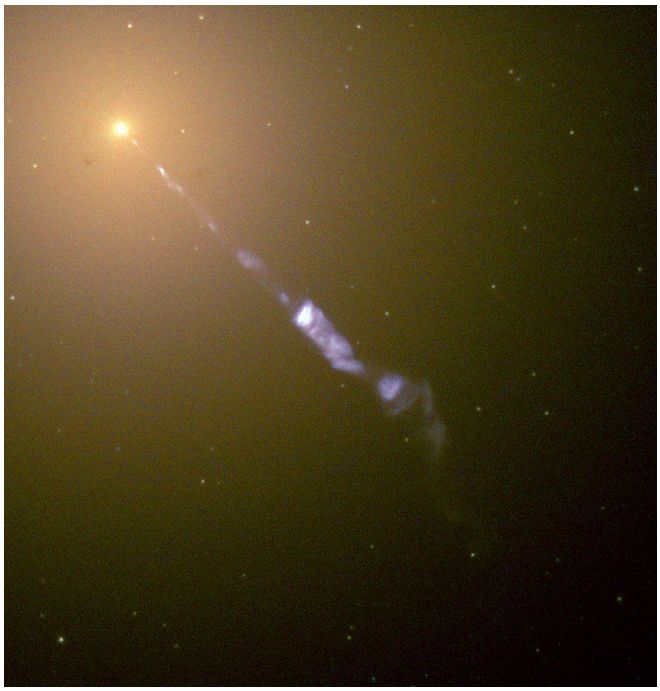

Figure 1.14: Messier 87 (M87) elliptical galaxy with its 5000 ly long plasma jet. Credit: NASA and The Hubble Heritage Team (STScI/AURA)

Radio galaxies are the ones that show the strongest radio output; if the radio luminosity is larger than 10^{34} W (roughly $10^{8} L_{\odot}$) then it is considered a radio galaxy. Note that radio galaxies are even stronger radio emitters than Seyfert galaxies. They are almost always elliptical galaxies and are very rare. In Seyfert galaxies the radio jets do not protrude much out of the disc, but in radio galaxies the jets can be very large, see Figure 1.14. The stronger the radio source, the larger the jets look. These radio jets "shine" the most at low radio frequencies. Around 10% of radio galaxies also emit synchroton radiation in the optical range.

Quasars are the AGNs that can outshine their host galaxies. These are the most luminous objects in the known Universe; they can be observed no matter how far they are in the visible Universe. The typical brightness for a quasar is around $10^{12} L_{\odot}$ (Kaspi and Netzer, 1999). Similar to Seyfert galaxies quasars are not the best radio emitters, but the ones with the strongest radio emissions also happen to be of the brightest quasars. Quasars are more frequently observed at redshift 2, just a few billion years after the Big Bang, and are rarer nowadays. This suggests that galaxies had a stronger nuclear activity when they were younger.

1.2 Disc galaxies: Density-Wave Theory and Resonances

The main topic studied in this thesis is resonances in disc galaxies, which is explained through density-wave theory. In the previous section, the general overview of galaxies, resonances were mentioned but not discussed extensively; they are explained further here.

1.2.1 Density-wave theory

To explain the formation of spiral arms in disc galaxies, nowadays, the well-established density-wave theory is used. The origin of this theory dates back to the 1920s and the pioneering work of the Swedish astronomer Bertil Lindblad (Lindblad, 1927; Pasha, 2004). For the next three to four decades the genesis of spiral arms still baffled astronomers and sparked debate; for instance, some speculated that spiral arms may be related to the galactic magnetic field (Hoyle and Ireland, 1961), which is implausible as it requires the galactic magnetic field to be much stronger than what is observed. One of the major issues facing any theory that attempts to explain the formation of spiral arms is the *winding dilemma* (Vorontsov-Velyaminov, 1958). In those days the spiral arms were thought to be "rigid" structures. This coupled with the differential rotation of matter in the disc gave rise to the winding dilemma, which states that "solid" spirals in a differentially rotating disc must twist tighter and tighter. The tightness of spiral arms is measured using the pitch angle, which is the angle between the tangent of the spiral arm and the tangent of a galactic-centered circle at any given galactic radius. In the book "Galactic Dynamics", Binney and Tremaine (2008) show that for a typical (flat rotation curve) galaxy after 10 Gyr the expected pitch angle is around 0.1°. This extremely small pitch angle does not agree with the observational pitch angles that are around 5° to 30° for Sa to Sc spiral galaxies. This disagreement is the basis for the winding dilemma.

Lindblad, in his many publications, linked the formation of spiral arms to gravitational forces and dealt with them as density-waves. Epicyclic frequencies (discussed in section 1.1.4) play an important role in the formation of these density-waves. Lindblad showed that if the value of $\Omega - \kappa/2$ (Ω is stellar angular velocity and κ is the epicyclic frequency) is constant over most of the disc, then the nonclosed rosette-like epicyclic orbits (see Figure 1.5) become closed ovals in the frame that rotates with this constant angular speed ($\Omega - \kappa/2$). In a galaxy these orbits are filled with stars and each of the closed ovals may have a different orientation in such a way that spiral-like kinematic density-waves are formed; see Figure 1.11. Note that $\Omega - \kappa/2$ is the angular speed of the density-wave structure; this is referred to as the pattern speed (Ω_p). When it comes to the winding dilemma, density-wave theory does not suffer from it under the theoretical assumption that the pattern speed is globally constant. However, in real galaxies the pattern speed is only approximately constant and this leads the density-waves to wind, although more slowly (by a factor of Ω_p/Ω) than the "rigid" structure case.

This early variation of the density-wave theory struggled to solve the seemingly unsolvable winding dilemma as well as to correctly implement random motions and self-gravity of the disc particles (Bertin and Lin, 1996). Moreover, the process that lead to the required orientation of the closed epicycles remained unexplained by density-wave theory. In 1964, Chia-Chiao Lin and Frank Shu started to successfully tackle these issues by assuming that the galaxy is made of self-gravitating matter in an infinitesimally thin disc; this addition of self-gravity to the kinematic density-waves gave rise to the so-called quasi-static spiral structure (QSSS) discussed by Lin and Shu (1964). It takes into account a stationary axisymmetric

gravitational potential, which is due to the gravity of the bulge, disc, and the halo. Moreover, it considers a small (perturbing) nonstationary nonaxisymmetric gravitational potential, which may be due to the rotating spiral arms, central bar, or a companion galaxy. The quasi-stationary assumption is made when the nonstationary perturbation is taken to be almost stationary when dealt with in the pattern speed frame. To ease the mathematical challenges, the WKBJ (Wentzel–Kramers–Brillouin–Jeffreys) approximation is used, which is a method utilized when solving linear differential equations. It is shown that there can be m tightly wound spiral arms with a $2\pi/m$ angular distance from each other. For example, the Milky Way is believed to have four spiral arms, i.e. $m_{\text{MW}} = 4$ (Vallée, 2014). Lin and Shu (1966) showed that self-gravity prevents the winding of the spiral structure, i.e. it is self-sustaining. It is theoretically found that the spiral density-wave only exists in the region where $|\nu| = |m(\Omega_p - \Omega)/\kappa| \leq 1$. This marks the radii, at $\nu = -1$ and $\nu = +1$, beyond which spiral arms cannot exist. These are, respectively, the Inner and Outer Lindblad resonances, which are discussed later.

In the case of a self-sustaining spiral structure where the perturbation amplitude is small, the linear dispersion relation[1] of the density-wave is of the form:

$$|k| \propto \frac{\kappa^2(1-\nu^2)}{\Sigma} \tag{1.1}$$

where Σ is the disc surface density (Shu, 2016). This explains one of the spiral arm tightness trends seen in the Hubble classification. It is consequent that the greater the bulge is, the more tightly wound the spiral arms become. This is because a larger bulge means a greater epicyclic frequency (κ), i.e. a larger central mass enhances the epicyclic perturbations. According to the dispersion relation, an increase in κ increases the wave number ($|k|$) and in turn the spiral arms become tighter. This trend was shown to hold by Fujii et al. (2018) through the use of highly realistic galactic disc N-body simulations. The exact dispersion relation is nonlinear and difficult to work with, so it is simplified to obtain:

$$(\omega - m\Omega)^2 = m^2(\Omega_p - \Omega)^2 = \kappa^2 + k^2a^2 - 2\pi G|k|\Sigma \tag{1.2}$$

where $\omega = m\Omega_p$, a is the sound speed, and G is the gravitational constant. Note that this is a different representation of the Equation 1.1 seen above. The difference is that, in Equation 1.2, there is an additional term (k^2a^2) representing hydrodynamic pressure. The first term on the right hand side is positive and relates to the epicyclic motion. This is the conservation of angular momentum that tries to fling matter away. The second term, which is also positive, pertains to the random motion caused by stellar pressure. This tries to move matter away from the density-wave as well. The third term, however, is negative. This is the self-gravity of the density-wave that tries to contain the matter within it. The combination of the three terms stabilizes the matter in the density-waves (spiral arms). The epicyclic term has the greatest contribution at smaller wave-numbers (large scale), whereas the pressure term has the greatest contribution at larger wave-numbers (small scale). The self-gravity of the density-wave is the strongest at intermediate wave-numbers. The wave number (k) solutions in the dispersion relation determine the nature of the possible density-waves. The dispersion relation can result in two wave modes: short (large $|k|$) and long (small $|k|$). Moreover, density-waves can be leading or trailing, which is determined by the sign of k. Trailing ($k < 0$) spiral arms have outer tips that point in the opposite direction of rotation, while leading ($k > 0$) spiral arms' outer tips point in the direction of rotation.

[1] A dispersion relation is an equation that relates angular frequency ω to the wave number k

In 1964, Alar Toomre showed that if the random velocities of particles within a galaxy disc are small enough (as compared to the surface density), then the disc is prone to experiencing unstable disturbances whose dimensions can be as large as the galactic radius and whose time-scales are of the order of the revolution period (Toomre, 1964). This Toomre stability criterion is quantitatively shown as:

$$Q \equiv \frac{\kappa a}{\pi G \Sigma} \geq 1 \tag{1.3}$$

where Q is the Toomre parameter and a is the sound speed (i.e. an indicator of the velocity dispersion). This equation has two extreme forms in the cases of purely-stellar and purely-gaseous discs, but realistically the condition is a combination of both cases as real galaxies contain both (Rafikov, 2001). For example, in case of stellar discs the sound speed (a) is replaced by the stellar root-mean-square radial velocity dispersion. The Toomre parameter, Q, is 1.4 in the vicinity of the Solar System.

Further development in the field has allowed the density-wave theory to evolve into a modal theory. In this modal theory, the density-waves may get reflected at various places in the galactic disc and form a feedback cycle (Mark, 1976). As an example of the density-wave reflections, in Toomre (1981), he describes "swing amplification": a powerful reflection that occurs when a leading density-wave is reflected as a trailing density-wave at the corotation radius. According to the modal density-wave theory, if the disc is dominated by one or only a few global density-wave modes then it is possible for it to host a large-scale QSSS (Bertin and Lin, 1996). More complex ideas have been developed in the context of density-wave theory (such as mode-coupling), which are not explored further here; see Shu (2016) for a more in-depth exploration of the density-wave theory and its history.

As early as the late 1960s, there was observational evidence in-line with the self-sustaining density-wave theory via its application to the Milky Way (Lin et al., 1969). Other observational agreements came as a result of investigating the enhanced star formation rates in the density-wave regions. Due to the differential rotation of the matter in the disc, at the extreme ends of the spiral where the matter angular velocity greatly differs from that of the spiral arms, matter experiences extreme shocks as it enters or leaves the arms. These shock waves are believed to boost star formation (Roberts, 1969). This theoretically creates a colour shift from bluish young stellar populations (where the enhanced density initiates a shock upon entry to the spiral arms) to reddish old stellar populations (where density levels drop to normal levels upon exit from the spiral arms) as discussed by Yuan and Grosbol (1981); see Figure 1.15. In practice, this relation is subject to controversy (Shu, 2016; Gonzalez and Graham, 1996; Rand, 1993). Further observational evidence in agreement with the density-wave theory came after radio observations of the M51 galaxy showed that synchrotron radiation is greatest at the spiral arms, which is indicative of a frozen-in magnetic field and enhanced regional interstellar matter density (Mathewson et al., 1972). Another example of a successful implementation of density-wave theory to observational data includes the modeling of M81's spiral structure (Visser, 1980). It is worthwhile to mention that there are other theories when it comes to explaining spiral arms formation. For example, tidal interactions may explain the spiral structures of M51 and M81 (Toomre and Toomre, 1972; Salo and Laurikainen, 1993, 2000a,b; Thomasson and Donner, 1993).

1.2.2 Resonances

In Physics, resonances occur when an oscillating system is perturbed by an external force such that its amplitude is greatly enhanced; this is possible if the external force is itself oscillating with a forcing

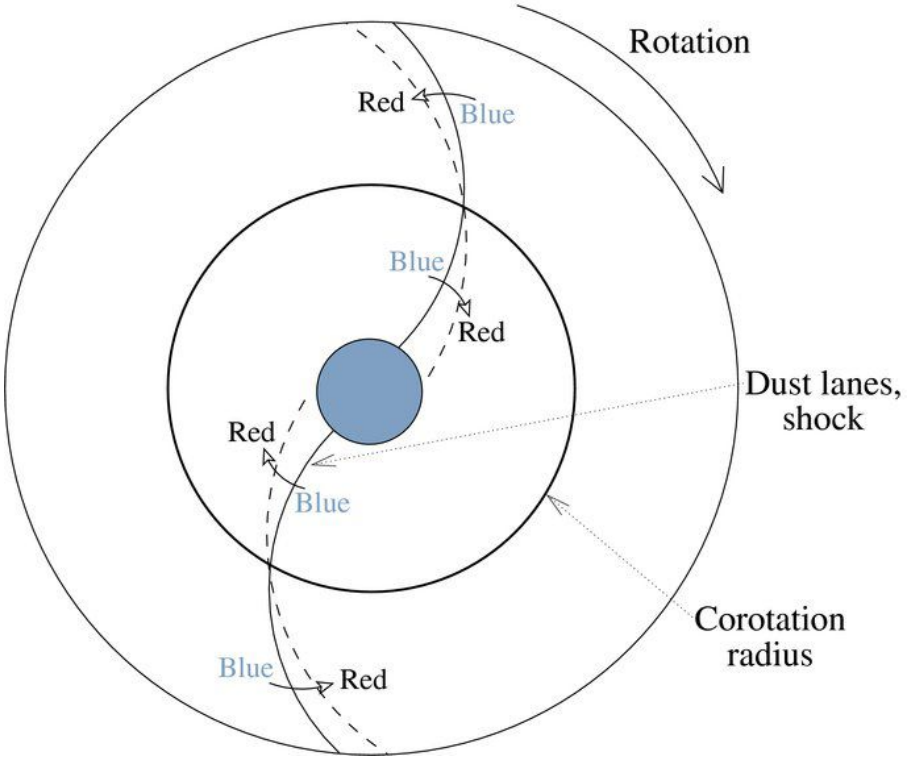

Figure 1.15: The colour shift observed as a result of star formation initiated by the shock front of the spiral arms. Within corotation radius the shock occurs when the matter catches up to the spiral arm, whereas outside of corotation radius the shock occurs as the spiral arm catches up with the matter. Credit: Martínez-García et al. (2009)

frequency that is equal or around one of the natural frequencies (a frequency at which an isolated oscillatory system tends to oscillate) of the main oscillating system. Resonances appear in various fields of Physics and by extension Engineering; they are dealt with in systems as diverse from each other as mechanical, electrical, optical, celestial, acoustic, and atomic. Our interest is their role in the field of Astronomy and, more specifically, how they affect disc galaxies.

In Astronomy, resonances generally come into play when studying Celestial Mechanics. Orbits of celestial bodies are oscillatory in nature[2] which means periodic forcing can alter their orbits and affect their trajectories. For example, the asteroids in the asteroid belt experience various resonance modes due to the influence of Jupiter. Regions whose orbital periods (dictated by their orbital radii) are small integer ratios of that of Jupiter experience a significant "pull" or "push" by Jupiter at a specific moment in their orbit regularly. This can catastrophically disrupt orbits as the eccentricity keeps increasing. This has resulted in the Kirkwood gaps in the asteroid belt; the most notable of these gaps are 3:1 (asteroids complete exactly three orbits as Jupiter completes one), 5:2, 7:3, 2:1, etc (Moons and Morbidelli, 1995). There are also regions in the asteroid belt in which asteroid population has been enhanced due to some constructive resonant effects making their orbits more stable. The most notable gap in Saturn's ring system (between rings A and B), Cassini's division, also has a resonant origin. This gap is formed because it lies at a radius that makes its orbital period to be half that of Saturn's moon Mimas, which puts the region at a 2:1 resonance with Mimas (Porco et al., 2005).

[2]For example, in case of a star in the disc of a galaxy, its natural oscillating frequencies are Ω (angular frequency), κ (epicyclic frequency), and ν_z (vertical frequency).

In the context of this thesis, the type of celestial resonance that we are interested in is the one that occurs in galaxy discs, which is explained via the density-wave theory. This type of celestial resonance is referred to as a *Lindblad* resonance, named after the Swedish astronomer Bertil Lindblad who made great contributions to this field. This type of resonance is also observed in a planetary ring system (most notably in Saturn's), which is another disc system where the density-wave theory is applicable (Goldreich and Tremaine, 1982). In fact, the aforementioned 2:1 resonance of the outer edge of Saturn's ring B with Mimas is an example of this. In general, Lindblad resonances occur when self-gravitating matter in a disc is subject to a nonstationary nonaxisymmetric gravitational potential in addition to the basic stationary axisymmetric gravitational potential (Julian and Toomre, 1966). In galaxies, the forcing nonstationary nonaxisymmetric potential can be due to the spiral arms, a bar, a satellite galaxy, or a companion galaxy nearby; whereas in case of planetary rings, this forcing potential is usually due to the moons orbiting in the vicinity of the rings.

Around a decade after the inception of the density-wave theory, it was shown that disc galaxies want to transfer angular momentum outwards and the nonaxisymmetric potentials, such as the bar and spiral structure, enable them to do so. More specifically, Lynden-Bell and Kalnajs (1972) showed that angular momentum is "emitted" at the inner Lindblad resonance (ILR) while it gets "absorbed" at the outer Lindblad resonance (OLR) and corotation resonance (CR). It is evident that resonances such as ILR, CR, and OLR play a crucial role in driving the structure of the disc and the dynamics of the matter within it through density-wave theory. These resonances occur in regions where there is a small integer ratio between the orbital frequency and epicyclic frequency. There are other resonances that occur, such as the inner and outer 4:1 resonances (respectively, I4R and O4R). The exact resonance conditions are:

$$\Omega_p = \Omega(r) \tag{1.4}$$

$$\Omega_p = \Omega(r) \pm \frac{\kappa}{m} \tag{1.5}$$

where Equation 1.4 refers to the CR condition and Equation 1.5 refers to other resonances. Ω_p is the pattern angular speed, $\Omega(r)$ is the angular speed of a given region (in terms of galactic radius r), κ is the epicyclic frequency, and m is number of spiral arms. For example, in a spiral arm dominated or a bar dominated galaxy the most common resonance conditions are $\Omega_p = \Omega - \kappa/2$, $\Omega_p = \Omega - \kappa/4$, $\Omega_p = \Omega$, $\Omega_p = \Omega + \kappa/4$, and $\Omega_p = \Omega + \kappa/2$, respectively refering to ILR, I4R, CR, O4R, and OLR.

It is possible to apply these conditions to the dispersion relation (Equation 1.2) to obtain the value of the wave number (k) at those radii. The resulting wave number always has two solutions such that the small one refers to long waves and the large one refers to short waves. The dispersion relation calculation in the cases of ILR and OLR gives 0 for the value of the small wave number (long waves). In other words, long waves do not propagate beyond ILR and OLR, meaning that spiral arms only exist within the region defined by these two resonances (Shu, 2016).

1.2.3 Resonance detection

Based on the theoretical explanations so far, it is clear that resonances in disc galaxies (in general, density-wave dominated disc systems) play a key role in determining the structural, gravitational, and kinematic properties of the disc. Therefore, a consistent and reliable detection of their positions can provide Astronomers with invaluable information to further understand the formation history, evolution,

and possibly dark matter content of galaxies. Over the past four decades many resonance detection methods have been proposed, many of which are very varied in nature. This is evident through their vastly different detection techniques, which range from direct measurements, simulation modelling, morphology-related patterns, to theoretically deduced properties. The aim of this thesis is to determine the reliability of one of these resonance detection methods, the Font-Beckman phase reversal method, so in the remaining parts of this introductory chapter these various resonance detection methods are investigated and described thoroughly.

As seen in the theory discussed above, resonances are closely related to the nonaxisymmetric perturbations that commonly exist in disc galaxies; such perturbations occur as a result of a rotating bar, spiral arms, and/or companion galaxies. All these nonaxisymmetric perturbers have one feature in common: they are nonstationary, i.e. they rotate, with respect to the disc matter. The angular velocity of this rotation is fundamentally linked to resonance locations, as seen in Equations 1.4 and 1.5; this angular velocity is the pattern speed (Ω_p). Since most disc galaxies have rigidly rotating strong central bars (Eskridge et al., 2000), finding the bar pattern speed is of utmost importance when it comes to resonance detection. Since bars are "rigid" structures their angular velocity (pattern speed) is constant while their physical velocity increases as a function of galactic radius; this means the more extended a bar is, the larger its maximum velocity is. It is known that the bar cannot be extended beyond its corotation radius (CR), i.e. the region where its velocity approaches the orbital velocity (Contopoulos, 1980), which puts an upper limit on its size. This allows for the introduction of a dimensionless parameter, $\mathcal{R}$, that represents how fast a bar rotates; mathematically it is written as $\mathcal{R} = R_{CR}/R_{bar}$, where R_{CR} is the bar corotation radius and R_{bar} is the semi-major axis of the bar. This parameter is used to define "fast" and "slow" bars; fast bars have $\mathcal{R} \leq 1.4$, while slow bars have $\mathcal{R} > 1.4$ (Debattista and Sellwood, 2000). Note that due to the aforementioned physical limitation on the bar size, the case of $\mathcal{R} < 1$ is physically impossible. N-body simulations show that some bars that originate from companion interactions are slow rotators and only extend to their ILR, as opposed to bars that form spontaneously (due to global bar instability) and are usually fast rotators (Miwa and Noguchi, 1998). It is also shown that resonant interactions with the halo can slow down the bar rotation through angular momentum transfer (Athanassoula, 2003), so if a galaxy has a high density halo in its inner regions then its bar may be significantly decelerated; this is also shown by N-body simulations (Debattista and Sellwood, 1998). Since the halo is thought to be rich in dark matter, this connection with the bar pattern speed can be used to estimate the dark matter content of galaxies.

To date the most reliable method devised that determines bar pattern speeds is the Tremaine-Weinberg (TW) method (Tremaine and Weinberg, 1984). Its high level of credibility is a result of it being model-independent; this also makes it unique among most other resonance detection methods which depend on models in one way or another. To use the TW method the required measurements are the surface brightness and radial velocity obtained along a slit parallel to the line of nodes; see Figure 1.16. These measurements are most reliably done using stellar absorption-line spectrometry, which limits this method's useful regime to mostly gas- and dust-free galaxies. Due to this, most of the early applications of the TW method were performed on a small number of early-type barred (stellar-dominated) galaxies.

The first TW application was done on NGC936 (SB0 type) by Kent (1987), who found $0.86 < \mathcal{R} < 1.80$; this is consistent with the results of another following work (Merrifield and Kuijken, 1995). The TW method was applied to a SBa galaxy, NGC4596, which resulted in $0.92 < \mathcal{R} < 1.53$ (Gerssen et al.,

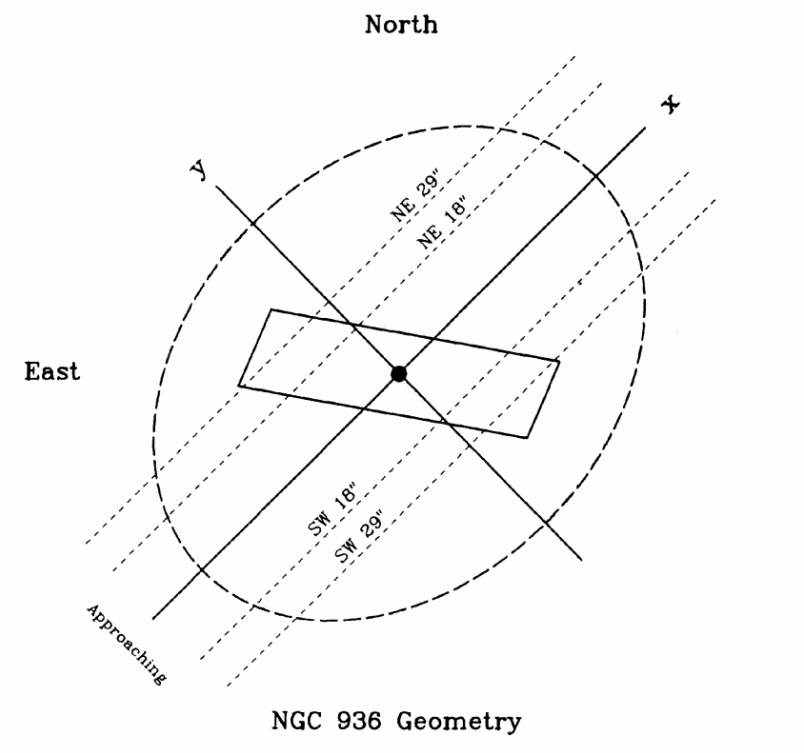

Figure 1.16: This shows the schematics of applying the TW method on a galaxy, in this example it is NGC936. Credit: Kent (1987)

1999). Another application of the method to a sample of 5 SB0 galaxies[3] found that the bar in all of them is fast, i.e. $1.0 < \mathcal{R} < 1.4$ (Aguerri et al., 2003). 4 other SB galaxies[4] were found to have fast bars except one (Gerssen et al., 2003). The first application of Fabry-Perot absorption-line spectroscopy was used in the application of TW method for the SB0 galaxy NGC7079, resulting in yet another fast bar (Debattista and Williams, 2004). A barred dwarf galaxy, NGC4431, was found to have a fast bar (Corsini et al., 2007). Galaxies NGC2523 and NGC4245 were also found to have fast bars (Treuthardt et al., 2007). A set of 15 galaxies[5] were studied using the TW method, which determined all to have fast bars (Aguerri et al., 2015). The largest collection of galaxies studied using the TW method was the sample of 53 barred galaxies[6] from the MaNGA project (Guo et al., 2019), most of which had fast rotating bars; additionally they found that the longer the bar is, the stronger it is.

The previously described studies all applied the TW method to stellar-dominated galaxies, however, there have been a number of studies that attempted to apply this method to gas-dominated galaxies despite

[3] 139-G009, IC874, NGC1308, NGC1440 and NGC3412

[4] NGC271, NGC1358, NGC3992, and ESO281-31

[5] NGC0036, NGC1645, NGC3300, NGC5205, NGC5378, NGC5406, NGC5947, NGC6497, NGC6941, NGC6945, NGC7321, NGC7563, NGC7591, UGC03253, and UGC12185

[6] PGC048479, UGC10842, PGC2547352, PGC2559103, PGC059448, KPG089, PGC012732, SDSSJ032248.51+000844.3, PGC2217551, PGC2272351, SDSSJ074813.26+433505.1, PGC2180324, SDSSJ075136.15+425231.9, PGC024194, PGC2396787, PGC025564, SDSSJ091009.60+461735.9, UGC05859, PGC032794, SDSSJ110632.23+460213.0, SDSSJ110106.82+445238.7, PGC032794, J162105.00+395502.6, PGC2176488, PGC056550, UGC08039, PGC045226, PGC048826, PGC2272149, PGC2292705, SDSSJ133330.80+403132.9, PGC2164620, PGC027014, UGC05016, PGC025475, PGC2162842, PGC030958, SDSSJ102716.54+481406.5, PGC056027, WINGSJ161149.41+491255.3, PGC057933, PGC2368366, PGC2279130, PGC2284351, PGC2285242, PGC057026, PGC2143630, PGC058733, PGC2143630, PGC169660, USGCU769, PGC3129160, and PGC059266

the challenges. The earliest examples are (Rand and Wallin, 2004)[7] and (Zimmer et al., 2004)[8] applying the method to CO observations, who were successful in measuring pattern speeds to some extent. The next application of the TW method to gas-rich disc (late-type barred) galaxies was done in (Fathi et al., 2009) to a sample of 10 galaxies[9] using Hα observations. Fathi et al. concluded that their CR determination results are successful as they are consistent with previous studies and morphological resonance predictions. They claimed that although Hα emitting gas does not obey the continuity equation (a fundamental assumption of the TW method), the TW method can still be used to derive bar pattern speed from gas observations. Meidt et al. in 2009, developed a variation of the TW method called the Radial Tremaine-Weinberg (RTW) method and applied it to 4 gas-rich galaxies[10] (Meidt et al., 2009). E. M. Corsini applied the TW method to a larger sample of gas-rich galaxies[11] and reached the same general trend seen previously that the bars are fast rotators (Corsini, 2011). Bovy et al. (2019) introduced a novel variation of the direct TW method which utilizes the stellar continuity equation. They applied their method to the Milky Way and found that the corotation radius is around 5.1 to 5.9 kpc, which gives $1 \lesssim \mathcal{R} \lesssim 1.2$ as the Milky Way bar is 5 kpc in size; this means the bar is dynamically fast.

It is also possible to determine the location of a resonance or pattern speed through identifying various photometric and morphological features. For example consider the case of galactic rings. It is observationally known that outer rings are located at roughly twice the bar radius distance from the galactic center, while inner rings are at roughly one bar radius distance. This is due to a net torque inflicted by the bar on the gas in the disc. The gas then flows radially dictated by this torque. The torque vanishes at the location of major resonances causing the gas to build up there, creating a ring structure (Buta and Combes, 1996). Further investigation by means of dynamical simulations and orbital analysis lead to the conclusion that the outer ring forms near OLR and the inner ring forms near I4R (inside CR); (Schwarz, 1981, 1984). If the rotation curve is known, these direct resonance identifications can give the pattern speed (Buta and Purcell, 1998). Another morphological method for resonance detection is described by Puerari and Dottori in a 1997 paper (Puerari and Dottori, 1997). This method studies the age of stars across an azimuthal direction. This azimuthal age gradient is linked to the density-wave shock-induced star formation described in the context of density-wave theory; see Figure 1.15. It is found that this azimuthal age gradient must have opposite signs on either side of CR, which can be used to pinpoint the location of CR. The method was applied to NGC7479 and NGC1832, which respectively had two and three resonance radii. This method was applied to a set of 10 galaxies[12] and it was concluded that late-type spirals may be slower rotators than early-type ones (Aguerri et al., 1998). Another study utilized this technique to locate resonance radii in a sample of 13 spiral galaxies[13] (Martínez-García et al., 2009). Sierra et al. applied this morphological method to the largest galaxy sample to date (57 galaxies[14]) and

[7] NGC1068, NGC3627, NGC4321, NGC4414, NGC4736, and NGC4826

[8] M51, M83, and NGC6946

[9] IC342, NGC2403, NGC4294, NGC4519, NGC5371, NGC5921, NGC5964, NGC6946, NGC7479, and NGC7741

[10] M101, IC342, NGC3938, and NGC3344

[11] ESO139-G09, ESO281-G31, IC874, NGC271, NGC936, NGC1023, NGC1308, NGC1358, NGC1440, NGC2523, NGC2950, NGC3412, NGC3992, NGC4245, NGC4431, NGC4596, and NGC7079

[12] NGC1073, NGC1530, NGC2273, NGC3359, NGC3504, NGC3516, NGC4123, NGC5921, NGC6951, and NGC 7743

[13] NGC578, NGC918, NGC4254, NGC4939, NGC3938, NGC7126, NGC1417, NGC7753, NGC6951, NGC5371, NGC3162, NGC1421, and NGC7125

[14] NGC0165, NGC0201, NGC0309, NGC0428, PGC07210, NGC1042, NGC1087, PGC12655, PGC13421, PGC21119, PGC21291, PGC21513, PGC21978, PGC22205, NGC2503, PGC23047, PGC23170, PGC23504, PGC24641, NGC2840, PGC26982, NGC2964, PGC29539, PGC29671, PGC31236, NGC3374, PGC32680, PGC32729, NGC3485, PGC33240, PGC33325, PGC33689, PGC34018, NGC3577, NGC3583, NGC3668, PGC35458, NGC3726, PGC35901, PGC36824,

found that the 17 galaxies which overlapped with other studies showed consistent results (Sierra et al., 2015). Furthermore, they found that around 60% of their sample had fast bars. Another example of this method being used to find resonance radii is seen in Seigar et al. (2018); in this study the galaxy under scrutiny is NGC613.

There are other morphological methods that are used for resonance detection. For example, there are dark gaps seen in early-to-intermediate-type barred galaxies. These are linked to Lagrangian points and are expected to lie close to CR of the bar. R. J. Buta in a 2017 paper used this theoretical connection to locate resonances (Buta, 2017). Using this so-called *gap method*, Buta found multiple resonance radii for each of the 54 spiral galaxies[15] in his sample. A controversial suggestion of this paper was that outer rings are found near O4R instead of OLR, which contradicts the findings of Schwarz (1981, 1984). Another morphological method that appears in the literature is the direct detection of resonances proposed by D. M. Elmegreen and B. G. Elmegreen in 1995 (Elmegreen and Elmegreen, 1995). They claim that "CR is optically visible in most spiral galaxies and is located near the radius of the endpoints of the highly symmetric part of the spiral arms". A resonance detection method used in this thesis that depends on photometry of the disc was mentioned in the previous section when describing luminosity profiles of disc galaxies. This method relies on the connection of Type II breaks and resonances.

In 2007, X. Zhang and R. J. Buta developed a new method to detect resonances, which uses properties related to the secular evolution of disc galaxies (Zhang and Buta, 2007). They called it the *potential-density phase-shift method*, which is related to how kinematics of galaxies and their morphology change over time. By calculating radial distribution of an azimuthal phase shift between the gravitational potential and the density-wave patterns, one can pinpoint the location of resonances. In the same paper they applied the method to a set of 9 galaxies[16] and found that all of them have at least two resonance radii with one having four. Two years later, Buta and Zhang applied their method to a set of 153 galaxies[17] (Buta and Zhang, 2009) from the Ohio State University Bright Galaxy Survey (OSUBGS); (Eskridge et al., 2002). They found that many of the galaxies have multiple resonance radii. For early-type galaxies they obtained an average $\mathcal{R}$ of 1.03 ± 0.37, while the average $\mathcal{R}$ for late-type galaxies was 1.15 ± 0.70.

Resonance radii can be detected with the use of models. It is possible to model individual galaxies

PGC37091, NGC4145, NGC4457, NGC4548, NGC4579, NGC4618, NGC4643, NGC4654, NGC4665, PGC44032, NGC4900, NGC4932, PGC45781, NGC5305, NGC5701, NGC5850, and NGC5921

[15]CGCG810, CGCG1375, CGCG652, CGCG674, CGCG7353, CGCG18514, CGCG26322, ESO32528, ESO36535, ESO4262, ESO43733, ESO43767, ESO56624, ESO57547, IC1223, IC1438, IC2473, IC2628, IC4214, MCG63224, MCG71840, NGC210, NGC1079, NGC1291, NGC1326, NGC1398, NGC1433, NGC2665, NGC2766, NGC3081, NGC3380, NGC4113, NGC4608, NGC4736, NGC4935, NGC5132, NGC5211, NGC5370, NGC5335, NGC5686, NGC5701, NGC6782, NGC7098, PGC54897, PGC1857116, PGC2570478, UGC4596, UGC4771, UGC5380, UGC5885, UGC9418, UGC10168, UGC10712, UGC12646

[16]NGC936, NGC1073, NGC1530, NGC4314, NGC4321, NGC4596, NGC4622, NGC4665, and NGC5247

[17]NGC150, NGC157, NGC210, NGC278, NGC289, NGC428, NGC488, NGC578, NGC613, NGC685, NGC864, NGC908, NGC1042, NGC1058, NGC1073, NGC1084, NGC1087, NGC1187, NGC1241, NGC1300, NGC1302, NGC1309, NGC1317, NGC1350, NGC1371, NGC1385, NGC1493, NGC1559, NGC1617, NGC1637, NGC1703, NGC1792, NGC1808, NGC1832, NGC2090, NGC2139, NGC2196, NGC2442, NGC2559, NGC2566, NGC2775, NGC2964, NGC3059, NGC3166, NGC3223, NGC3227, NGC3261, NGC3275, NGC3319, NGC3338, NGC3423, NGC3504, NGC3507, NGC3513, NGC3583, NGC3593 , NGC3596, NGC3646, NGC3675, NGC3681, NGC3684, NGC3686, NGC3726, NGC3810, NGC3887, NGC3893, NGC3938, NGC3949, NGC4027, NGC4030, NGC4051, NGC4123, NGC4136, NGC4145, NGC4151, NGC4212, NGC4242, NGC4254, NGC4293, NGC4303, NGC4314, NGC4394, NGC4414, NGC4450, NGC4457, NGC4487, NGC4496, NGC4504, NGC4527, NGC4548, NGC4571, NGC4579, NGC4580, NGC4593, NGC4618, NGC4643, NGC4647, NGC4651, NGC4654, NGC4665, NGC4689, NGC4691, NGC4699, NGC4772, NGC4775, NGC4781, NGC4900, NGC4902, NGC4930, NGC4939, NGC4941, NGC4995, NGC5005, NGC5054, NGC5085, NGC5101, NGC5121, NGC5247, NGC5248, NGC5334, NGC5427, NGC5483, NGC5643, NGC5676, NGC5701, NGC5713, NGC5850, NGC5921, NGC5962, NGC6215, NGC6221, NGC6300, NGC6384, NGC6753, NGC6782, NGC6902, NGC6907, NGC7083, NGC7205, NGC7213, NGC7217, NGC7412, NGC7418, NGC7479, NGC7552, NGC7582, NGC7713, NGC7723, NGC7727, NGC7741, IC4444, IC5325, and ESO13810

such that their pattern speeds are found by comparing the simulated morphology to the observed one. To simulate a model galaxy precisely such parameters as mass-to-luminosity ratio, orientation, and internal geometry are needed; these can be assumed or their values can be restricted via kinematical observations. For example, consider the cases of NGC3992 which was modelled in 1988 by Hunter et al. (Hunter et al., 1988), NGC4321 which was modelled in 1995 by Sempere et al. (Sempere et al., 1995), NGC1300 which was modelled in 1996 by Lindblad and Kristen (Lindblad and Kristen, 1996), IC4214 which was modelled in 1999 by Salo et al. (Salo et al., 1999), and ESO566-24 which was modelled in 2004 by Rautiainen et al. (Rautiainen et al., 2004). In 2008, Rautiainen et al. applied simulation modelling techniques with collisionless and inelastically colliding test particles, using the same technique as in Salo et al. (1999) and Rautiainen et al. (2004), to a sample of 38 galaxies[18] and obtained such properties as pattern speeds and resonance radii (Rautiainen et al., 2005, 2008). They found the average dimensionless pattern speed, $\mathcal{R}$, to be around 1.2 for early-type barred galaxies, 1.4 for intermediate types, and 1.8 for late-type barred galaxies. Additionally, they found that the slowest bars are also the shortest ones with respect galactic size. In general, these simulation models tend to have smaller errors when determining resonance radii as compared to the TW method.

A new method proposed in 2014 by S. Roca-Fàbrega et al. uses the vertex deviation, which is the deviation of the stellar velocity distribution ellipsoid from the radial and azimuthal axes of the galaxy (Roca-Fàbrega et al., 2014). This deviation is linked to the nonaxisymmetric potentials of the galaxy (Vorobyov and Theis, 2008). It is shown that when the spiral arms are noncorotating, between CR and OLR, the average vertex deviation has a positive value in-front of the spiral arm, while its value is negative behind the spiral arm; the situation is reversed when the regions inside CR and outside OLR are considered, as shown by S. Roca-Fàbrega et al. in 2014. They used these sign reversals of the vertex deviation to locate resonances. They checked their method analytically and via comparison with simulations. This method is suggested to be useful in applications to the Milky Way galaxy, whose exact CR has been subject to much debate. Unfortunately, there are no vertex deviation measurements for external galaxies yet, making this method not useful in those cases.

The remaining methods of resonance detection rely on the theoretical prediction that matter in the disc changes its streaming direction (in the disc rotation frame) at resonance locations (Kalnajs, 1978; Contopoulos, 1981). This is best visible in gas-rich discs. To obtain a map that allows for the detection of a change in the streaming motion in the rotation frame, one needs to have the *residual velocity map*. This is the observed line-of-sight velocity map of the galaxy, which had the basic circular velocity (i.e. the velocity induced by the stationary axisymmetric potential) removed from it; see Figure 1.18. B. Canzian in 1993 proposed that a CR can be identified by studying the morphological patterns that emerge from a galaxy's residual velocity map; it was shown that in the residual velocity map the morphology inside the CR is distinct from that outside the CR (Canzian, 1993); see Figure 1.17. The Canzian method was applied, for the first time, to NGC4321 by Sempere et al. in 1995, where they compared its results to a model-based analysis of the same galaxy (Sempere et al., 1995). They found that the Canzian method is in good agreement with the model-based prediction of CR.

The last, but not least, method to be described is the Font-Beckman phase reversal method (occasionally

[18]NGC0289, NGC0578, NGC0613, NGC1073, NGC1187, NGC1241, NGC1302, NGC1317, NGC1832, NGC3261, NGC3275, NGC3504, NGC3507, NGC3513, NGC3583, NGC3686, NGC3726, NGC4051, NGC4123, NGC4303, NGC4314, NGC4394, NGC4450, NGC4457, NGC4548, NGC4579, NGC4643, NGC4665, NGC4902, NGC4930, NGC4995, NGC5701, NGC5850, NGC5921, NGC6384, NGC6782, NGC7552, and NGC7723

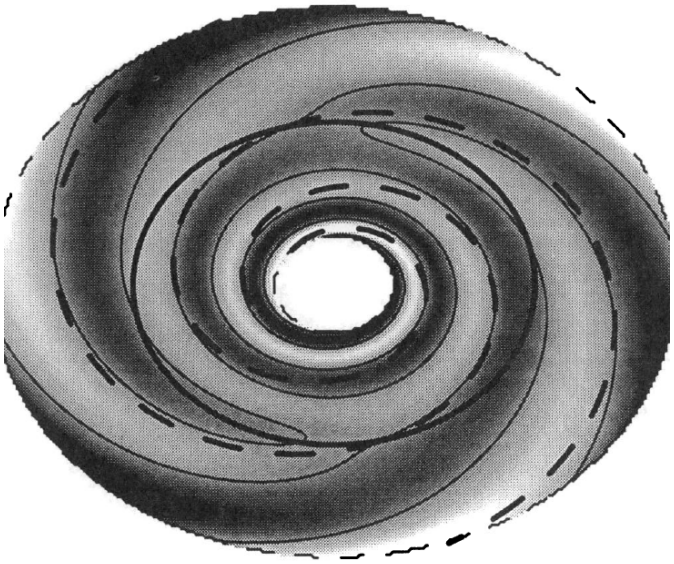

Figure 1.17: This is a model residual velocity map. The disc is contained between ILR and OLR. The solid oval line in the middle is CR. The dashed spiral is the minima of the two-armed spiral pattern. The lighter shade represents a region of approaching matter, while the darker shade represents a region of receding matter. Canzian brought attention to the spiral structure formed by these shaded regions; inside CR the shaded region forms one continuous spiral structure, whereas outside CR the shaded region forms three separate spiral patterns. Credit: Canzian (1993)

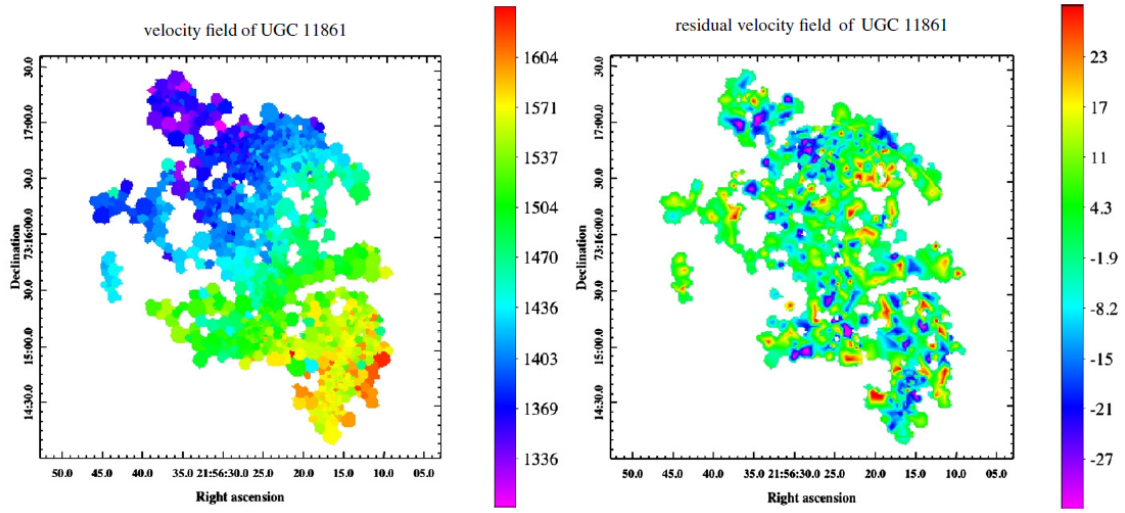

Figure 1.18: The left image is the line-of-sight velocity map of UGC11861 and the right image is the residual velocity map of the same galaxy. Credit: Font et al. (2014a)

referred to as the *FB method* in this thesis), first described by Font et al. in 2011 (Font et al., 2011). The aim of this thesis is to put this method to test by comparing its results with other resonance detection methods as well as testing its predictions by applying it to simulated galaxies with known resonances. The basic idea behind this method is similar to the Canzian method as both utilize the residual velocity map. In contrast to the Canzian method (a morphological approach to analyzing the residual velocity map), the Font-Beckman phase reversal method identifies regions in the residual velocity map that experience a

reversal of sign; these regions are then interpreted as resonance locations. The test is done on a pixel-by-pixel basis and there are multiple tests in-place to rule out false signals. The intricacies of the FB method are explained step-by-step in great detail in the method section of this thesis. In a 2014 paper, Font et al. applied this freshly conceived method to a set of 104 galaxies[19] (Font et al., 2014a) from the GHASP data base (Epinat et al., 2008). Note that line-of-sight measurements are needed to obtain residual maps; although these measurements are possible in case of gas-poor discs, the best line-of-sight measurements are obtained from gas-rich discs. This is because stellar absorption lines are hard to measure as compared to gas emission lines; additionally, gas is usually dynamically colder so that the emission lines in gas are well-defined. Therefore, the FB method and the Canzian method so far have only been applied to gas-rich galaxies. The resonance radii that Font et al. found are sharp with small errors, however, the number of different resonance radii for a single galaxy obtained is large (sometimes as many as seven). At first, they linked these different resonances to various pattern speeds (Font et al., 2011), but later they found connections between various resonant modes of two pattern speeds (Font et al., 2014c). They found that, in more than 70% of the sample, the OLR of Ω_1 coincides with the CR of Ω_2 and the CR of Ω_1 coincides with the I4R of Ω_2, where Ω_1 and Ω_2 are two different pattern speeds in the galaxy. They also obtained 1.3 as an average $\mathcal{R}$, which increased for later-types. Moreover, they had 8 double-barred galaxies, regarding which the FB method showed that the inner bar rotates more rapidly than the outer bar by a factor of 3.3 to 3.6 (Font et al., 2014b). In 2017, Font et al. used their resonance radii predictions of the 2014 paper (Font et al., 2014a) to obtain pattern speeds for 68 S^4G galaxies, which were then compared with simulation results with success (Font et al., 2017). Their final conclusion was that dark matter halos slow down bar rotation on a timescale of Gyr, which is in agreement with previous studies. The latest application of the FB method is done by Salak et al. in 2019; they had a sample of over 10 galaxies[20] from the COMING (CO Multi-line Imaging of Nearby Galaxies) project and found that $\mathcal{R}$ is between 0.8 to 1.6 (Salak et al., 2019).

[19]NGC266, NGC428, NGC672, NGC674, NGC753, NGC864, NGC925, UGC2080, NGC1012, NGC1058, UGC2855, NGC1530, UGC3273, UGC3463, UGC3574, UGC3685, UGC3691, NGC2342, NGC2344, NGC2276, NGC2336, UGC3826, UGC3876, UGC3915, NGC2500, NGC2543, NGC2541, NGC2552, NGC2595, NGC2649, NGC2805, NGC2977, UGC5228, NGC3003, NGC2985, NGC3041, NGC3061, NGC3104, NGC3162, NGC3147, NGC3310, NGC3344, NGC3346, NGC3430, NGC3504, NGC3596, NGC3719, NGC3720, NGC3726, NGC3840, NGC3893, NGC4045, NGC4062, NGC4145, NGC4242, NGC4303, NGC4559, NGC4605, NGC4618, NGC4625, NGC4635, NGC4651, NGC4713, NGC5055, NGC5112, NGC5204, NGC5297, NGC5376, NGC5430, NGC5585, NGC5622, NGC5678, NGC5668, NGC5676, NGC5727, NGC5874, NGC5879, NGC5949, NGC5970, NGC5985, NGC6015, NGC6140, UGC10445, NGC6217, UGC10502, NGC6207, NGC6236, NGC6248, NGC6283, UGC10757, NGC6412, NGC6503, UGC11124, NGC6643, UGC11283, NGC6764, UGC11466, UGC11557, UGC11861, NGC7177, NGC7217, NGC7440, NGC7479, and NGC7741

[20]NGC157, NGC613, NGC2903, NGC2967, NGC3147, NGC3627, NGC3893, NGC4303, NGC4579, NGC5248, NGC5678, and NGC7479

Chapter 2

Data

In this chapter the data used in the calculations and simulations are presented in nine tables.

The first table, Table 2.1, represents the Font-Beckman resonances that are used in this thesis. The following Table 2.2 presents the common galactic information that are needed in this thesis, such as the radii at which the brightness drops below specific values, distance to the galaxy, inclination, and the galaxy's bar status. Table 2.3 follows next, which shows the radii at which truncations of all types occur in the galaxies. The Table 2.4 shows the Type-II only truncation radii, Table 2.5 shows the Type-II-OLR only truncation radii, and Table 2.6 shows the Type-III only truncation radii. These truncation radii were measured in my Bachelor thesis[1].

Table 2.7 includes the mean ring radii of the galaxies, while Table 2.8 contains the interlocking Font-Beckman resonances. The final Table 2.9 consists of some overlapping galaxies that have their resonances found via the Font-Beckman method and another resonance indicator method; these *other* resonance indicator methods include the "traditional" ways of finding resonances such as the Tremaine-Weinberg method (Tremaine and Weinberg, 1984) or rather recent methods such as the Buta-Zhang method (Zhang and Buta, 2007).

[1]Pouya Mahmoudikouchaksaraei BSc Thesis (2017) at University of Oulu: *http://jultika.oulu.fi/Record/nbnfioulu-201709262924*

Table 2.1: Font-Beckman resonance radii (arcsec)									
Galaxy	FB1	FB2	FB3	FB4	FB5	FB6	FB7	FB no.	Ref.
IC0167	10.5	26.3	48.2	66.1	–	–	–	4	1
IC1251	12.4	22.5	–	–	–	–	–	2	1
NGC0157	–	–	–	–	–	–	–	0	2
NGC0428	40.6	51.9	98.6	129.1	–	–	–	4	1
NGC0613	61.0	–	–	–	–	–	–	1	2
NGC0672	10.9	36.6	58.7	90.7	113.7	–	–	5	1
NGC0864	5.8	29.7	56.1	84.4	102.1	–	–	5	1
NGC2500	16.4	25.6	48.9	65.3	75.4	–	–	5	1
NGC2541	10.8	31.4	52.9	68.1	93.8	–	–	5	1
NGC2543	7.7	31.8	47.4	79.6	–	–	–	4	1
NGC2552	16.6	49.4	67.2	–	–	–	–	3	1
NGC2805	16.9	34.8	70.8	82.6	102.2	112.3	137.7	7	1
NGC2985	43.2	58.8	70.4	82.9	–	–	–	4	1
NGC3003	12.9	47.4	70.2	87.4	102.6	110.8	–	6	1
NGC3041	16.0	35.2	48.7	71.7	–	–	–	4	1
NGC3061	9.3	16.2	21.8	25.8	33.1	–	–	5	1
NGC3104	19.3	33.0	51.1	62.0	77.0	92.3	–	6	1
NGC3147	7.0	16.3	34.7	54.3	76.7	–	–	5	1
NGC3162	13.6	30.8	36.7	46.7	54.4	66.5	–	6	1
NGC3310	20.6	29.0	43.6	63.0	80.1	–	–	5	1
NGC3344	31.6	60.9	79.7	93.1	120.6	–	–	5	1
NGC3346	15.5	23.4	66.4	–	–	–	–	3	1
NGC3430	11.7	52.6	68.3	80.0	96.2	–	–	5	1
NGC3504	9.9	19.2	29.1	37.6	43.7	66.6	–	6	1
NGC3596	8.3	23.6	33.2	47.5	–	–	–	4	1
NGC3627	104.0	–	–	–	–	–	–	1	2
NGC3726	35.8	59.8	105.8	122.0	143.7	–	–	5	1
NGC3893	13.0	34.9	63.0	75.2	88.8	–	–	5	1
NGC4045	7.6	18.5	39.4	–	–	–	–	3	1
NGC4062	43.9	54.2	85.4	–	–	–	–	3	1
NGC4145	18.1	46.3	63.4	135.3	187.0	–	–	5	1
NGC4242	13.8	44.7	92.4	117.7	130.1	–	–	5	1
NGC4303	4.6	26.6	36.1	49.9	60.4	68.0	–	6	1
NGC4559	15.8	37.3	51.6	60.0	89.6	–	–	5	1
NGC4579	61.9	76.5	–	–	–	–	–	2	2
NGC4605	4.7	17.8	41.3	53.2	63.0	–	–	5	1
NGC4618	41.7	54.5	87.1	–	–	–	–	3	1
NGC4625	15.2	31.1	37.1	–	–	–	–	3	1
NGC4635	19.6	28.7	43.9	–	–	–	–	3	1
NGC4651	15.6	48.6	58.0	80.4	–	–	–	4	1

NGC4713	12.6	27.6	38.3	54.5	72.5	–	–	5	1
NGC5055	12.6	28.8	47.0	71.7	89.7	129.5	205.1	7	1
NGC5112	30.8	44.5	51.7	70.4	86.6	105.9	–	6	1
NGC5204	9.4	19.3	31.6	49.5	67.7	–	–	5	1
NGC5248	45.5	–	–	–	–	–	–	1	2
NGC5297	17.2	27.9	50	73.9	92.7	–	–	5	1
NGC5376	10.0	26.8	32.7	–	–	–	–	3	1
NGC5430	15.2	25.2	33.3	47.5	–	–	–	4	1
NGC5585	19.5	34.4	48.1	74.3	100.8	144.7	–	6	1
NGC5668	36.7	47.4	62.0	–	–	–	–	3	1
NGC5676	11.6	21.3	36.9	47.2	–	–	–	4	1
NGC5678	14.7	30.4	39.3	–	–	–	–	3	1
NGC5879	12.2	30.6	–	–	–	–	–	2	1
NGC5949	31.2	–	–	–	–	–	–	1	1
NGC5970	19.1	34.4	52.2	59.7	69.7	–	–	5	1
NGC5985	27.7	40.1	57.3	67.2	82.3	105.5	–	6	1
NGC6015	9.7	35.6	54.2	93.2	127.5	–	–	5	1
NGC6140	16.6	32.7	58.3	–	–	–	–	3	1
NGC6207	12.6	24.3	38.0	49.5	55.4	64.1	–	6	1
NGC6217	11.3	35.6	43.9	57.8	65.7	–	–	5	1
NGC6236	28.1	38.9	47.5	55.7	–	–	–	4	1
NGC6412	7.5	19.0	26.3	36.4	42.6	–	–	5	1
NGC6503	21.8	37.2	56.8	89.3	–	–	–	4	1
NGC7479	12.7	36.3	52.4	75.1	91.1	–	–	5	1
NGC7741	28.6	46.5	69.6	83.7	95.4	106.3	–	6	1
UGC05228	16.6	30.4	50.1	59.7	–	–	–	4	1
UGC10445	6.0	28.5	55.3	–	–	–	–	3	1

Table 2.1: This table gives the Font-Beckman resonance values of the galaxies studied in this thesis. The first column, "Galaxy", refers to the name of the galaxy. The following columns, "FB1" to "FB7", are the Font-Beckman resonance radii (see Font et al. (2014a)) of the galaxy, if they exist. The column, "FB no.", refers to the total number of Font-Beckman resonances for the galaxy. The last column, "Ref.", refers to the source of these Font-Beckman resonances; 1 indicates Font et al. (2014a) and 2 indicates Salak et al. (2019).

Table 2.2: General galactic information						
Galaxy	R_{24}	R_{25}	R_{26}	Dist.	Incl.	Bar
IC0167	51	71	88	2.9	56.2	1
IC1251	34	43	53	22.2	51.7	1
NGC0157	118	141	175	21.5	61.8	1
NGC0428	90	113	123	16.2	29.6	1
NGC0613	158	185	228	17.5	35.7	1
NGC0672	150	191	240	8.2	62.8	1
NGC0864	107	127	145	21.5	47	1
NGC2500	82	100	114	9.38	28.5	1
NGC2541	99	127	150	9.94	59.2	0
NGC2543	74	87	101	35.9	59.9	1
NGC2552	70	95	117	9.6	45.2	1
NGC2805	100	136	162	28	38.3	1
NGC2985	146	203	253	22.9	38.2	0
NGC3003	115	143	169	23.6	76.1	0
NGC3041	99	116	137	21.7	51.2	1
NGC3061	47	55.5	66	38.1	34.1	1
NGC3104	53	86.5	119.0	9.44	53.8	1
NGC3147	116	141	158	42.7	34.3	1
NGC3162	66	82	95	20.9	30.7	0
NGC3310	73	101	128	18	27.9	1
NGC3344	150	258	310	6.35	27	1
NGC3346	81	93	105	20.9	32.6	1
NGC3430	83	101	116	26	58.5	1
NGC3504	83	100	118	25.4	12.8	1
NGC3596	77	103	128	20.6	21.4	0
NGC3627	294	351	444	10.7	67.5	1
NGC3726	168	191	218	15.7	51	1
NGC3893	109	130	160	17.9	50.8	0
NGC4045	83	108	132	30.3	48.4	1
NGC4062	128	148	170	9.5	66.6	1
NGC4145	148	175	195	18.6	54.5	1
NGC4242	120	147	169	8.02	45.7	1
NGC4303	176	221	251	13.1	27.1	1
NGC4559	209	256	321	9	63	1
NGC4579	189	231	267	22.2	41.9	1
NGC4605	141	182	230	4.04	77.3	0
NGC4618	121	139	159	8	42	1
NGC4625	48	56	73	9.58	20	1
NGC4635	62	76	96	13.1	48.1	0
NGC4651	114	143	183	13.1	54.6	1

NGC4713	69	79	104	13.11	49.5	1
NGC5055	378	477	576	7.59	56.2	0
NGC5112	95	113	127	18.4	48.3	1
NGC5204	87	114	146	5.12	50.5	0
NGC5248	158	192	227	17.5	56.4	1
NGC5297	99	119	158	37.8	73.6	0
NGC5376	60	71	84	33.6	54.3	1
NGC5430	63	75	89	45.4	48.6	1
NGC5585	118	154	179	7.06	51.5	1
NGC5668	77	96	112	25.8	31.6	1
NGC5676	104	122	151	34.2	59.8	1
NGC5678	88	104	131	31.6	56.9	0
NGC5879	103	129	156	16	67.4	0
NGC5949	64	76	91	10.65	63.1	0
NGC5970	79	91	104	30.9	50.3	1
NGC5985	129	151	170	39.7	59.1	1
NGC6015	131	163	198	17	66	0
NGC6140	78	103	119	18.2	31.1	1
NGC6207	70	86	112	17	55.2	1
NGC6217	73	91	107	24.1	23.5	1
NGC6236	57	73	87	23.2	52.1	1
NGC6412	67	77	87	23.5	18.5	1
NGC6503	170	220	275	4.69	69.4	0
NGC7479	119	134	154	34.4	41.2	1
NGC7741	104	120	132	13.2	45.5	1
UGC05228	70	83	104	26.7	72.3	0
UGC10445	43	59	76	18.3	46.1	1

Table 2.2: This table contains some of general information about the galaxies studied in this thesis. The first column, "Galaxy", is the galaxy name. The columns "R_{24}", "R_{25}", and "R_{26}" refer to the radius of the galaxy at which its brightness drops below 24 mag/arcsec^2, 25 mag/arcsec^2, and 26 mag/arcsec^2, respectively. The column "Dist." refers to the distance (in Mpc) of the galaxy to Earth; these distances are taken from the NED database. The column "Incl." refers to the inclination of the galaxy, which is given in degrees. The last column, "Bar", refers to the galaxy being barred or unbarred; if the galaxy is barred then the value of "Bar" is 1 and in case of an unbarred galaxy its value is 0.

Table 2.3: Truncation radii (arcsec) of all types									
Galaxy	T1	T2	T3	T4	T No.	Mag1	Mag2	Mag3	Mag4
IC0167	35.45	52.31	–	–	2	70.10	5.36	–	–
IC1251	12.76	18.48	–	–	2	1.69	1.56	–	–
NGC0428	51.82	107.93	–	–	2	1.57	2.52	–	–
NGC0672	–	–	–	–	0	–	–	–	–
NGC0864	77.03	–	–	–	1	1.75	–	–	–
NGC2500	31.02	65.04	–	–	2	43.42	1.68	–	–
NGC2541	38.58	54.37	–	–	2	4.76	3.00	–	–
NGC2543	31.67	–	–	–	1	2.54	–	–	–
NGC2552	53.93	84.15	91.74	–	3	1.72	5.48	5.21	–
NGC2805	27.03	42.09	–	–	2	4.82	1.67	–	–
NGC2985	48.33	73.75	122.90	–	3	3.36	1.92	2.51	–
NGC3003	71.02	78.43	–	–	2	3.97	2.93	–	–
NGC3041	36.01	70.65	–	–	2	2.15	1.80	–	–
NGC3061	41.51	–	–	–	1	1.70	–	–	–
NGC3104	20.65	52.91	–	–	2	35.65	2.53	–	–
NGC3147	81.24	–	–	–	1	1.29	–	–	–
NGC3162	32.18	47.96	67.86	–	3	1.45	1.96	1.55	–
NGC3310	19.84	46.87	86.57	–	3	2.44	1.96	1.77	–
NGC3344	54.16	85.61	–	–	2	1.64	1.75	–	–
NGC3346	60.36	–	–	–	1	2.71	–	–	–
NGC3430	19.85	81.91	–	–	2	1.92	1.43	–	–
NGC3504	32.64	44.35	59.50	–	3	1.49	3.91	2.54	–
NGC3596	23.54	41.55	69.37	–	3	4.89	5.71	2.61	–
NGC3726	39.87	148.83	–	–	2	12.63	1.85	–	–
NGC3893	55.70	65.10	–	–	2	22.58	22.52	–	–
NGC4045	32.04	62.96	–	–	2	1.74	1.16	–	–
NGC4062	24.28	36.75	45.68	99.47	4	2.21	4.94	5.27	1.31
NGC4145	31.54	147.42	–	–	2	5.31	2.99	–	–
NGC4242	42.66	104.48	–	–	2	1.89	2.23	–	–
NGC4303	35.68	47.97	–	–	2	1.87	1.38	–	–
NGC4559	72.80	–	–	–	1	1.17	–	–	–
NGC4605	47.52	94.82	–	–	2	1.47	2.22	–	–
NGC4618	64.88	92.09	–	–	2	21.46	30.92	–	–
NGC4625	19.34	34.48	49.33	–	2	5.55	7.11	1.50	–
NGC4635	38.67	45.12	–	–	2	8.95	12.53	–	–
NGC4651	44.43	91.04	123.98	–	3	2.38	1.23	1.68	–
NGC4713	24.94	36.73	–	–	2	2.74	3.34	–	–
NGC5055	162.92	–	–	–	1	2.46	–	–	–
NGC5112	56.55	82.63	–	–	2	4.41	6.35	–	–
NGC5204	–	–	–	–	0	–	–	–	–

NGC5297	50.64	98.88	–	–	2	1.59	1.70	–	–
NGC5376	24.55	–	–	–	1	2.24	–	–	–
NGC5430	14.95	–	–	–	1	1.40	–	–	–
NGC5585	70.67	132.59	–	–	2	2.01	2.79	–	–
NGC5668	57.49	76.39	–	–	2	1.67	2.13	–	–
NGC5676	24.16	29.55	–	–	2	42.87	44.69	–	–
NGC5678	21.53	25.12	–	–	2	9.30	9.87	–	–
NGC5879	36.47	–	–	–	1	2.61	–	–	–
NGC5949	28.18	–	–	–	1	2.48	–	–	–
NGC5970	37.82	56.53	–	–	2	1.52	1.54	–	–
NGC5985	21.15	60.13	–	–	2	4.90	2.64	–	–
NGC6015	66.24	111.32	134.76	–	3	1.98	2.11	1.61	–
NGC6140	36.94	97.05	–	–	2	2.25	1.97	–	–
NGC6207	74.92	–	–	–	1	1.54	–	–	–
NGC6217	40.19	61.79	–	–	2	3.86	1.94	–	–
NGC6236	74.28	–	–	–	1	3.01	–	–	–
NGC6412	16.18	33.62	59.60	–	3	5.81	3.90	1.36	–
NGC6503	38.97	118.23	–	–	2	2.02	2.23	–	–
NGC7479	26.62	98.06	–	–	2	3.04	2.45	–	–
NGC7741	26.81	43.17	108.26	–	3	35.29	13.59	2.75	–
UGC05228	30.29	50.99	–	–	2	1.25	1.26	–	–
UGC10445	36.22	55.36	–	–	2	2.17	2.03	–	–

Table 2.3: This table describes the truncations that were detected in my Bachelor thesis after analyzing each of the galaxies' luminosity profile. This table includes all the truncation types. The first column, "Galaxy", gives the name of the galaxy. The columns, "T1" to "T4", refer to the truncations that a galaxy may have. The column, "T No.", shows the total number of truncations that each galaxy possesses. The columns, "Mag1" to "Mag4", show the value of the magnitude of the aforementioned truncations. The truncation magnitudes are calculated using the Bachelor thesis data and are explained in more details later (see section 3.2). In short, a truncation is defined by two straight-line fits; the magnitude of the truncation is calculated by finding the largest possible absolute ratio of the gradients of the two straight-line fits.

Table 2.4: Type-II truncation radii (arcsec)							
Galaxy	T(II)1	T(II)2	T(II)3	T(II) No.	Mag1	Mag2	Mag3
IC0167	52.31	–	–	1	5.36	–	–
IC1251	18.48	–	–	1	1.56	–	–
NGC0428	107.93	–	–	1	2.52	–	–
NGC0672	–	–	–	0	–	–	–
NGC0864	77.03	–	–	1	1.75	–	–
NGC2500	31.02	65.04	–	2	43.42	1.68	–
NGC2541	54.37	–	–	1	3.00	–	–
NGC2543	31.67	–	–	1	2.54	–	–
NGC2552	53.93	91.74	–	2	1.72	5.21	–
NGC2805	42.09	–	–	1	1.67	–	–
NGC2985	73.75	–	–	1	1.92	–	–
NGC3003	78.43	–	–	1	2.93	–	–
NGC3041	36.01	70.65	–	2	2.15	1.80	–
NGC3061	41.51	–	–	1	1.70	–	–
NGC3104	20.65	–	–	1	35.65	–	–
NGC3147	–	–	–	0	–	–	–
NGC3162	32.18	67.86	–	2	1.45	1.55	–
NGC3310	–	–	–	0	–	–	–
NGC3344	85.61	–	–	1	1.75	–	–
NGC3346	60.36	–	–	1	2.71	–	–
NGC3430	19.85	–	–	1	1.92	–	–
NGC3504	32.64	59.50	–	2	1.49	2.54	–
NGC3596	41.55	–	–	1	5.71	–	–
NGC3726	39.87	148.83	–	2	12.63	1.85	–
NGC3893	65.10	–	–	1	22.52	–	–
NGC4045	–	–	–	0	–	–	–
NGC4062	24.28	45.68	99.47	3	2.21	5.27	1.32
NGC4145	147.42	–	–	1	2.99	–	–
NGC4242	104.48	–	–	1	2.23	–	–
NGC4303	47.97	–	–	1	1.38	–	–
NGC4559	–	–	–	0	–	–	–
NGC4605	47.52	–	–	1	1.47	–	–
NGC4618	92.09	–	–	1	30.92	–	–
NGC4625	34.48	–	–	1	7.11	–	–
NGC4635	45.12	–	–	1	12.53	–	–
NGC4651	91.04	–	–	1	1.23	–	–
NGC4713	36.73	–	–	1	3.34	–	–
NGC5055	–	–	–	0	–	–	–
NGC5112	82.63	–	–	1	6.35	–	–
NGC5204	–	–	–	0	–	–	–

NGC5297	50.64	–	–	1	1.59	–	–
NGC5376	24.55	–	–	1	2.24	–	–
NGC5430	–	–	–	0	–	–	–
NGC5585	132.59	–	–	1	2.79	–	–
NGC5668	76.39	–	–	1	2.13	–	–
NGC5676	29.55	–	–	1	44.69	–	–
NGC5678	25.12	–	–	1	9.87	–	–
NGC5879	–	–	–	0	–	–	–
NGC5949	28.18	–	–	1	2.48	–	–
NGC5970	56.53	–	–	1	1.54	–	–
NGC5985	60.13	–	–	1	2.64	–	–
NGC6015	66.24	134.76	–	2	1.98	1.61	–
NGC6140	97.05	–	–	1	1.97	–	–
NGC6207	–	–	–	0	–	–	–
NGC6217	40.19	–	–	1	3.86	–	–
NGC6236	74.28	–	–	1	3.01	–	–
NGC6412	33.62	59.60	–	2	3.90	1.36	–
NGC6503	38.97	–	–	1	2.02	–	–
NGC7479	98.06	–	–	1	2.45	–	–
NGC7741	43.17	108.26	–	2	13.59	2.75	–
UGC05228	50.99	–	–	1	1.26	–	–
UGC10445	36.22	–	–	1	2.17	–	–

Table 2.4: This table describes the Type-II truncations that were detected in my Bachelor thesis after analyzing each of the galaxies' luminosity profile. Note that this table only includes Type-II truncations. The first column, "Galaxy", gives the name of the galaxy. The columns, "T(II)1" to "T(II)3", refer to the Type-II truncations that a galaxy may have. The column, "T(II) No.", shows the total number of Type-II truncations that each galaxy possesses. The columns, "Mag1" to "Mag3", show the value of the magnitude of the aforementioned Type-II truncations. The truncation magnitudes are calculated using the Bachelor thesis data and are explained in more details later (see section 3.2). In short, a truncation is defined by two straight-line fits; the magnitude of the truncation is calculated by finding the largest possible absolute ratio of the gradients of the two straight-line fits.

Table 2.5: Type-II-OLR truncation radii (arcsec)			
Galaxy	T(II-OLR)	T(II-OLR) No.	Mag
IC0167	52.31	1	5.36
IC1251	18.5	1	1.56
NGC0428	107.93	1	2.52
NGC0672	–	0	–
NGC0864	77.03	1	1.75
NGC2500	65.04	1	1.68
NGC2541	54.37	1	3.00
NGC2543	–	0	–
NGC2552	–	0	–
NGC2805	–	0	–
NGC2985	73.75	1	1.92
NGC3003	78.43	1	2.93
NGC3041	70.65	1	1.80
NGC3061	41.51	1	1.70
NGC3104	–	0	–
NGC3147	–	0	–
NGC3162	32.18	1	1.45
NGC3310	–	0	–
NGC3344	85.61	1	1.75
NGC3346	60.36	1	2.71
NGC3430	–	0	–
NGC3504	32.64	1	1.49
NGC3596	41.55	1	5.71
NGC3726	148.83	1	1.85
NGC3893	65.10	1	22.52
NGC4045	–	0	–
NGC4062	45.68	1	5.27
NGC4145	–	0	–
NGC4242	104.48	1	2.23
NGC4303	–	0	–
NGC4559	–	0	–
NGC4605	–	0	–
NGC4618	92.09	1	30.92
NGC4625	34.48	1	7.11
NGC4635	45.12	1	12.53
NGC4651	91.04	1	1.23
NGC4713	36.73	1	3.34
NGC5055	–	0	–
NGC5112	82.63	1	6.35
NGC5204	–	0	–

NGC5297	50.64	1	1.59
NGC5376	–	0	–
NGC5430	–	0	–
NGC5585	132.59	1	2.79
NGC5668	–	0	–
NGC5676	29.55	1	44.69
NGC5678	25.12	1	9.87
NGC5879	–	0	–
NGC5949	–	0	–
NGC5970	56.53	1	1.54
NGC5985	60.13	1	2.64
NGC6015	66.24	1	1.98
NGC6140	–	0	–
NGC6207	–	0	–
NGC6217	40.19	1	3.86
NGC6236	–	0	–
NGC6412	33.62	1	3.90
NGC6503	38.97	1	2.02
NGC7479	98.06	1	2.45
NGC7741	108.26	1	2.75
UGC05228	50.99	1	1.26
UGC10445	36.22	1	2.17

Table 2.5: This table describes the Type-II-OLR truncations that were detected in my Bachelor thesis after analyzing each of the galaxies' luminosity profile. Note that this table only includes Type-II-OLR truncations. The first column, "Galaxy", gives the name of the galaxy. The column, "T(II-OLR)", refers to the Type-II-OLR truncation that a galaxy may have. The column, "T(II-OLR) No.", shows the number of Type-II-OLR truncation that each galaxy possesses. The column, "Mag", shows the value of the magnitude of the aforementioned Type-II-OLR truncation. Note that this magnitude is calculated from the Bachelor thesis data and its process is explained later (see section 3.2).

Table 2.6: Type-III truncation radii (arcsec)							
Galaxy	T(III)1	T(III)2	T(III)3	T(III) No.	Mag1	Mag2	Mag3
IC0167	35.45	–	–	1	70.10	–	–
IC1251	12.76	–	–	1	1.69	–	–
NGC0428	51.82	–	–	1	1.57	–	–
NGC0672	–	–	–	0	–	–	–
NGC0864	–	–	–	0	–	–	–
NGC2500	–	–	–	0	–	–	–
NGC2541	38.58	–	–	1	4.76	–	–
NGC2543	–	–	–	0	–	–	–
NGC2552	84.15	–	–	1	5.48	–	–
NGC2805	27.03	–	–	1	4.82	–	–
NGC2985	48.33	122.90	–	2	3.36	2.51	–
NGC3003	71.02	–	–	1	3.97	–	–
NGC3041	–	–	–	0	–	–	–
NGC3061	–	–	–	0	–	–	–
NGC3104	52.91	–	–	1	2.53	–	–
NGC3147	81.24	–	–	1	1.29	–	–
NGC3162	47.96	–	–	1	1.96	–	–
NGC3310	19.84	46.87	86.57	3	2.44	1.96	1.77
NGC3344	54.16	–	–	1	1.64	–	–
NGC3346	–	–	–	0	–	–	–
NGC3430	81.91	–	–	1	1.43	–	–
NGC3504	44.35	–	–	1	3.91	–	–
NGC3596	23.54	68.37	–	2	4.89	68.37	–
NGC3726	–	–	–	0	–	–	–
NGC3893	55.70	–	–	1	22.58	–	–
NGC4045	32.04	62.96	–	2	1.74	1.16	–
NGC4062	36.75	–	–	1	4.94	–	–
NGC4145	31.54	–	–	1	5.31	–	–
NGC4242	42.66	–	–	1	1.89	–	–
NGC4303	35.68	–	–	1	1.87	–	–
NGC4559	72.80	–	–	1	1.17	–	–
NGC4605	94.82	–	–	1	2.22	–	–
NGC4618	64.88	–	–	1	21.46	–	–
NGC4625	19.34	49.33	–	2	5.55	1.50	–
NGC4635	38.67	–	–	1	8.95	–	–
NGC4651	44.43	123.98	–	2	2.38	1.68	–
NGC4713	24.94	–	–	1	2.74	–	–
NGC5055	162.92	–	–	1	2.46	–	–
NGC5112	56.55	–	–	1	4.41	–	–
NGC5204	–	–	–	0	–	–	–

NGC5297	98.88	–	–	1	1.70	–	–
NGC5376	–	–	–	0	–	–	–
NGC5430	14.95	–	–	1	1.40	–	–
NGC5585	70.67	–	–	1	2.01	–	–
NGC5668	57.49	–	–	1	1.67	–	–
NGC5676	24.16	–	–	1	42.87	–	–
NGC5678	21.53	–	–	1	9.30	–	–
NGC5879	36.47	–	–	1	2.61	–	–
NGC5949	–	–	–	0	–	–	–
NGC5970	37.82	–	–	1	1.52	–	–
NGC5985	21.15	–	–	1	4.90	–	–
NGC6015	111.32	–	–	1	1.98	–	–
NGC6140	36.94	–	–	1	2.25	–	–
NGC6207	74.92	–	–	1	1.54	–	–
NGC6217	61.79	–	–	1	1.94	–	–
NGC6236	–	–	–	0	–	–	–
NGC6412	16.18	–	–	1	5.81	–	–
NGC6503	118.23	–	–	1	2.23	–	–
NGC7479	26.62	–	–	1	3.04	–	–
NGC7741	26.81	–	–	1	35.29	–	–
UGC05228	30.29	–	–	1	1.25	–	–
UGC10445	55.36	–	–	1	2.03	–	–

Table 2.6: This table describes the Type-III truncations that were detected in my Bachelor thesis after analyzing each of the galaxies' luminosity profile. Note that this table only includes Type-III truncations. The first column, "Galaxy", gives the name of the galaxy. The columns, "T(III)1" to "T(III)3", refer to the Type-III truncations that a galaxy may have. The column, "T(III) No.", shows the total number of Type-III truncations that each galaxy possesses. The columns, "Mag1" to "Mag3", show the value of the magnitude of the aforementioned Type-II truncations. Note that this magnitude is calculated from the Bachelor thesis data and its process is explained later (see section 3.2).

Table 2.7: Ring radii (arcsec)			
Galaxy	Ring 1	Ring 2	Ring No.
IC0167	–	–	0
IC1251	–	–	0
NGC0428	–	–	0
NGC0672	96.6	–	1
NGC0864	36.45	–	1
NGC2500	–	–	0
NGC2541	–	–	0
NGC2543	–	–	0
NGC2552	54.45	–	1
NGC2805	15.3	48.15	2
NGC2985	41.25	90.75	2
NGC3003	40.05	–	1
NGC3041	36.6	–	1
NGC3061	16.35	–	1
NGC3104	–	–	0
NGC3147	21.9	–	1
NGC3162	–	–	0
NGC3310	7.8	–	1
NGC3344	29.85	–	1
NGC3346	17.25	–	1
NGC3430	–	–	0
NGC3504	27.75	59.55	2
NGC3596	–	–	0
NGC3726	42.75	–	1
NGC3893	–	–	0
NGC4045	20.7	50.1	2
NGC4062	25.05	–	1
NGC4145	21.45	–	1
NGC4242	–	–	0
NGC4303	46.65	–	1
NGC4559	–	–	0
NGC4605	–	–	0
NGC4618	37.5	75	2
NGC4625	9.45	27.9	2
NGC4635	–	–	0
NGC4651	24.75	–	1
NGC4713	15.45	–	1
NGC5055	18.9	38.25	2
NGC5112	33.75	–	1
NGC5204	–	–	0

NGC5297	–	–	0
NGC5376	18.3	–	1
NGC5430	42.9	–	1
NGC5585	–	–	0
NGC5668	12.6	–	1
NGC5676	–	–	0
NGC5678	35.85	66.9	2
NGC5879	19.35	–	1
NGC5949	–	–	0
NGC5970	–	–	0
NGC5985	–	–	0
NGC6015	–	–	0
NGC6140	–	–	0
NGC6207	16.35	–	1
NGC6217	36.9	81.15	2
NGC6236	–	–	0
NGC6412	11.55	–	1
NGC6503	–	–	0
NGC7479	84.15	–	1
NGC7741	89.25	–	1
UGC05228	45.9	–	1
UGC10445	–	–	0

Table 2.7: This table describes the mean ring radii of the galaxies studied in this thesis. The first column, "Galaxy", gives the name of the galaxy. The columns, "Ring 1" and "Ring 2", refer to the mean ring radii that a galaxy may have. The column, "Ring No.", shows the total number of mean ring radii that each galaxy possesses. These mean ring radii values are taken from Comerón et al. (2014).

Table 2.8: Font-Beckman Interlocking resonance radii (arcsec)							
Galaxy	FB-IL1	FB-IL2	FB-IL3	FB-IL4	FB-IL5	FB-IL6	FB-IL No.
IC0167	10.5	26.3	48.2	–	–	–	3
IC1251	–	–	–	–	–	–	0
NGC0428	40.6	98.6	–	–	–	–	2
NGC0672	–	–	–	–	–	–	0
NGC0864	–	–	–	–	–	–	0
NGC2500	25.6	48.9	–	–	–	–	2
NGC2541	10.8	31.4	52.9	93.8	–	–	4
NGC2543	–	–	–	–	–	–	0
NGC2552	16.6	49.4	–	–	–	–	2
NGC2805	34.8	82.6	–	–	–	–	2
NGC2985	43.2	58.8	70.4	82.9	–	–	4
NGC3003	12.9	47.4	102.6	–	–	–	3
NGC3041	16	35.2	71.7	–	–	–	3
NGC3061	9.3	16.2	21.8	33.1	–	–	4
NGC3104	–	–	–	–	–	–	0
NGC3147	7	16.3	34.7	54.3	76.7	–	5
NGC3162	13.6	30.8	–	–	–	–	2
NGC3310	29	80.1	–	–	–	–	2
NGC3344	31.6	60.9	–	–	–	–	2
NGC3346	23.4	66.4	–	–	–	–	2
NGC3430	52.6	96.2	–	–	–	–	2
NGC3504	9.9	19.2	43.7	–	–	–	3
NGC3596	8.3	23.6	–	–	–	–	2
NGC3726	35.8	59.8	105.8	122	–	–	4
NGC3893	13	34.9	75.2	–	–	–	3
NGC4045	7.6	18.5	–	–	–	–	2
NGC4062	43.9	85.4	–	–	–	–	2
NGC4145	18.1	46.3	–	–	–	–	2
NGC4242	13.8	44.7	117.7	–	–	–	3
NGC4303	26.6	36.1	60.4	68	–	–	4
NGC4559	15.8	37.3	–	–	–	–	2
NGC4605	–	–	–	–	–	–	0
NGC4618	–	–	–	–	–	–	0
NGC4625	–	–	–	–	–	–	0
NGC4635	–	–	–	–	–	–	0
NGC4651	48.6	80.4	–	–	–	–	2
NGC4713	12.6	27.6	38.3	54.5	72.5	–	5
NGC5055	12.6	28.8	–	–	–	–	2
NGC5112	–	–	–	–	–	–	0
NGC5204	–	–	–	–	–	–	0

NGC5297	–	–	–	–	–	–	0
NGC5376	10	26.8	–	–	–	–	2
NGC5430	15.2	25.2	33.3	47.5	–	–	4
NGC5585	19.5	48.1	74.3	144.7	–	–	4
NGC5668	–	–	–	–	–	–	0
NGC5676	11.6	21.3	36.9	–	–	–	3
NGC5678	14.7	30.4	–	–	–	–	2
NGC5879	12.2	30.6	–	–	–	–	2
NGC5949	–	–	–	–	–	–	0
NGC5970	19.1	34.4	59.7	–	–	–	3
NGC5985	27.7	40.1	57.3	67.2	82.3	105.5	6
NGC6015	9.7	35.6	93.2	–	–	–	3
NGC6140	–	–	–	–	–	–	0
NGC6207	12.6	24.3	38	55.4	–	–	4
NGC6217	11.3	35.6	65.7	–	–	–	3
NGC6236	28.1	38.9	47.5	55.7	–	–	4
NGC6412	–	–	–	–	–	–	0
NGC6503	37.2	89.3	–	–	–	–	2
NGC7479	–	–	–	–	–	–	0
NGC7741	28.6	83.7	–	–	–	–	2
UGC05228	–	–	–	–	–	–	0
UGC10445	–	–	–	–	–	–	0

Table 2.8: This table describes the interlocking Font-Beckman resonances which are taken from Font et al. (2014a). The first column, "Galaxy", gives the name of the galaxy. The columns, "FB-IL1" to "FB-IL6", refer to the interlocking Font-Beckman resonances that a galaxy may have. The column, "FB-IL No.", shows the total number of interlocking Font-Beckman resonances that each galaxy possesses.

Table 2.9: Buta-Zhang and "traditional" resonance radii (arcsec)											
Galaxy	BZ1	BZ2	BZ3	BZ4	BZ5	BZ No.	Trd1	Trd2	Trd No.	Trd Meth.	Trd Ref.
NGC0428	54.8	–	–	–	–	1	–	–	–	–	–
NGC0864	6.5	33	57.3	–	–	3	–	–	–	–	–
NGC3162	–	–	–	–	–	–	48	–	1	PD	1
NGC3344	–	–	–	–	–	–	56.5	–	1	TW	2
NGC3504	24.3	41.9	–	–	–	2	47	–	1	TW	3
NGC3596	12.3	32.2	49.8	71.1	–	4	–	–	–	–	–
NGC3726	21.9	65.2	114.1	–	–	3	83.5	–	1	Sim	4
NGC3893	20.8	61	–	–	–	2	–	–	–	–	–
NGC4145	46.6	122.4	–	–	–	2	–	–	–	–	–
NGC4242	30.4	–	–	–	–	1	–	–	–	–	–
NGC4303	20.8	48.8	69.6	84.9	134	5	89.1	–	1	Sim	4
NGC4618	83.0	–	–	–	–	1	–	–	–	–	–
NGC4651	6.1	36.5	51.8	88.9	–	4	–	–	–	–	–
NGC5676	23.2	38.2	61.2	–	–	3	–	–	–	–	–
NGC7479	6.3	57.7	–	–	–	2	94	–	1	TW	5
NGC7741	51.9	–	–	–	–	1	109	–	1	TW	5
NGC0157	6.4	40	72.9	–	–	3	–	–	–	–	–
NGC0613	5.0	55.1	88	–	–	3	126.2	–	1	Sim	4
NGC3627	–	–	–	–	–	–	80	120	2	TW	6
NGC4579	8.7	24.7	48	81.3	–	4	71.1	–	1	Sim	4
NGC5248	12.5	69.6	–	–	–	2	–	–	–	–	–

Table 2.9: This table describes the resonances of a small number of overlapping galaxies that have their resonances predicted via a new and some "traditional" resonance indicators as well as the Font-Beckman method. The first column, "Galaxy", shows the name of the galaxy. The columns, "BZ1" to "BZ5", refer to the Buta-Zhang resonances (Zhang and Buta, 2007; Buta and Zhang, 2009). The column, "BZ No.", shows the total number of Buta-Zhang resonances that a galaxy possesses. The columns, "Trd1" and "Trd2", show the resonances of the galaxies as predicted by "traditional" methods; *traditional* is used to distinguish the more commonly used resonance prediction methods from the rather recent ones, i.e. Font-Beckman and Buta-Zhang. The column, "Trd No.", shows the total number of resonances found via one of these "traditional" methods. The column, "Trd Meth.", shows the "traditional" method that is used; there are three of these, namely the Puerari-Dottori (PD) method (Puerari and Dottori, 1997), the Tremaine-Weinberg (TW) method (Tremaine and Weinberg, 1984), and the simulation (Sim) method (for e.g. see Rautiainen et al. 2008). The last column, "Trd Ref.", gives the article reference from which these resonances originate; 1 refers to Martínez-García et al. (2009), 2 refers to Meidt et al. (2009), 3 refers to Aguerri et al. (1998), 4 refers to Rautiainen et al. (2005), 5 refers to Fathi et al. (2009), and 6 refers to Rand and Wallin (2004).

Chapter 3

Methods

The aim of this thesis is to assess the reliability of the Font-Beckman phase reversal model in predicting resonance radii in disc galaxies. The assessment is done via two main approaches. First, the Font-Beckman method is applied to simulated galaxies with known resonance radii. Second, Monte Carlo simulations are used to examine how much Font-Beckman resonance radii predictions differ from randomly assigned radii. The two approaches are explored in full below.

3.1 Simulation application

To begin with the Font-Beckman phase reversal method is re-coded from scratch with improvements to ensure that it can be applied to simulated galaxies. The simulations are done based on the method discussed in Wada (1994).

3.1.1 Font-Beckman phase reversal method

The Font-Beckman model starts off by taking in the residual velocity map of the galaxy. This map is obtained by removing the model velocity from the line-of-sight velocity map of the galaxy observed.

Upon reading the residual velocity map, a list of pixels which have defined residual velocity values covering the galaxy is obtained. Then a radial slit of a desired length (input parameter) is placed on each pixel. The value of residual velocity along these unique slits is found by interpolation.

The Font-Beckman method as described in their 2014 paper (Font et al., 2014a) continues by selecting a pair of "inner" and "outer" pixels for each pixel using the observation angular resolution, a parameter which depends on the seeing. If the residual velocities in the "inner" and "outer" pixels have a different sign and the respective residual velocities are larger than the velocity uncertainty (input parameter based on spectral resolution), then a phase reversal is accounted for; see Figure 3.1. Additionally, we have introduced a slight alteration of the aforementioned phase reversal identification technique. In this case instead of selecting a single pair of "inner" and "outer" pixels, three "inner" and three "outer" adjacent pixels are selected. To check the overall "inner" and "outer" sign, the three "inner" pixels are averaged and the three "outer" pixels are averaged and their signs are compared. The rest is identical to the original Font-Beckman method.

Now that the phase reversals are identified the ones that are overlapping must be rejected. The rejection technique that Font and Beckman use starts off by selecting the pixels corresponding to the

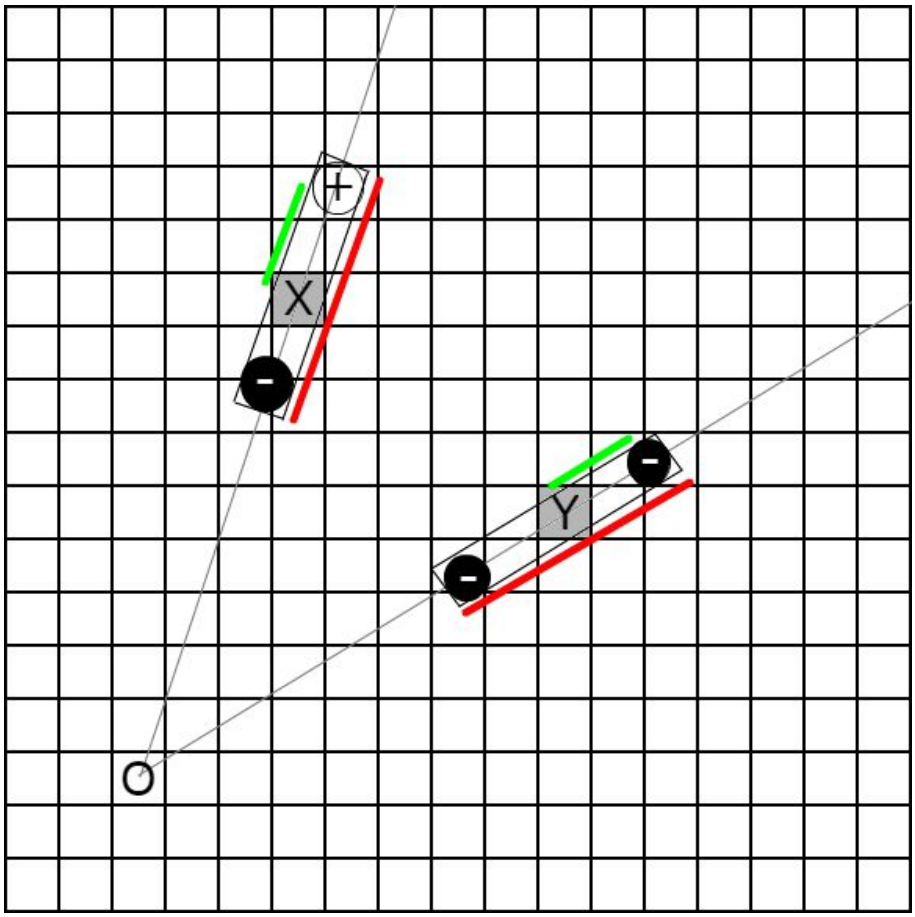

Figure 3.1: In this example sketch the center of the galaxy is at O. There are two pixels of interest: X and Y. On both pixels, a radial slit (represented by the rectangle) of a given size (represented by the red line) is created. The residual values along this radial slit is found by interpolation. According to the original Font-Beckman method, "inner" and "outer" pixels (represented by circles) are selected which are one angular resolution (represented by the green line) apart from the pixels of interest along the slit. In this example, pixel X shows a change in sign from its "inner" to "outer" pixel, whereas in case of pixel Y there is no sign change. Hence, pixel Y is not a phase reversal, but pixel X might be if its "inner" and "outer" pixels are larger than the velocity uncertainty.

phase reversals and placing a horizontal slit (along x-axis) with the same length as the previous slit used. Then the residual velocity values are obtained via interpolation. A residual velocity gradient is obtained by derivating the residual velocity with respect to x. The gradient of interest is found at the pixel itself where x is half of the slit length. The same process is repeated along the y-axis by placing a vertical slit to obtain the residual velocity gradient with respect to y. These are combined to obtain the residual velocity gradient with respect to the radial direction at the pixel. Then the phase reversal values are sorted with decreasing gradient and the pixel distance between each phase reversal pixel with another is found. The phase reversals that are closer to each other than half of the angular resolution (seeing) are all rejected except the one with the greatest gradient; see Figure 3.2.

We have made a slight alteration to this rejection technique. In this case the slits are not placed horizontally and vertically, but radially. Using an interpolation along the radial slit the residual velocity is calculated and the residual velocity gradient space is found by directly derivating the residual velocity along the radial direction. Afterwards, the process follows as it did in the previous case; phase reversals

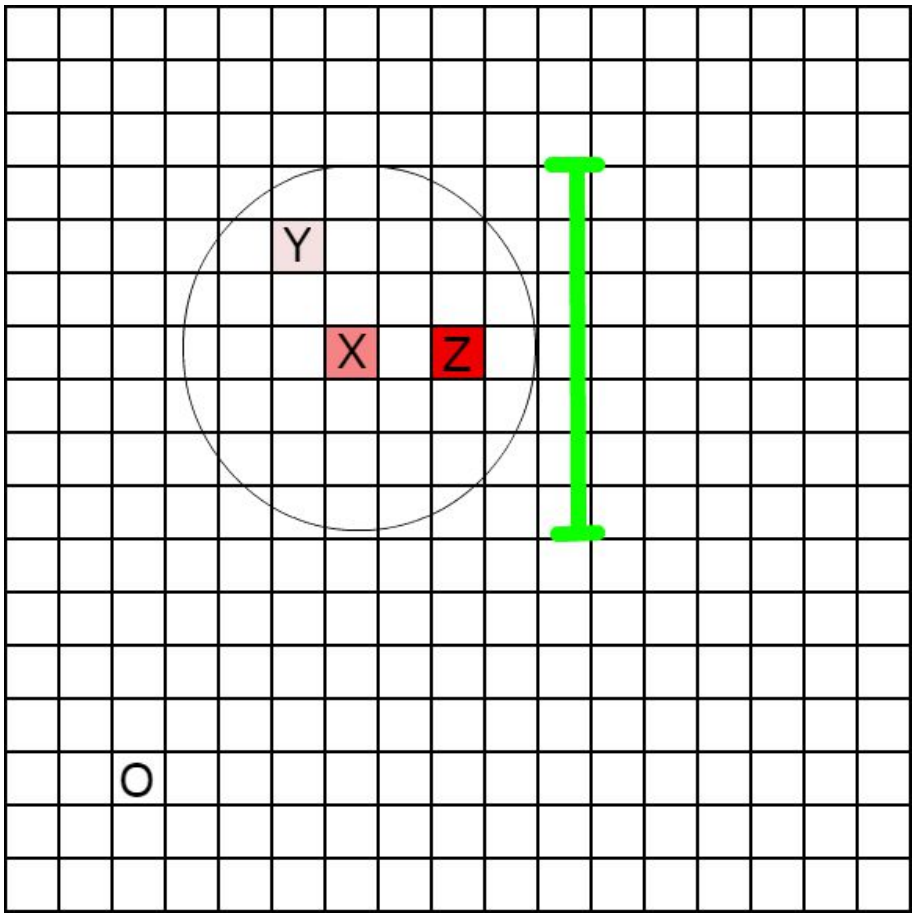

Figure 3.2: In this example sketch the circle centered at pixel X has a diameter equal to the angular resolution (seeing), represented by the green line. There are two other pixels Y and Z in this circle. Assuming that all three have phase reversals, according to the Font-Beckman method only the one that possesses the greatest residual velocity gradient is considered as a phase reversal while the other two are rejected. In this example, the residual velocity gradient of each pixel is represented by the degree of its redness, i.e. the redder it is, the greater its residual velocity gradient is. Therefore, in this case pixel Z is taken as the phase reversal while pixels X and Y are rejected.

within a diameter equal to the angular resolution are rejected apart from the one with the greatest gradient.

With one of the aforementioned rejection techniques the undesirable phase reversals are identified and rooted out. In the following step the radii of these phase reversals are obtain from the Cartesian coordinates and are accordingly deprojected. All the "accepted" phase reversals have their positions marked on a ds9 region file with corresponding reversal directions; positive to negative or vice versa. See Figure 3.3.

Finally, the phase reversals are represented in histogram of a given bin size (input parameter) with respect to the galactic radius. As a final reliability test the radial bins that only have one phase reversal and are within 5% to 95% of the galactic radius have their corresponding phase reversal rejected. A Gaussian fit aiming to find the best estimate for peak strength (phase reversal number), radial location, and radial error is performed as a final touch; see Figure 3.4.

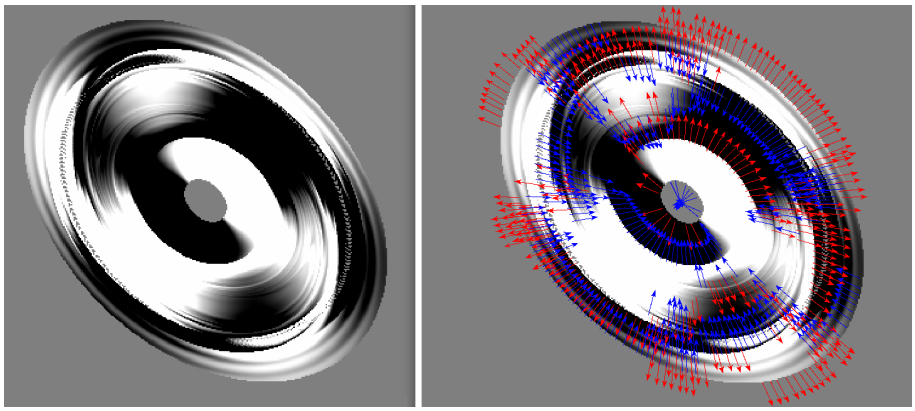

Figure 3.3: The simulation shown here had 4M initial starting particles arranged in 2k rings (2k particles per ring). The inclination was 45 degrees and the perturbation strength scale was 0.05. The image on the left is the residual field of the simulated galaxy, while the image on the right is the same galaxy's residual field upon application to the Font-Beckman method. The red and blue arrows pinpoint the exact pixels where Font-Beckman phase reversals are measured; the colour blue represents a negative-to-positive reversal, whereas the colour red indicates a positive-to-negative reversal.

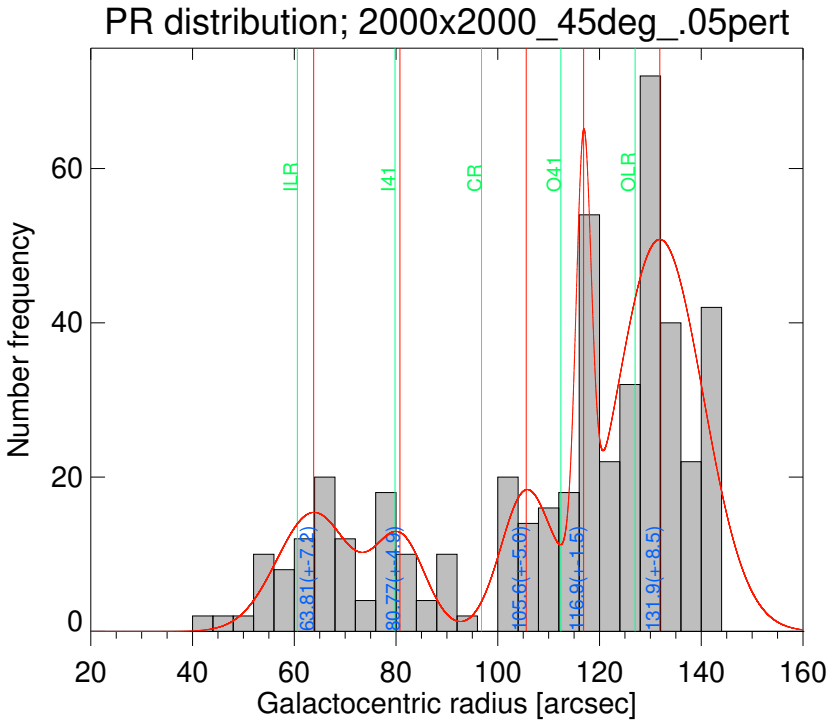

Figure 3.4: The simulation galaxy from Figure 3.3 was applied to the Font-Beckman method to obtain the number of acceptable phase reversals, which is represented by the histogram frequency (y-axis). The x-axis shows the radii at which these phase reversals were detected. The red curve is a Gaussian fit, used to pinpoint the locations of resonance radii which are shown by the red vertical lines. The value of the Font-Beckman resonance radii are given in blue and their uncertainty values (width of the Gaussian fit) are given in brackets. In this example, there are five resonance radii detected. The height of the Gaussian fit (maximum y-value of the red curve) gives the strength of the peak. Note that the Gaussian fit is performed with input initial values, so it is done on a per-case basis. The theoretical resonance locations of this example galaxy are shown as green vertical lines; see the description of Figure 3.6 for the exact values.

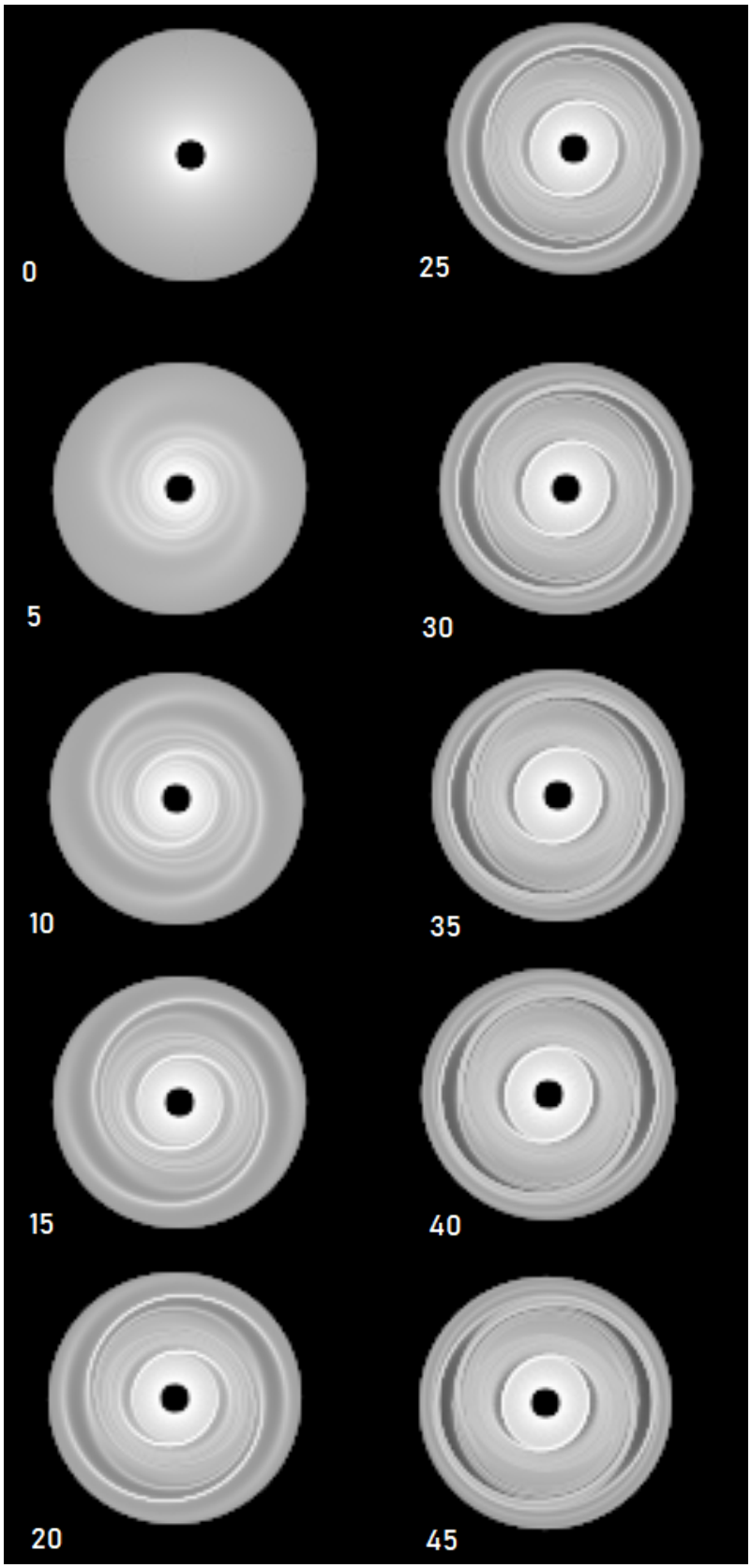

Figure 3.5: The series of images show snapshots of the simulation process of the galaxy seen in Figure 3.3. The images are 5 simulation time units apart and the simulation goes on for 50 time units. The time unit lapsed since the start of the simulation for each snapshot is given next to them.

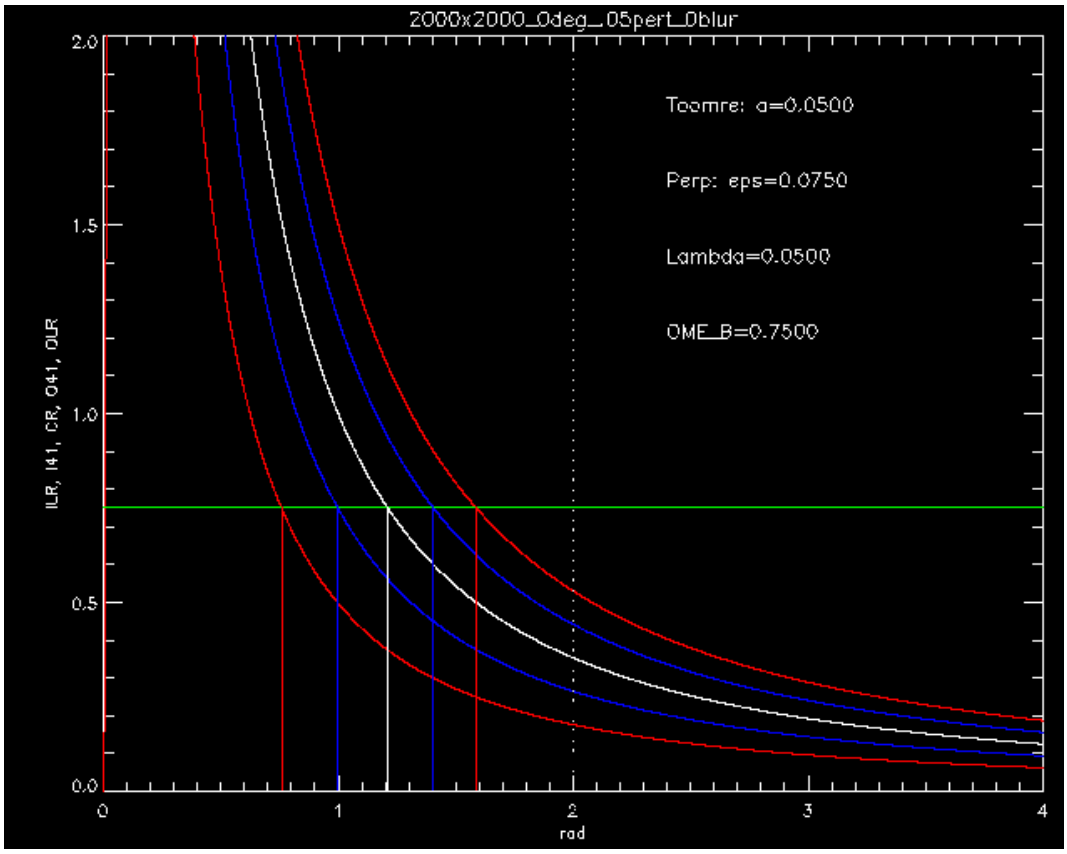

Figure 3.6: This graph shows the theoretical values of the simulated galaxy's resonance radii. The white curve corresponds to the CR, the red curves correspond to the ILR and OLR, and the blue curves correspond to the I41 and O41 resonances. The calculations and the graph are explained in Wada's paper (Wada, 1994). The theoretical resonance radii values for this example are: ILR=60.6, I4R=79.8, CR=96.8, O4R=112.4, and OLR=127.0, all units here are in arcsec; these were converted from simulation distance units to arcsec.

3.1.2 Wada galaxy simulations

All credits for the Wada simulation code in this thesis goes to Prof. Heikki Salo. The simulation code used in this thesis is almost his original code apart from some slight alterations.

The Wada simulation (Wada, 1994) uses weak-bar perturbations to the base circular Toomre potential to simulate a disc galaxy with nonself-gravitating gas. The main purpose of this simulation in this thesis is to act as a theoretical test to the Font-Beckman method. As it can create a plausible disc galaxy, see Figure 3.5, with theoretically known resonance radii (see Figure 3.6), which can then be applied to the Font-Beckman method to compare the resonance radii. A comparison between two different simulation times is shown in Figure 3.7; in this figure the unperturbed and perturbed velocity fields as well as the residual ones are shown.

The simulation starts with setting a particle number and how particles are to be distributed along the disc. It can be completely random along the disc or random in rings that are placed within the disc. The latter results in more realistic-looking galaxies at the end. The base circular gravitational field used is the Toomre potential. The formulas used to calculate the perturbations, resonance radii, force fields, and particle values (positions and velocities) are given in Wada's paper (Wada, 1994).

Using the Runge–Kutta 4 (RK4) integration method the particle positions and velocities at every step

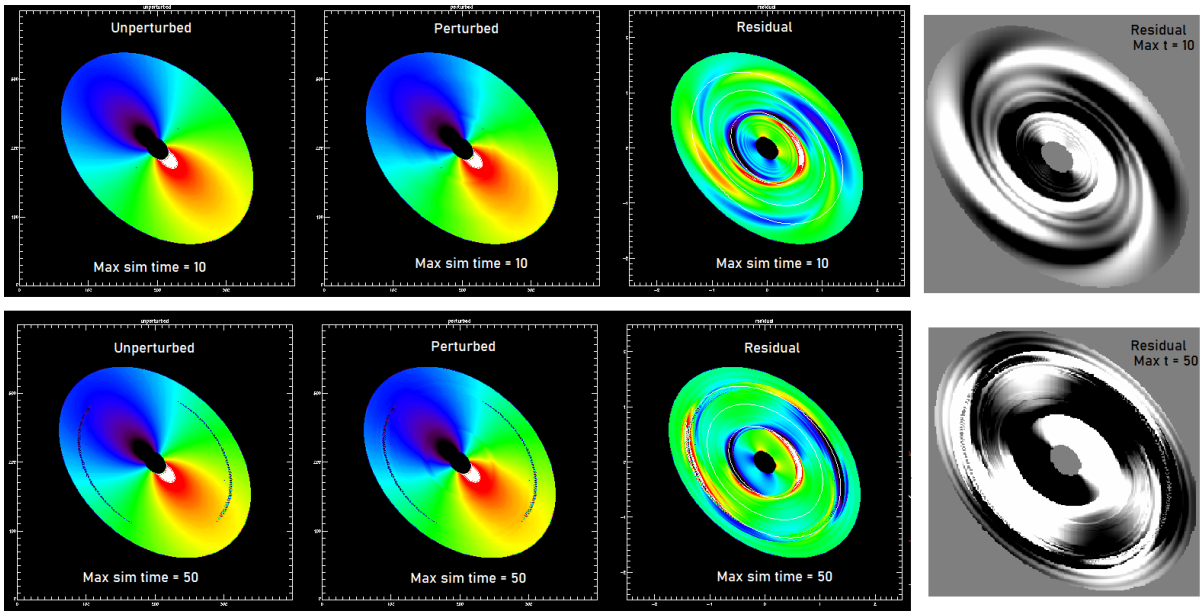

Figure 3.7: This figure shows a comparison between the unperturbed, perturbed, and residual velocity fields when the simulation goes on for 10 simulation time units (top row) and 50 simulation time units (bottom row). The left most column shows the unperturbed velocity fields, the second column shows the perturbed velocity field, the third column shows the residual velocity fields (the difference between the perturbed and unperturbed velocity fields), and the last column shows the same residual fields as plotted in ds9. In the third column, the white ellipses on the rainbow-coloured residual velocity fields show the location of the ILR, CR, and OLR. Note that the residual velocity field in the case of the shorter simulation resembles the Canzian residual field (see Figure 1.17) a lot more than the longer case. This matter and its relation to the Font-Beckman method is discussed later on. The Wada simulations used in testing the Font-Beckman method are all run for 50 simulation time units.

are calculated. The step length and total number of iterations are chosen at will as input parameters. Once the final step is reached the final positions and velocities for each particle are obtained, thus simulating a disc galaxy with potentially visible spiral arms as a prominent feature. This simulated galaxy needs to be projected to the sky to be more observation-like before being fed into the Font-Beckman method; see Figure 3.8. The projection is done via a transformation using the desired position angle, inclination, and base rotation. The projected map is then pixelated and mean line-of-sight velocities for each pixel is obtained.

Three FITS files are created: unperturbed map, perturbed map, and residual map. The unperturbed map is the line-of-sight velocity map of the galaxy without any of the weak-bar perturbations, i.e. just the Toomre potential. The perturbed map is the line-of-sight velocity map of the galaxy with the weak-bar perturbations, i.e. the realistic case. We have also enabled a blurring feature to be done on this map if desired. The blurring is a simple Gauss smoothing function of a given strength (σ of the Gauss function in terms of pixels). This blurring emulates the way a galaxy might look like when observed through a telescope due to seeing and other blurring effects. Finally, the residual map is obtained by obtaining the difference between the perturbed map and the unperturbed map. This is the map that one feeds into the Font-Beckman method to check the reliability of their resonance radii predictions; see Figure 3.9.

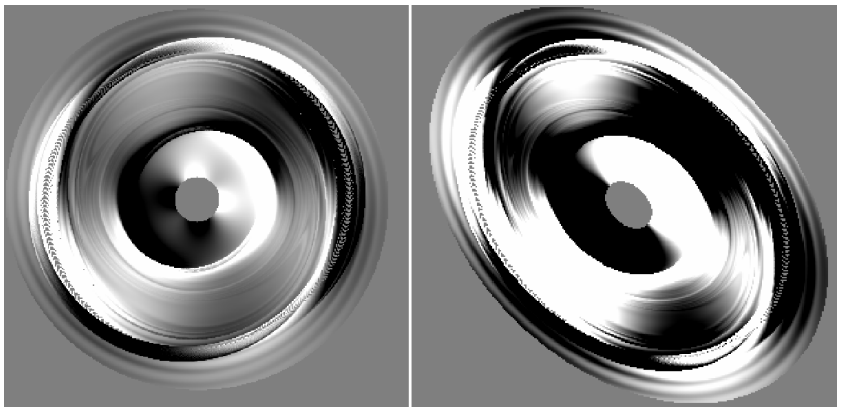

Figure 3.8: The simulation galaxy from Figure 3.3 has been projected to the sky to be at 45 degrees inclination (right image). The left image shows the same galaxy before being projected to the sky-view.

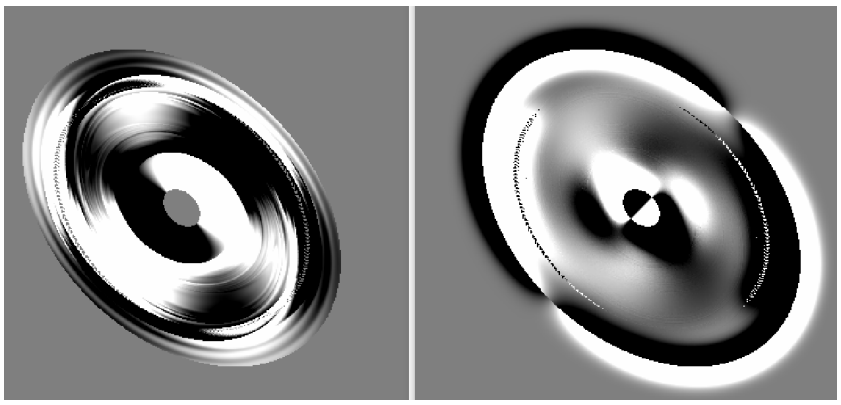

Figure 3.9: The simulation galaxy from Figure 3.3 was blurred with a Gaussian smoothing strength (σ) of 10 pixels. The left image is the original simulation result, while the right one is the blurred result. Note that all data points outside of the galaxy are ignored as those are unwanted artifacts of the blurring process. Note that the most extreme smoothing performed in this study uses a sigma of 10 pixels, so this example is used to show the case of greatest blurring.

3.2 Monte Carlo analysis

The purpose of the Monte Carlo analysis is to compare the Font-Beckman (FB) resonance radii to a number of "traditional" resonance radii, which are traditionally used to find resonance locations. These "traditional" resonance radii are referred to as resonance indicators (RI) in this section and later on. These are the resonance radii determined by some of the methods discussed in section 1.2.3. There are multiple resonance indicators used in this thesis to put the Font-Beckman method to test; the details of these various resonance indicators are discussed below.

The reliability of the Font-Beckman method is tested by attempting to see if its findings are random in nature or not. If it is random in nature then it is an unreliable method, while if its predictions are "better" than random resonances (statistically more significant) then perhaps it is a reliable method of finding resonance locations. To check this statistical significance, a number of random resonances are generated. These random resonances are not just purely random in nature, meaning that a set of random numbers is carefully vetted before being selected as resonances (the details are explained later). The random resonances are generated to emulate the FB resonances of a galaxy. As a result, for a given

galaxy, the number of generated resonances must match the number of FB resonances. The purpose of this is to simultaneously compare the FB and random resonances with the RI resonances. Under the assumption that RI resonances are reliable, this comparison reveals whether FB resonances are statistically more significant than the random ones. If FB resonance radii are closer to RI resonances than random resonances are, then that is indicative of the Font-Beckman method to be not random in nature. The stronger the FB resonances correlate with the RI resonances, the more likely it is that the Font-Beckman method is a reliable resonance detection method. The Monte Carlo analysis in this case refers to the algorithms that allow for a large number of random resonances to be generated and sensibly utilized in this comparison scheme. Several Monte Carlo algorithms were designed to perform a wide range of tests and comparisons. These Monte Carlo algorithms are discussed below; see subsections 3.2.3, 3.2.4, 3.2.5, and 3.2.6.

3.2.1 Resonance indicators

There exist a number of "traditional" methods that could indicate the presence of a resonance in a disc galaxy; see section 1.2.3. One of them is the existence of Type-II truncations in the radial surface brightness profiles of those galaxies, especially the ones that are found around two to three times the distance of the bar, as that is usually where outer Lindblad resonance (OLR) occurs (Erwin et al., 2008). Additionally, observable rings on the disc of the galaxies are believed to indicate the presence of resonances (Schwarz, 1981, 1984).

The resonance indicators (RI) that we have decided to use to test the Font-Beckman predictions of the paper Font et al. (2014a) are mainly the truncations calculated in my Bachelor Thesis[1]. The papers Laine et al. (2014) and Laine et al. (2016) were considered as other sources for the truncation values, however, due to lack of any significant overlap between the galaxy samples they were ignored. Although not all types of truncations are known to indicate resonances, in this thesis as a test, one of the RI used is truncations of all types, Type-II, Type-II-OLR, and Type III truncations are also taken as RI. The analysis also includes a limiting "truncation magnitude" option; such that the greater the truncation magnitude is, the stronger its supposed connection to a resonance is. Truncation magnitude is determined by taking the absolute value of the ratio of the larger slope to the smaller slope that form the truncation itself. Moreover, ring radii from Comerón et al. (2014) are taken as RI in some experiments.

The literature investigation of section 1.2.3 revealed that there are around 20 galaxies [2] galaxies that have their resonances found by the FB method and another "traditional" method. These various non-FB methods' predictions of the resonance radii are also used as resonance indicators. Note that most of the overlap is with the potential-density phase-shift method described by Zhang and Buta (2007), which is itself a new (not well-established) method for finding resonances, just like the Font-Beckman method. For this reason, this method is dealt with separately from the other less controversial methods, i.e. the potential-density phase-shift resonances are separately taken as resonance indicators. The second most

[1] Pouya Mahmoudikouchaksaraei BSc Thesis (2017) at University of Oulu: *http://jultika.oulu.fi/Record/nbnfioulu-201709262924*

[2] From Font et al. (2014a): NGCNGC428, NGC864, [NGC1058], [NGC1530], NGC3162*, (NGC3147), NGC3344*, NGC3504*, NGC3596, NGC3726*, NGC3893, NGC4145*, NGC4242, NGC4303*, NGC4618*, NGC4651, (NGC5678), NGC5676, [NGC7217], NGC7479*, NGC7741*. Only from Salak et al. (2019): NGC157, NGC613*, NGC3627*, NGC4579*, NGC5248. In case of Font et al. (2014a) the round brackets, (), mean that the overlap is only with the other FB method application (Salak et al., 2019). The square brackets, [], mean that the galaxy was ignored due to a lack of a consistent method of finding maximum radius with regards to the other galaxies (all of which are from S4G). The asterisk, *, means that the galaxy has its resonances also found by a method other than the potential-density phase-shift method (see Zhang and Buta (2007)).

overlap is with the simulation method described in Rautiainen et al. (2008). This method is preferred over any other method (specifically the star formation method of Puerari and Dottori 1997, which works best for the nuclear region and is completely ignored), except the direct TW methods. These methods' resonances are collectively taken as resonance indicators as well. In Font et al. (2014a), some of the Font-Beckman resonances are identified to be interlocking with others. A case where only these interlocking resonances are taken as the FB resonances is also investigated in this thesis.

There are some technical aspects used to run further tests that are unrelated to resonance indicators but depend on the galactic property. For example, a threshold for the galactic inclination is set such that only galaxies with inclinations smaller than 50 degrees are taken into the galactic sample. Or a separation of barred and unbarred galaxies can be made in the galaxy sample. Also the inner and outer bounds of the random-resonance-generating region are changed to check if that affects the results.

3.2.2 Units of radial measurement

In general there are three radial distance units used in the calculations. The first one is arcseconds. This is obviously not ideal as its value is dependent on how far the galaxy of interest is located from Earth. The other two are in parsecs and relative to the galactic size. The radial distances in parsecs are simply obtained from arcsec radial distances and by taking into account the distance to the galaxy. The relative radial distances are found by setting a value of unity to the outer bound of the galaxy. This is achieved via dividing all the distances by the maximum galactic radius. This maximum radius is taken to be the radius at which the average surface brightness of the galaxy drops below 25 mag arcsec^{-2}. To ensure that this choice has no effect on the final results, in a few of the experiments explained later the maximum radius is taken to be the radii at which the surface brightness drops below 24 mag arcsec^{-2} and 26 mag arcsec^{-2}. The results from the 24 mag arcsec^{-2} and 26 mag arcsec^{-2} brightness cut-offs are then compared with the result of the 25 mag arcsec^{-2} brightness cut-off.

3.2.3 Monte Carlo I

The following steps are performed in the Monte Carlo I technique:

(1) A galaxy from the galaxy sample is picked and its data is read.

(2) A pull of random numbers is created with a uniform distribution between 0 and and the maximum radius (at 25 mag arcsec^{-2}).

(3) A random set is created by selecting numbers from the random pull; the count of the selected numbers depends on the count of the FB resonances of the galaxy at hand.

(4) The selected set is sorted from smallest to largest, such that the smallest emulates the first resonance, the second smallest emulates the second resonance, and so on.

(5) The sorted set is tested against the condition that: (i) any number in the set is farther out than the inner 10% of the galaxy, and (ii) all of the numbers in the set are at least 5% of the maximum radius apart from one another.

(6) If the set passes the test then it is chosen as an accepted random resonance set, otherwise the set is rejected.

(7) This process is repeated until there exists a desired number of accepted random resonance sets.

(8) The distance to the closest RI resonance for each of the random resonances within a set is found, i.e. the distance between the first random resonance and its closest RI resonance is found, the distance between the second random resonance and its closest RI resonance is found, etc.

(9) The previous step is performed for all the accepted random resonance sets, which yields a large number of distances between random resonances and their closest RI resonance; note that there are multiple distance values between the first random resonances (of the many different accepted sets) and their closest RI resonance, likewise there are multiple distance values for the second random resonances and their closest RI resonance, and so on.

(10) These multiple distance values between random resonances and their corresponding closest RI resonance are averaged with respect to the order of the random resonance, i.e. all the distances between the first random resonances and their closest RI resonances are averaged, all the distances between the second random resonances and their closest RI resonances are averaged, and so on. This process yields possibly multiple (depends on the count of the FB resonances of the galaxy) averaged distances between random resonances and their closest RI resonance for the galaxy at hand.

(11) A new galaxy from the sample is picked and the previous steps are repeated to obtain averaged distances between random resonances and their closest RI resonance for this new galaxy.

(12) This is repeated until there are averaged distances between random resonances and their closest RI resonance (averaged random-RI distances) for all the galaxies in the galaxy sample.

(13) Simultaneous to the averaged random-RI distance calculations, the distances between FB resonances and their closest RI resonance for each galaxy are found, i.e. the distance of the first FB resonance to its closest RI resonance is found, the distance of the second FB resonance to its closest RI resonance is found, etc. This yields a number (obviously dependant on the count of the FB resonances of the galaxy) of distances between the FB resonances and their closest RI resonance (FB-RI distances) for the galaxy at hand. As the process goes through all the galaxies in the sample, at the end of the simulation there are FB-RI distances for all the galaxies in the galaxy sample.

(14) To compare the averaged random-RI distances and FB-RI distances a histogram is plotted; see Figure 3.10 for an example case. The x-axis of this histogram represents the distance to the closest RI resonance. Note that the histogram is a global one meaning that it represents the distribution of the averaged random-RI distances (in red) and the FB-RI distances (in black) over the entire galaxy sample. A quantitative comparison between the two histograms is done with the help of the Kolmogorov-Smirnov (K-S) test. The K-S significance level, shown in blue as a percentage in Figure 3.10, shows the probability that the two histogram samples are identical. A low K-S probability means the two samples are very different from each other and vice versa.

(15) As another comparison between the averaged random-RI distances and FB-RI distances, a scatter plot is plotted; for an example case see Figure 3.11. This is also a global plot as it visualizes the distribution of the two distance value sets over the entire galaxy sample. The scatter plot relies on the one-to-one nature of the averaged random-RI distances and FB-RI distances; the x-axis is FB-RI

distance value and the y-axis is the averaged random-RI distance value such that a point on this plot has a coordinate of (FB-RI distance, averaged random-RI distance). The equality line is the line y=x, which is represented on the scatter plot as a visual cue. To quantitatively compare the FB-RI distances and random-RI distances the binomial statistical test is utilized. The aim is to find the probability of obtaining a given scatter plot under the assumption that, in the most probable scenario, the spread of points is symmetrical with respect to the equality line. This means that the placement of points above or below the equality line is essentially a coin toss. Under this assumption, the binomial statistical test has an individual probability of 50% and by counting the number of points above the equality line as well as the total number of points, the binomial test yields the probability of the given scatter plot to be drawn from a random binomial distribution. The binomial probability is seen in Figure 3.11 as a red percentage.

The algorithm of Monte Carlo I is shown in the flowchart in Figure 3.16.

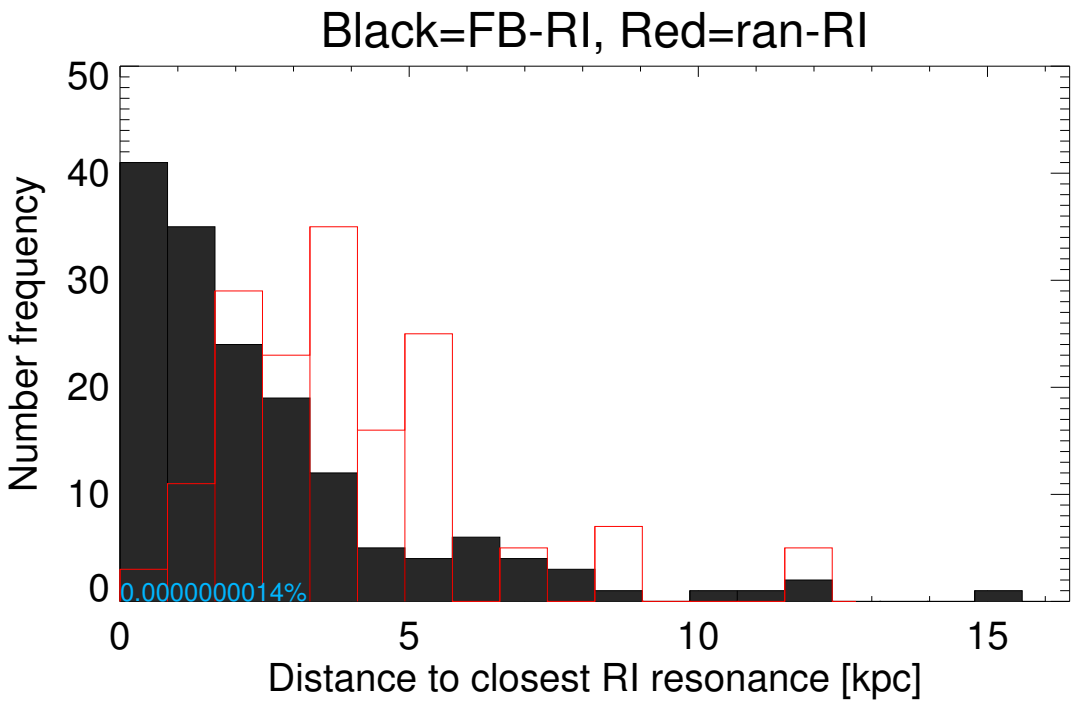

Figure 3.10: This is an example of the histogram plotted in MC I. In this example rings were used as RI, the measurement unit was kpc, and there were 100k random resonance sets accepted. The black histogram represents the distance between FB resonances and the closest RI resonance. The red histogram represents the average distance between random resonances and the closest RI resonance. The blue percentage is the K-S probability, which is the probability of two samples being drawn from the same distribution.

3.2.4 Monte Carlo II

The following steps are performed in the Monte Carlo II technique:

(1) – (7) are identical to those of Monte Carlo I.

(8) The average distance of all of the random resonances within a set to the closest RI resonance is found. Note that in Monte Carlo I this step potentially yielded multiple random-RI distances, whereas in

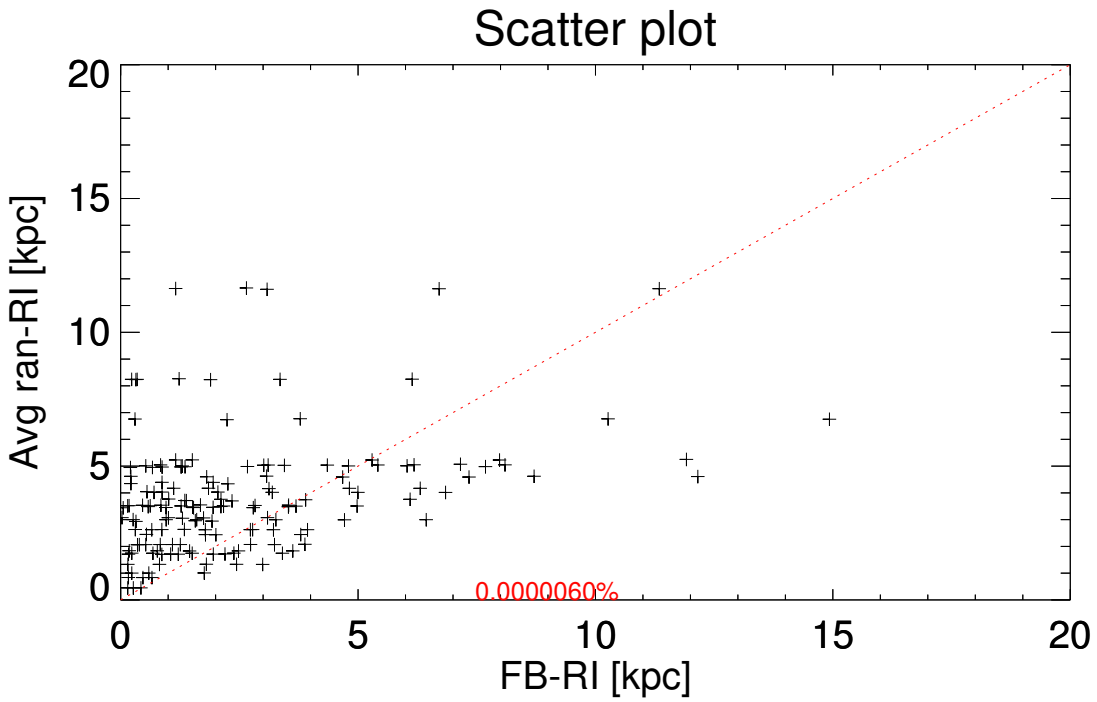

Figure 3.11: This is an example of the scatter plot obtained from the MC I algorithm. This example is the same simulation as the one seen in the histogram example (Figure 3.10); rings were used as RI, the unit of measurement was kpc, and 100k random sets were accepted. The red dotted line is the line of y=x, which is used to better visualize the distribution of the points. The binomial probability of the scatter is shown as the red percentage; this is the probability to have the observed number of points above the line of equality assuming a 50%-50% chance of points landing above or below the line.

Monte Carlo II there is only one averaged random-RI distance for each accepted random resonance set, i.e. the order of resonances is ignored in Monte Carlo II.

(9) The previous step is repeated for all the accepted random resonance sets to obtain one averaged random-RI distance for each of them.

(10) These multiple averaged random-RI distances are all further averaged to obtain a single averaged random-RI distance for the galaxy at hand.

(11) A new galaxy from the sample is picked and the previous steps are repeated to obtain an averaged random-RI distance for this new galaxy.

(12) This is repeated until there are averaged random-RI distances for all the galaxies in the galaxy sample.

(13) Simultaneous to the averaged random-RI distance calculations, the distances between FB resonances and their closest RI resonance for each galaxy are found and then averaged. As the process goes through all the galaxies in the sample, at the end of the simulation there is a single averaged FB-RI distance for each galaxy in the galaxy sample.

(14) A histogram is plotted, similar to that seen in step (14) of Monte Carlo I. See Figure 3.10 for a general example.

(15) A scatter plot is plotted, similar to that seen in step (15) of Monte Carlo I. See Figure 3.11 for a general example.

The algorithm of Monte Carlo II is shown in the flowchart in Figure 3.17.

3.2.5 Monte Carlo II-i

This technically falls under the Monte Carlo II approach, but it is listed as a separate procedure due to the presentation of its final results being of a different nature. It is more individualized with regards to each galaxy hence the name Monte Carlo II-i, where 'i' stands for individual. The following steps are performed in the Monte Carlo II-i technique:

(1) – (9) are identical to those of Monte Carlo II.

(10) A histogram is plotted showing the distribution of the averaged random-RI distances of each accepted set for the galaxy at hand. This is an individual histogram for the galaxy; see Figure 3.12 for an example.

(11) The previous steps are repeated until there are individual histograms for all the galaxies in the galaxy sample.

(12) Simultaneous to the random-RI distance calculations, the distance between FB resonances and their closest RI resonance is found and averaged for each galaxy. This averaged FB-RI distance (a single value per galaxy) is overplotted on the individual histogram of all galaxies.

(13) For each galaxy, the fraction of random resonance sets resulting in averaged random-RI distances to be smaller than averaged FB-RI distances is calculated. This fraction is also overplotted on the individual histograms.

(14) A global histogram for the entire galaxy sample is plotted, which shows the distribution of the fraction of random resonance sets resulting in averaged random-RI distances to be smaller than averaged FB-RI distances. See Figure 3.13 for an example. The light blue percentage in the figure is the ratio of galaxies with a fraction less than 25%; the red dotted-line shows the 25% mark.

The algorithm of Monte Carlo II-i is shown in the flowchart seen in Figure 3.18.

3.2.6 Monte Carlo III

The following steps are performed in the Monte Carlo III technique:

(1) – (6) are identical to those of Monte Carlo I.

(7) The average distance of all of the random resonances within the set to the closest RI resonance is found. Note that this is a single averaged random-RI distance for the only accepted random resonance set from the previous step.

(8) A new galaxy from the galaxy sample is selected and the previous steps are repeated for it.

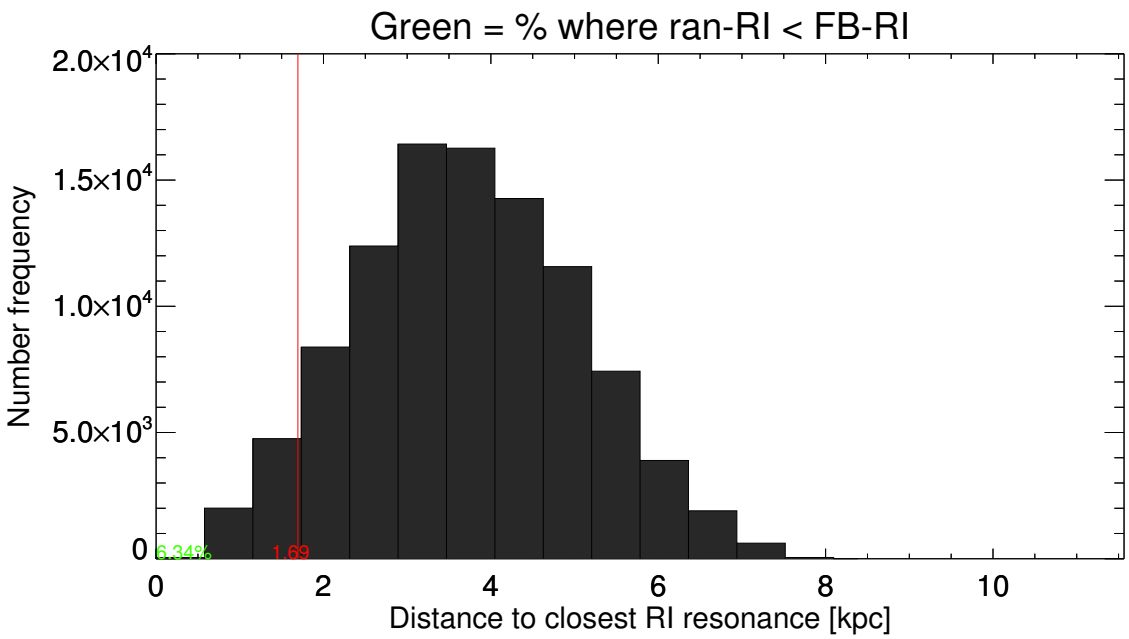

Figure 3.12: This is an example of a MC II-i individual histogram. This histogram belongs to the case of NGC5376 taking rings as RI, kpc as distance unit, and 100k accepted random resonance sets (same as the one in Figure 3.10 and Figure 3.11). The red line represents the mean FB resonance distance to the closest RI resonance. The histogram shows the distribution of the averaged random-RI distances. The green number on the bottom left corner of the graph shows the fraction (in %) of averaged random-RI distances that are smaller than the averaged FB-RI distance.

(9) This is repeated until all the galaxies in the galaxy sample have a single averaged random-RI distance. Note that this is similar to step (12) of Monte Carlo II, but the difference in case of Monte Carlo III is that these averaged random-RI distances are obtained from only one accepted random resonance set.

(10) These averaged random-RI distances are further averaged over the galaxy sample to obtain a globally averaged random-RI distance.

(11) The previous steps of obtaining a globally averaged random-RI distance is repeated until there are as many of them as desired, i.e. multiple iterations of the previous steps are performed to obtain a desired number of globally averaged random-RI distances.

(12) Simultaneous to the averaged random-RI distance calculations, the distance between FB resonances and their closest RI resonance for each galaxy is found and then averaged. These per galaxy averages are then further averaged over the entire galaxy sample to obtain a globally averaged FB-RI distance.

(13) The results are represented via a global histogram; see Figure 3.14 for an example plot. The histogram represents the distribution of the globally averaged random-RI distances. The globally averaged FB-RI distance is also overplotted to visually show the fraction of the globally averaged random-RI distances that are smaller than it; the exact fraction is calculated and shown in the plot.

The algorithm of Monte Carlo III is shown in the flowchart seen in Figure 3.19.

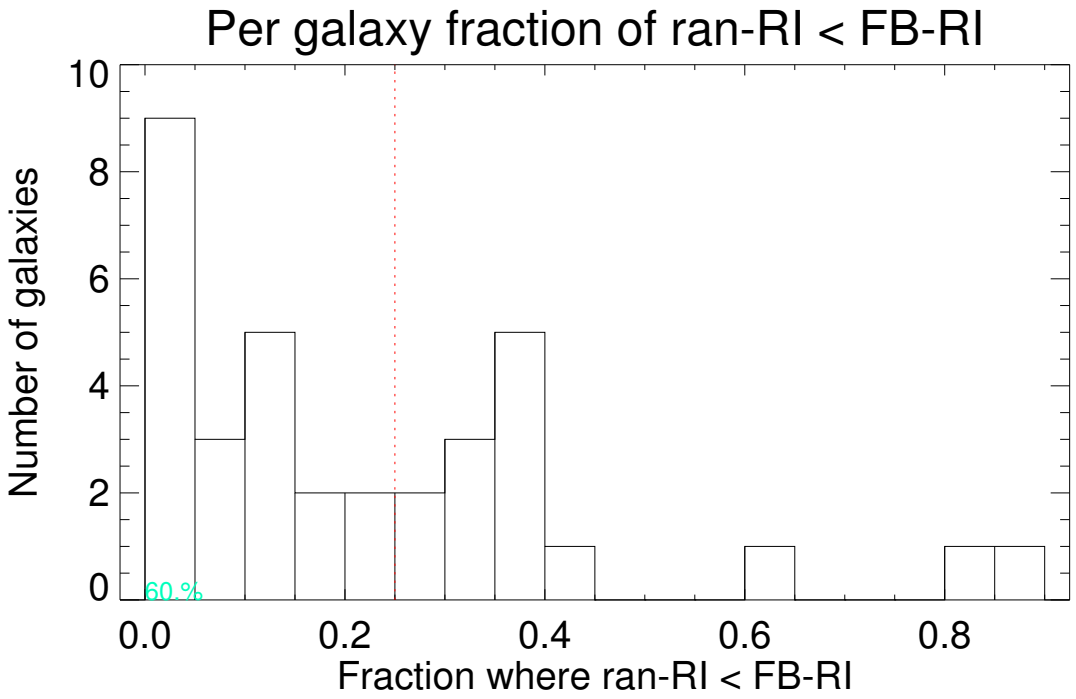

Figure 3.13: This is an example of the MC II-i global histogram that represents the distribution of the fractions of random resonance sets for which the averaged random-RI distances are smaller than the averaged FB-RI distances. In essence, this is a histogram of the green number seen in the individual histograms (see Figure 3.12) over the entire galaxy sample. The light blue percentage is the fraction of galaxies whose fraction is less than 25% and this 25% mark is shown by the red dotted-line. This example simulation is the same as the one seen in Figure 3.10, Figure 3.11, and Figure 3.12.

3.2.7 Reverse comparison

So far all the four Monte Carlo techniques discussed relied on the assumption that the aforementioned resonance indicators (RI) can reliably predict the position of a resonance, while the Font-Beckman (FB) resonances were potentially just random in nature with no significance. The aim was to check the reliability of FB resonances, so the strategy was to compare the FB resonances and random resonances with RI resonances. However, it is important to note that the resonance indicators are not necessarily perfect in doing their job and may give unreliable results. Therefore, as a test, all the four Monte Carlo techniques can be reversed. This means that the comparison scheme is reversed such that RI resonances and random resonances are compared with FB resonances, i.e. the role of FB resonances and RI resonances are reversed. This reverse comparison scheme is visualized in Figure 3.15.

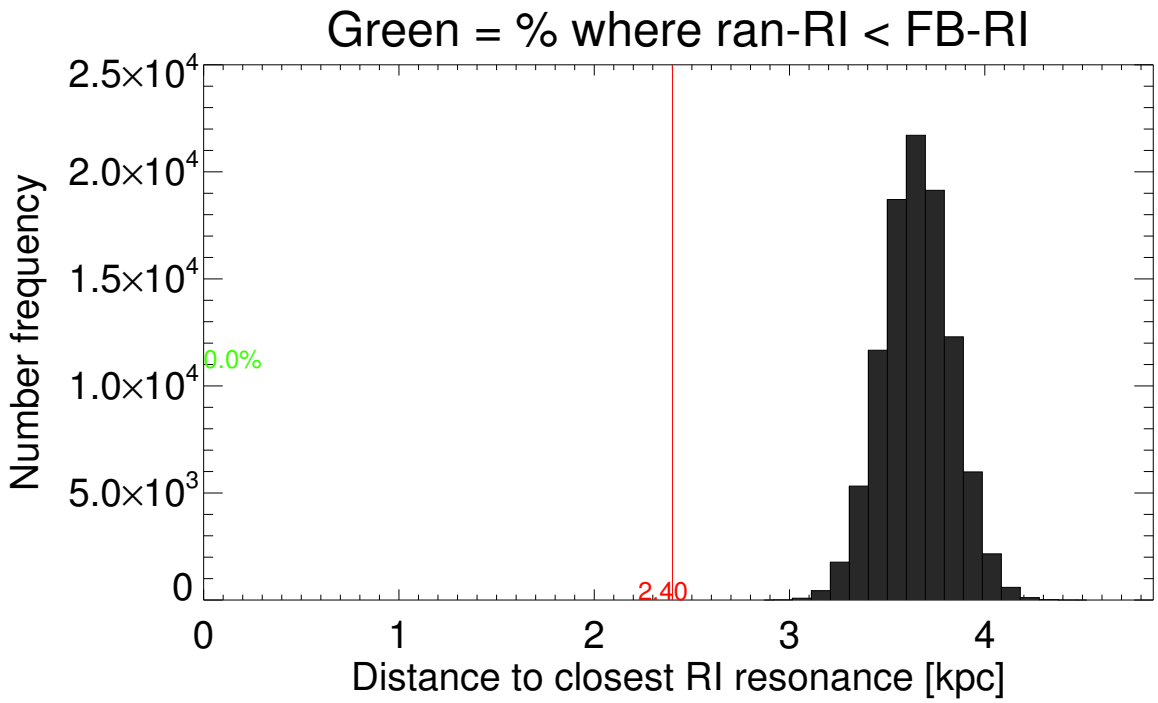

Figure 3.14: This is an example of the MC III histogram. This example simulation is done with kpc as distance unit, all types of truncations as RI, and 100k runs over the entire galaxy sample. The x-axis is the average distance to the closest RI resonance and the y-axis is the number frequency. The histogram itself shows the distribution of the globally averaged random-RI distances for each run over the entire galaxy sample. The red line shows the globally averaged FB-RI distance. The green number is the fraction (in %) of each run (over the entire galaxy sample) that results in a globally averaged random-RI distance to be smaller than the globally averaged FB-RI distance; in this case this number is 0% as none of the globally averaged random-RI distances were smaller than the globally averaged FB-RI distance.

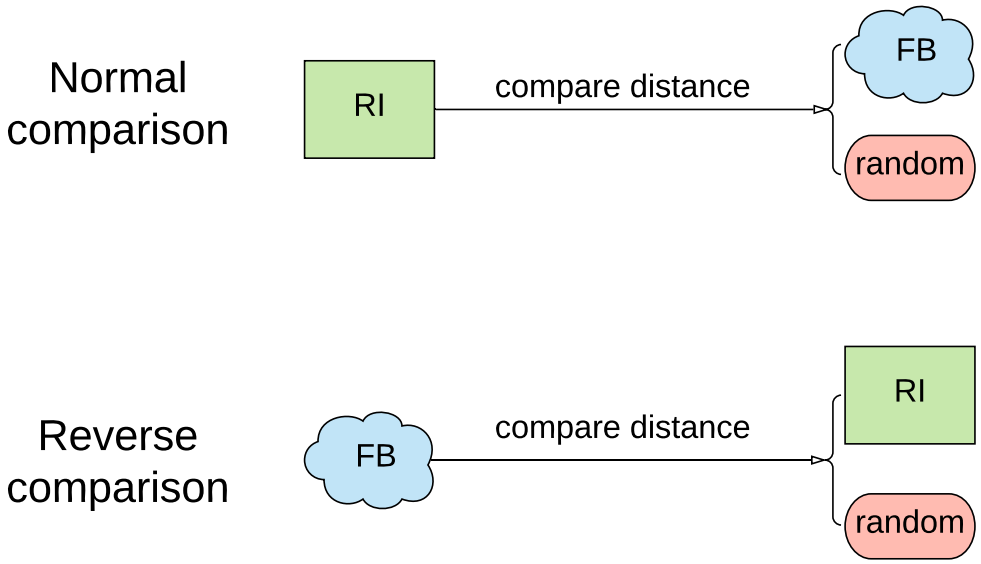

Figure 3.15: The top chart shows the comparison scheme of the normal Monte Carlo algorithms. The bottom chart shows the comparison scheme when it is reversed. Note that the reversal of the roles of FB resonances and RI resonances is the only difference between the two schemes.

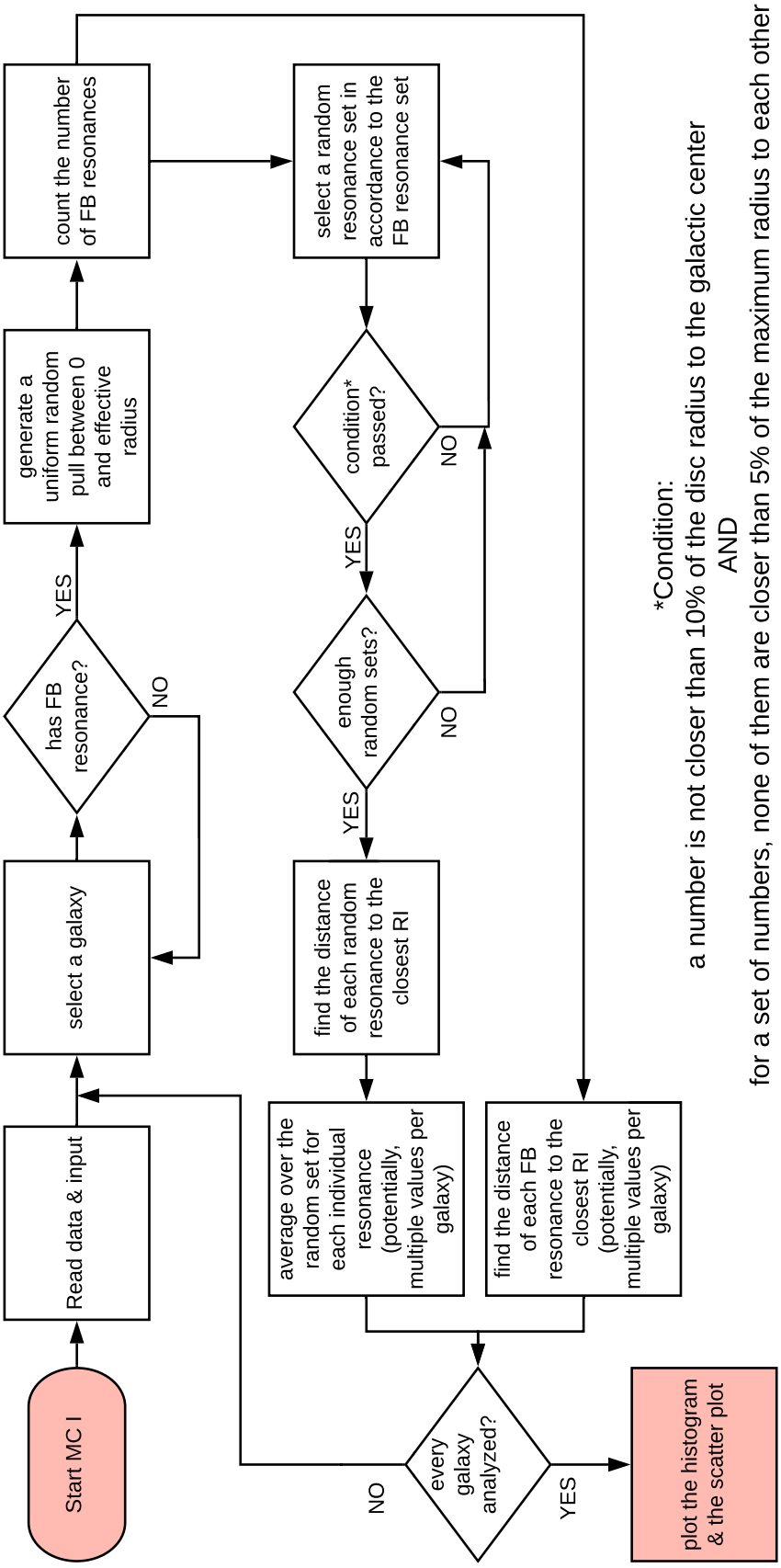

Figure 3.16: This flowchart shows the algorithm used in the Monte Carlo I technique.

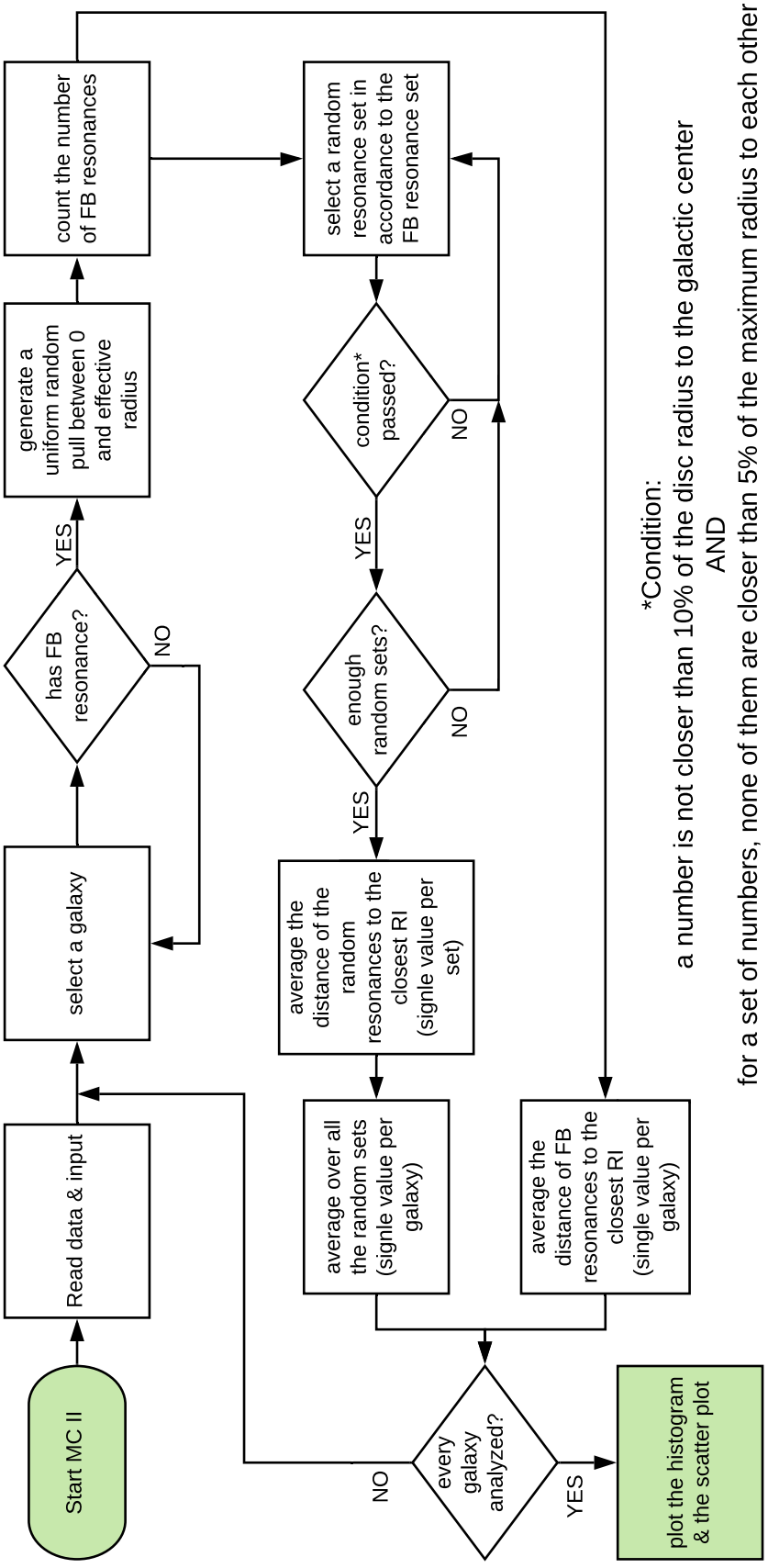

Figure 3.17: This flowchart shows the algorithm used in the Monte Carlo II technique.

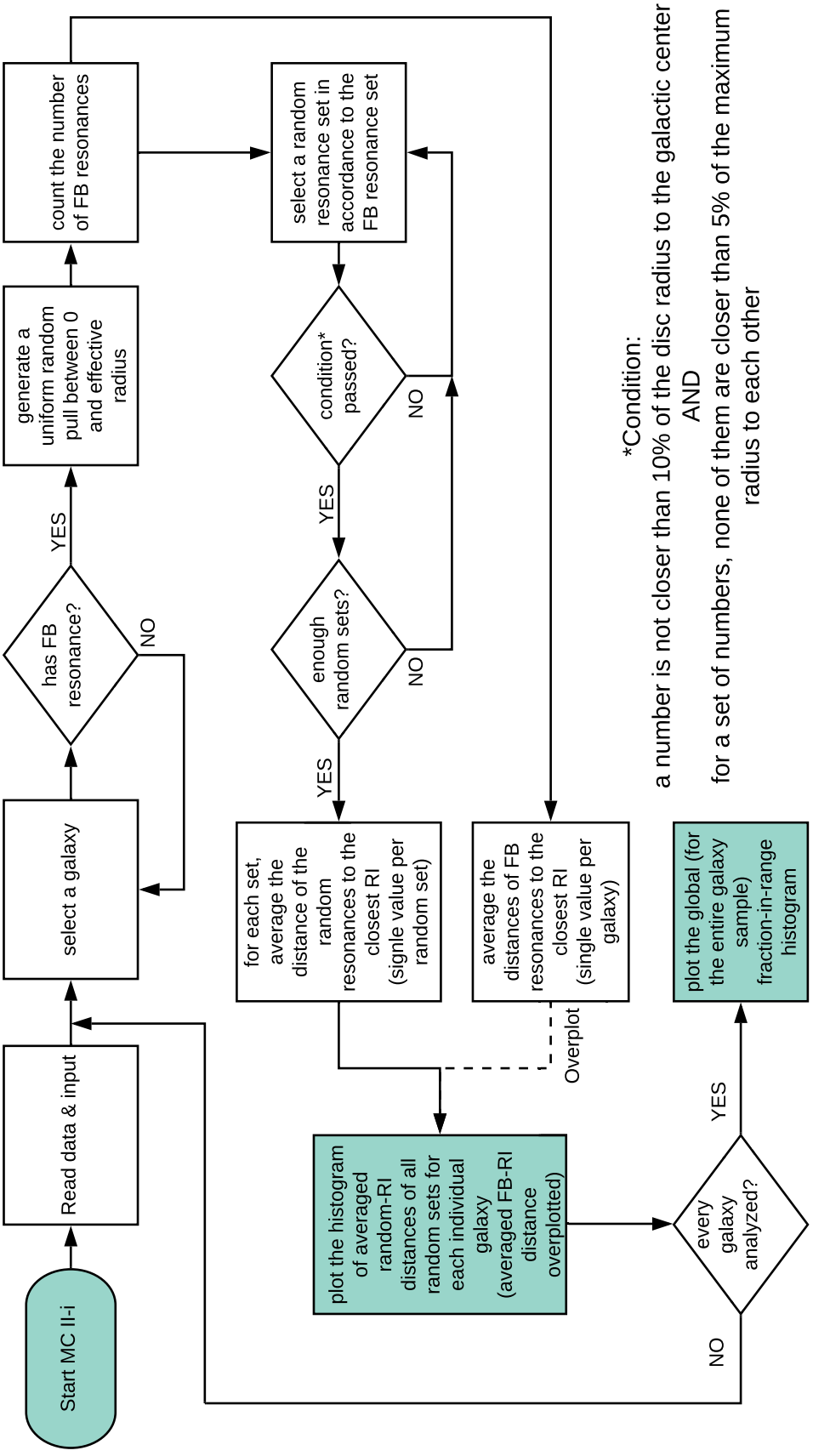

Figure 3.18: This flowchart shows the algorithm used in the Monte Carlo II-i technique.

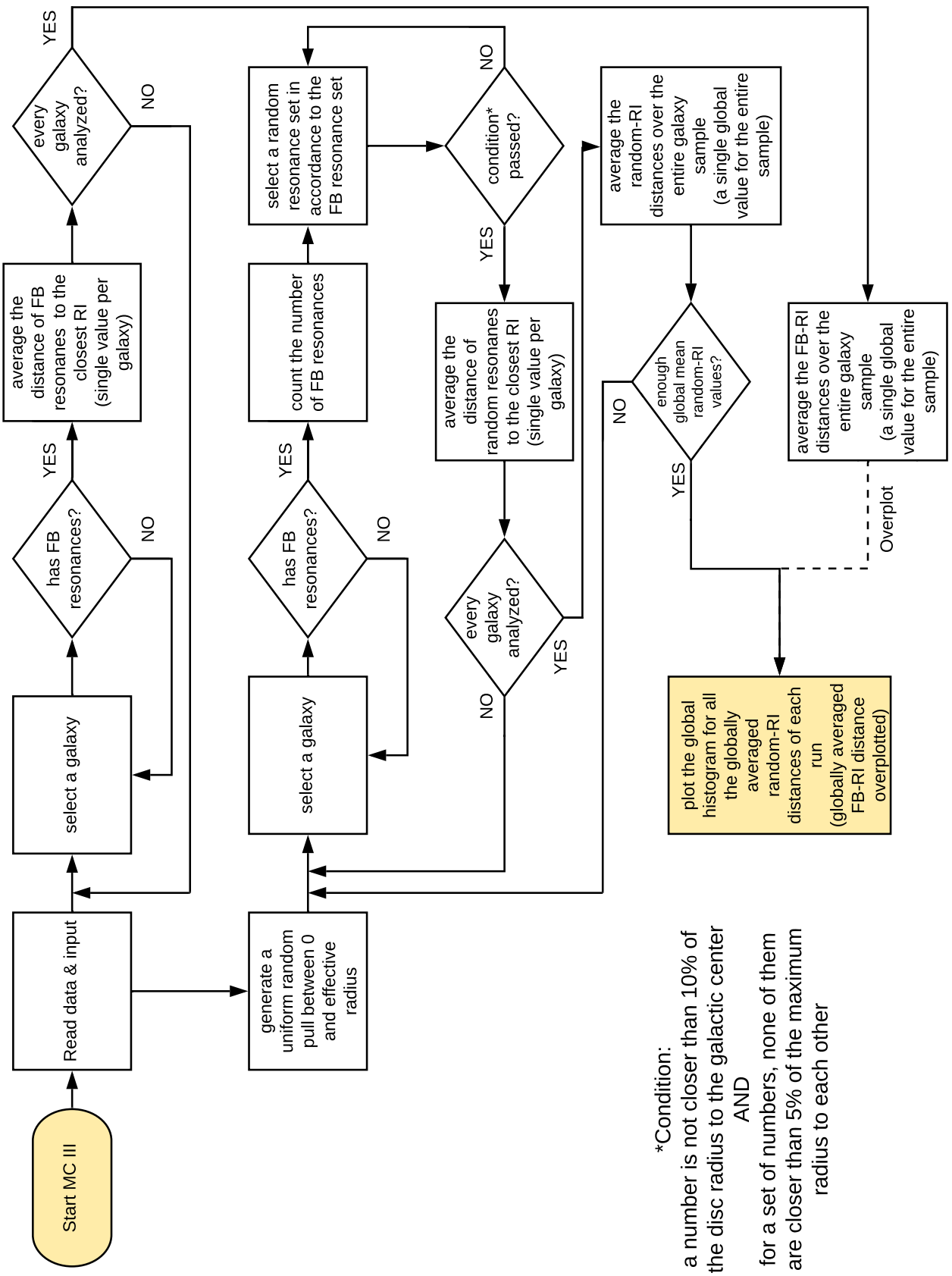

Figure 3.19: This flowchart shows the algorithm used in the Monte Carlo III technique.

Chapter 4

Results

The results of the study are presented in this chapter. The first subsection pertains to the simulation and the theoretical application of the Font-Beckman method. The second subsection contains the results of the Monte Carlo analysis of the Font-Beckman method.

4.1 Simulation application

In this section the application of the Font-Beckman method to a number of simulated galaxies is shown. The galaxies are simulated using the Wada method (explained in section 3.1.2) such that the position of their resonances is theoretically known. See Figure 3.6 for an example simulated galaxy with its resonance locations known; such simulated galaxies with known resonances are used to put the Font-Beckman method to the test. This allows for a clear comparison with the Font-Beckman determination of resonance locations. The Wada simulation is done with varying parameters, which results in a number of distinct simulated galaxies. These parameters are particle count, initial particle arrangement (semi-random or random), perturbation strength, inclination, and maximum radius. The option of adding blurring to mimic seeing to the simulated galaxies also exists; this allows for converting the clean simulated galaxy into a more observation-like galaxy. On top these options, the Font-Beckman method (re-coded for this thesis) can use two different ways of selecting pixels to find resonances and two distinct ways of rejecting phase reversals, as explained previously in section 3.1.1. The pixel selection methods are the original Font-Beckman one and the pixel averaging method. The phase reversal rejection methods are the original Font-Beckman one and the direct derivation method. Furthermore, the effect of the value of the Font-Beckman phase reversal velocity threshold is observed. The effect of the duration of the Wada simulation is also investigated, i.e. testing how the length of the simulation affects the resonances.

In the following controlled comparisons the effect of each of these parameters is represented; these are controlled comparisons because only one or two of the parameters changed while the rest were kept constant. The histograms show phase reversal distributions as found by the Font-Beckman algorithm. The peaks in this distribution, found by fitting a multi-peak Gaussian function, represent the resonance locations of the simulated galaxy. These locations are shown by the red vertical lines and the uncertainty in the radius of the estimate is represented by the width of the Gaussian peak; note that the exact Font-Beckman resonance location estimates and their uncertainties are given in blue. The green vertical lines represent the theoretical resonance locations (known from the Wada simulation).

The first parameter to be studied is the particle count. This determines the number of particles placed semi-randomly or randomly in a disc to undergo the Wada simulation. In general, the larger this number is the more detailed the simulated galaxy becomes; however, this enhancement of the intricacies of the galaxy comes at the cost of computing power and time. There are three particle numbers used for this comparison as seen in Figure 4.1, which are 400k, 4M, and 40M. Note that these particles are all initially randomly arranged in 2000 rings (semi-random arrangement). Moreover, there is no blurring, the perturbation strength is 0.05, the inclination is 45°, the maximum radius is 160 arcsec, the phase reversal velocity threshold is 10^{-5} simulation velocity units, the simulation duration is 50 simulation time units, and the original Font-Beckman methods for pixel selection of phase reversal rejection are used.

The next parameter of interest is the initial arrangement of these particles. As mentioned previously, this can be purely random or semi-random. In the purely random case, the initial particles are randomly placed on the whole disc, which can result in unnatural clumps of initial particles. The semi-random case uses "guiding" rings to guide the placement of the initial particles; they are still randomly placed in each ring, however, the number of particles in each ring remains constant and the ring distribution remains ordered throughout the disc. This semi-random particle placement results in more realistic simulated galaxies. A comparison between semi-random (rings) and random (no ring) particle placement is shown in Figure 4.2. Note that in both of the galaxies there is no blurring, the particle count is 4M, the perturbation strength is 0.05, the inclination is 45°, the maximum radius is 160 arcsec, the phase reversal velocity threshold is 10^{-5} simulation velocity units, the simulation duration is 50 simulation time units, and the original methods of pixel selection and phase reversal rejection are used.

The perturbation strength determines the amplitude of the perturbing force applied to the particles. The comparison of three different perturbation strengths is shown in Figure 4.3; these, in simulation units[1], are 0.01, 0.05, and 0.09. Note that in all the three cases there is no blurring, the particle count is 4M, the particles are initially placed in 2k rings, the inclination is 45°, the maximum radius is 160 arcsec, the phase reversal velocity threshold is 10^{-5} simulation velocity units, the simulation duration is 50 simulation time units, and the original methods of pixel selection and phase reversal rejection are used.

The inclination of the galaxy plays an important role in the application of the Font-Beckman method. The line-of-sight velocities are directly affected by this tilt due to the orientation of the galaxy. A comparison of five different inclination values is shown in Figure 4.4; the comparison inclinations are 15°, 30°, 45°, 60°, and 75°. The extreme inclination values of 0° and 90° are not of interest. In all the five galaxies there is no blurring, the particle count is 4M, the particles are initially placed in 2k rings, the perturbation strength is 0.05, the maximum radius is 160 arcsec, the phase reversal velocity threshold is 10^{-5} simulation velocity units, the simulation duration is 50 simulation time units, and the original methods of pixel selection and phase reversal rejection are used.

A comparison between three galaxies of different maximum radii is shown in Figure 4.5; the different radii are 120 arcsec, 160 arcsec, and 200 arcsec. All the simulated galaxies have an inner edge (i.e. inner radius) which is kept at 20 arcsec. This is also the case for the previously mentioned simulated galaxies. This inner radius is not used for comparison purposes because, unlike the outer regions, the inner regions of the simulated galaxies are generally too small for the Font-Beckman method to reliably

[1]There are many instances where simulation units of various types are used in this study. It is crucial to note that the units used within the simulation are of no importance to the purpose of this study; we aim to simulate galaxies with known resonances in order to test the Font-Beckman method. So the vagueness of the simulation units is of no concern. The only important unit that is needed in the Font-Beckman method is the pixel size, which we have defined to be 1 arcsec for all the simulated galaxies.

find resonances. The maximum radius comparison is done in the case of no blurring, particle count of 4M, initial particle placement within 2k rings, perturbation strength of 0.05, inclination of 45°, phase reversal velocity threshold of 10^{-5} simulation velocity units, and simulation duration of 50 simulation time units, while the original methods of pixel selection and phase reversal rejection are utilized.

The two pixel selection methods and the two phase reversal rejection methods are collectively compared in Figure 4.6. The combination of these results is four distinct cases: (1) when both the selection and rejection are done originally as intended by the Font-Beckman method, (2) when the selection is done by pixel averaging while the rejection is the original, (3) when the selection is done according to the original Font-Beckman method while the rejection utilizes direct derivation, and (4) when the selection uses pixel averaging and the rejection is done by direct derivation. In all four cases there is no blurring, the particle count is 4M, the particles are initially placed in 2k rings, the perturbation strength is 0.05, the inclination is 45°, the maximum radius is 160 arcsec, the phase reversal velocity threshold is 10^{-5} simulation velocity units, and the simulation duration is 50 simulation time units.

The value of the Font-Beckman phase reversal velocity threshold is important in determining the pixels where such phase reversals occur. If this value is small then more phase reversals are counted (less are rejected) while a large threshold results in less phase reversals being counted (more are rejected). The default value of this parameter is 10^{-5} in simulation velocity units. The effect of changing this parameter is shown in Figure 4.7; the values are 10^{-2}, 10^{-3}, 10^{-4}, 10^{-5}, and 10^{-6} in simulation velocity units. This comparison is done in the case of no blurring, particle count of 4M, initial particle placement within 2k rings, perturbation strength of 0.05, inclination of 45°, the maximum radius is 160 arcsec, and the simulation duration is 50 simulation time units, while the original methods of pixel selection and phase reversal rejection are utilized.

The duration of the simulation affects the residual velocity map (see Figure 3.7). The comparison in Figure 4.8 shows how the simulation duration may affect the Font-Beckman results. The duration values are 10, 50, and 90 simulation time units. The default simulation duration value is 50 units in all the other controlled tests. This comparison is done in the case of no blurring, particle count of 4M, initial particle placement within 2k rings, perturbation strength of 0.05, inclination of 45°, the maximum radius is 160 arcsec, and the phase reversal velocity threshold is 10^{-5} simulation velocity units, while the original methods of pixel selection and phase reversal rejection are utilized.

The last three comparison panels seen in Figure 4.9, Figure 4.10, and Figure 4.11 show the effect of adding Gaussian blurring to the simulated galaxies, respectively for perturbation strengths of 0.01, 0.05, and 0.09. The blurring strength is measured in terms of the standard deviation of the Gaussian smooth function in units of pixels. This value ranges from σ being 0 (i.e. no blurring) to σ being 10 pixels across five stages of increasing blurring (σ) for both of the comparison panels. For all of these simulated galaxies the particle count is 4M, the particles are initially placed in 2k rings, the inclination is 45°, the maximum radius is 160 arcsec, the phase reversal velocity threshold is 10^{-5} simulation velocity units, and the simulation duration is 50 simulation time units, while the original methods of pixel selection and phase reversal rejection are utilized.

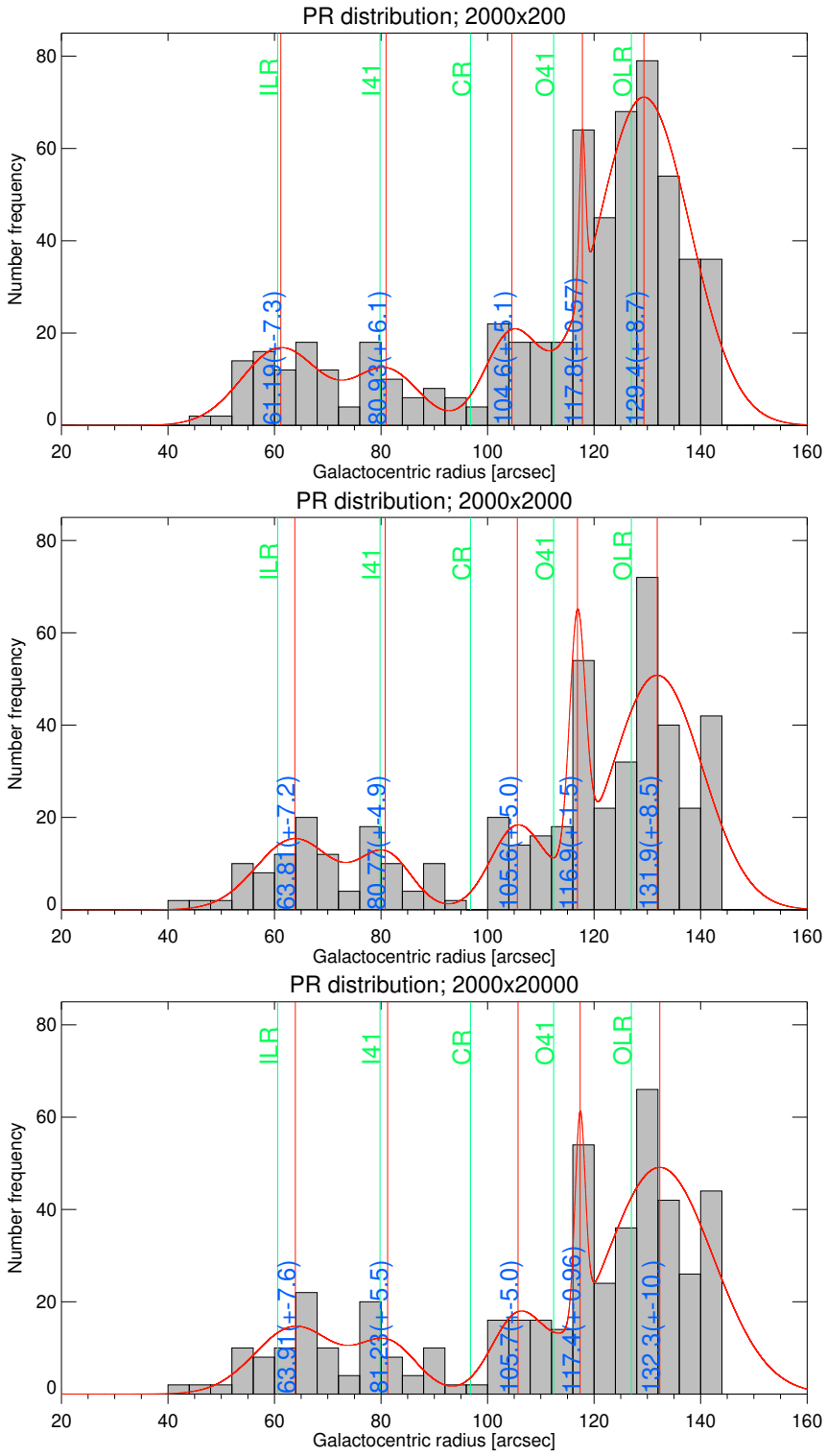

Figure 4.1: Particle number comparison; 400k, 4M, and 40M. The controlled parameters are no blurring, semi-random initial distribution in 2k rings, perturbation strength of 0.05, inclination of 45°, maximum radius of 160 arcsec, phase reversal velocity threshold of 10^{-5} simulation velocity units, simulation duration of 50 simulation time units, and the original methods of pixel selection and phase reversal rejection. The green vertical lines are the theoretical (known from Wada simulation) resonances. The red curve is the Gaussian fit and the red vertical lines represent where the Gaussian peaks are located. The radial value of the Gaussian peaks is given as the blue number and their uncertainty (width of the Gaussian peak) is given in brackets.

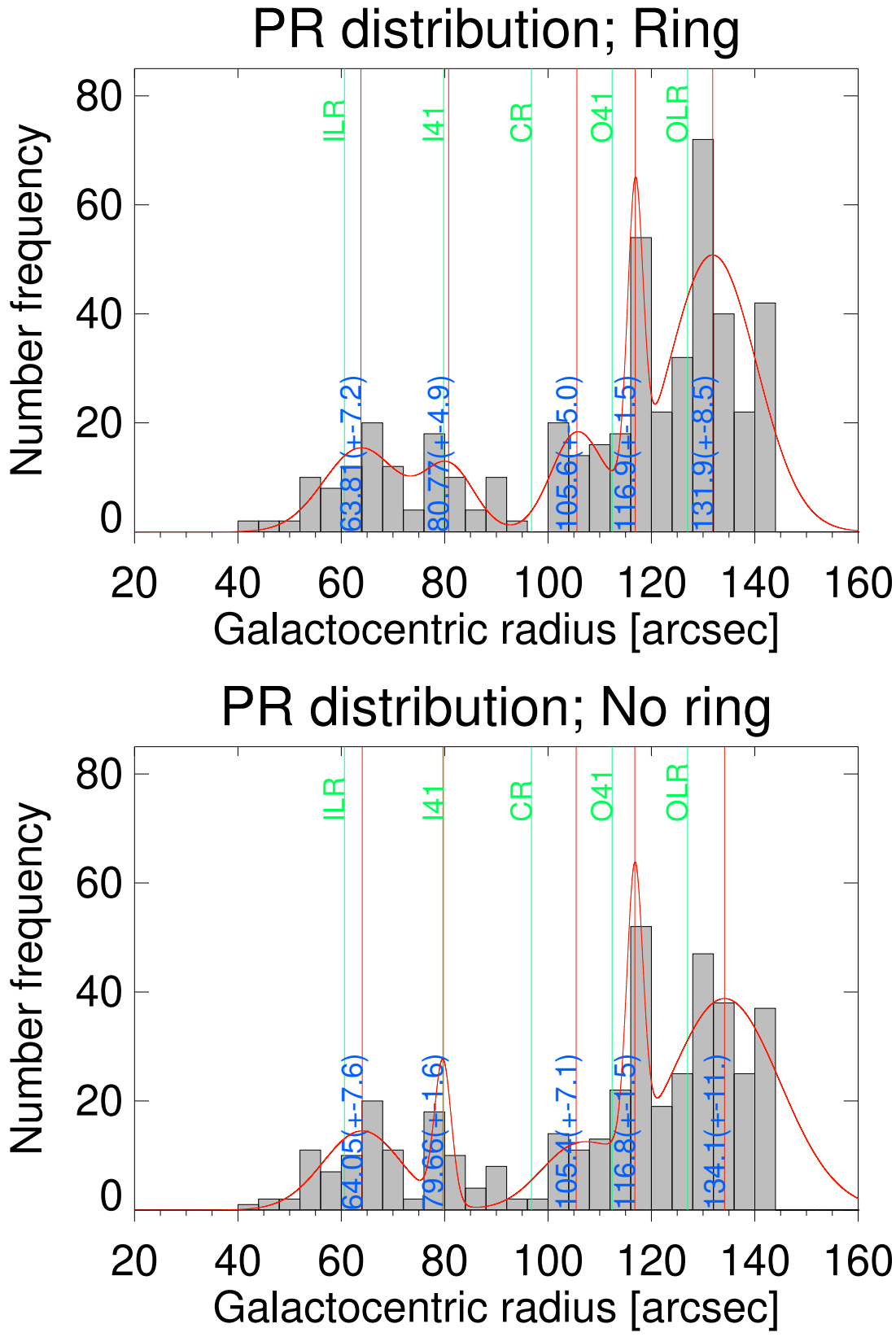

Figure 4.2: Initial particle arrangement comparison; semi-random (ring) versus random (no ring). The controlled parameters are no blurring, particle count of 4M, perturbation strength of 0.05, inclination of 45°, maximum radius of 160 arcsec, phase reversal velocity threshold of 10^{-5} simulation velocity units, simulation duration of 50 simulation time units, and the original methods of pixel selection and phase reversal rejection. The graph layout is as in Figure 4.1.

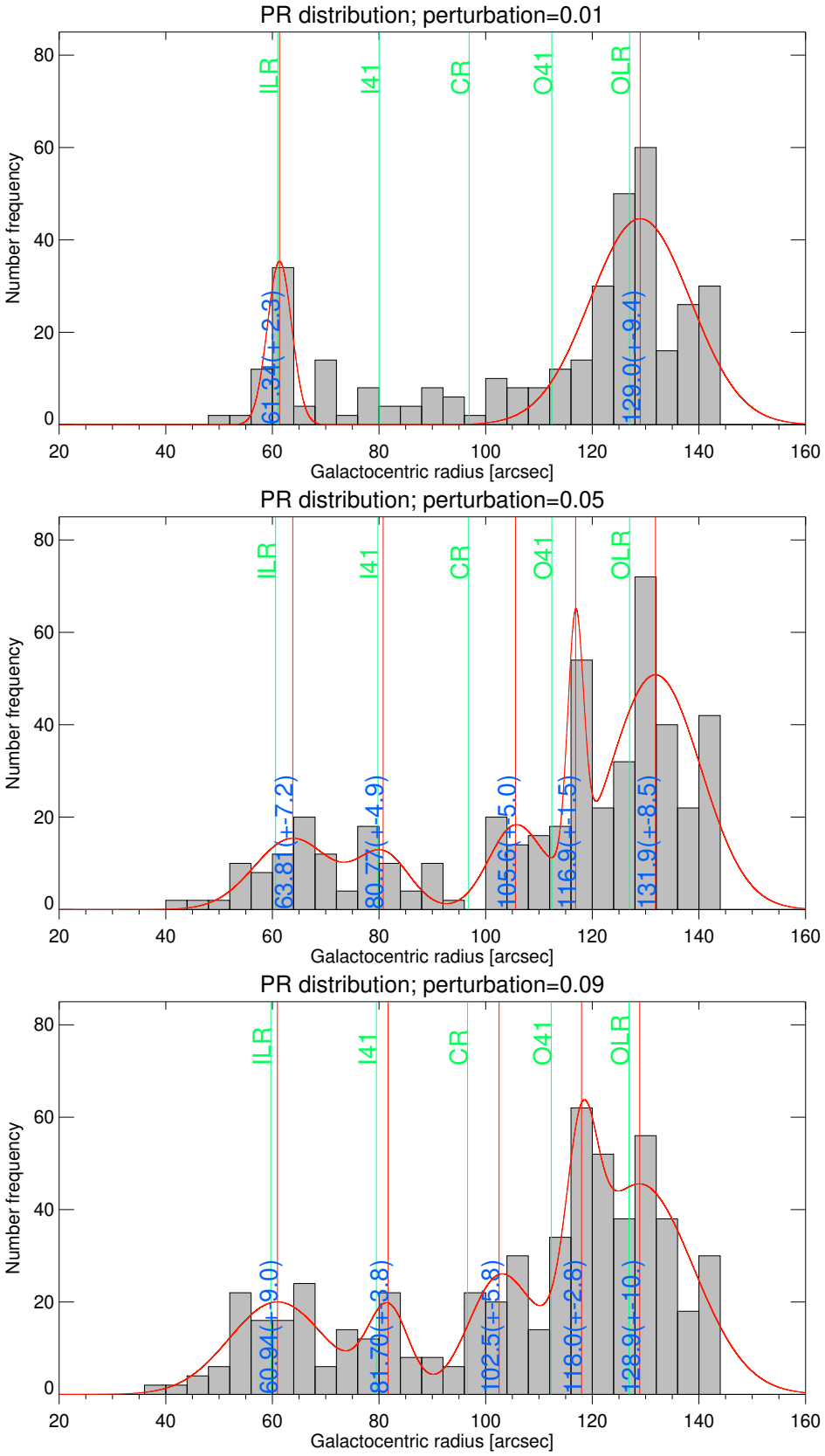

Figure 4.3: Perturbation strength comparison; 0.01, 0.05, and 0.09. The controlled parameters are no blurring, particle count of 4M, semi-random distribution in 2k rings, inclination of 45°, maximum radius of 160 arcsec, phase reversal velocity threshold of 10^{-5} simulation velocity units, simulation duration of 50 simulation time units, and the original methods of pixel selection and phase reversal rejection. The graph layout is as in Figure 4.1.

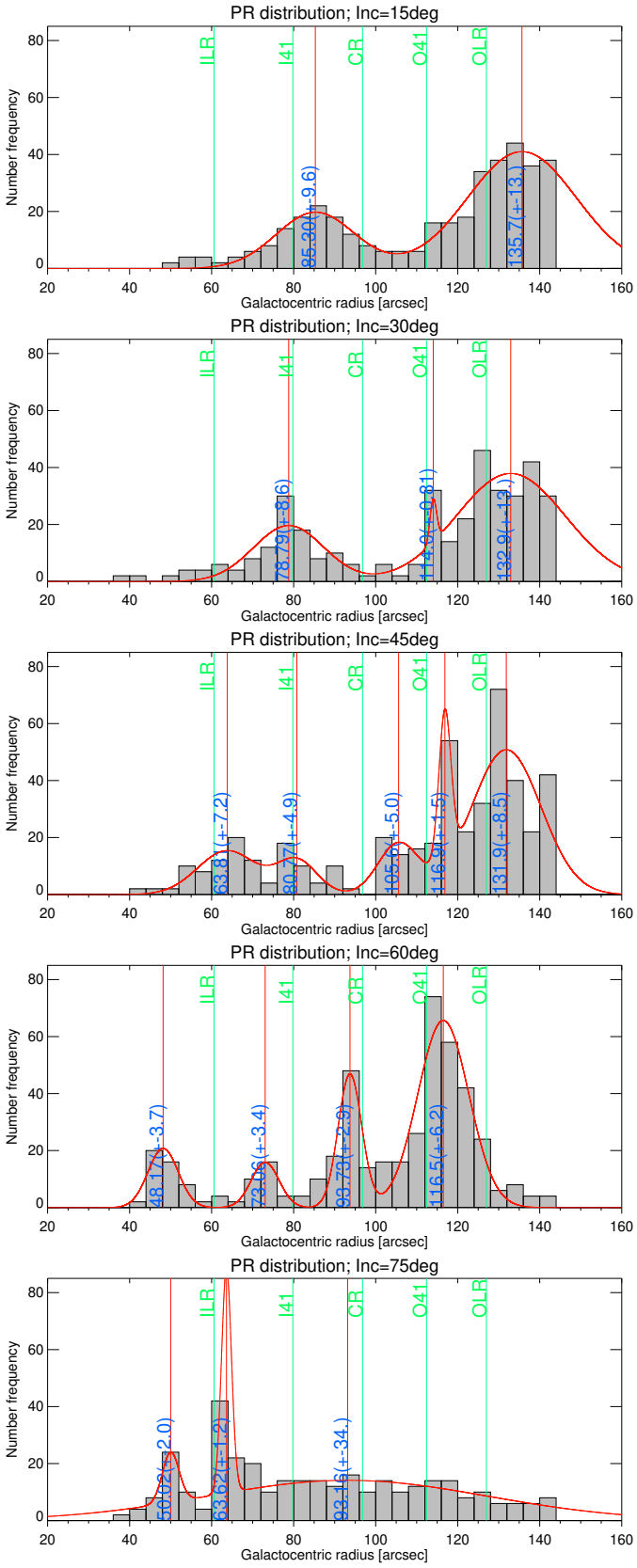

Figure 4.4: Inclination comparison; 15°, 30°, 45°, 60°, and 75°. The controlled parameters are no blurring, particle count of 4M, semi-random distribution in 2k rings, perturbation strength of 0.05, maximum radius of 160 arcsec, phase reversal velocity threshold of 10^{-5} simulation velocity units, simulation duration of 50 simulation time units, and the original methods of pixel selection and phase reversal rejection. The graph layout is as in Figure 4.1.

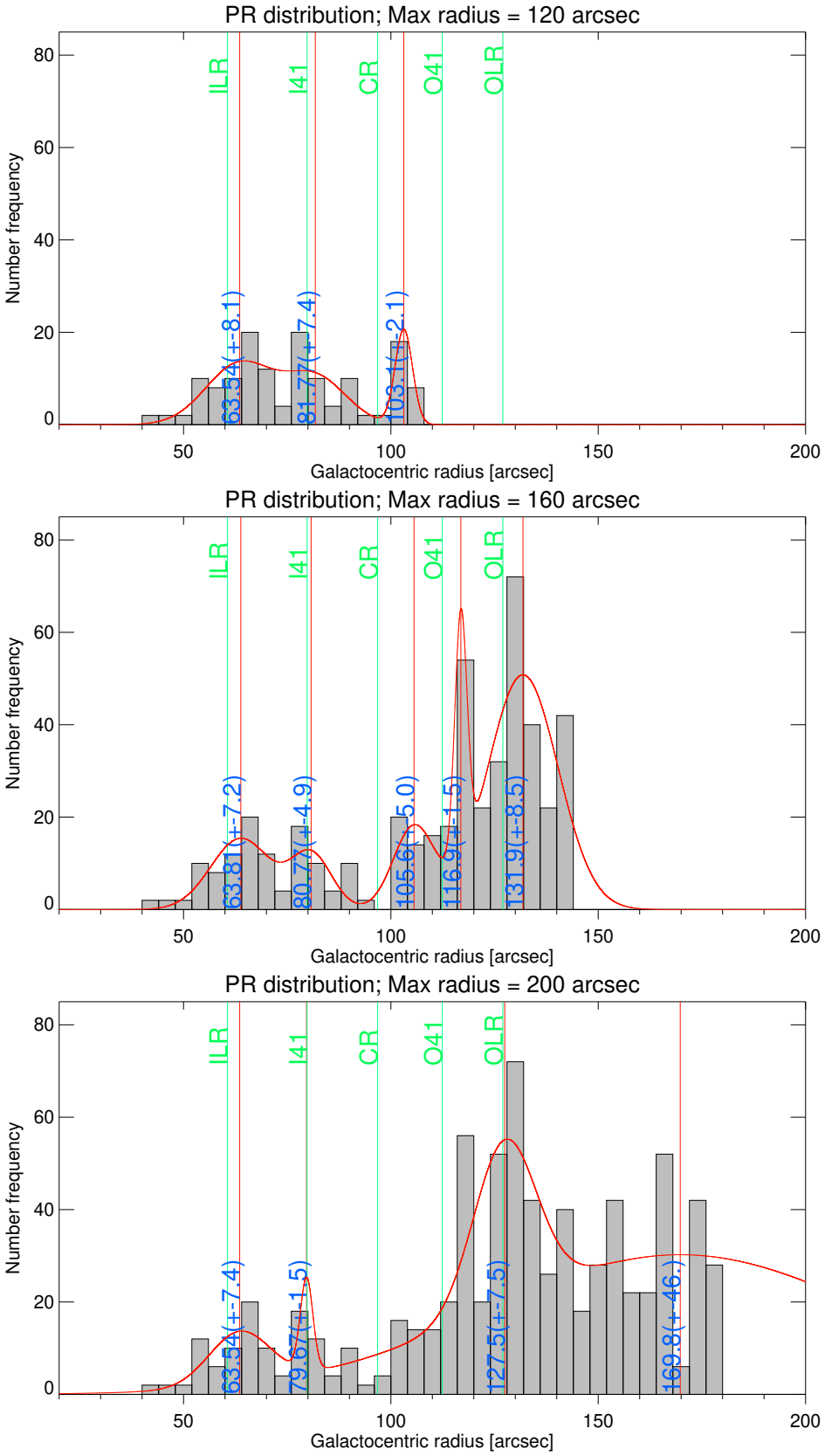

Figure 4.5: Maximum radius comparison; 120 arcsec, 160 arcsec, and 200 arcsec. The controlled parameters are no blurring, particle count of 4M, semi-random distribution in 2k rings, perturbation strength of 0.05, inclination of 45°, phase reversal velocity threshold of 10^{-5} simulation velocity units, simulation duration of 50 simulation time units, and the original methods of pixel selection and phase reversal rejection. The graph layout is as in Figure 4.1.

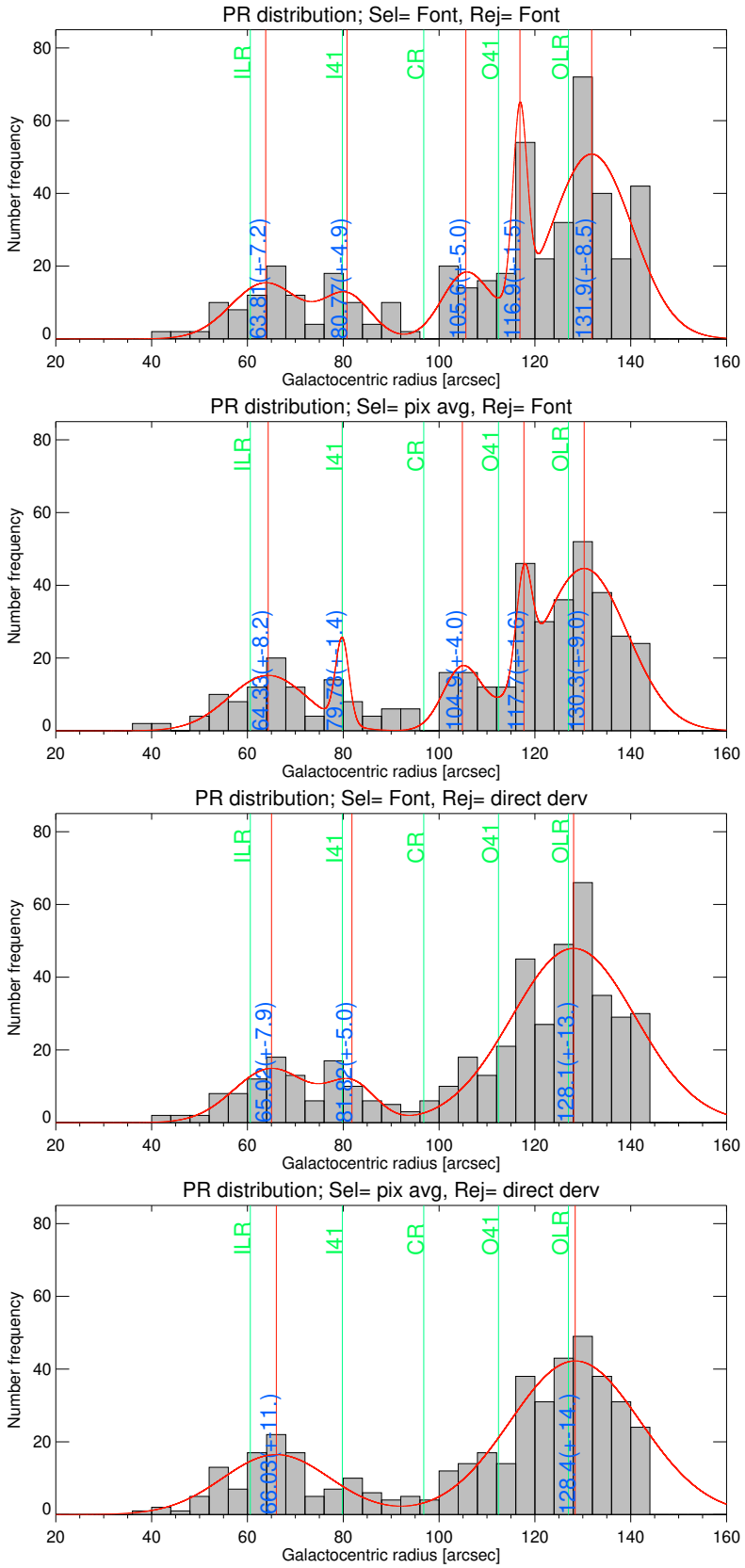

Figure 4.6: Pixel selection and phase reversal rejection methods comparison; both are original, selection is alternative while rejection is original, selection is original while rejection is alternative, and both are alternative. The controlled parameters are no blurring, particle count of 4M, semi-random distribution in 2k rings, perturbation strength of 0.05, inclination of 45°, maximum radius of 160 arcsec, phase reversal velocity threshold of 10^{-5} simulation velocity units, and simulation duration of 50 simulation time units. The graph layout is as in Figure 4.1.

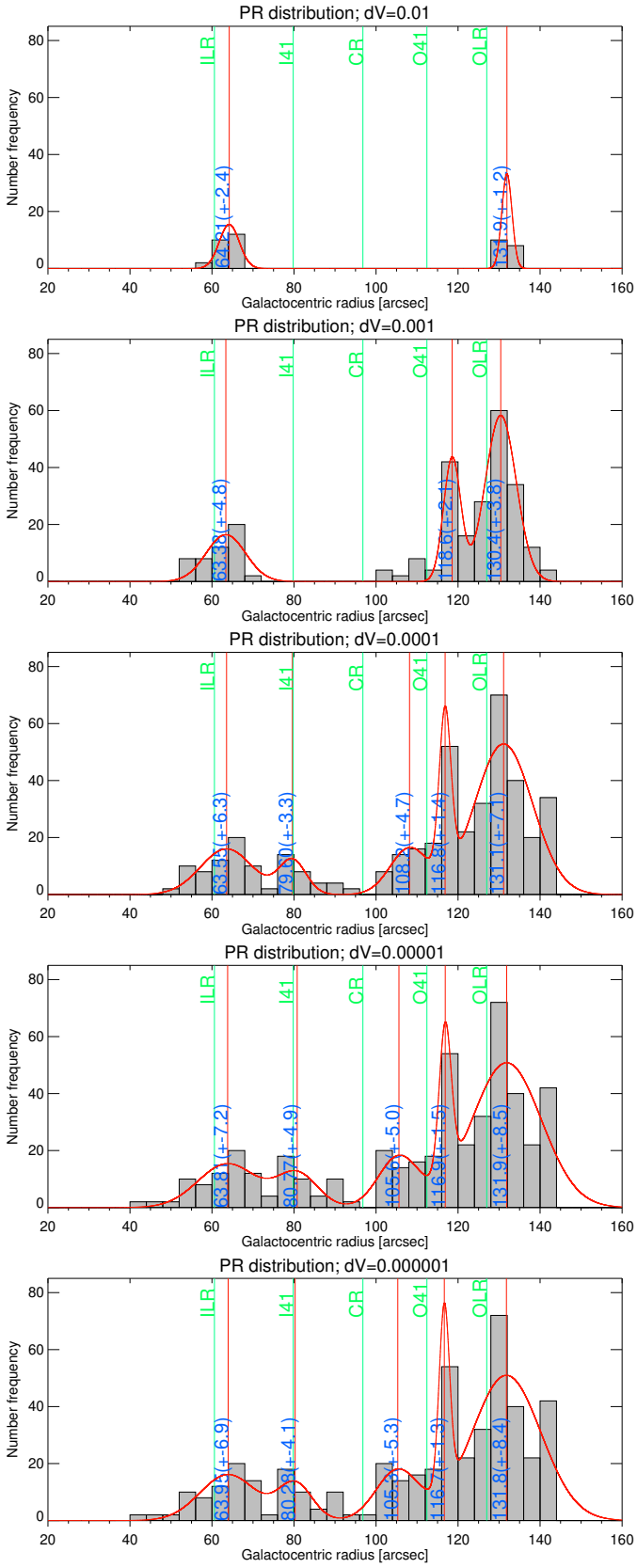

Figure 4.7: Font-Beckman's phase reversal velocity sensitivity comparison; 10^{-2}, 10^{-3}, 10^{-4}, 10^{-5}, and 10^{-6} in simulation velocity units. The controlled parameters are no blurring, particle count of 4M, semi-random distribution in 2k rings, perturbation strength of 0.05, inclination of 45°, maximum radius of 160 arcsec, simulation duration of 50 simulation time units, and the original methods of pixel selection and phase reversal rejection. The graph layout is as in Figure 4.1.

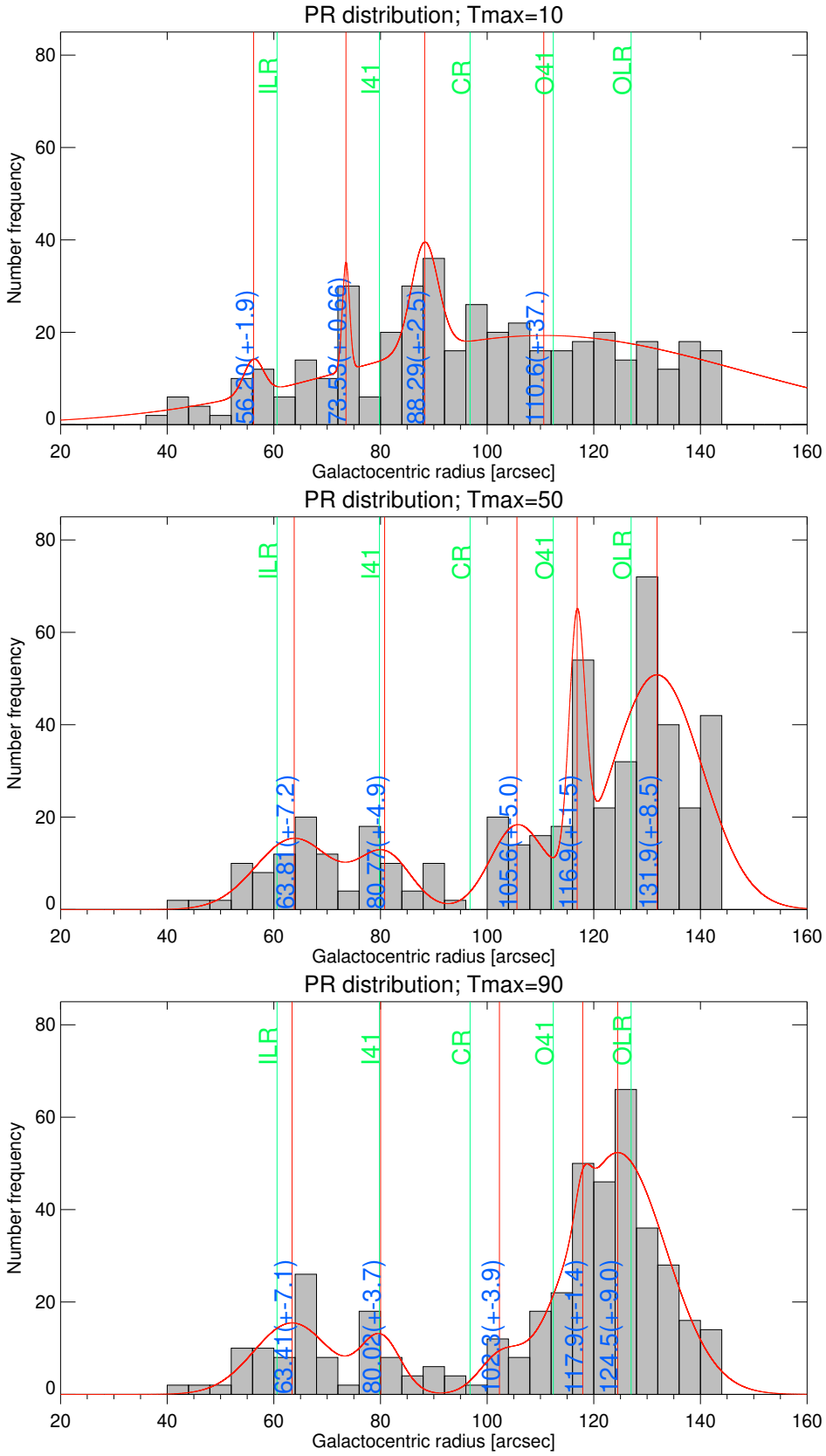

Figure 4.8: Maximum simulation duration comparison; 10, 50, and 90 in simulation time units. The controlled parameters are no blurring, particle count of 4M, semi-random distribution in 2k rings, perturbation strength of 0.05, inclination of 45°, maximum radius of 160 arcsec, phase reversal velocity threshold of 10^{-5} simulation velocity units, and the original methods of pixel selection and phase reversal rejection. The graph layout is as in Figure 4.1.

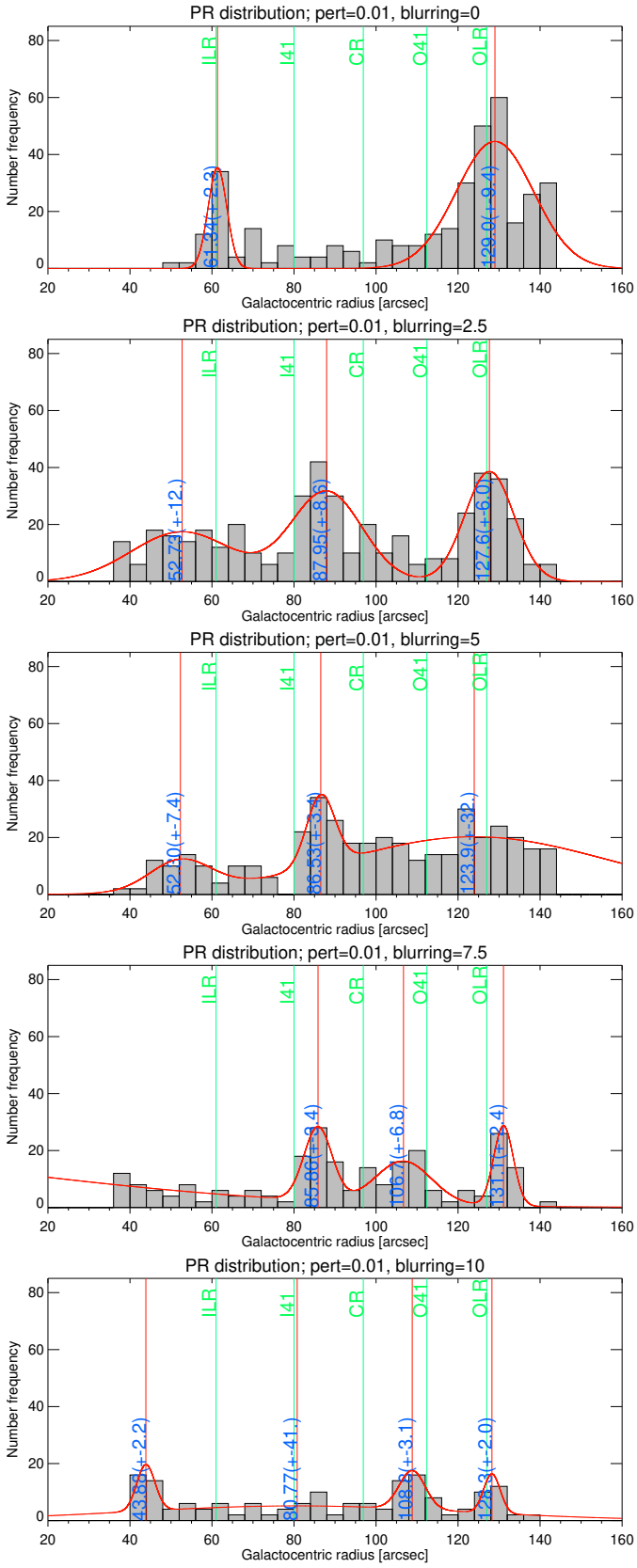

Figure 4.9: Blurring comparison for the perturbation strength of 0.01; blurring of $\sigma = 0$, $\sigma = 2.5$, $\sigma = 5$, $\sigma = 7.5$, and $\sigma = 10$ (all in units of pixels). The controlled parameters are particle count of 4M, semi-random distribution in 2k rings, inclination of 45°, maximum radius of 160 arcsec, phase reversal velocity threshold of 10^{-5} simulation velocity units, simulation duration of 50 simulation time units, and the original methods of pixel selection and phase reversal rejection. The graph layout is as in Figure 4.1.

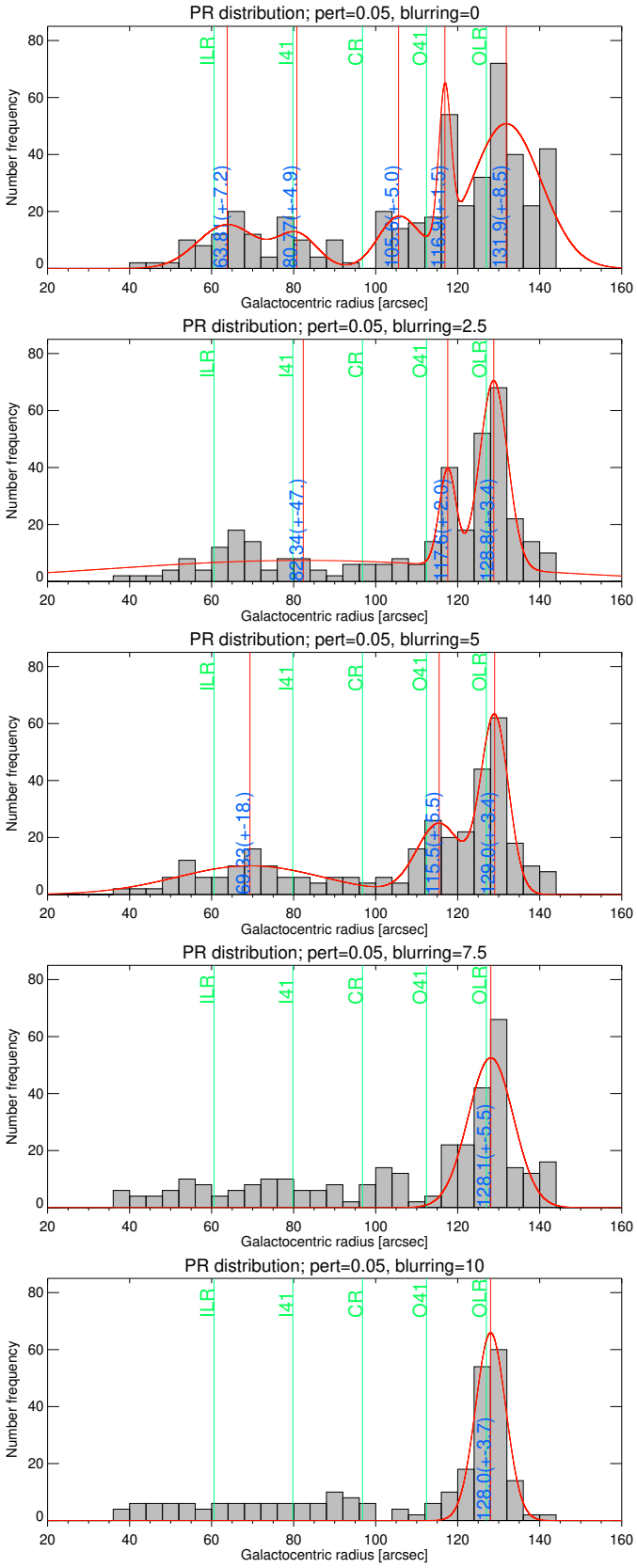

Figure 4.10: Blurring comparison for the perturbation strength of 0.05; blurring of $\sigma = 0$, $\sigma = 2.5$, $\sigma = 5$, $\sigma = 7.5$, and $\sigma = 10$ (all in units of pixels). The controlled parameters are particle count of 4M, semi-random distribution in 2k rings, inclination of 45°, maximum radius of 160 arcsec, phase reversal velocity threshold of 10^{-5} simulation velocity units, simulation duration of 50 simulation time units, and the original methods of pixel selection and phase reversal rejection. The graph layout is as in Figure 4.1.

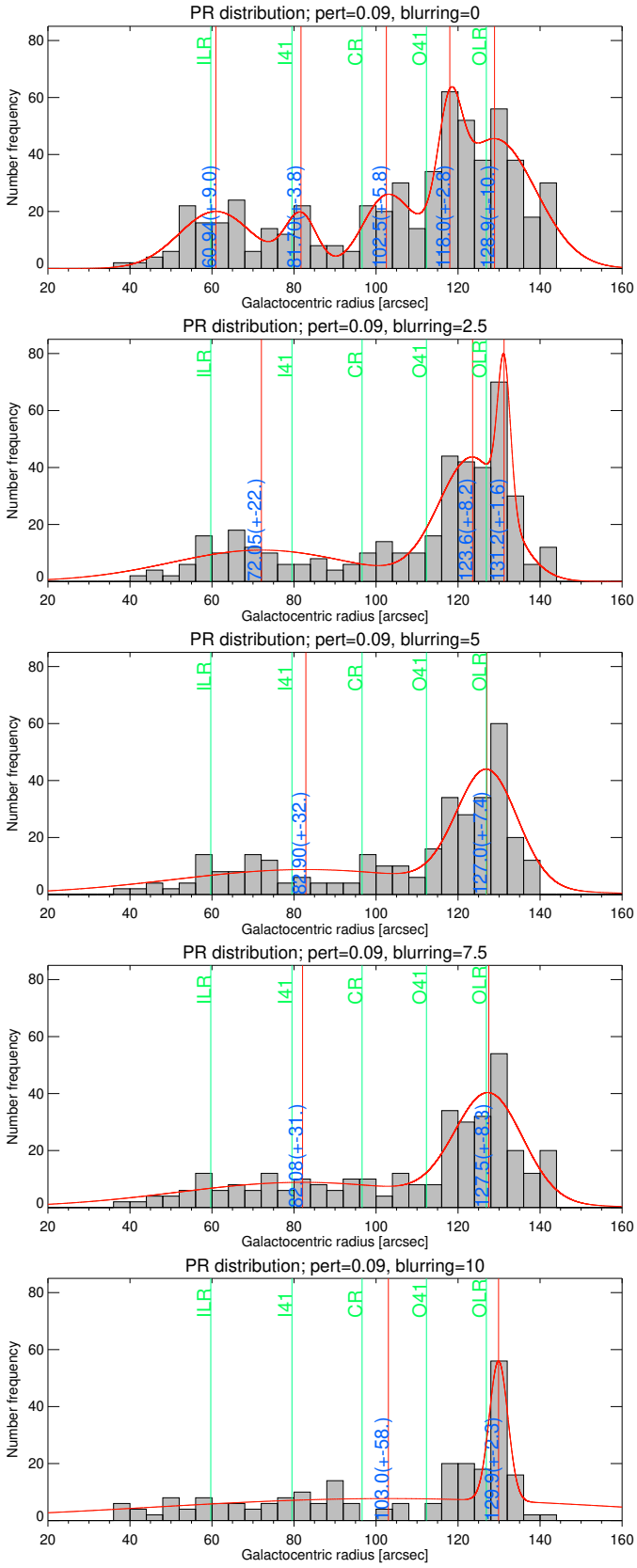

Figure 4.11: Blurring comparison for the perturbation strength of 0.09; blurring of $\sigma = 0$, $\sigma = 2.5$, $\sigma = 5$, $\sigma = 7.5$, and $\sigma = 10$ (all in units of pixels). The controlled parameters are particle count of 4M, semi-random distribution in 2k rings, inclination of 45°, maximum radius of 160 arcsec, phase reversal velocity threshold of 10^{-5} simulation velocity units, simulation duration of 50 simulation time units, and the original methods of pixel selection and phase reversal rejection. The graph layout is as in Figure 4.1.

4.2 Monte Carlo analysis

The Monte Carlo (MC) analysis of the observational data, presented in this section, contains a large number of different parameters. These parameters are divided into two categories: primary and secondary. The primary parameters are the ones that form the framework of the Monte Carlo analysis and its comparison process; these are the Monte Carlo algorithm type, unit of distance, random resonance number[2], the resonance indicator (RI) type, and the Font-Beckman (FB) resonance choice[3]. The secondary parameters are those that do not fundamentally define the Monte Carlo run but affect the galaxies involved in the Monte Carlo process; these are the maximum galactic radius over which random resonances are simulated, the inner forbidden limit for resonances[4], the inbetween forbidden limit for resonances[5], the inclination limit, the truncation strength limit, and the barredness of the galaxy.

It is apparent that the results section becomes excessively long if all the unique combinations of the aforementioned parameters are to be thoroughly tested and compared. To make this section as concise as possible, we have devised a number of controlled tests that show the effects changing each of the parameters may have on the Monte Carlo results. The controlled tests are done such that only the parameter of interest is changed while the other parameters are kept, i.e. controlled, at reasonable[6], constant values; these controlled tests are shown below.

Before showcasing the controlled tests, let us briefly explain the role of the resonance indicator (RI) type which is one of the primary parameters of the Monte Carlo analysis. The RI resonances are the basis of comparison for the FB resonances. In the Monte Carlo analysis of this thesis, the available RI options are truncations (all-types, Type-II, Type-II-OLR, and Type-III), rings, Buta-Zhang resonances (i.e. potential-density phase-shift method), and traditional resonances (includes Tremaine-Weinberg resonances and simulation modeling resonances). However, the upcoming controlled tests are performed for only two of these available RI options: Type-II truncations and rings; the reason for this is discussed in Section 5.2. Moreover, the final Monte Carlo result, seen in Section 4.2.3, is essentially a controlled comparison between most[7] of the available RI options.

4.2.1 Type-II truncations as RI

In this subsection the controlled tests are done when the Type-II truncations are chosen as RI.

Primary parameters

There are four distinct Monte Carlo algorithms; these are Monte Carlo I (MC1), Monte Carlo II (MC2), Monte Carlo II-i (MC2i), and Monte Carlo III (MC3). A comparison between these four Monte Carlo types is shown in Figure 4.12. In addition to these, the reverse Monte Carlo (same algorithm as the previous four, but the role of RI and FB resonances are reversed) results are shown in Figure 4.13. In both of these Monte Carlo type comparisons the other parameters are kept constant; namely the distance unit is

[2]This determines the number of accepted random resonances in the Monte Carlo algorithm on hand.

[3]There are two different FB resonance choices: 'basic' and 'interlocking'. The 'basic' one does not make a distinction between interlocking and non-interlocking FB resonances, i.e. includes all the FB resonances. The 'interlocking' one only limits the FB resonances to those that are interlocking, i.e. all the non-interlocking FB resonances are ignored.

[4]Random resonances that are closer to the galactic center than the inner forbidden limit are rejected.

[5]Random resonances that are closer than the inbetween forbidden limit to each other are rejected.

[6]This is justified in the controlled parameters' own controlled tests.

[7]All available RI options, except all-types and Type-III truncations.

kpc, the random resonance number is 100k, the resonance indicator is Type-II truncations, and the FB resonances are basic. For MC1 and MC2, the illustration is done via two graphs: the histogram and the scatter plot. For MC2i, the individual histograms for each galaxy are not shown as there are too many of them; for an example see Figure 3.12. The global histogram of MC2i, showing the distribution of the fraction where random resonances are closer to the resonance indicator than the FB ones, is given. The last histogram in the panel is the final histogram of MC3.

There are three possible distance units that the Monte Carlo algorithms may use; namely arcsec, kpc, and relative. Arcsec is the distance unit that the observations are made in. This unit is not representative of the real size of the galaxy as it does not take into account how far the observed objects are. The real distance is obtained from the arcsec measurements and the Hubble-Lemaître distance[8] of the object; the real distance is measured in kiloparsecs (kpc). The relative distance unit is obtained when the real distances of the galaxy are normalized using its maximum radius. A comparison between the MC results of these three units is shown in Figure 4.14. Note that MC1 is omitted as its results are similar but less visually appealing as compared to MC2's results. The constant primary parameters are similar to above comparisons: RI is Type-II truncations, random resonance number is 100k, and FB resonances are basic.

The random resonance number is the number of accepted random resonances in each of the four MC algorithms. These accepted random numbers are dealt with differently in each, sometimes kept raw and sometimes averaged out. Regardless of how they are implemented into the MC algorithm, the bigger this number is the more reliable the random element of the algorithm becomes. However, larger random resonance numbers generally require greater calculation times and computing power. A comparison between 10k, 100k, and 1M random resonance numbers (with Type-II truncations as RI, kpc as distance unit, and basic FB resonances) is shown in Figure 4.15. A problem that may arise when using small random resonance numbers is replicability of the MC results. This is because when the random numbers are too few, possible random variations are not averaged out and the result may swing to extreme values, whereas a large enough selection of random numbers evens out such random deviations and the MC results become stable; this is an example of the central limit theorem in action. To see if the common choice of 100k for the random resonance number is stable enough consider the comparison given in Figure 4.16. In this comparison the MC analysis is repeated four times for the exact same parameters of Type-II truncations as RI, kpc as distance unit, 100k as random resonance number, and basic FB resonances.

The choice of FB resonances can be basic, i.e. all the resonances found as explained by Font et al. (2014a), or it can be interlocking. In the interlocking case only the FB resonances that show interlocking properties (see Font et al., 2014a) are selected as FB resonances. The comparison in Figure 4.17 shows the difference between the basic FB choice and the interlocking FB choice. The comparison is done with Type-II truncations as RI, kpc as distance unit, and 100k as random resonance number.

In the case of truncations, the truncation type is a primary parameter as it is, in essence, a choice of the RI type. There are four different truncation types to be used as the RI, which are all-types, Type-II, Type-II-OLR, and Type-III truncations. These are compared in Figure 4.18. In this comparison kpc is used as a distance unit, the random resonance number is 100k, and the FB choices are basic.

[8]The Hubble-Lemaître distance is measured from the recession velocity of an object due to the expansion of the Universe.

Secondary parameters

The comparison in Figure 4.19 shows the cases where the maximum galactic radius is taken to be the radius where the surface brightness drops to 24, 25, and 26 mag/arcsec^2, respectively from the top row to the second and the third. The primary parameters during this comparison are Type-II truncations as RI, kpc as distance unit, 100k as random resonance number, and basic FB resonance. The default choice of the maximum radius is the radius at 25 mag/arcsec^2; this was the case in the primary comparisons done above.

Figure 4.20 shows the comparison between the cases where the inner forbidden limit of the random resonances is 0%, 10%, and 20% of the galactic radius, respectively from top to bottom. The 0% case means that there is no inner limit for where resonances may be found in the galactic disc. The default value of the inner limit is 10%; this is the value used in all the other comparisons. The comparison for the inbetween forbidden limit of the random resonances is shown in Figure 4.21, where from top to bottom the rows correspond to 2.5%, 5%, and 7.5% of the galactic radius limit, respectively. The default inbetween forbidden limit for resonances is set to be 5% of the galactic radius. Note that both of these resonance condition limit comparisons are done under the parameters Type-II truncations as RI, kpc as distance unit, 100k as random resonance number, and basic FB resonances.

The effect of limiting the inclination within the galaxy sample is illustrated in Figure 4.22. Just as the previous cases, this comparison is done with Type-II truncations as RI, kpc as distance unit, 100k as random resonance number, and basic FB resonances. The comparison from the top row to the bottom one pertains to the case, respectively, the inclination is between 0° and 30°, between 30° and 60°, and between 60° and 90°. A similar limiting comparison for the truncations (only applicable to the case of Type-II truncations as RI) is performed as well; this is shown in Figure 4.23. In this case from the top row to the bottom, respectively, the truncation strength is smaller than 2 (between 0 and 2), between 2 and 4, and greater than 4. Note that a truncation is made of two straight-line fits touching; the ratio of the greater absolute gradient to the smaller absolute gradient of these straight-lines is the strength of the truncation.

The comparison seen in Figure 4.24 shows the cases where both barred and unbarred galaxies are considered into the sample (default case), with the case where only barred galaxies are considered and the case where only unbarred galaxies are considered, respectively, from the top to row to the bottom one. Just as it has been the case so far, the primary parameters used in this comparison are Type-II truncations as RI, kpc as distance unit, 100k as random resonance number, and basic FB resonances.

4.2.2 Rings as RI

In this subsection the controlled tests are done when rings are chosen as RI. As the main structure of this subsection is identical to the previous one (Subsection 4.2.1) some details are omitted, it is advised that the reader goes through the previous subsection before this.

Primary parameters

A comparison between the four Monte Carlo types (MC1, MC2, MC2i, and MC3) is shown in Figure 4.25. In addition to these, the reverse Monte Carlo results are shown in Figure 4.26. In both of these Monte Carlo type comparisons the other parameters are kept constant; namely the distance unit is kpc, the random resonance number is 100k, the resonance indicator is rings, and the FB resonances are basic.

A comparison between the MC results of the units (arcsec, kpc, and relative) is shown in Figure 4.27. Note that MC1 is omitted as its results are similar but less visually appealing as compared to MC2's results. The constant primary parameters are similar to above comparisons: RI is rings, random resonance number is 100k, and FB resonances are basic.

A comparison between 10k, 100k, and 1M random resonance numbers (with rings as RI, kpc as distance unit, and basic FB resonances) is shown in Figure 4.28. To see if the common choice of 100k for the random resonance number is stable enough consider the comparison given in Figure 4.29. In this comparison the MC analysis is repeated four times for the exact same parameters of rings as RI, kpc as distance unit, 100k as random resonance number, and basic FB resonances.

The comparison in Figure 4.30 shows the difference between the basic FB choice and the interlocking FB choice. The comparison is done with rings as RI, kpc as distance unit, and 100k as random resonance number.

Secondary parameters

The comparison in Figure 4.31 shows the cases where the maximum galactic radius is taken to be the radius where the surface brightness drops to 24, 25, and 26 mag/arcsec^2, respectively from the top row to the second and the third. The primary parameters during this comparison are rings as RI, kpc as distance unit, 100k as random resonance number, and basic FB resonance. The default choice of the maximum radius is the radius at 25 mag/arcsec^2; this was the case in the primary comparisons done above.

Figure 4.32 shows the comparison between the cases where the inner limit is 0%, 10%, and 20% of the galactic radius, respectively from top to bottom. The default value of the inner limit is 10%; this is the value used in all the other comparisons. The comparison for the inbetween limit is shown in Figure 4.33, where from top to bottom the rows correspond to 2.5%, 5%, and 7.5% of the galactic radius limit, respectively. The default inbetween forbidden limit for resonances is set to be 5% of the galactic radius. Note that both of these resonance condition limit comparisons are done under the parameters rings as RI, kpc as distance unit, 100k as random resonance number, and basic FB resonances.

The effect of limiting the inclination within the galaxy sample is illustrated in Figure 4.34. Just as in the previous cases, this comparison is done with rings as RI, kpc as distance unit, 100k as random resonance number, and basic FB resonances. The comparison from the top row to the bottom one pertains to the case, respectively, the inclination is between 0° and 30°, between 30° and 60°, and between 60° and 90°.

The comparison seen in Figure 4.35 shows the cases where both barred and unbarred galaxies are considered into the sample (default case), with the case where only barred galaxies are considered and the case where only unbarred galaxies are considered, respectively, from the top to row to the bottom one. Just as it has been the case so far in this subsection, the primary parameters used in this comparison are rings as RI, kpc as distance unit, 100k as random resonance number, and basic FB resonances.

4.2.3 Final Monte Carlo comparison

In the previous two sections the effects of various parameters on the Monte Carlo simulation results were represented. A reasonable (explained in the discussion chapter, see Chapter 5.2) set of parameters is selected to obtain the final results of the Monte Carlo analysis; they are illustrated in Figure 4.36 and Figure 4.37. It is possible to obtain final results for many more sets of parameters but the results

become significantly lengthier, so we limit the parameter set to be kpc as distance unit, 100k as random resonance number, and basic FB resonances. The main comparison is between the choice of the RI: Type-II, Type-II-OLR, rings, Buta-Zhang resonances, and traditional resonances, which are respectively seen in Figure 4.36 and Figure 4.37 from top to bottom. The reason for omitting all truncation types and Type-III truncations as RI in the final comparison is explained in the next chapter.

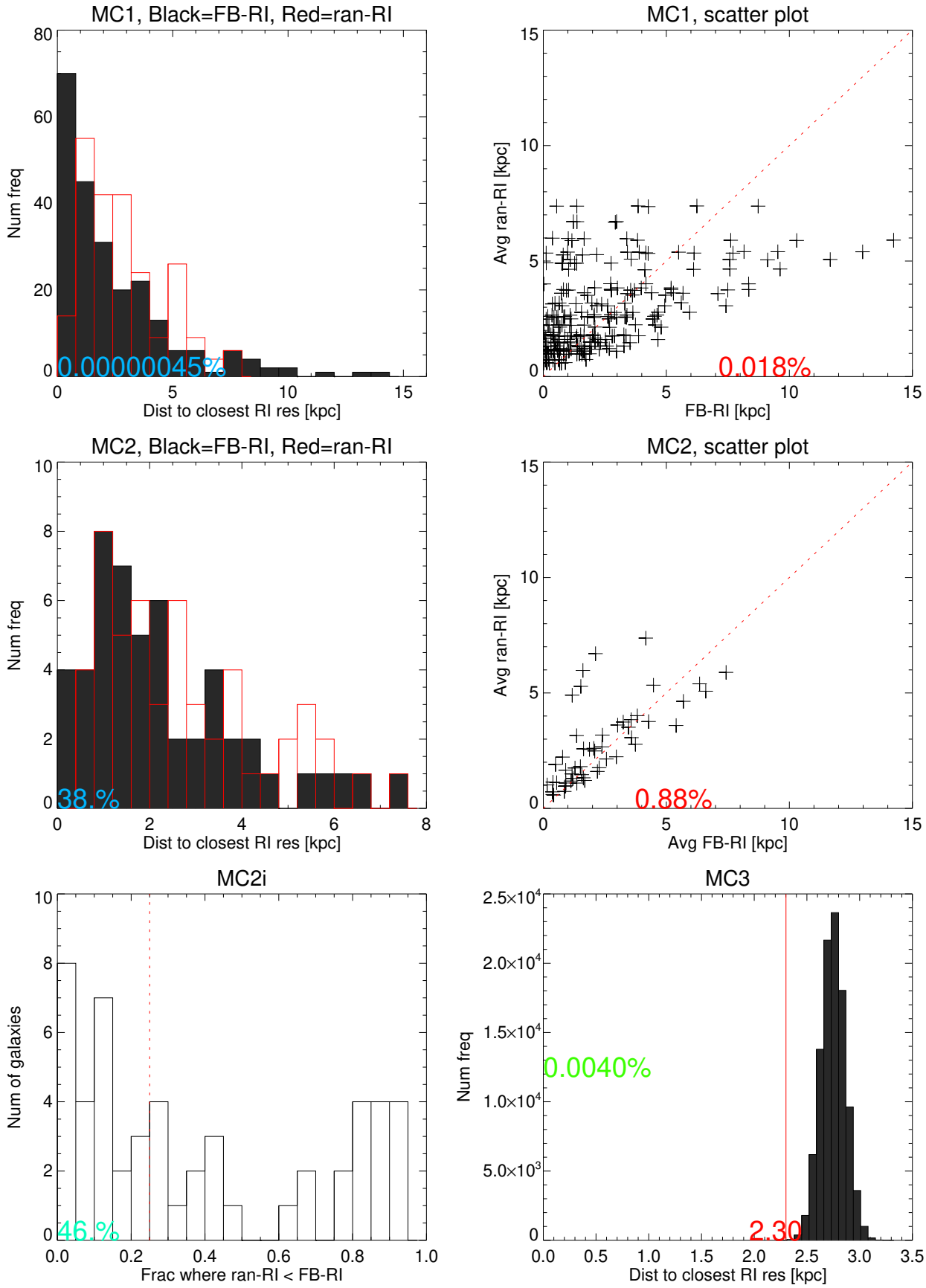

Figure 4.12: This is a comparison between the four MC algorithms. The controlled primary parameters are Type-II truncation as RI (limiting the number of galaxies to 52), kpc as distance unit, 100k as random resonance number, and basic FB resonances.

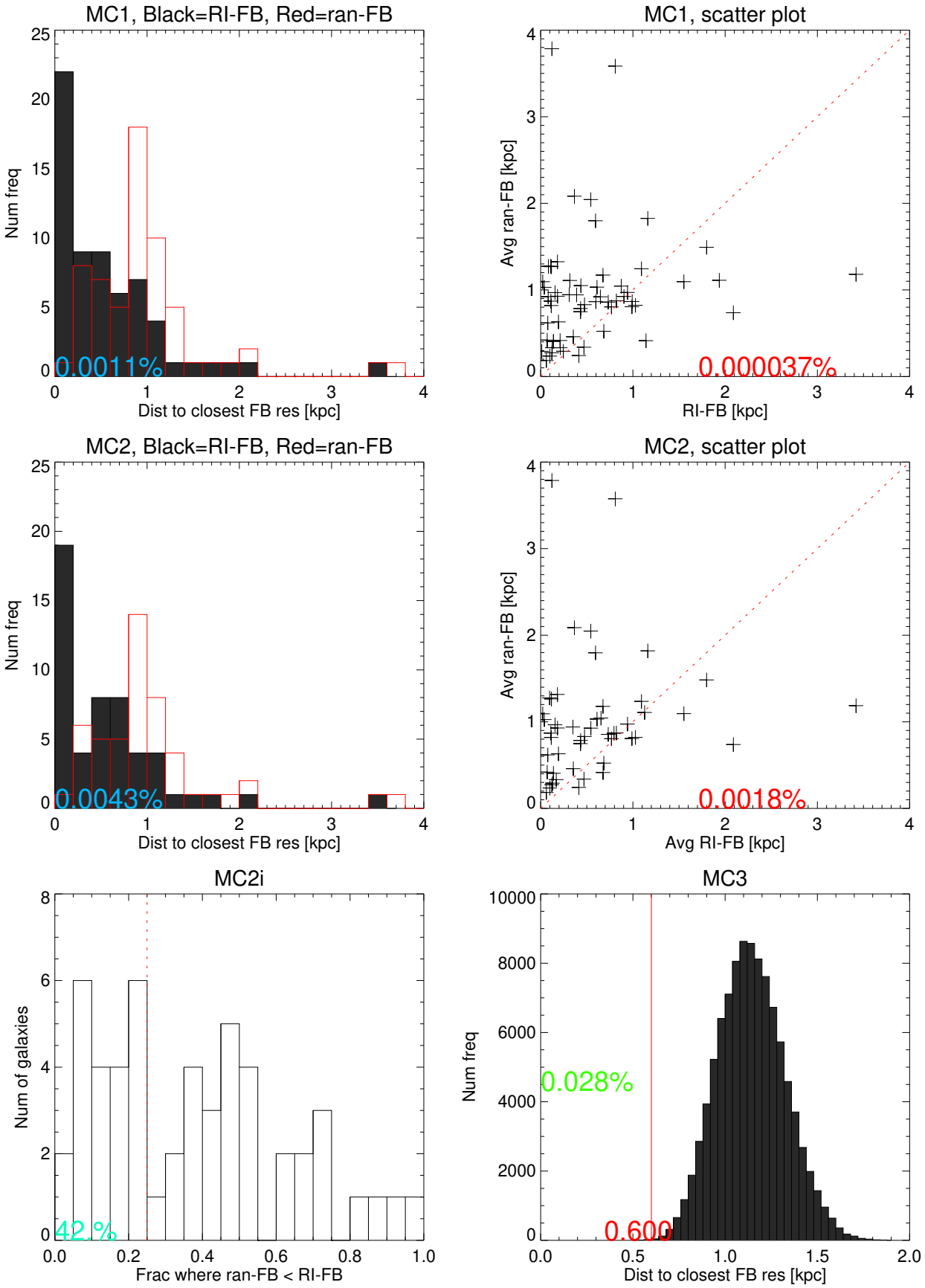

Figure 4.13: This is a comparison between the four MC algorithms, but RI and FB resonances have reversed roles. The controlled primary parameters are Type-II truncation as RI (limiting the number of galaxies to 52), kpc as distance unit, 100k as random resonance number, and basic FB resonances.

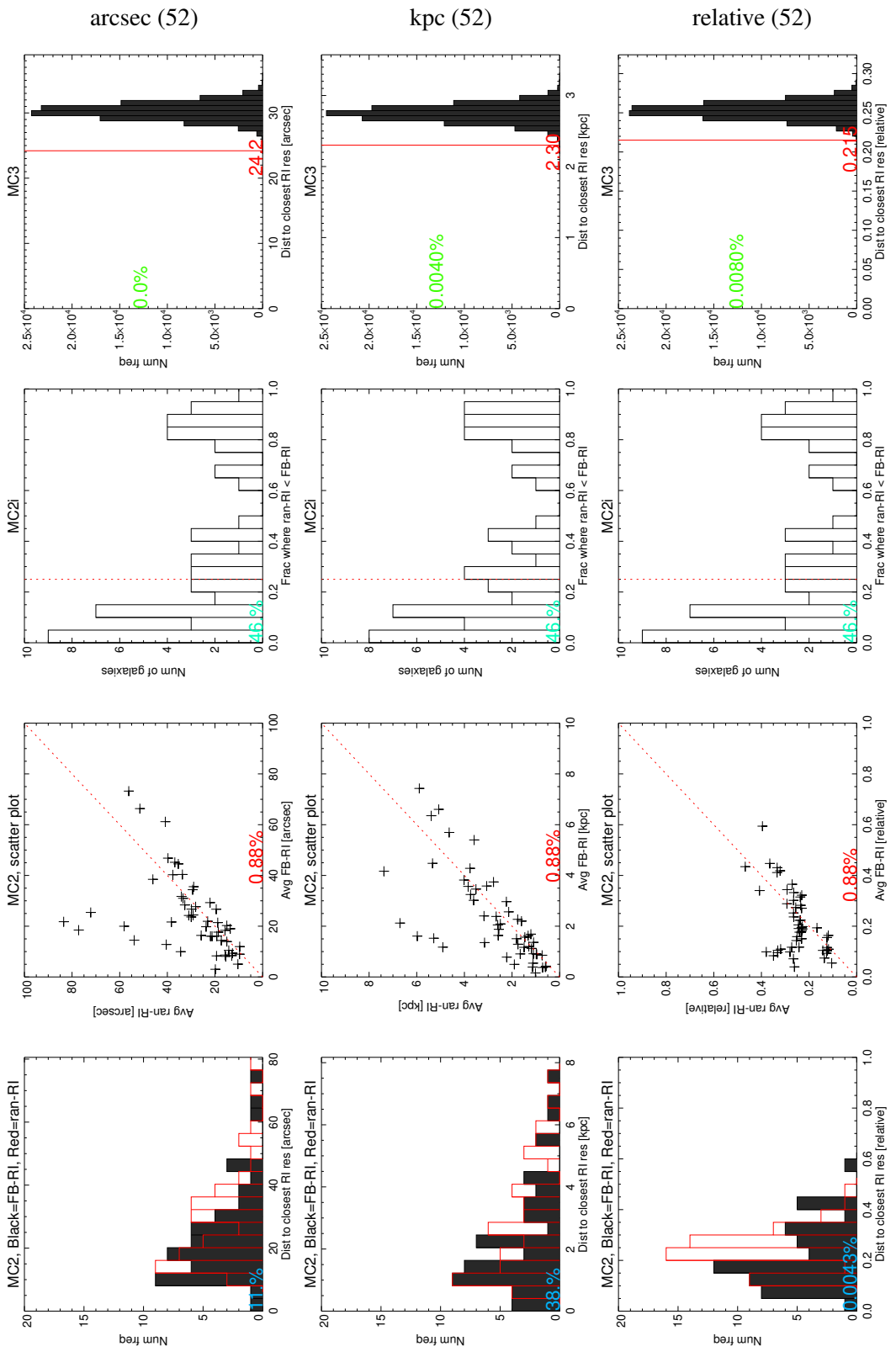

Figure 4.14: This is a comparison between the three usable distance units in the MC algorithms. Form top to bottom, respectively, the distance units are arcsec, kpc, and relative. The controlled primary parameters are Type-II truncation as RI (limiting the number of galaxies to 52), 100k as random resonance number, and basic FB resonances. The number of galaxies in each column is given in brackets.

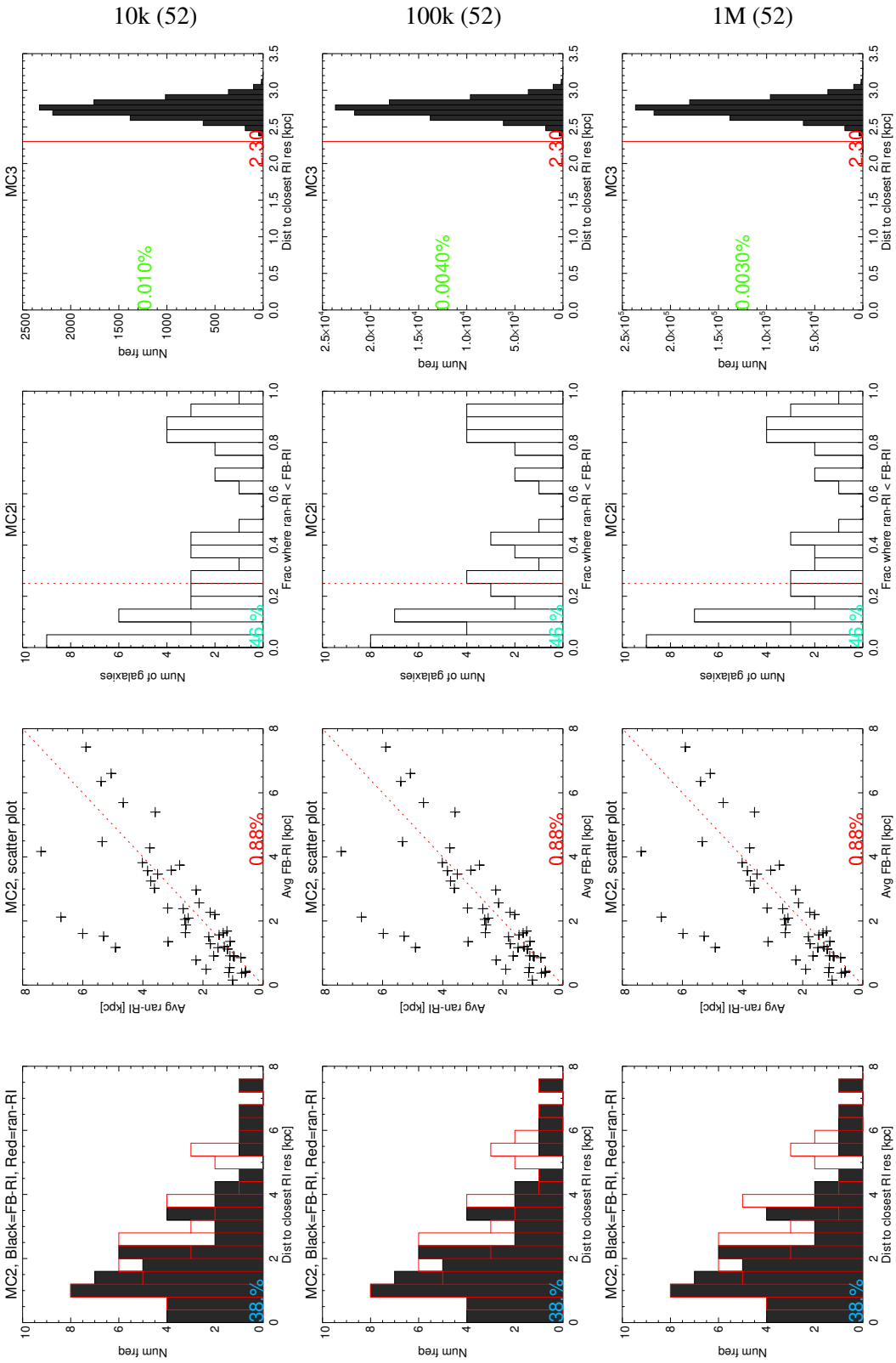

Figure 4.15: This is a comparison between different random resonance numbers in the MC algorithms. Form top to bottom, respectively, the random resonance numbers are 10k, 100k, and 1M. The controlled primary parameters are Type-II truncation as RI (limiting the number of galaxies to 52), kpc as distance unit, and basic FB resonances. The number of galaxies in each column is given in brackets.

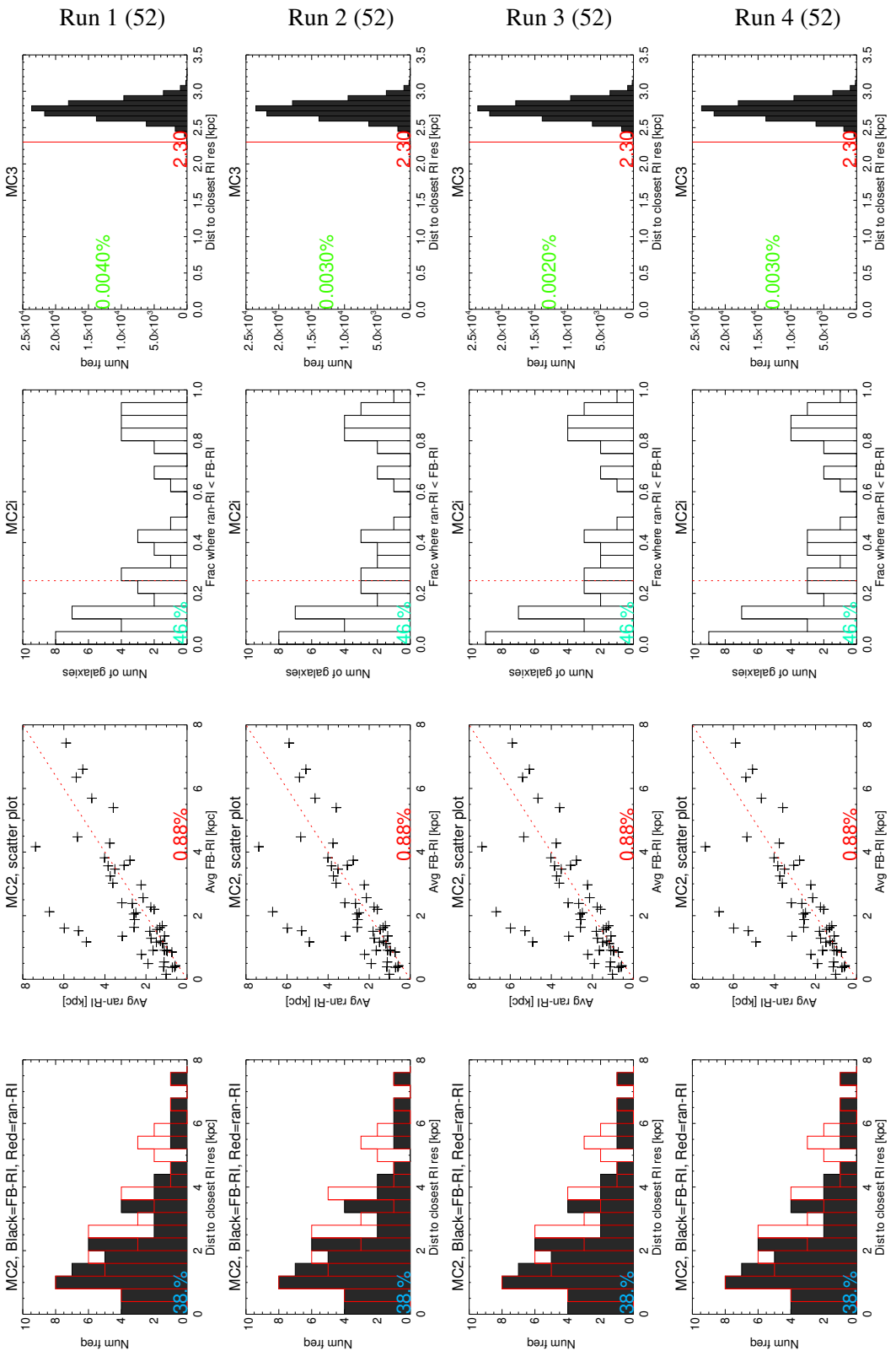

Figure 4.16: This is a comparison between four identical runs of the MC algorithms. The controlled primary parameters are Type-II truncation as RI (limiting the number of galaxies to 52), kpc as distance unit, 100k as random resonance number, and basic FB resonances. The number of galaxies in each column is given in brackets.

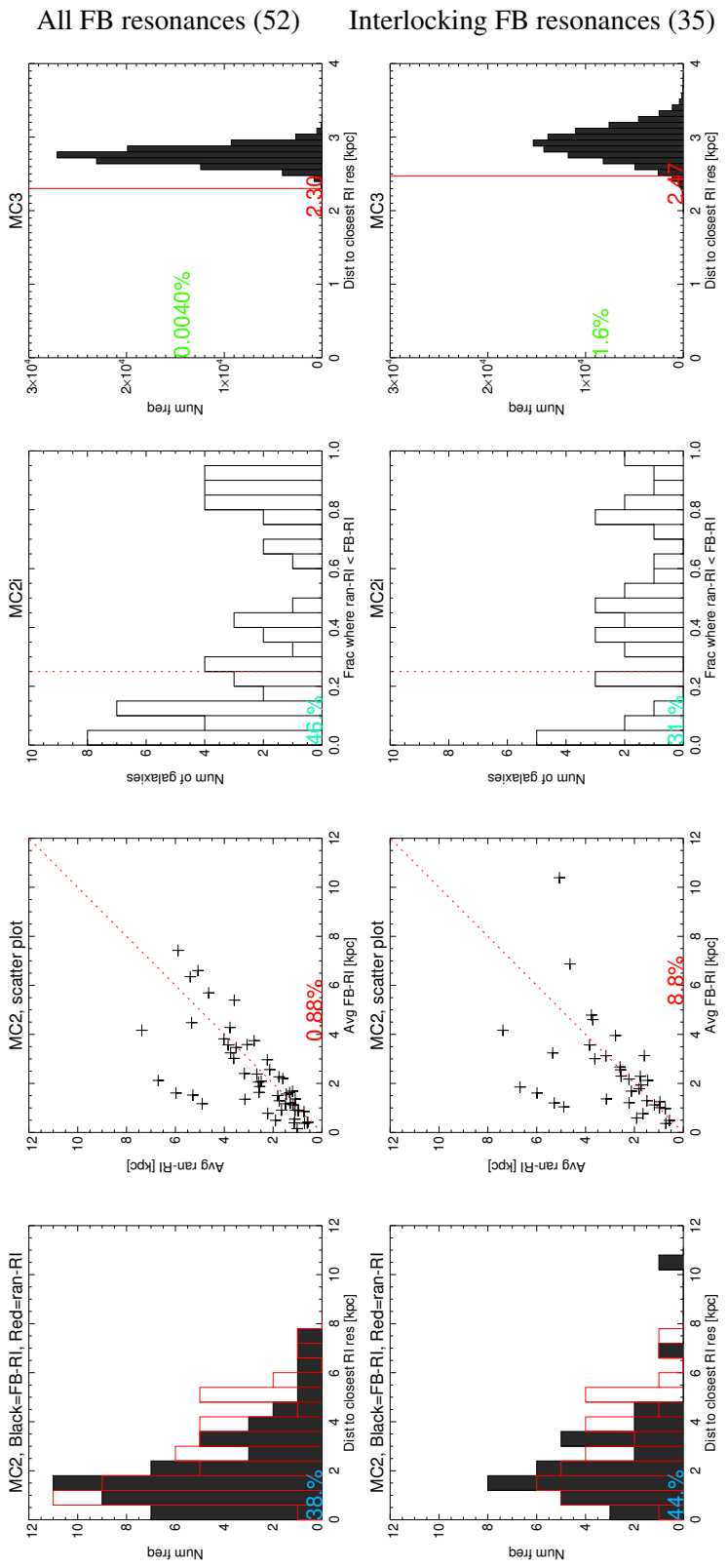

Figure 4.17: This is a comparison between the basic FB resonances and the interlocking FB resonances in the MC algorithms. The controlled primary parameters are Type-II truncation as RI, kpc as distance unit, and 100k as random resonance number. The number of galaxies in each column is given in brackets.

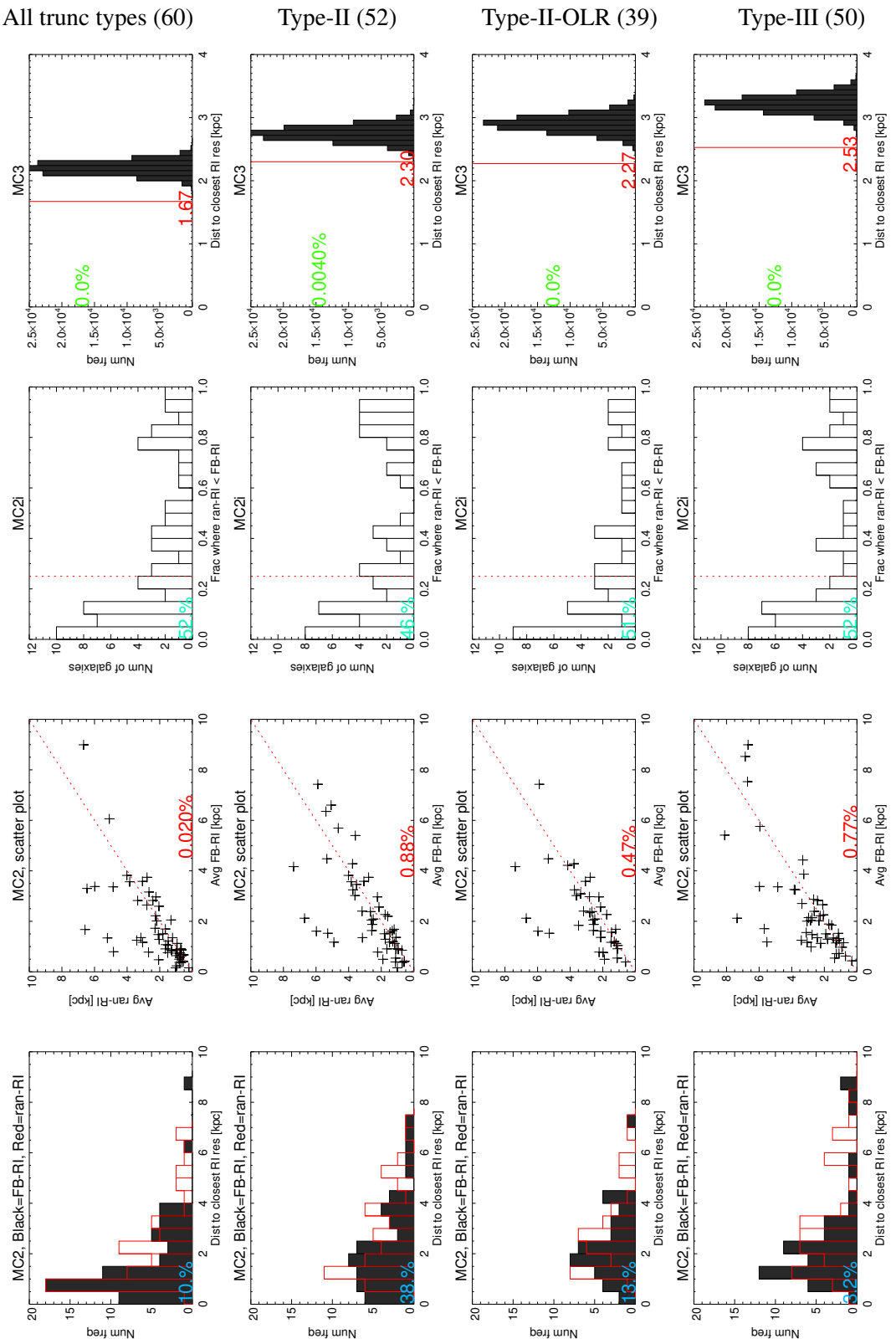

Figure 4.18: This is a comparison between the four truncation types usable as RI in the MC algorithms. From top to bottom, respectively, the truncation type as RI used is all-types, Type-II, Type-II-OLR, and Type-III. The controlled primary parameters are kpc as distance unit, 100k as random resonance number, and basic FB resonances. The number of galaxies in each column is given in brackets.

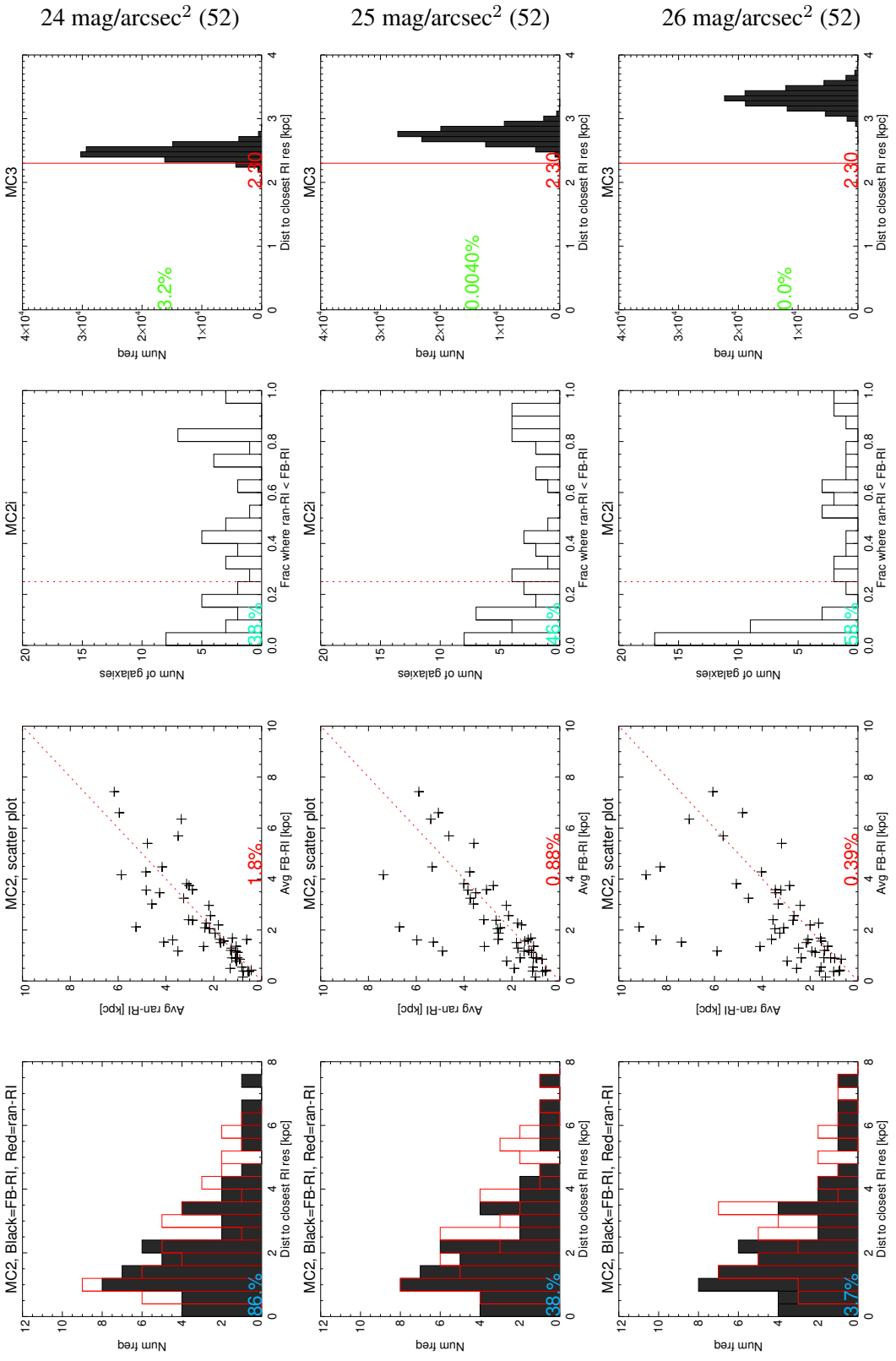

Figure 4.19: This is a comparison between three different maximum galactic radii in the MC algorithms. From top to bottom, respectively, the maximum galactic radius is the radius at which surface brightness drops to 24, 25, and 26 mag/arcsec^2. The controlled primary parameters are Type-II truncation as RI (limiting the number of galaxies to 52), kpc as distance unit, 100k as random resonance number, and basic FB resonances. The number of galaxies in each column is given in brackets.

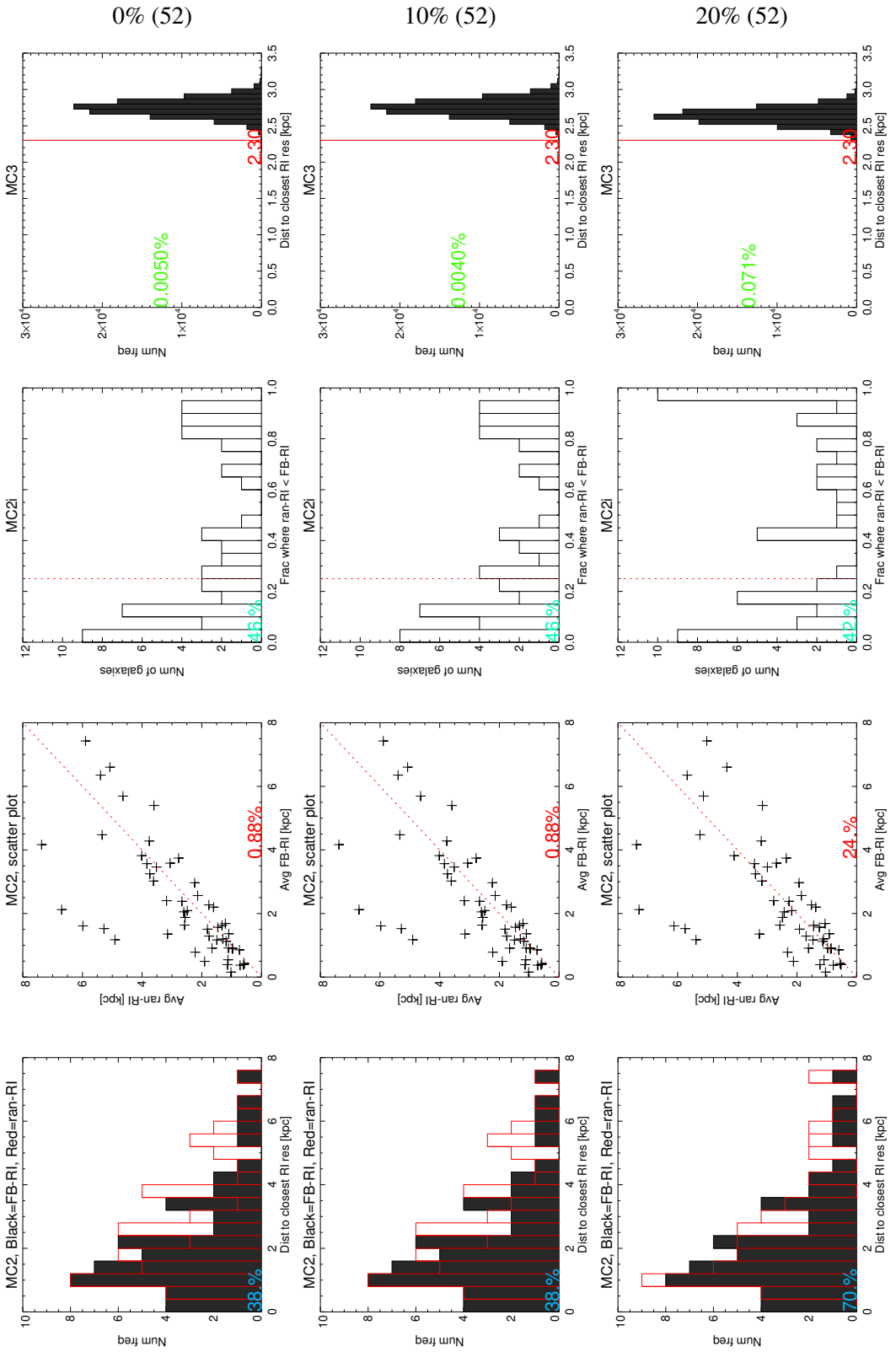

Figure 4.20: This is a comparison between three different inner forbidden limits for resonances in the MC algorithms. From top to bottom, respectively, the inner limits are 0%, 10%, and 20% of the maximum galactic radius. The controlled primary parameters are Type-II truncation as RI (limiting the number of galaxies to 52), kpc as distance unit, 100k as random resonance number, and basic FB resonances. The number of galaxies in each column is given in brackets.

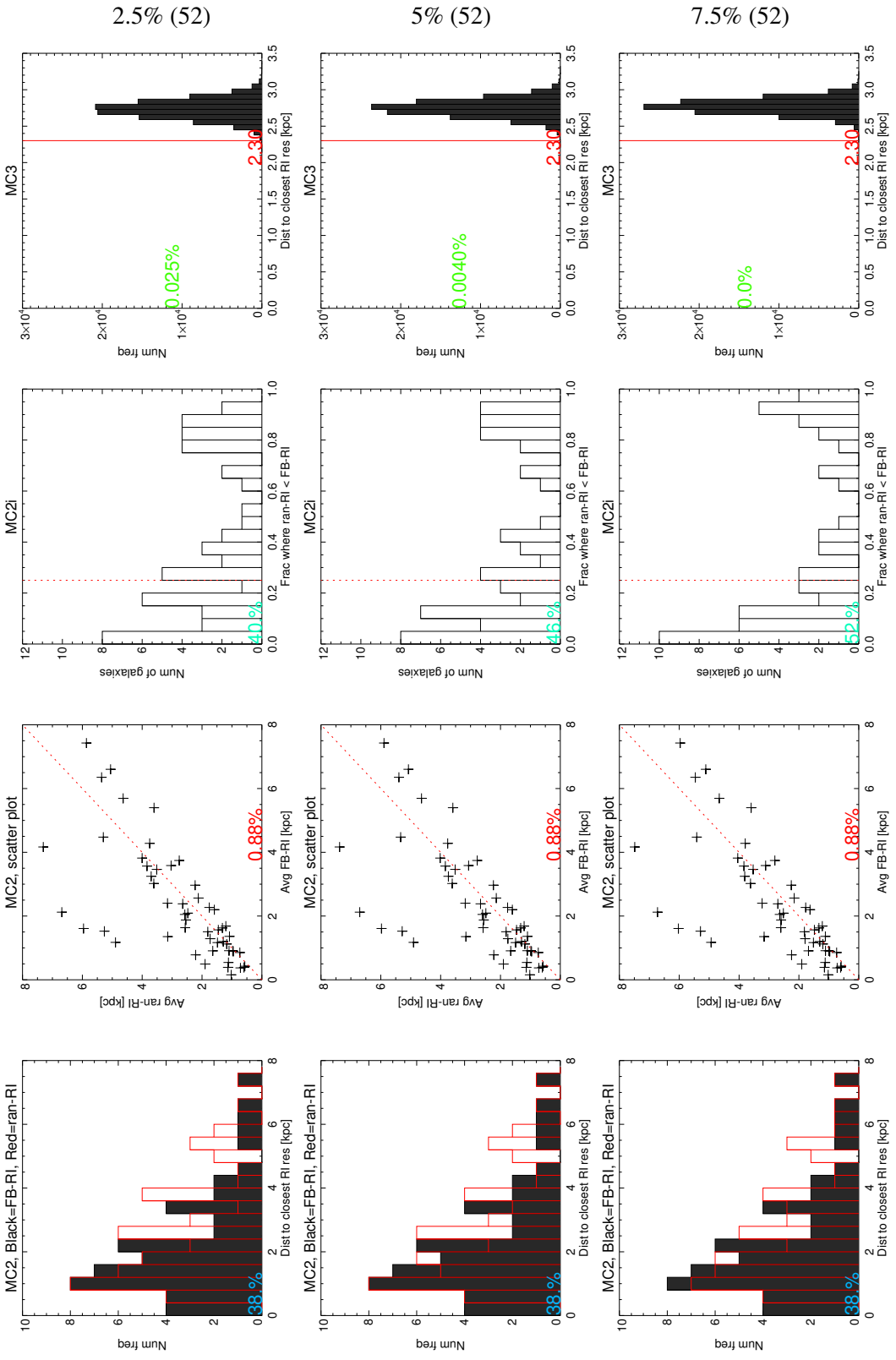

Figure 4.21: This is a comparison between three different inbetween forbidden limits for resonances in the MC algorithms. From top to bottom, respectively, the inbetween limits are 2.5%, 5%, and 7.5% of the maximum galactic radius. The controlled primary parameters are Type-II truncation as RI (limiting the number of galaxies to 52), kpc as distance unit, 100k as random resonance number, and basic FB resonances. The number of galaxies in each column is given in brackets.

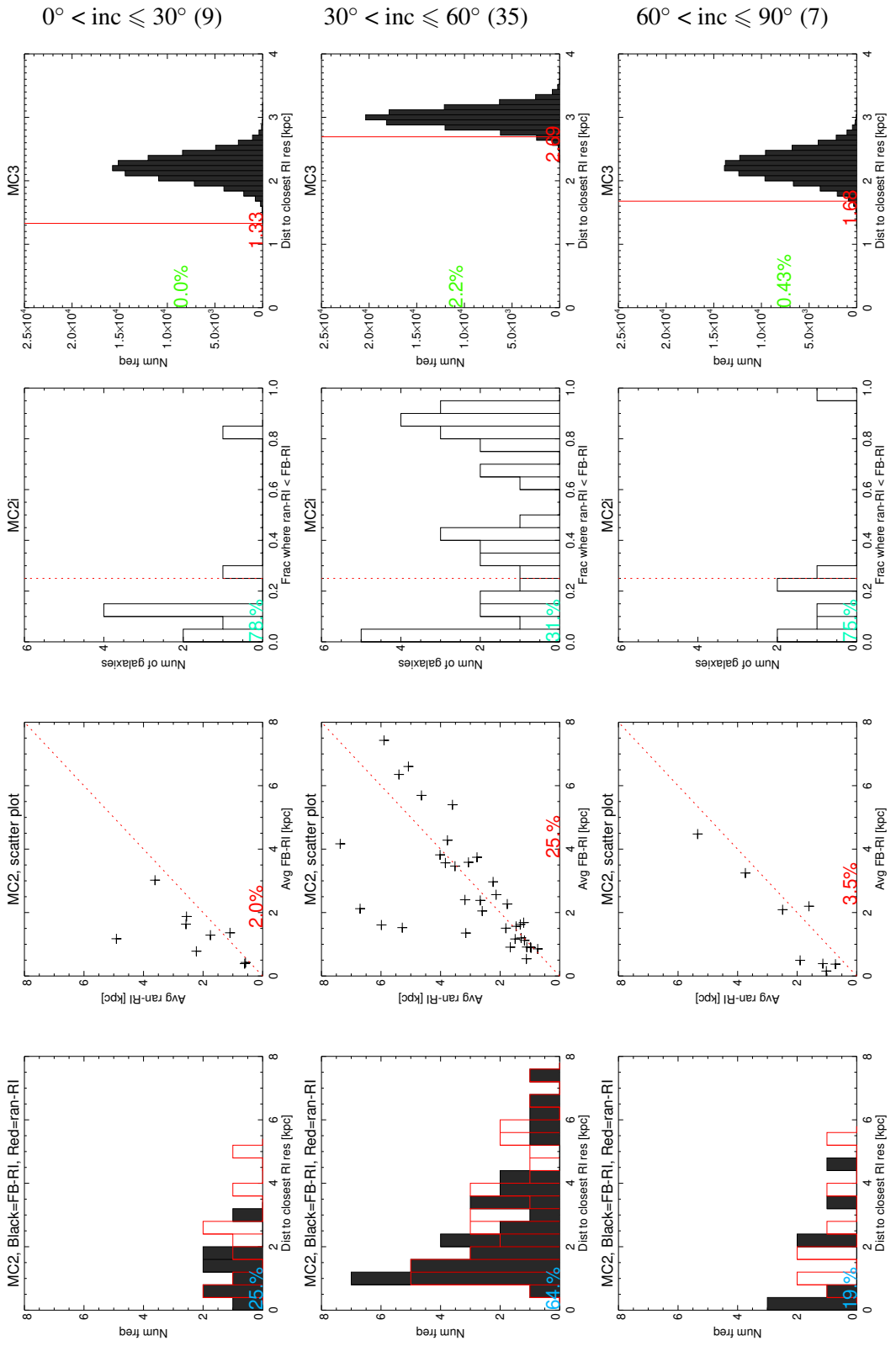

Figure 4.22: This is a comparison between three different inclination limits in the MC algorithms. From top to bottom, respectively, the inclination is between 0° and 30°, between 30° and 60°, and between 60° and 90°. The controlled primary parameters are Type-II truncation as RI, kpc as distance unit, 100k as random resonance number, and basic FB resonances. The number of galaxies in each column is given in brackets.

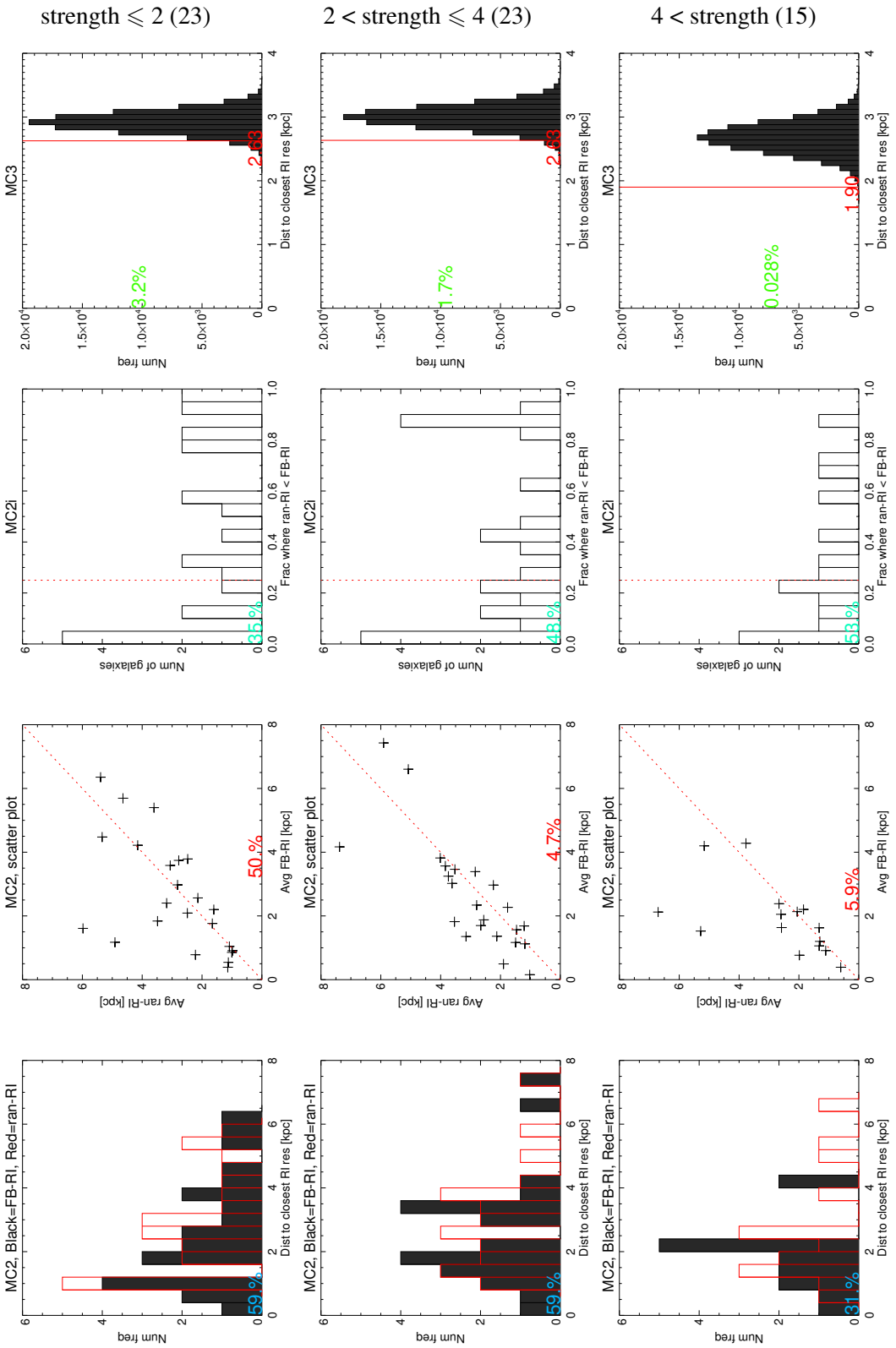

Figure 4.23: This is a comparison between three different truncation strength limits in the MC algorithms. From top to bottom, respectively, the truncation strength is smaller than 2 (between 0 and 2), between 2 and 4, and greater than 4. The controlled primary parameters are Type-II truncation as RI, kpc as distance unit, 100k as random resonance number, and basic FB resonances. The number of galaxies in each column is given in brackets.

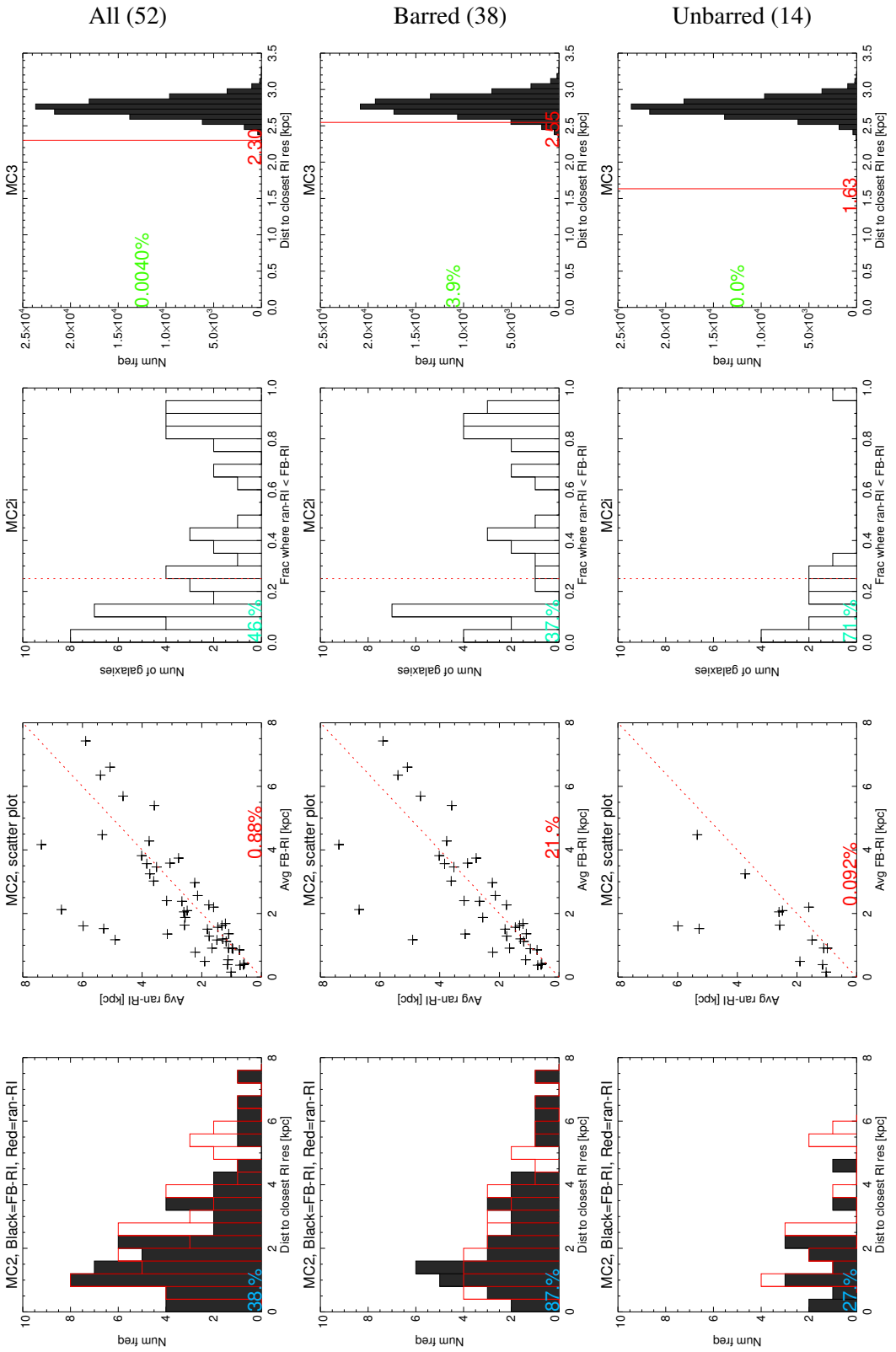

Figure 4.24: This is a comparison between barred and unbarred galaxy samples in the MC algorithms. From top to bottom, respectively, the galaxy sample includes both barred and unbarred galaxies, only barred galaxies, and only unbarred galaxies. The controlled primary parameters are Type-II truncation as RI, kpc as distance unit, 100k as random resonance number, and basic FB resonances. The number of galaxies in each column is given in brackets.

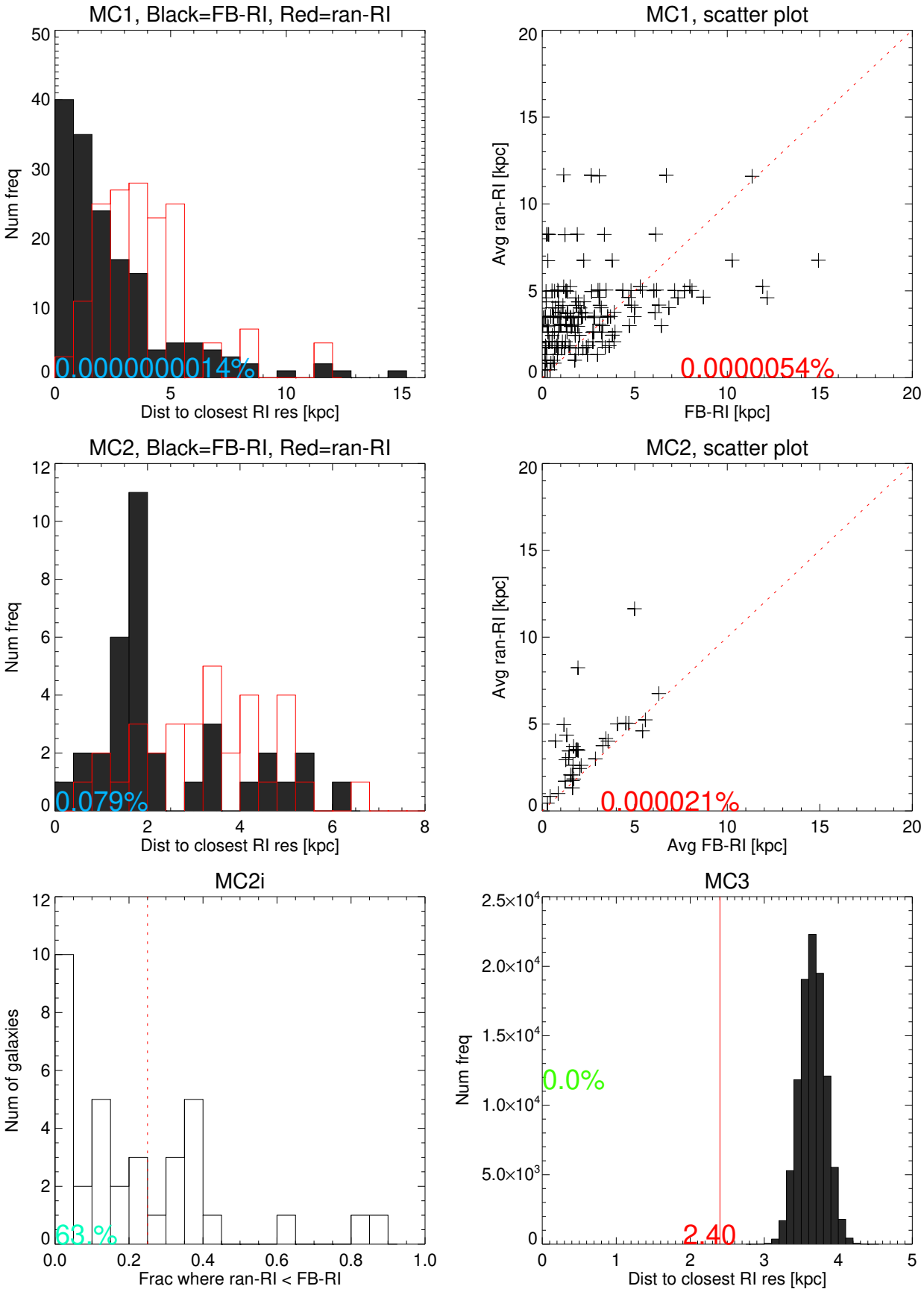

Figure 4.25: This is a comparison between the four MC algorithms. The controlled primary parameters are rings as RI (limiting the number of galaxies to 35), kpc as distance unit, 100k as random resonance number, and basic FB resonances.

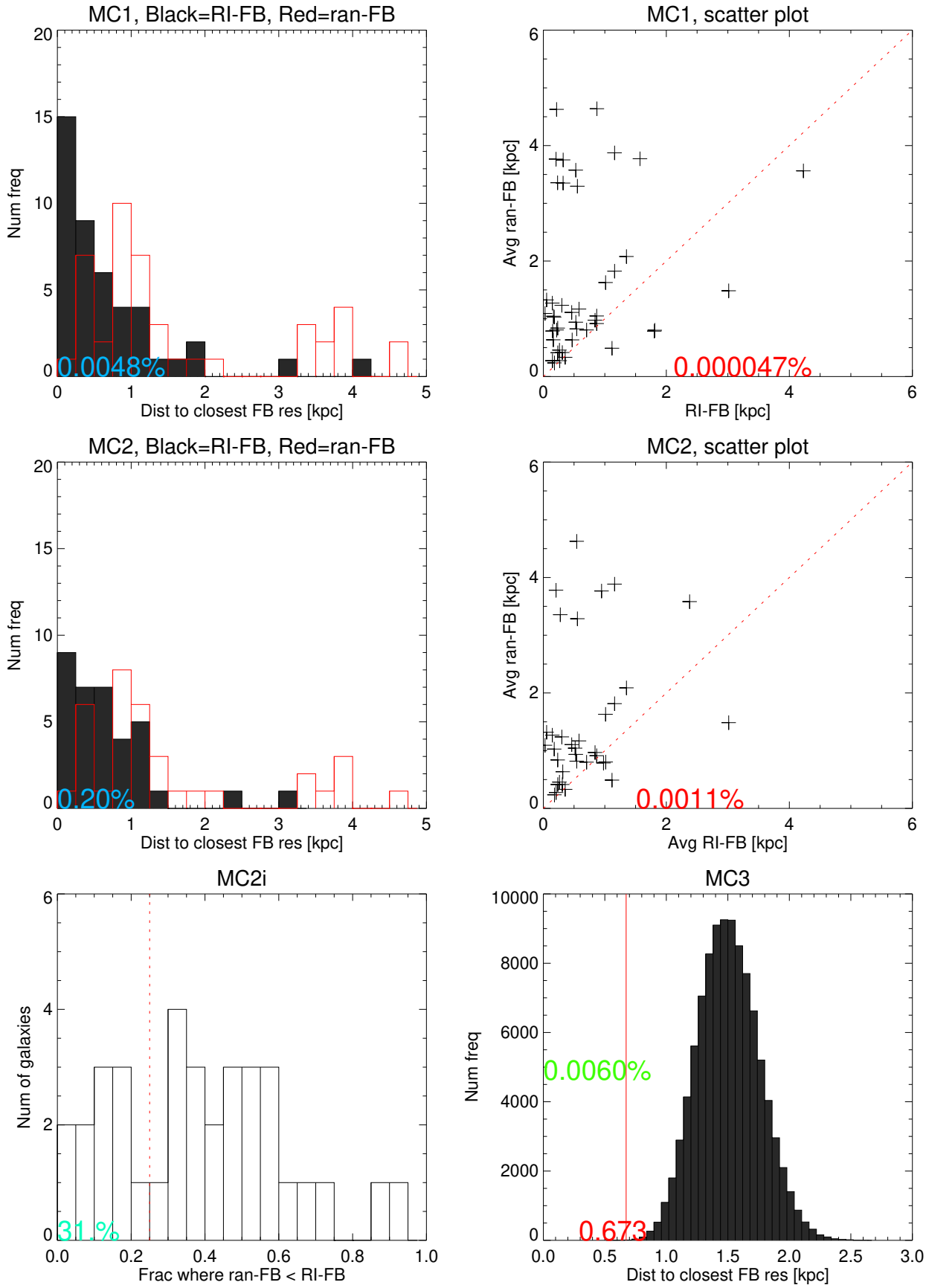

Figure 4.26: This is a comparison between the four MC algorithms, but RI and FB resonances have reversed roles. The controlled primary parameters are rings as RI (limiting the number of galaxies to 35), kpc as distance unit, 100k as random resonance number, and basic FB resonances.

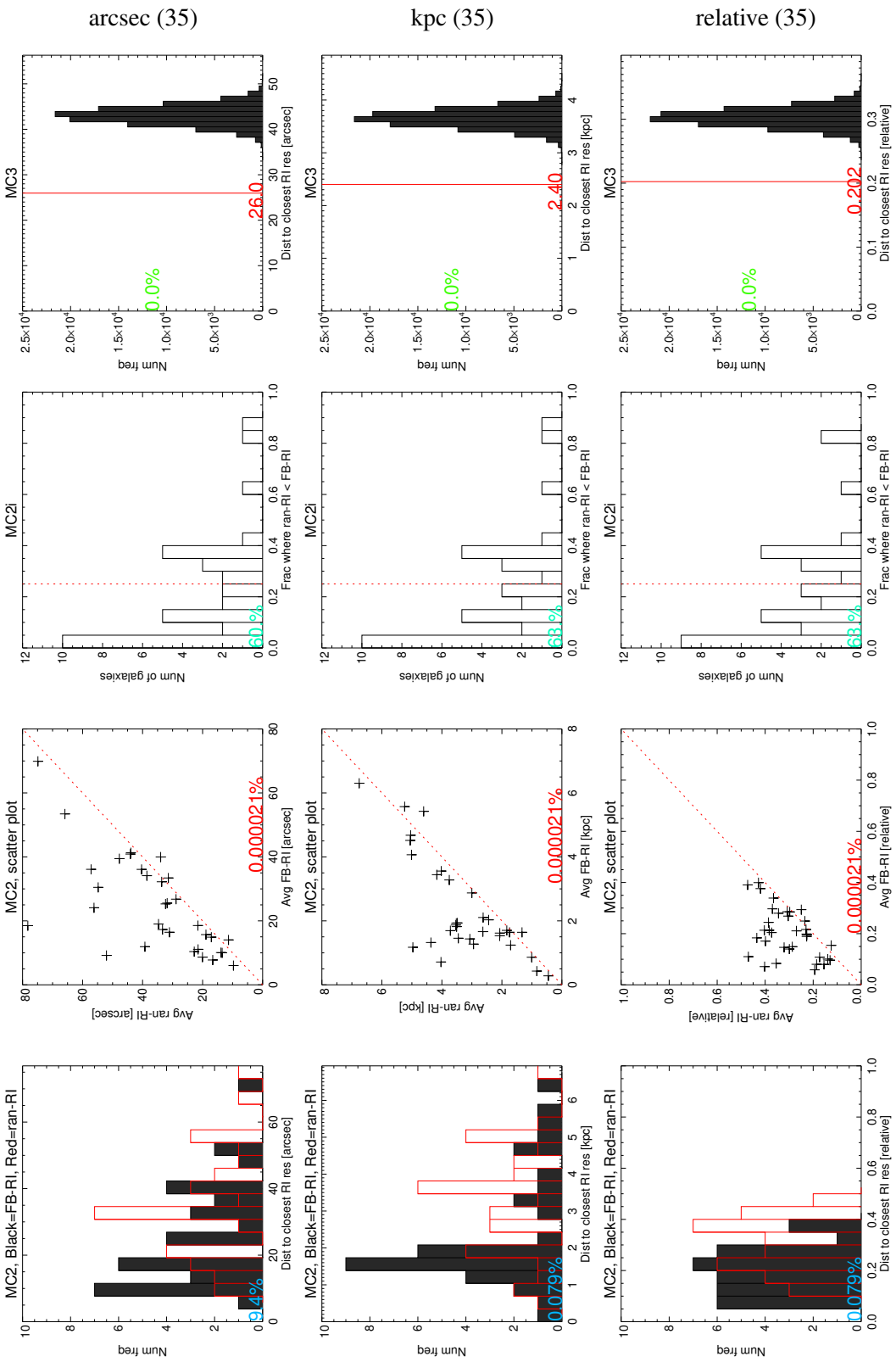

Figure 4.27: This is a comparison between the three usable distance units in the MC algorithms. Form top to bottom, respectively, the distance units are arcsec, kpc, and relative. The controlled primary parameters are rings as RI (limiting the number of galaxies to 35), 100k as random resonance number, and basic FB resonances. The number of galaxies in each column is given in brackets.

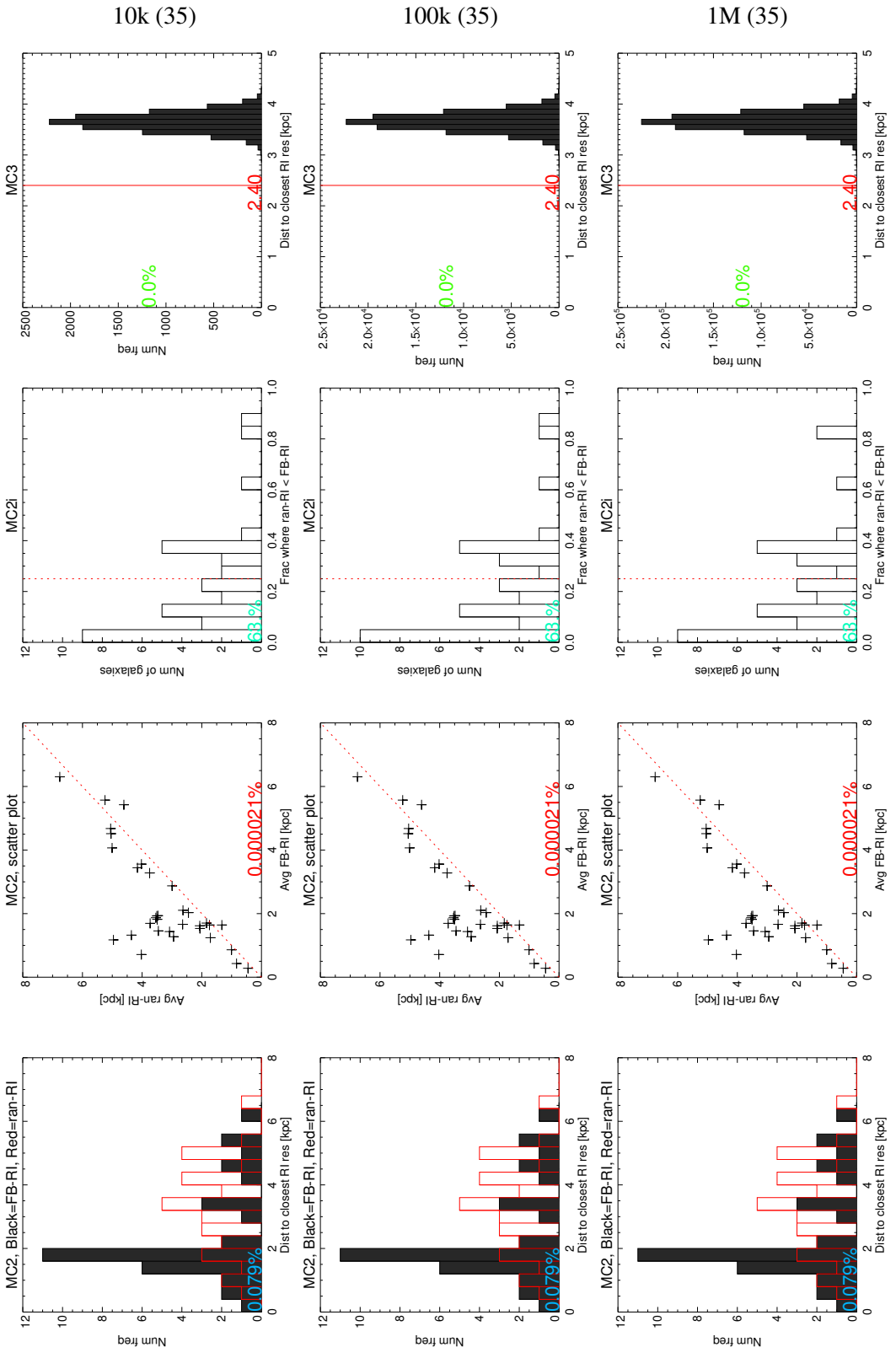

Figure 4.28: This is a comparison between different random resonance numbers in the MC algorithms. Form top to bottom, respectively, the random resonance numbers are 10k, 100k, and 1M. The controlled primary parameters are rings as RI (limiting the number of galaxies to 35), kpc as distance unit, and basic FB resonances. The number of galaxies in each column is given in brackets.

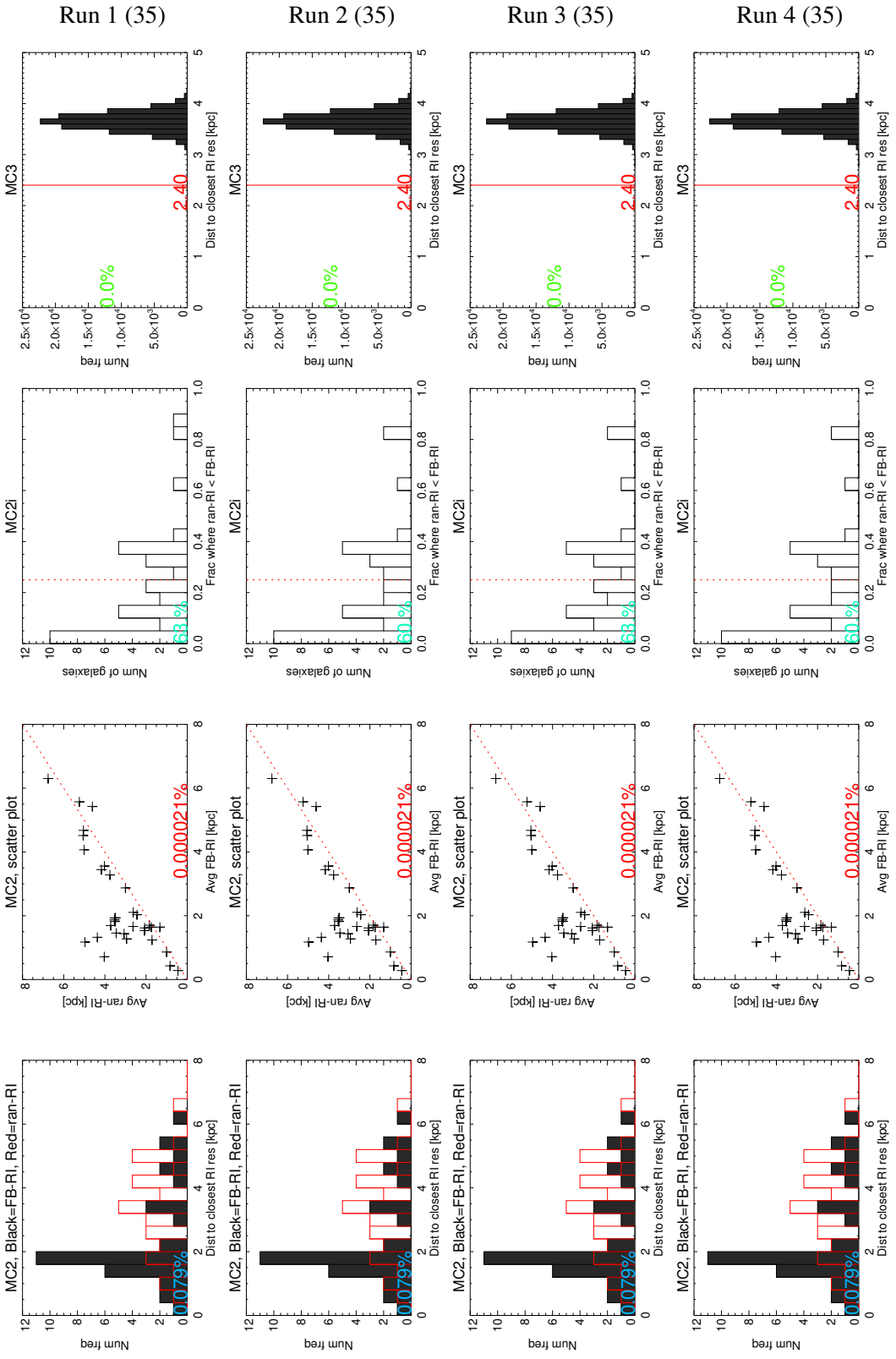

Figure 4.29: This is a comparison between four identical runs of the MC algorithms. The controlled primary parameters are rings as RI (limiting the number of galaxies to 35), kpc as distance unit, 100k as random resonance number, and basic FB resonances. The number of galaxies in each column is given in brackets.

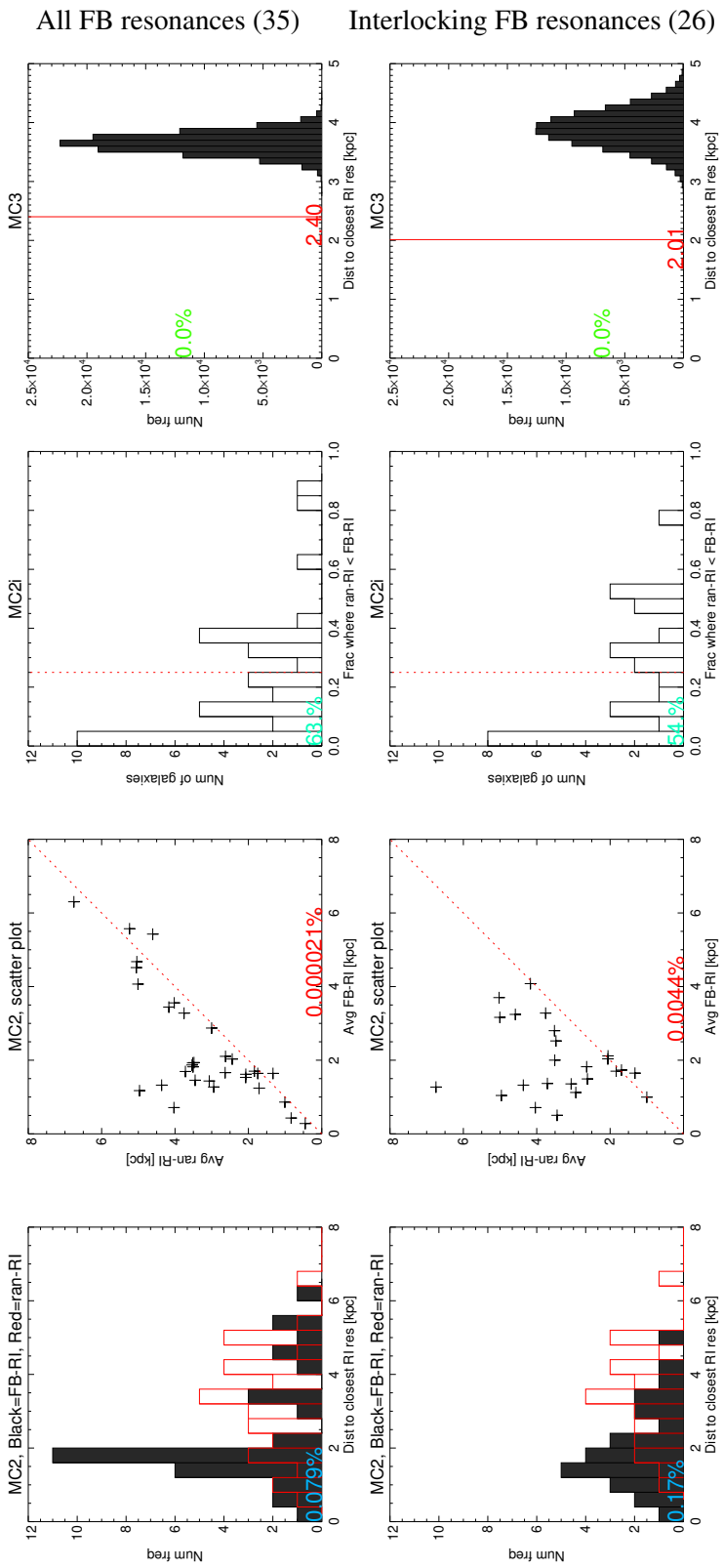

Figure 4.30: This is a comparison between the basic FB resonances and the interlocking FB resonances in the MC algorithms. The controlled primary parameters are rings as RI, kpc as distance unit, and 100k as random resonance number. The number of galaxies in each column is given in brackets.

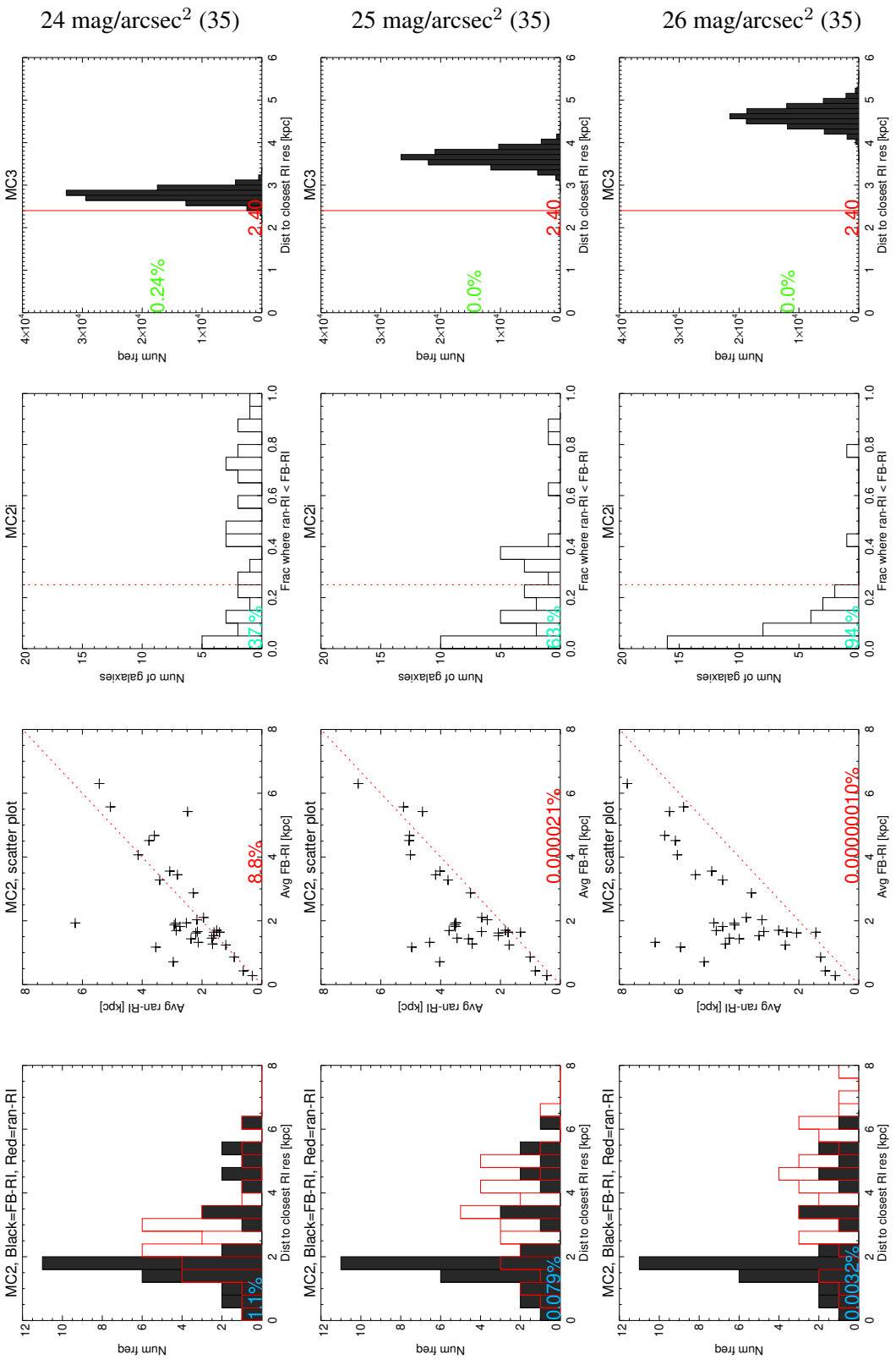

Figure 4.31: This is a comparison between three different maximum galactic radii in the MC algorithms. From top to bottom, respectively, the maximum galactic radius is the radius at which surface brightness drops to 24, 25, and 26 mag/arcsec^2. The controlled primary parameters are rings as RI (limiting the number of galaxies to 52), kpc as distance unit, 100k as random resonance number, and basic FB resonances. The number of galaxies in each column is given in brackets.

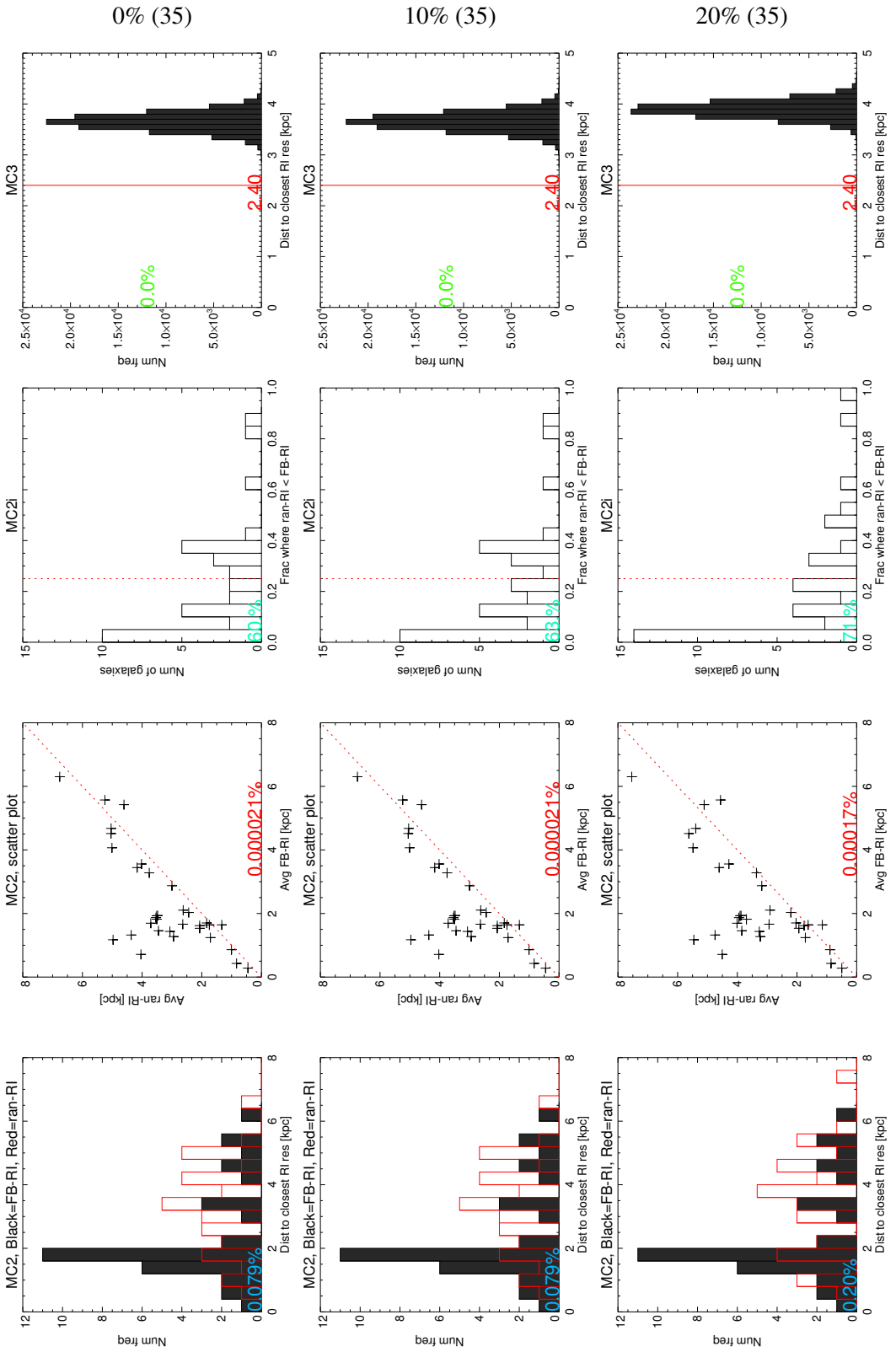

Figure 4.32: This is a comparison between three different inner forbidden limits for resonances in the MC algorithms. From top to bottom, respectively, the inner limits are 0%, 10%, and 20% of the maximum galactic radius. The controlled primary parameters are rings as RI (limiting the number of galaxies to 52), kpc as distance unit, 100k as random resonance number, and basic FB resonances. The number of galaxies in each column is given in brackets.

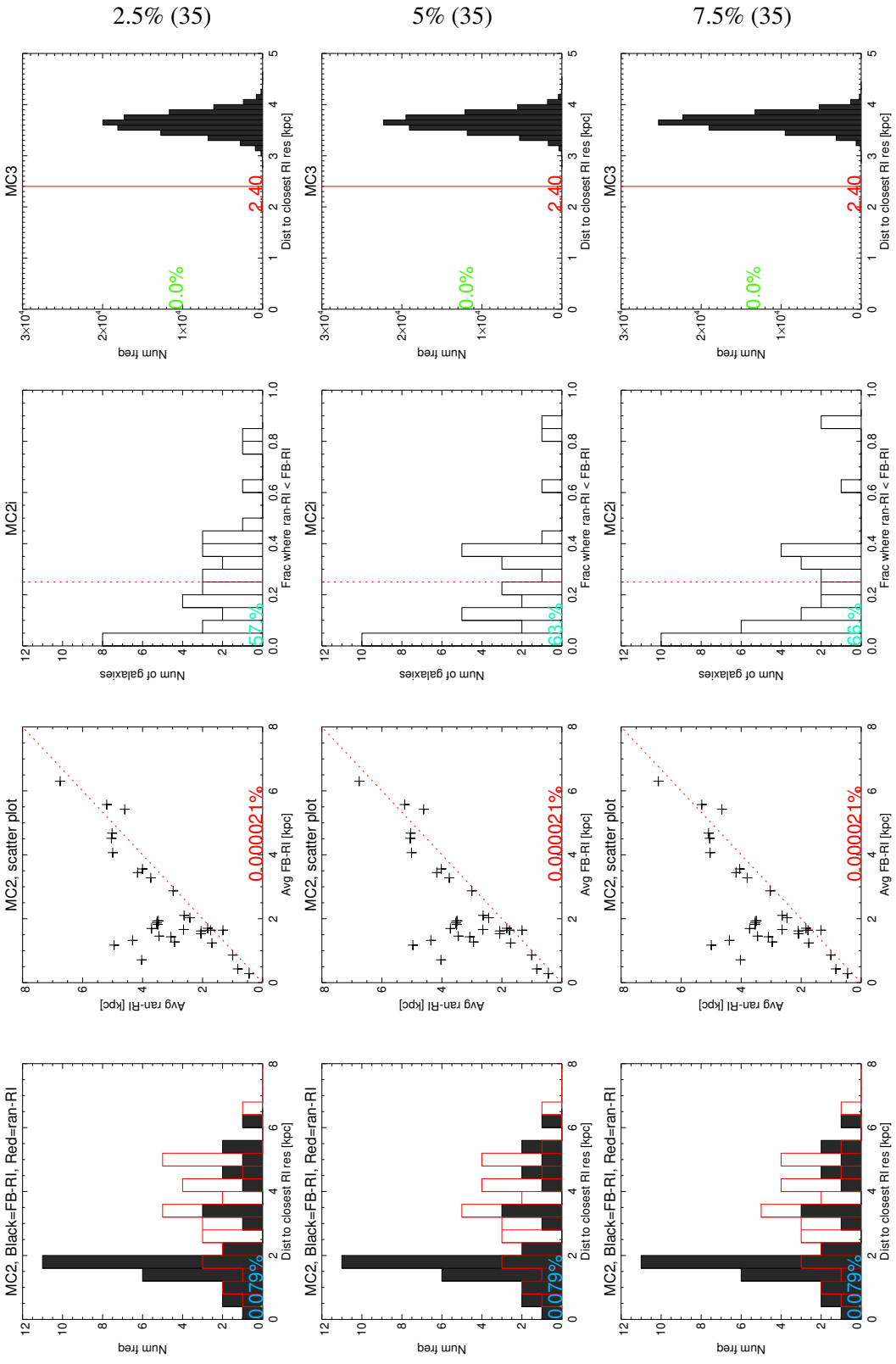

Figure 4.33: This is a comparison between three different inbetween forbidden limits for resonances in the MC algorithms. From top to bottom, respectively, the inbetween limits are 2.5%, 5%, and 7.5% of the maximum galactic radius. The controlled primary parameters are rings as RI (limiting the number of galaxies to 52), kpc as distance unit, 100k as random resonance number, and basic FB resonances. The number of galaxies in each column is given in brackets.

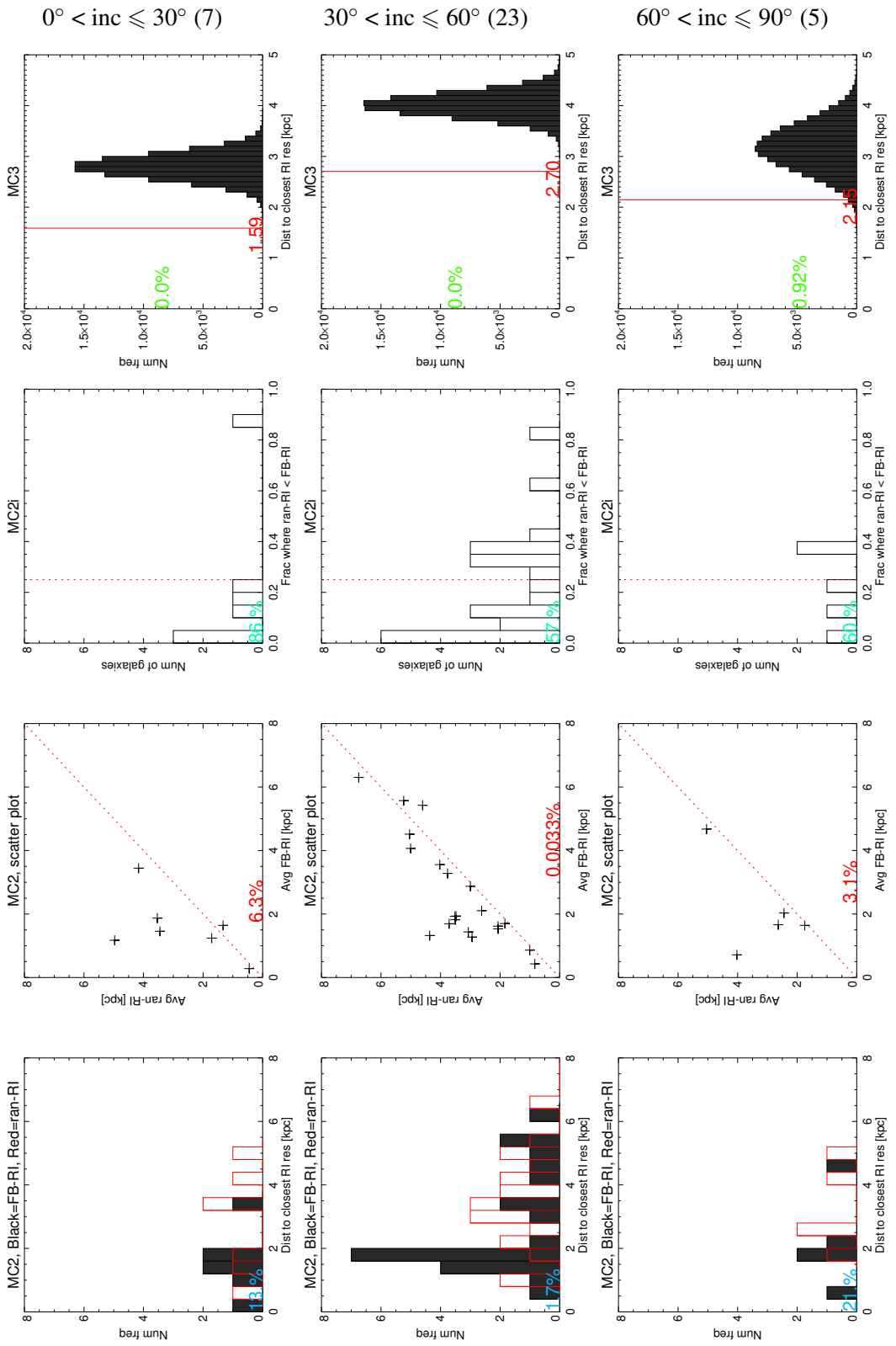

Figure 4.34: This is a comparison between three different inclination limits in the MC algorithms. From top to bottom, respectively, the inclination is between 0° and 30°, between 30° and 60°, and between 60° and 90°. The controlled primary parameters are rings as RI, kpc as distance unit, 100k as random resonance number, and basic FB resonances. The number of galaxies in each column is given in brackets.

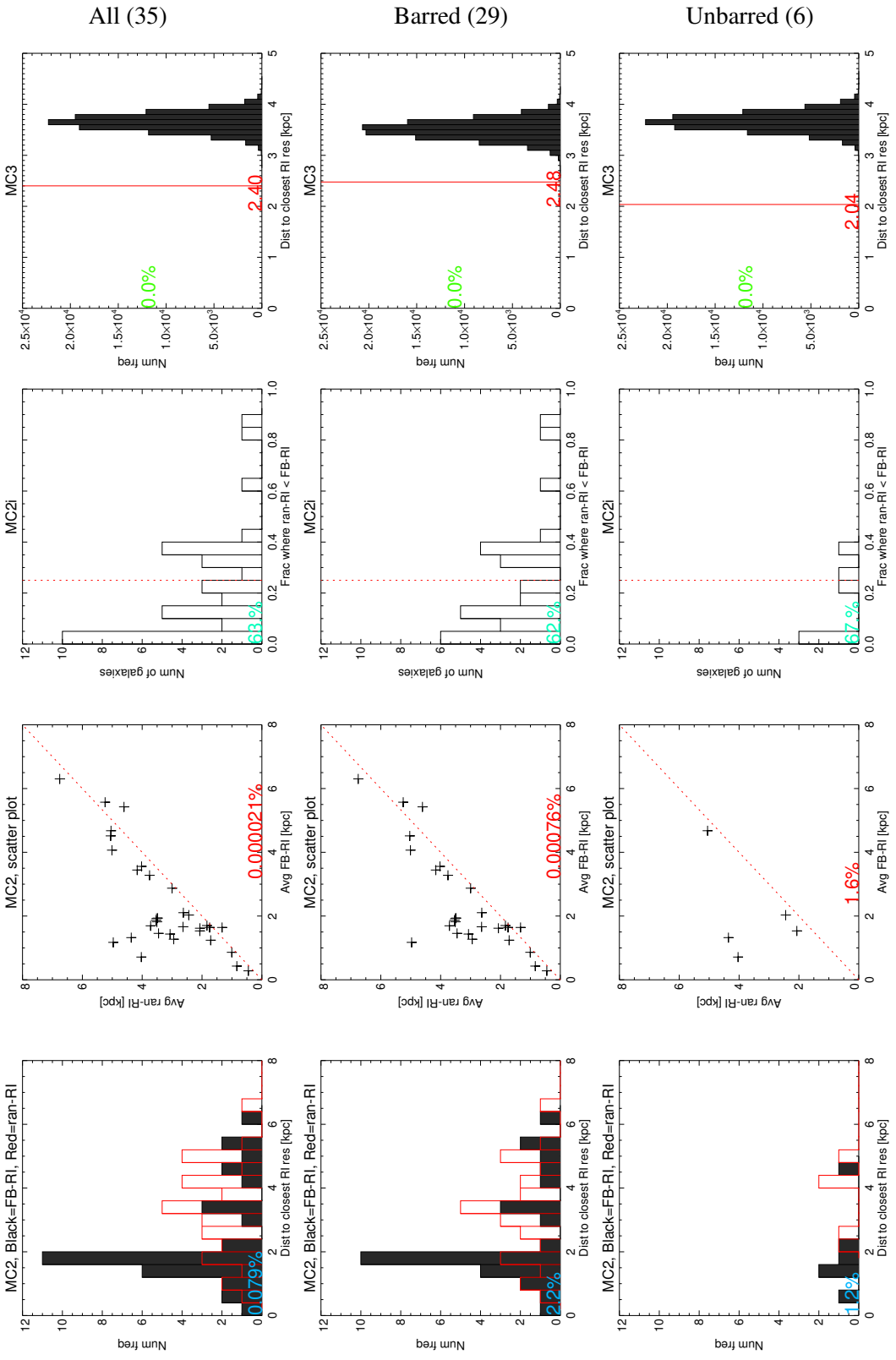

Figure 4.35: This is a comparison between barred and unbarred galaxy samples in the MC algorithms. From top to bottom, respectively, the galaxy sample includes both barred and unbarred galaxies, only barred galaxies, and only unbarred galaxies. The controlled primary parameters are rings as RI, kpc as distance unit, 100k as random resonance number, and basic FB resonances. The number of galaxies in each column is given in brackets.

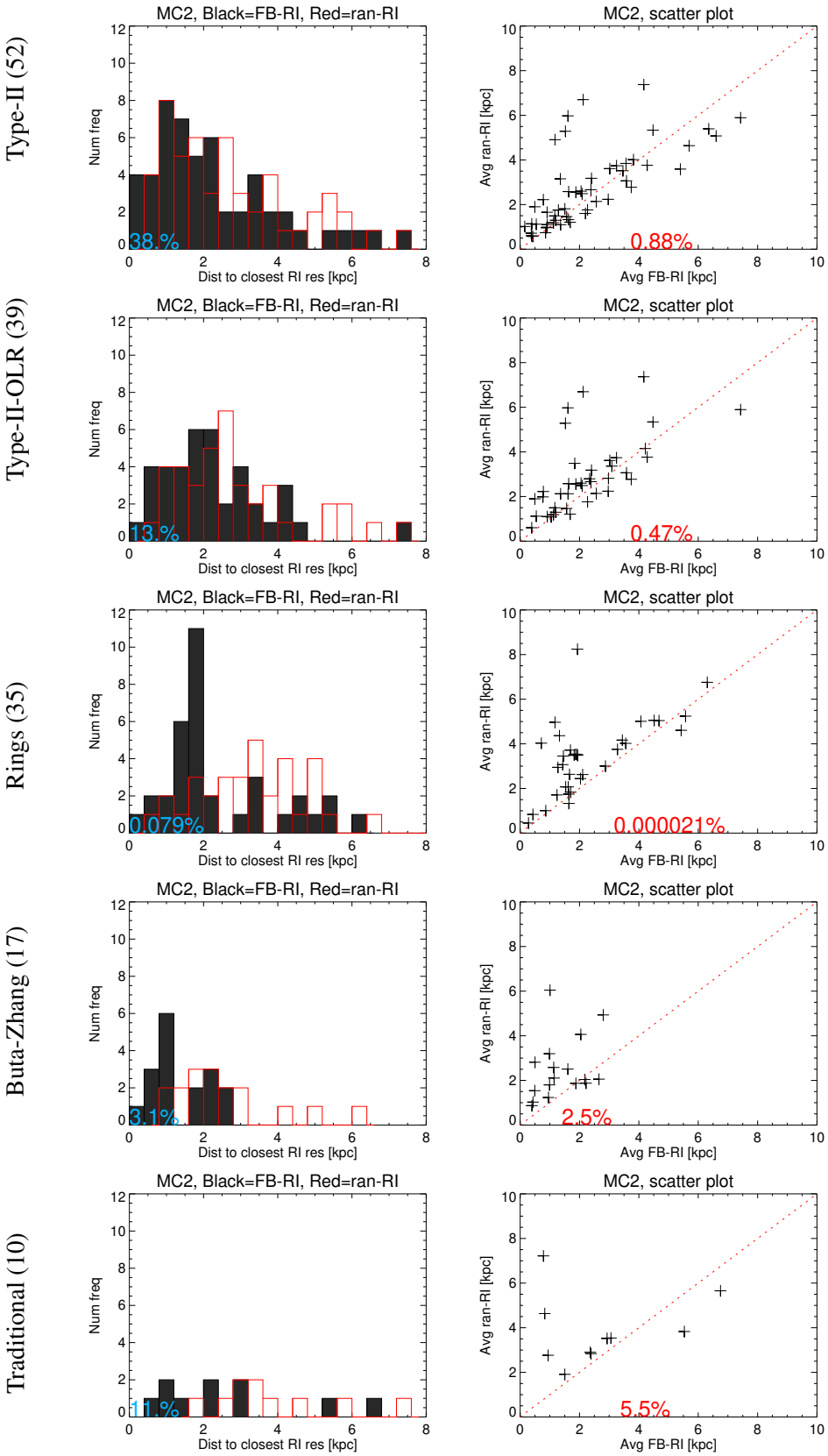

Figure 4.36: This is a final comparison between the relevant RI choices for MC2. From top to bottom, respectively, the RI choices are Type-II truncations, Type-II-OLR truncations, rings, Buta-Zhang resonances, and traditional resonances. The controlled primary parameters are kpc as distance unit, 100k as random resonance number, and basic FB resonances. The number of galaxies in each row is given in brackets.

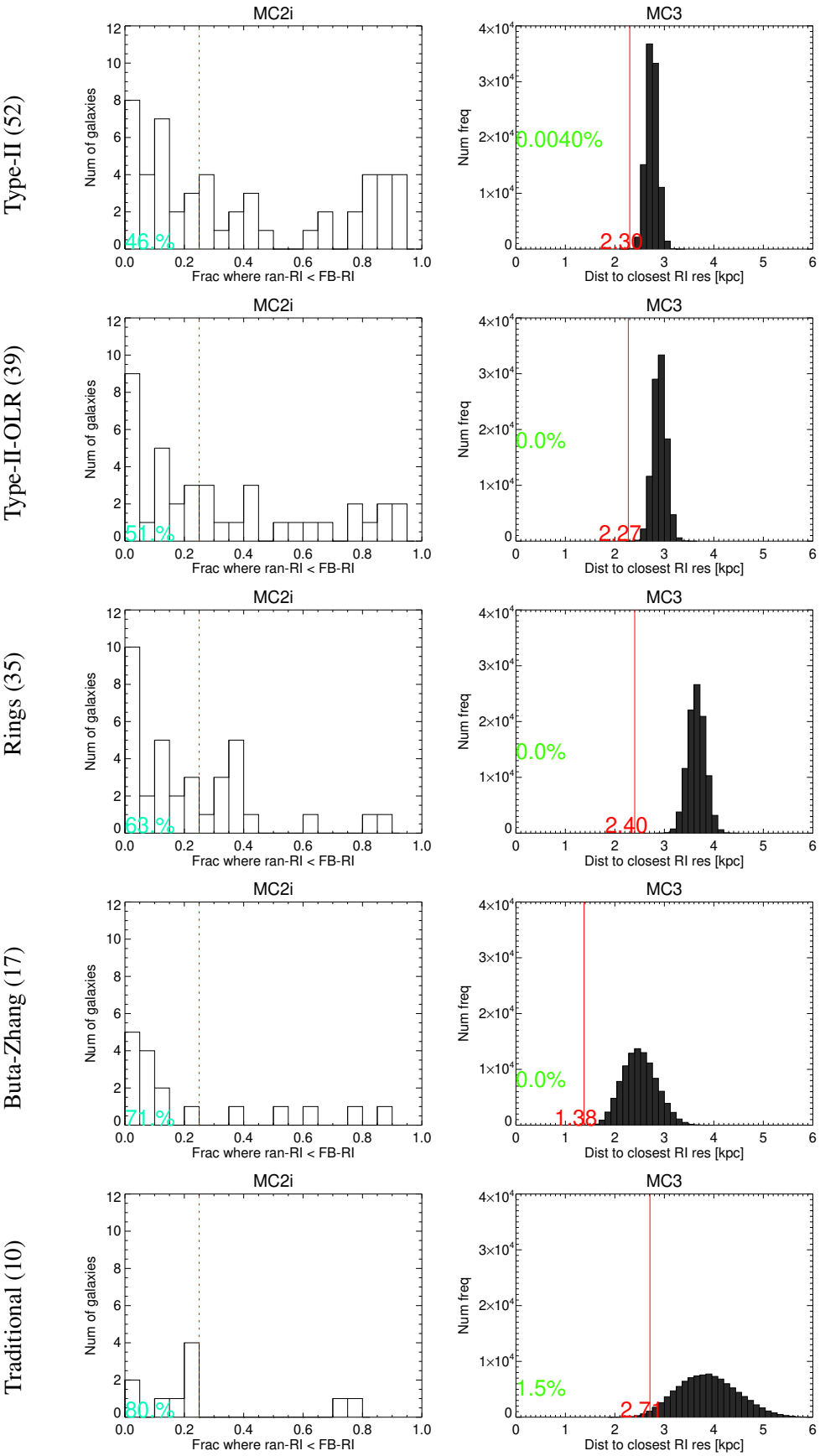

Figure 4.37: This is a final comparison between the relevant RI choices for MC2i and MC3. From top to bottom, respectively, the RI choices are Type-II truncations, Type-II-OLR truncations, rings, Buta-Zhang resonances, and traditional resonances. The controlled primary parameters are kpc as distance unit, 100k as random resonance number, and basic FB resonances. The number of galaxies in each row is given in brackets.

Chapter 5

Discussion

In this chapter the results are discussed and the reasons for the various parameter choices are explained. A discussion, short or long, regarding each result from the results chapter is presented here.

5.1 Simulation application

The Wada simulation used for simulating galaxies with known resonances has many parameters. The results of changing these parameters were shown in section 4.1. Here we discuss the implications of these changes and comment on the extent of Font-Beckman method's success, if there is any.

The first result to discuss is that of Figure 4.1, where the simulation was performed with varying particle numbers. The size of the simulated galaxy's image, in pixels, is 400 by 400. This translates to a total pixel count of 160000. The galaxy itself takes less space in the image so it is represented by fewer pixels, but let us assume the extreme value of 160000 for the total number of pixels used to represent the galaxy. The particle number values tested were 400k, 4M, and 40M. These, respectively, correspond to 2.5, 25, and 250 particles per pixel on average. Of course it is best to have as many particles in a pixel as possible since that increases the signal-to-noise ratio. This larger number of particles comes at the cost of computing power and time. The test of Figure 4.1 shows that, in this comparison, the particle number does not make a significant difference. The default value of the particle number used in all other tests is 4M, which translates to at least 25 particles per pixel on average.

The simulation has the option of arranging the initial particles in either a semi-random or a fully random manner. The difference that this choice makes is seen in Figure 4.2. The "Ring" refers to the semi-random arrangement as those particles were randomly placed in an ordered set of rings. The "No ring" refers to the fully random arrangement in which there were no ordered structures involved in the particle placement. It is clear that the difference when applied to the Font-Beckman method is insignificant. However, the default choice for all the other tests is the semi-random arrangement as that yields a slightly more visually-appealing galaxy.

The comparison in Figure 4.3 shows the effect of changing the perturbation strength. It is noteworthy that the weakest perturbation (0.01) seemingly gives the worst results as compared to the other two perturbations (0.05 and 0.09). In the case of 0.01 perturbation strength, the FB resonances seem to only correlate with two of the five real resonances (ILR and OLR), seen as green lines in the plots. While in the case of 0.05 and 0.09 perturbation strengths, the FB resonances show some correlation with all five of the real resonances. This is investigated further and in more detail, with the help of a systematic scoring of the

correlations, in the final part of this section. In short, it is found that in the weakest perturbation (0.01) case only two of the five theoretical resonances are found by the FB method, however, these two are considered to be definite correlations (the meaning of this is introduced and discussed later in this section). In the case of 0.05 perturbation strength four of the five theoretical resonances are somewhat found, although all four are considered to be potential correlations (also introduced and explained later in this section). Lastly, the case of 0.09 perturbation strength finds all the five theoretical resonances, albeit only one of them is a definite correlation and the remaining four are potential correlations. Generally, it appears that when the perturbation strength goes from 0.01 to 0.09 the success rate of the FB method improves. However, as we will see later in this section, this trend weakens as the simulated seeing (strength of the blurring) increases. Taking into account all the comparisons (including all the different blurring strength cases) one finds that increasing the perturbation strength from 0.01 to 0.09 makes no significant difference to the success rate of the FB method (justified with success rate values later in this section).

The next comparison, seen in Figure 4.4, shows the effect of changing the inclination of the simulated galaxy. The inclinations tested were 15°, 30°, 45°, 60°, and 75°. The best correlation between FB resonances and real resonances is in the case of 45° inclination, followed by 30°, 60°, 15°, and 75°. Since 45° inclination gives the best results, it is the default choice of inclination in all the other tests. The reason behind this growing failure of the FB method as the inclination shifts from 45° is its reliance on the residual velocity map and likewise on the line-of-sight velocity of each pixel. The line-of-sight velocity is best studied when the object has a tilt rather than being nearly face-on, because if the galaxy is nearly face-on and it has most of its motion along the disc plane (this is exacerbated in our case since we use small perturbations to keep the residual structures clean) then the line-of-sight velocity becomes negligible. On the other hand, if the tilt is too great (the object is nearly edge-on) then the disc features are not properly distinguished and the line-of-sight readings become less reliable. This is clearly visible in the results of Figure 4.4, as 15° is too small of an inclination for line-of-sight velocities to be properly detected while 75° is too great of an inclination for disc features to be correctly distinguished, therefore, the Font-Beckman method suffers in both cases.

The effect of changing the maximum radius of the simulated galaxy is seen in Figure 4.5. It is clear that changing the maximum radius does not affect the FB resonances but simply their cut-off radius. In case of the 120 arcsec maximum radius, the same FB resonances exist (correlating to ILR, I41, and CR) with even almost identical phase reversal values (all three are around 20) as the 160 arcsec maximum radius case. The 200 arcsec maximum radius case shows some extra noise beyond OLR which may incorrectly be interpreted as FB resonances if one does have the privilege to know the real resonances, which is the case when trying to use the FB method in real life. In all other tests the maximum radius is taken to be 160 arcsec as that gives the best results.

The comparison between various pixel selection and phase reversal rejection methods is given in Figure 4.6. Interestingly, the "improvements" that we made to the original FB pixel selection and phase reversal rejection methods are more deteriorating than improving in nature. The effect of going from the original FB methods to the ones introduced by us is a small weakening of the weaker peaks and when combined this reduction is noticeable. It is important to remember that this test is done on the very "clean" (high signal-to-noise ratio) simulated galaxies with known resonances; perhaps, in real "unclean" (low signal-to-noise ratio) galaxies one would prefer to use the methods that reduce the weaker peaks which are more likely to be noise rather than real signals.

The next comparison is seen in Figure 4.7, which shows the effect of changing the velocity threshold that is used to determine whether a phase reversal has taken place or not. In short, a phase reversal is measured if two neighbouring pixels have residual velocities with differing sings and their velocity difference is larger than this threshold. Therefore, a large threshold means that fewer pixels are selected as phase reversals whereas a small threshold means that more pixels are selected as phase reversals. The aim of the comparison in Figure 4.7 is to show how sensitive the FB method is with regards to this phase reversal velocity threshold (when being applied to the simulated galaxies). It is clear that changing the phase reversal velocity threshold from 10^{-2} to 10^{-6} simulation velocity units has a significant effect on the FB resonances. However, it is also apparent that there is not much difference in the cases of 10^{-4}, 10^{-5}, and 10^{-6} phase reversal velocity thresholds; this indicates that the smallest velocity differences in neighbouring pixels are around 10^{-4} simulation velocity units. Thus, a selection of any phase reversal velocity threshold smaller than 10^{-4} is going to yield a similar graph as the 10^{-4} case; this means that our choice of 10^{-5} as the phase reversal velocity threshold is a reasonable one. It is interesting to note that the 10^{-3} case shows the same general peaks as the 10^{-4} (or any smaller threshold) case but without some of the weaker peaks. So it is possible to somewhat reduce the effect of weaker peaks without a loss of generality by increasing the phase reversal velocity threshold. When applying the FB method to real observations one must expect a smaller signal-to-noise ratio as compared to the simulation results here, which means that it might be helpful to increase the phase reversal velocity threshold to reduce potential effects of noise in real galaxies.

The comparison in Figure 4.8 shows the effect of simulation duration on the FB method. The duration are 10, 50, and 90 simulation time units. A visual difference between the duration of 10 and 50 time units is seen in Figure 3.7. It is clear that the duration of 10 time units gives a far worse FB result than duration of 50 and 90 time units; when comparing 50 and 90 time units together, it appears that 50 is slightly better. This result gets even more interesting when one takes Figure 1.17 (the Canzian residual map) into account. Comparing the simulated galaxy's residual map after 10 time units to the Canzian residual map, one finds that there are striking similarities between their features. As the simulation is run for longer, these features tend to get compressed into ring-like structures; note that the same Canzian features still exist, but in a more compact form covering a smaller region of the disc. This has crucial consequences for the FB method, because the FB method relies on finding phase reversals which are then counted radially. This means that if the residual velocity map has somewhat continuous features (like the Canzian residual map) then the FB method would find phase reversals at a continuous range of radii. This reduces the number of strong peaks and increases the number of peaks of medium-to-low strength. However, if the residual velocity map has features that are radially restricted to a compact region of the disc (like the simulated galaxies with longer duration) then the FB method would find more phase reversals at the radius with the features. This increases the number of strong peaks and reduces the number of peaks of medium-to-low strength. This phenomenon is clearly visible in Figure 3.7, when comparing duration 10 and 50 time units. This result suggests that the FB method is not a suitable method of finding resonances when the residual map shows strong, radially-continuous Canzian features. The default choice of the simulation duration in the other comparisons is 50 simulation time units as that clearly results in galaxies with better FB applicability.

The final three comparisons in Figure 4.9, Figure 4.10, and Figure 4.11 show the effect adding blurring. The Gaussian blurring ranges from none to a σ of 10 pixels. The blurring aims to replicate the effect of

seeing in real galaxies. To make concrete conclusions about the success of the FB method when applied to these simulated galaxies, let us introduce the following systematic comparison scheme.

The success rate of the FB method is taken as the number of FB resonances that correlate with the real resonances divided by the total number of real resonances. When determining correlation let us use a score of 0 for no correlation, ½ for a potential correlation, and 1 for a definite correlation. These numbers allow us to get upper and lower estimates on the success rate of the FB method. Before setting conditions for scoring the correlations, the concept of a unique peak is introduced. A bin is counted as a unique peak if the bin has the largest frequency as compared to the two bins before and after it; additionally, at the third bins before and after it, the frequency has at least dropped to below half of its own frequency. Note that all the bins in all the test histograms (of this section) have the same value of 4 arcsec, which is a value of the order of the simulated seeing. Additionally, the average seeing used by Font et al. (2014a) is 3.59 arcsec[1] which shows that our choice of 4 arcsec for the seeing is a reasonable one. See the example in Figure 5.1 for a visual representation of the scheme; peak A is a unique peak while peak B is not.

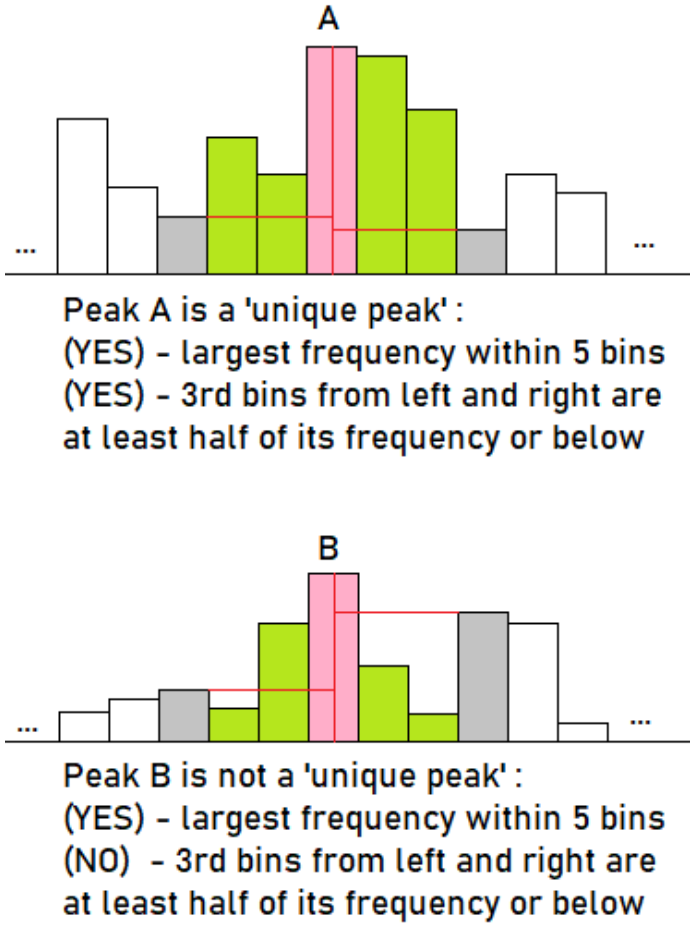

Figure 5.1: This is a simple way of determining unique peaks. A bin is considered unique if it passes the two conditions shown in the figure. In this example, peak A is unique while peak B is not. Note that in all the cases where this criterion is applied the size of the bin is always 4 arcsec; this is chosen as it is close to the simulated seeing and it additionally yields nice-looking histograms.

[1]This is calculated by averaging all the seeings in Table 3 of Font et al. (2014a).

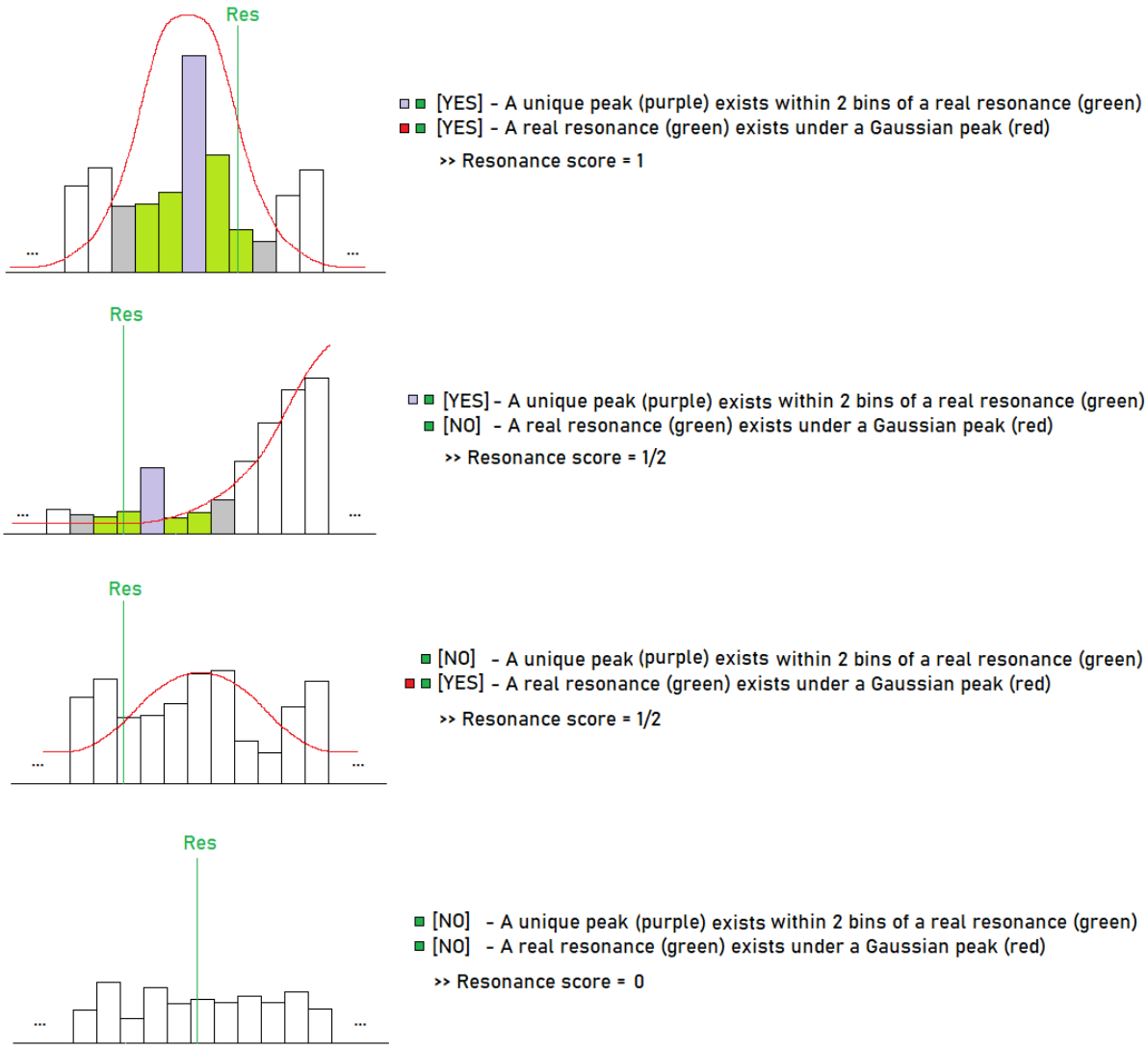

Figure 5.2: This figure aims to show how the peak-scoring criterion is used via a few example histograms. The first sketch is the case where the resonance (shown by a vertical green line) is given a score of 1. The second and the third sketches have their resonances given a score of ½, while the last one has a score of 0. Note that the scoring is done for each of the real resonances; there are five real resonances (ILR, I41, CR, O41, and OLR) in each of our histograms.

In order to measure a definite correlation (score of 1), firstly a unique peak must exist no farther than two bins distance from a real resonance (if there are multiple then only the closest to the real resonance is selected) and secondly the real resonance must fall under a Gaussian peak. In order to measure a potential correlation (score of ½), either a unique peak exists no farther than two bins distance from a real resonance (if there are multiple then only the closest to the real resonance is selected) or the real resonance falls under a Gaussian peak (if there are multiple real resonances under a single Gaussian peak then the correlation is only with the one that is closest to the Gaussian's fitted center). In order to measure no correlation (score of 0) a real resonance must be farther than two bins distance from the closest unique peak and it does not fall under a Gaussian peak. See Figure 5.2 which shows how the scoring system is implemented in a few example histograms.

According to the aforementioned scoring rules the real resonances (ILR, I41, CR, O41, and OLR) in each case are analyzed and their correlation is scored. The scores are given in Table 5.1. Note that, at times, this scoring system appears too harsh as some "strong" peaks (based on visual inspection) are downgraded from definite peaks to potential peaks. This strictness is necessary to pass fair judgement on the success of the FB method. Note that the success rate of each individual part is also given. When calculating the success rate the lower-end the ½ scores are counted as 0, but when calculating the upper-end the ½ scores are counted as 1. The correlation scores and the FB success rates (in percentage) are shown in Table 5.2.

σ	ILR			I41			CR			O41			OLR			Scr
–	.01	.05	.09	.01	.05	.09	.01	.05	.09	.01	.05	.09	.01	.05	.09	–
0	1	½	½	0	½	1	0	0	½	0	½	½	1	½	½	3–11
2.5	½	1	½	1	0	0	0	0	0	0	½	½	1	½	½	3–9
5	½	1	½	1	0	½	0	0	½	0	½	0	½	1	1	4–10
7.5	0	½	½	1	0	½	0	½	0	½	0	0	1	1	1	4–9
10	0	0	0	1	0	0	0	½	½	1	0	0	1	1	1	5–7
Scr	3–11			5–8			0–5			1–7			10–15			–

Table 5.1: This table shows the correlation score of each real resonance with the FB resonances found in Figure 4.9, Figure 4.10, and Figure 4.11. Note that "Scr" is short for score and in both score panels (horizontal and vertical) the maximum possible score is 15.

σ	ILR	I41	CR	O41	OLR	Rate
0	1–3	1–2	0–1	0–2	1–3	47%±27%
2.5	1–3	1	0	0–2	1–3	40%±20%
5	1–3	1–2	0–1	0–1	2–3	47%±20%
7.5	1–2	1–2	0–1	0–1	3	43%±17%
10	0	1	0–2	1	3	40%±7%
Rate	47%±27%	43%±10%	17%±17%	27%±20%	84%±16%	Global = 43%±18%

Table 5.2: This table shows the correlation scores of each resonance type seen in Table 5.1 as well as the success rates of the FB method in percentage. The "Global" (in the bottom right corner of the table) is the global success rate of the FB method as by counting the correlation score of all resonances types along with all blurring strengths. The uncertainty of the success rates (in percentage) is simply half of the total difference between the upper and the lower success rate estimates. Note that the individual scores in all sections are out of a maximum possible score of 3.

Table 5.2 shows that as blurring strengthens the success rate of the FB method stays roughly stable around 40%, however, the uncertainty of the success rates get smaller. The uncertainty of each success rate is half of the distance between the upper and the lower success rate estimates. This means that as blurring strengthens the difference between the upper and lower estimates of the FB success rate drops; in other words, with increased blurring it is easier to judge the state of a correlation, i.e. easier to definitely

call it a resonance (score of 1) or not (score of 0), instead of counting it as a potential resonance (score of ½). Furthermore, Table 5.2 shows that, by far, the strongest correlation between FB resonances and real resonances occurs in the case of OLR. That is followed by ILR and I41 resonances. The weakest correlation is observed in the case of O41 resonances and, lastly, CR. Finally, taking into account the correlation with the entire 75 real resonances in the 15 simulated galaxies, the global success rate of the FB method turns out to be 43%±18%. It is apparent that one cannot claim the FB method is an overwhelming success when applied to these simulated galaxies, even in the case of the "cleanest" residual velocity maps; however, at the very least, it is undeniably apparent that the FB method is able to locate OLR successfully (success rate of 84%±16%) as well as ILR (success rate of 47%±27%) and I41 (success rate of 43%±10%) resonances somewhat reliably.

From Table 5.1 one can also measure the total success rate for each of the three perturbation strengths. In the case of 0.01, the score tallies to 10–14 out of 25. For 0.05, the score is 5–15 out of 25. For 0.09, the score is 4–17 out of 25. These in percentage are 40%–56% (∼48%±8%) for 0.01 perturbation strength, 20%–60% (∼40%±20%) for 0.05 perturbation strength, and 16%–68% (∼42%±26%) for 0.09 perturbation strength. Note that earlier in this section when we discussed the results of Figure 4.3, we came to the superficial conclusion that 0.01 perturbation strength is showing a worse correlation than the other two, but now that we have constructed a clearer picture that does not seem to be strictly correct. If the potential resonances are taken as definite resonances (the upper value of the success rate) then indeed the FB resonances in the cases of 0.05 and 0.09 show a better correlation with the real resonances than the 0.01 case. However, if the potential resonances are rejected (the lower value of the success rate) then this conclusion does not hold. If one only considers the average success rates then increasing the perturbation strength seems to have no significant effect on the success rate as all three seem to be around 40% (very close to the global success rate value).

It is noteworthy to mention the increasing uncertainty of the success rate with increasing perturbation strength. This means that as the perturbation strength increases, it becomes harder to judge the true nature of the FB resonances (if they definitely exist or not versus if they are potential). This is a bad sign when it comes to applying the FB method to real galaxies. In real galaxies the perturbation situation is far more complex than what we have here, i.e. there may be multiple sources of perturbation with varying intensities and potentially with far greater strengths than what we have simulated. This means that, even if one ignores the low signal-to-noise ratio of the real observations, a stronger perturbation inherently induces uncertainty into the final FB result making it harder to judge the true nature of the FB resonances (a definite resonance or not versus a potential resonance).

5.2 Monte Carlo analysis

This section deals with the results of the Monte Carlo tests.

5.2.1 Type-II truncations as RI

It is commonplace to find links between Type-II truncations and resonances when exploring the literature of galactic studies. A special case of Type-II truncations, Type-II-OLR, is thought to be directly linked to the OLR as the name suggests. This is a Type-II truncation that occurs at a radius around 2 to 3 of that of the galactic bar; see Erwin et al. (2008). For this reason, Type-II truncations are used as a resonance

indicator (RI) in this thesis as are rings. Ideally, Type-II-OLR truncations are better suited for such a task but the number of galaxies that show Type-II-OLR truncations is smaller than that of Type-II truncations. Additionally, Type-II-OLR truncations only pertain to one resonance, the OLR, whereas we are interested in all the main resonances (ILR, CR, and OLR) as well as the inner (I41) and outer 4:1 (O41) resonances, not just the OLR.

To start the discussion one can look at the truncation comparison, seen in Figure 4.18, where truncations of all types, Type-II, Type-II-OLR, and Type-III are compared. This comparison is used as a starting example to thoroughly explain the comparison tools used in the graphs; for this reason the discussion of this first comparison is prolonged, unlike the comparisons that follow it. The first column shows the MC2 histograms, in which the Kolmogorov-Smirnov (KS) test gives a numerical representation of how probable it is for the two distributions to be drawn from the same parent distribution. A big KS probability means the two distributions are almost identical while a small KS probability means the opposite. The black histogram shows the average distance between the Font-Beckman (FB) resonances and their closest RI resonance (in short, FB-RI) whereas the red histogram shows the average distance between random resonances and their closest RI resonance (in short, ran-RI). Note that the smaller the KS probability is, the more probable it is that the FB and RI resonances are correlated; this is because a smaller KS probability means that the FB-RI distribution is less likely to be identical to the ran-RI distribution, i.e. FB-RI distribution is less random. The MC2 histograms in Figure 4.18 show no significant correlation between FB resonances and any of the truncation types. Curiously, the weakest correlation is found in the case of Type-II (KS of 38%) followed by Type-II-OLR (KS of 13%), all types (KS of 10%), and lastly Type-III (KS of 3.2%).

The second column in Figure 4.18 shows the scatter plots where FB-RI (x-axis) are plotted against ran-RI (y-axis). The red percentage shows the chance to obtain the scatter at hand if a given point has a 50% chance of landing above or below the line of equality (the red dotted line); this is calculated using the binomial distribution of 0.5 probability (Bp0.5). Note that the smaller this Bp0.5 probability is, the more probable it is that the FB and RI resonances are correlated; this is due to having more and more points falling above the line of equality. In a purely random scenario (ran-RI versus ran-RI) the expected result is a scatter that symmetrically populates the region of the line of equality, i.e. equal points above and below it; however, if the population in the scatter plot shows a skew to one side of the line of equality then that means the distribution being plotted against the random one is less likely to be random. In the scatter plots of Figure 4.18 where x-axis is FB-RI and y-axis is ran-RI, an upward skew of the population indicates that the FB-RI distribution not likely to be random in nature; this is numerically shown via the Bp0.5 probability. Once again, the truncation comparison yields the weakest correlation to be in the case of Type-II truncations (Bp0.5 of 0.88%). This is followed by Type-III (Bp0.5 of 0.77%), Type-II-OLR (Bp0.5 of 0.47%), and lastly all types (Bp0.5 of 0.02%). Note that both the MC2 histograms and MC2 scatter plots are using the MC2 algorithm which means that both of their FB-RI and ran-RI distributions identical; the only difference is how the distributions are visualized and compared.

The third column in Figure 4.18 shows the MC2i global (over the entire galaxy sample) histogram plots, which is a distribution of the fraction where ran-RI is less than FB-RI for each galaxy. This refers to the fraction where, over many MC runs, the average distance between the random resonances and their closest RI resonance (ran-RI) is smaller than the average distance between the FB resonances and their closest RI resonance (FB-RI); this fraction for each galaxy is then represented in the MC2i global

histogram. The more skewed this distribution is towards the smaller side, the more probable it is that FB and RI resonances are correlated. A skew towards the smaller side means that there is a larger number of galaxies where most MC runs ended up having FB-RI to be smaller than ran-RI (using the fact that a 0.2 fraction where ran-RI < FB-RI is identical to a 0.8 fraction where FB-RI < ran-RI); therefore, a skew towards the smaller side means FB resonances are less likely to be random. To show this shift of the distribution numerically, the percentage of galaxies (shortened as GalPerc) within the galaxy sample where their fraction (where ran-RI < FB-RI) is 0.2 or smaller is shown. The larger this number is, the more the distribution is skewed towards the smaller side, i.e. higher chance of correlation between FB and RI resonances. The truncation comparison of Figure 4.18, yet again, gives the weakest correlation in case of Type-II (GalPerc of 46%) followed by Type-II-OLR (GalPerc of 51%), Type-III (GalPerc of 52%), and all types (GalPerc of 52%).

The final column in Figure 4.18 shows the MC3 global histogram, which represents the FB-RI of the entire galaxy sample as a single averaged value, i.e. globally averaged FB-RI, (shown as the red vertical line) as well as the distribution of the globally (over the entire galaxy sample) averaged ran-RI over many MC runs (shown as the black histogram). The fewer globally averaged ran-RI smaller than globally averaged FB-RI are, the more probable it is for FB and RI resonances to be correlated. This is because on average FB resonances are closer to RI resonances as compared to random resonances, as a result they are less likely to be random in nature. This is numerically represented by showing the percentage of globally averaged ran-RI smaller than globally averaged FB-RI. The smaller this percentage (shortened as MC3Perc) is, the greater the chance of FB and RI resonances being correlated is. The truncation comparison of Figure 4.18 gives the weakest correlation in the case of Type-II (MC3Perc of 0.004%) while the other three truncations (all types, Type-II-OLR, and Type-III) all show MC3Perc of 0%, which means that none of the globally averaged ran-RI were smaller than the globally averaged FB-RI over 100k MC runs.

It is useful to note the number of galaxies in each galaxy sample. This is given in each result's description and shown in the row description where relevant. For instance, in the case of Figure 4.18 there are 60 galaxies with truncations of all types, 52 galaxies with Type-II truncations, 39 galaxies with Type-II-OLR truncations, and 50 galaxies with Type-III truncations. It is obvious that a larger number of galaxies in the sample increases the reliability of the MC analysis as the effect of random error is diminished. In the case of the truncation comparison, although galaxies with Type-II-OLR truncations are around 35% less in number as compared to all types of truncations, it is big enough to obtain stable results. The number of galaxies in the sample plays a crucial role in some of the other comparisons where the number of galaxies drops to a dozen or less.

The overall conclusion that can be made form the truncation comparison in Figure 4.18 is that Type-II truncations are the weakest of all truncations when it comes to correlation with the FB resonances. Despite this weakness, Type-II truncations are still used as one of the two main RI used to run further tests, along with rings. The state of rings and their tests are shown in the next subsection. Type-II-OLR truncations seem to be slightly more correlated with FB resonances as compared to Type-II ones, even though the correlation is still rather weak. Truncations of all types and Type-III seem to be even better than Type-II and Type-II-OLR at tracing FB resonances; this finding is in somewhat of a contrast with the current general consensus of galactic astronomy. It is of utmost importance to note that the truncations used in this thesis are the ones found in my BSc thesis, which did not use a standardized algorithm for

finding resonances. In that study, the truncations were found manually which is prone to human error and inconsistencies; unfortunately, this leads to a set of truncation values that are more subjective than objective. This can be improved by doing multiple tests using a diverse set of truncation values from various sources. An even better approach would be to standardize the way truncations are identified to minimize human error as much as possible (for example see Watkins et al. 2019), but this is beyond the scope of this study with the given time frame.

The next comparison panel to discuss is the one in Figure 4.12, which aims to compare the results of the four Monte Carlo algorithms, namely MC1, MC2, MC2i, and MC3. The first row shows the histogram and scatter plot of MC1, the second row shows those of MC2, and the third row shows the results of MC2i and MC3. Note that the visualization technique of the results of MC1 as well as the numerical tests used (KS for the histograms and Bp0.5 for the scatter plots) are identical to those of MC2. The difference between the results of MC1 and MC2 is that in MC1 there are as many data points as there are individual FB resonances whereas in MC2 there are as many data points as there are galaxies. This is because in MC2 the individual FB resonances are averaged out to obtain a single FB value per galaxy; the same is done to their corresponding random resonances such that a single average random resonance value per galaxy is obtained. In this study's galaxy sample, there are two galaxies with seven and many more with six FB resonances which makes the final result of the MC1 algorithm rather messy and overpopulated. Furthermore, averaging over the galaxy reduces the effect of potential anomalies within each galaxy. For these reasons, MC2 is preferred over MC1 when doing the parameter tests as well as representing the final comparisons.

Figure 4.13 shows the same comparison between the four MC algorithms with the difference that the role of FB and RI resonances is now reversed. The biggest difference is seen in the MC1 and MC2 results; the reverse MC algorithm shows a stronger correlation between FB resonances and Type-II truncations than the normal MC algorithm. This is the opposite in MC3; reverse MC3 appears to show a worse correlation. At this points it is useful to remember that the aim of this study is to test the reliability of the FB resonances. Using a Monte Carlo technique, it is logical to parallel the FB resonances with the randomly generated resonances, which allows us to see if the FB resonances are random in nature or not by comparing them to the "true" RI resonances. An issue arises when one looks into how *true* these RI really are. The best RI is the Tremaine-Weinberg (TW) method but its results are only available for a small number of galaxies. This leaves us with the more ambiguous RI, such as truncations or rings, whose values are available for a large number of galaxies. The lack of data from reliable methods such as TW forces this study to use the less reliable RI to test the FB method. This unreliability of such RI inspired the need for showing the case where the roles of the "true" RI resonances is switched with that of FB resonances. So the reverse MC algorithm parallels the RI resonances with random resonances to see if they are random in nature by comparing them to the "true" FB resonances. Perhaps, the results of the reverse MC algorithms do not lead to any useful conclusions but it is intriguing to see the effects of such a reversal.

The first parameter test to be discussed is seen in Figure 4.14, where distance units are compared. The main choice of distance unit is kpc. This is because arcsec is objectively an unreasonable unit to use for the purposes of this test. It is crucial to note that arcsec is a unit that depends on how far the object is so it does not give a true measurement of the distance on the galaxy. The relative measurement is obtained by dividing the kpc measurement by the maximum extent of the galactic disc; this means its value depends

on the maximum extent of the galaxy. The relative distance unit may be useful, for example, when trying to study structures which are relative to the bar size. However, in this study, we are generally interested in finding out how close two resonances are from each other (regardless of the size of the galaxy), thus the default choice of the distance unit is kpc. When it comes to the effect of the choice of distance unit on the MC results, the biggest one is seen in MC2 histograms.

Figure 4.15 shows a comparison where the only different parameter was the number of MC simulations. This number has slightly different roles in each of the algorithms, but in general it represents the random iterations in the MC runs. The larger it is, the more reliable the results are. However, a larger MC number significantly reduces the calculation speed. As a result a compromise is found to be 100k. This comparison shows that a much larger MC number, such as 1M, still gives the same result as 100k. Interestingly, even a MC number of 10k is stable enough. Following up on the stability of the test, Figure 4.16 shows a comparison between four identical runs of the MC algorithms with the exact same parameters. This shows that the results are indeed stable and do not change every time the algorithms are run.

Figure 4.17 shows a comparison between all the FB resonances and only interlocking FB resonances as the resonances to be tested. It is clear that exclusively using the interlocking FB resonances results in a weaker correlation between FB resonances and Type-II truncations.

Figure 4.19 shows a comparison of the MC results when the maximum radii of the galaxies were taken at different surface brightness limits. It is clear that as the maximum radius of the galaxy is taken farther and farther out, the results shift in favor of a correlation between FB resonances and Type-II truncations. This means that all the MC algorithms are highly sensitive towards the choice of the maximum radius. This is expected as the maximum radius is farther out, i.e. when the surface brightness limit is larger, the range between which random resonances are generated grows. This means the average distance between a randomly generated resonance and a RI resonance increases. Note that a change in the maximum radius does not affect the FB-RI distance. This means that for greater maximum radii, more data points satisfy the condition where FB-RI is less than ran-RI, which translates to a better correlation between FB and RI resonances. Therefore, it is extremely important for the maximum radius limit to be as accurate and realistic as possible, otherwise the MC results become unreliable. A reasonable choice for the maximum radius may be the radius where one stops being able to identify surface brightness breaks with the data at hand. In this study, the main choice of the maximum radius is taken where the surface brightness drops below 25 mag/arcsec^2, which is a reasonable choice for the S^{4}G data.

Figure 4.20 shows a comparison between MC results where their inner limits are different. The inner limit of each case refers to the inner cut-off of where random resonances can be generated. It is reasonable to have an inner limit as, in real observations, resonances are not detected right at the galactic core. The main choice of inner limit used in this study is 10% of the galactic radius. It is clear that absence of an inner limit (the 0% row) and the 10% inner limit case behave similarly. However, the case of 20% inner limit appears to significantly weaken the correlation. This means the MC algorithms are sensitive to the inner limit choice and one must take caution when choosing it; similar to the maximum radius limit. This sensitivity is most likely a result of the range at which the random resonances are generated; selecting a larger inner limit reduces this range, which in turn makes ran-RI smaller on average such that more and more ran-RI become smaller than FB-RI, i.e. the correlation weakens. Figure 4.21 shows a comparison between MC results where their inbetween limits are different. The inbetween limit of each case refers to the inbetween cut-off of how close the random resonances can be to each other. This means if any

two random numbers are closer to each other than the inbetween limit, then they are not taken as random resonances. It appears that changing the inbetween limit has no significant effect on the MC results, apart from a small improvement in correlation in case of MC3 as the inbetween limit increases.

Figure 4.22 shows a comparison between MC results where a different limit on the inclination is set in each case. Note that the number in parenthesis for each case refers to the number of galaxies in the sample. Unfortunately, by setting a limit the number of galaxies in the sample drops, which reduces the reliability of the result. For example, the cases of inclination smaller than 30° and bigger than 60° have only nine and seven galaxies, respectively. Although these two cases have too few galaxies in their samples to be reliable, it does appear that they show a stronger correlation than the mid-range inclination (inclination between 30° and 60°) case. This weakening of the correlation with the removal of the extreme inclinations is also seen when comparing the mid-range inclination case to the unlimited (inclination-wise) cases seen in the previous comparisons; when the extreme inclinations are removed, the correlation weakens in all four panels. This may be due to the overall reduction in the number of galaxies in the sample.

Figure 4.23 shows a comparison between MC results where truncations are limited by different truncation strengths. Once again, limiting the truncation reduces the number of galaxies in the sample. For instance, the case where the truncation limit is 4 only possesses fifteen galaxies that significantly reduces its reliability; although this is not as bad as the extreme inclination limits cases seen above. It appears that only taking the stronger truncations leads to a stronger correlation between Type-II truncations and FB resonances.

Figure 4.24 shows a comparison between MC results where galaxies are distinguished by their bar status. Intriguingly, the case where only barred galaxies are considered (38 galaxies in the sample) shows a clear weakening of the correlation between FB resonances and Type-II truncations. This is surprising because, in theory, the presence of a bar should induce and strengthen resonances as it acts as a strong perturber.

5.2.2 Rings as RI

In this subsection the results of MC algorithms where rings are used as the main RI are shown. Most of the parameter tests are similar to those of the previous subsection, where Type-II truncations were the main RI.

The first MC comparison with rings as the RI is seen in Figure 4.25, where the histogram and scatter plot of MC1 is seen in the first row. Likewise, the histogram and scatter plot of MC2 are in the next row. The MC2i global plot and the MC3 histogram are shown in the last row. It is clear that both of the MC1 plots show a stronger correlation as compared to the MC2 ones (just as it was the case when using Type-II truncations as RI); however, the MC1 plots are overpopulated, messy, and potentially anomalous (individual outliers may exist as no averaging within each galaxy is done in MC1). It is appropriate to compare the results of Figure 4.25 (rings as RI) with Figure 4.12 (Type-II truncations as RI); it is clear that in all the six plots the case where rings are used as RI shows a much better correlation than the case where Type-II truncations are used as RI.

Moving on to Figure 4.26, one can see the reverse MC comparisons. Comparing this figure to Figure 4.25, it is evident that in the case of rings as RI all the reversed MC algorithms show a worse correlation between RI and FB resonances. This is interesting because a similar trend was not observed when reversing the MC algorithms in the case of Type-II truncations as RI. When comparing Figure 4.12 and its

reverse algorithm results in Figure 4.13, we found that in three (MC1 scatter, MC2 histogram, and MC2 scatter) of the six plots the correlation strengthened when reversing the MC algorithms.

Figure 4.27 shows the distance unit comparisons of the case of rings as RI. It is important to remember that in this thesis the preferred unit of distance is kpc. It is worthwhile to compare this rings as RI result to the Type-II truncations as RI result seen in Figure 4.14; once again, the rings as RI case shows a better correlation in all three distance unit cases and in all MC algorithms shown than the Type-II truncations as RI case.

Figure 4.28 is a random number test in the case of rings as RI which aims to see how a change in the random number might affect the MC result. It is clear that the result is stable and the preferred random number (100k) is acceptable. The stability test in the case of rings as RI is shown in Figure 4.29 which confirms that the result is indeed stable. Once more it is interesting to compare these rings as RI result to the Type-II truncations as RI results (compare Figure 4.28 with Figure 4.15 and compare Figure 4.29 with Figure 4.16) which show a better correlation in the case of rings as RI.

Figure 4.30 shows the comparison between all FB resonances and only interlocking FB resonances in the case of rings as RI. The correlation weakens when only utilizing interlocking FB resonances, which was also seen in the case of Type-II truncations as RI. By comparing Figure 4.30 (rings as RI) with Figure 4.17 (Type-II truncations as RI), one finds that the correlation is stronger in the case of rings as RI for all the plots.

Figure 4.31 shows a comparison of different maximum radial limits in the case of rings as RI. Just as it was deduced in the case of Type-II truncations as RI that the choice maximum radius is extremely important, it is evident here as well. A larger maximum radial limit means that on average a larger number of FB-RI is smaller than ran-RI (better correlation) as ran-RI lengthens with increasing maximum radial limit. If one compares Figure 4.31 (rings as RI) with Figure 4.19 (Type-II truncations as RI), one finds that the case of rings as RI shows a stronger correlation than Type-II truncations as RI regardless of the choice of maximum radius.

Figure 4.32 shows the comparison of different inner limit values in the case of rings as RI. A trend similar to that in the case of Type-II truncations as RI is seen here; no inner limit and 10% inner limit cases are similar whereas the 20% inner limit case shows a slight weakening of correlation in MC2. Figure 4.33 shows the comparison of different inbetween limit values in the case of rings as RI. It is evident that changing the inbetween values does not affect the results, as it was the case previously. When it comes to comparing the correlation strength in the cases of rings as RI and Type-II truncations as RI (compare Figure 4.32 with Figure 4.20 and compare Figure 4.33 with Figure 4.21), the rings as RI case shows a significantly higher correlation regardless of the inner or inbetween limit values.

The next comparison panel is seen in Figure 4.34 which shows how limiting the inclination in the galaxy sample affects the MC results. The case of rings as RI seems to behave differently from that seen in the case of Type-II truncations as RI where the extreme inclination cases (one must note the extremely limited number of galaxies in the sample) seemed to show a stronger correlation than the mid-range inclination case in every single panel. However, in this case (rings as RI), that does not seem to be the case. However, a similar behaviour between the rings as RI and Type-II truncations as RI is seen when comparing the mid-range inclination case to the unlimited (inclination-wise) cases seen previously; it appears that in the case of rings as RI the correlation weakens in every panel when the extreme inclinations are absent (this trend was observed in the case of Type-II truncations as RI as well). This weakening could

be due to the overall reduction in the number of galaxies in the sample. It is interesting to note that this finding contradicts what we found in the simulation section; we had found that the FB method works best in the case of mid-range inclinations, which seems to be the opposite of what we find here in the MC analysis. Comparing the cases of rings as RI (Figure 4.34) and Type-II truncations as RI (Figure 4.22) indicates that the rings as RI case has a significantly higher correlation regardless of the inclination limits.

The final comparison in the case of rings as RI is shown in Figure 4.35, which is inconclusive in the unbarred case and shows a slight decrease in correlation in the barred case. Regardless of the bar choice, it appears that the rings as RI case shows a stronger correlation than the Type-II truncations as RI case; seen by comparing Figure 4.35 (rings as RI) with Figure 4.24 (Type-II truncations as RI).

5.2.3 Final Monte Carlo comparison

In this subsection the final remarks regarding the MC results are presented and the final MC comparison plots between different RI choices are discussed.

Figure 4.36 (MC2) and Figure 4.37 (MC2i and MC3) show the final MC comparisons where different RI choices are made. The compared RI choices are Type-II truncations, Type-II-OLR truncations, rings, Buta-Zhang resonances, and traditional ways of finding resonances. Of the truncations, only Type-II and Type-II-OLR are chosen as these are the truncations that seem to show some correlation to resonances according to the literature. Rings are also another galactic property that have links to resonances. Buta-Zhang resonances are themselves in the position of Font-Beckman resonances, in the sense that the Buta-Zhang method is a recent development and its reliability is yet to be determined. Nevertheless, Buta-Zhang resonances are used as RI for FB resonances just to study the two methods' relation. Lastly, the traditional resonances are those which are found via some of the longstanding resonance determination methods, such as Tremaine-Weinberg, simulations, and so on.

The following Table 5.3 represents the correlation indicators of each MC algorithm used in Figure 4.36 and Figure 4.37 to make the comparison between them easier. Remember that the correlation indicator is KS in MC2 histograms (the smaller it is, the stronger the correlation is), Bp0.5 in MC2 scatter plots (the smaller it is, the stronger the correlation is), GalPerc in MC2i global histogram (the larger it is, the stronger the correlation), and MC3Perc in MC3 histogram (the smaller it is, the stronger the correlation). Using these correlation indicators, it is now possible to rank the correlation of each RI with FB resonances in each MC algorithm tested. Table 5.3 shows that the strongest to the weakest correlation of RI with FB resonances, in the case of MC2 histograms, is rings (KS of 0.079%), Buta-Zhang resonances (KS of 3.1%), traditional resonances (KS of 11%), Type-II-OLR truncations (KS of 13%), and lastly Type-II truncations (KS of 38%). Similarly, the strongest to the weakest correlation of RI with FB resonances, in the case of MC2 scatter plots, is rings (Bp0.5 of 0.000021%), Type-II-OLR truncations (Bp0.5 of 0.47%), Type-II truncations (Bp0.5 of 0.88%), Buta-Zhang resonances (Bp0.5 of 2.5%), and lastly traditional resonances (Bp0.5 of 5.5%). Moreover, the strongest to the weakest correlation of RI with FB resonances, in the case of MC2i global histograms, is traditional resonances (GalPerc of 80%), Buta-Zhang resonances (GalPerc of 71%), rings (GalPerc of 63%), Type-II-OLR truncations (GalPerc of 51%), and lastly Type-II truncations (GalPerc of46%). Furthermore, the strongest to the weakest correlation of RI with FB resonances, in the case of MC3 histograms, is Type-II-OLR truncations, rings, Buta-Zhang resonances (all three are tied with MC3Perc of 0% and cannot be distinguished any further), followed by Type-II truncations (MC3Perc of 0.0040%), and lastly traditional resonances (MC3Perc of

1.5%).

It is crucial to note the number of galaxies in each RI's galaxy sample. Type-II truncations' galaxy sample has 52 galaxies, the of Type-II-OLR truncations has 39, that of rings has 35, that of Buta-Zhang resonances has 17, and that of traditional resonances has 10. The larger this number is, the more trustworthy the correlation indicator is. Taking everything into consideration, from MC2 and MC3 one can conclude that the strongest correlation with FB resonances is seen in the case of rings. In the case of truncations, it is evident that Type-II-OLR truncations are slightly better than Type-II truncations when it comes to their correlation with FB resonances. This is somewhat expected as Type-II-OLR truncations are Type-II truncations that occur in regions where the outer Lindblad resonance (OLR) is theorized to exist. However, Type-II-OLR truncations are nowhere as closely correlated to FB resonances as rings are. This could perhaps be due to Type-II-OLR truncations only having one value in any galaxy (by definition there is only one OLR of a perturber in any galaxy) whereas galaxies may possess more than one ring. The RI that potentially has multiple values in a galaxy is more closely related to FB resonances because the FB method regularly predicts multiple resonances in any given galaxy. This property of the FB method potentially helps rings to be more closely correlated to FB resonances than Type-II-OLR truncations are. Moreover, Type-II-OLR truncations are generally found in the outskirts of the galaxy (by definition as truncations are only considered as Type-II-OLR if a Type-II truncation is around 2 to 3 times the bar size from the galactic center) which causes their average distance to a randomly-generated resonance to be greater than the average distance of another RI, which may reside anywhere in the galaxy, to the same randomly-generated resonance; this potentially hinders the Type-II-OLR correlation chances even further. When it comes to Buta-Zhang resonances and traditional resonances, they both have a small number of galaxies in the sample. Regardless of the galaxy samples, it appears that Buta-Zhang resonances have a slightly better correlation with FB resonances than traditional resonances, albeit much weaker than rings and somewhat weaker than Type-II-OLR truncations.

RI choice (No. of galaxies)	MC2 (histogram)	MC2 (scatter)	MC2i	MC3
Type-II (52)	38%	0.88%	46%	0.0040%
Type-II-OLR (39)	13%	0.47%	51%	0%
Rings (35)	0.079%	0.000021%	63%	0%
Buta-Zhang (17)	3.1%	2.5%	71%	0%
Traditional (10)	11%	5.5%	80%	1.5%

Table 5.3: This table shows the indicators of correlation between RI and FB resonances from the final MC comparison panels, seen in Figure 4.36 and Figure 4.37.

Chapter 6

Conclusion

In this chapter the final conclusions of this thesis are listed; the conclusions are divided into two parts: the simulation-related ones and the Monte Carlo related ones.

Simulation

- The Font-Beckman method works best on galaxies that are mid-way between being edge-on (inclination of 90°) and face-on (inclination of 0°), i.e. if the inclination is around 45°. This is related to the fundamental dependence of the Font-Beckman method on the line-of-sight velocity of the galaxy, which is best measured if the galaxy is tilted but not too much.
- If a galaxy has a disc that extends beyond the OLR, then the Font-Beckman method may incorrectly recognize some noise spikes as real resonances.
- The original Font-Beckman pixel selection and phase reversal rejection techniques are best used in high signal-to-noise ratio residual velocity maps, whereas they may prioritize some noise as real resonances in low signal-to-noise ratio residual velocity maps.
- In high signal-to-noise ratio residual velocity maps, a small choice of the phase reversal velocity threshold in the Font-Beckman method is good enough to successfully find real resonances. However, in low signal-to-noise ratio residual velocity maps, the choice of the phase reversal velocity threshold may make the difference between recognizing some noise spikes as resonances and successfully avoiding such mistakes. In other words, when applying the Font-Beckman method to real galaxies (which commonly have low-signal-to-noise ratio residual velocity maps) one must be extra careful when choosing the value of the phase reversal velocity threshold.
- The Font-Beckman method does not work correctly when the residual velocity map shows radially-continuous (arm-like) Canzian features. Whereas it works best when the residual velocity map has its Canzian features in a radially-compact (ring-like) region of the disc. The Wada simulations performed in this thesis show that perturbations start off as radially-continuous (arm-like) Canzian features on the residual velocity map, but get compressed into radially-compact (ring-like) Canzian features as the simulation is run for a longer period of time.
- An increased blurring to simulate seeing on the simulated galaxies does not seem to improve or worsen the correlation between real resonances and the Font-Beckman resonances, i.e. the average

success rates remain stable and close to global average success rate ($\sim$40%). However, increasing the blurring does improve the judgement made regarding the resonances. In other words, when the blurring is stronger it is easier to categorize a correlation as a definite yes or no as opposed to having to categorize it as a potential correlation.

- Increasing the perturbation strength does not improve or worsen the correlation between the real resonances and the Font-Beckman ones, i.e. the average success rates remain stable and close to global average success rate ($\sim$40%), although it does worsen the judgement made regarding the resonances. In other words, with increased perturbation it becomes harder to categorize a correlation as a definite yes or not as opposed to having to categorize it as a potential correlation. This means that when one applies the Font-Beckman method to real galaxies, which have more complex and stronger perturbations, the Font-Beckman resonances become inherently less reliable in nature; note that this reduction in reliability is not due to a lower signal-to-noise ratio but a mere increase in perturbation strength.

- The Font-Beckman method, when applied to the simulated galaxies of various perturbation strengths and differing blurring (simulating seeing) strengths, has shown to be capable of locating the OLR successfully (success rate of 84%$\pm$16%). Additionally, it is shown that the Font-Beckman method can somewhat reliably locate the ILR (success rate of 47%$\pm$27%) and I41 (success rate of 43%$\pm$16%) resonances. However, it does not show much success in identifying CR (success rate of 17%$\pm$17%) which is what Font et al. (2014a) claim that their method is doing.

Monte Carlo

- Comparing truncations as resonance indicators (RI) to each other, one finds that Type-II truncations have the weakest correlation with the Font-Beckman (FB) resonances than all the other three truncation types (Type-II-OLR, Type-III, and all types of truncations). Amongst the truncations that are relevant to resonances (namely Type-II and Type-II-OLR truncations, based on the current consensus of the field), Type-II-OLR truncations are more strongly related to FB resonances than Type-II truncations. Limiting the strengths of the truncations showed that the stronger the truncations are, the stronger the correlations between Type-II truncations and FB resonances are. It must be noted that the truncations used in this thesis may be somewhat unreliable as they were obtained in a non-systematic way, potentially prone to human-error. A more systematic approach to determining truncations could improve the reliability of the comparisons made amongst the truncation types.

- For both Type-II truncations and rings as RI, only using interlocking FB resonances (as opposed to using all types of FB resonances) weakened the correlation between the RI and FB resonances.

- For both Type-II truncations and rings as RI, removing the galaxies with extreme inclinations (below 30° and above 60°) from the sample weakened the correlation between the RI and FB resonances. This finding contradicts with our results from the simulation section, where we found that the FB method works best in the case of mid-range inclinations. It is worthwhile to remember that this weakening of the correlation may simply be due to the reduction in the number of galaxies in the sample.

- For both Type-II truncations and rings as RI, only selecting barred galaxies (as opposed to both barred and unbarred galaxies) from the sample weakened the correlation between the RI and FB resonances.
- Evidently, the Monte Carlo (MC) methods devised in this thesis are highly sensitive on the choice of the maximum galactic radius and the inner forbidden limit (for the random resonances). It is crucial that these two parameters are chosen carefully, systematically, and accurately to avoid getting false results from the MC algorithms.
- The comparison between different RI show that the strongest correlation is seen between rings and FB resonances. Also note that all the controlled tests of Section 5.2 showed a much better correlation between rings and FB resonances than Type-II truncations.
- The Buta-Zhang and traditional resonances may only approximately be compared to each other as they both possess a much smaller galaxy overlap than the other RI. It appears that Buta-Zhang resonances have a slightly better correlation with the FB resonances as compared to the traditional resonances, although the Buta-Zhang correlation with the FB resonances is still weaker than the rings and slightly weaker than Type-II-OLR truncations (this may be due to the aforementioned smaller number of galaxy overlap in the case of Buta-Zhang resonances).

Bibliography

Aguerri, J. A. L., J. E. Beckman, and M. Prieto

1998. Bar Strengths, Bar Lengths, and Corotation Radii, Derived Photometrically for 10 Barred Galaxies. *Astronomical Journal*, 116(5):2136–2153.

Aguerri, J. A. L., V. P. Debattista, and E. M. Corsini

2003. Measurement of fast bars in a sample of early-type barred galaxies. *Monthly Notices of the Royal Astronomical Society*, 338(2):465–480.

Aguerri, J. A. L., J. Méndez-Abreu, J. Falcón-Barroso, A. Amorin, J. Barrera-Ballesteros, R. Cid Fernandes, R. García-Benito, B. García-Lorenzo, R. M. González Delgado, B. Husemann, V. Kalinova, M. Lyubenova, R. A. Marino, I. Márquez, D. Mast, E. Pérez, S. F. Sánchez, G. van de Ven, C. J. Walcher, N. Backsmann, C. Cortijo-Ferrero, J. Bland-Hawthorn, A. del Olmo, J. Iglesias-Páramo, I. Pérez, P. Sánchez-Blázquez, L. Wisotzki, and B. Ziegler

2015. Bar pattern speeds in CALIFA galaxies. I. Fast bars across the Hubble sequence. *Astronomy and Astrophysics*, 576:A102.

Athanassoula, E.

2003. What determines the strength and the slowdown rate of bars? *Monthly Notice of the Royal Astronomical Society*, 341(4):1179–1198.

Athanassoula, E.

2005. On the nature of bulges in general and of box/peanut bulges in particular: input from N-body simulations. *Monthly Notices of the Royal Astronomical Society*, 358(4):1477–1488.

Bender, R., S. Doebereiner, and C. Moellenhoff

1988. Isophote shapes of elliptical galaxies. I. The data. *Astronomy and Astrophysics, Supplements*, 74:385–426.

Bertin, G. and C. C. Lin

1996. *Spiral structure in galaxies a density wave theory*.

Binney, J. and S. Tremaine

2008. *Galactic Dynamics: Second Edition*.

Bosma, A.
1981. 21-cm line studies of spiral galaxies. II. The distribution and kinematics of neutral hydrogen in spiral galaxies of various morphological types. *Astronomical Journal*, 86:1825–1846.

Bovy, J., H. W. Leung, J. A. S. Hunt, J. T. Mackereth, D. A. García-Hernández, and A. Roman-Lopes
2019. Life in the fast lane: a direct view of the dynamics, formation, and evolution of the Milky Way's bar. *Monthly Notices of the Royal Astronomical Society*, 490(4):4740–4747.

Buta, R. and F. Combes
1996. Galactic Rings. *Fundamental Cosmic Physics*, 17:95–281.

Buta, R. and D. A. Crocker
1991. The Outer Lindblad Resonance and the Morphology of Early Type Disk Galaxies. *Astronomical Journal*, 102:1715.

Buta, R. and G. B. Purcell
1998. NGC 3081: Surface Photometry and Kinematics of a Classic Resonance Ring Barred Galaxy. *Astronomical Journal*, 115(2):484–501.

Buta, R. J.
2017. Galactic rings revisited. II. Dark gaps and the locations of resonances in early-to-intermediate-type disc galaxies. *Monthly Notices of the Royal Astronomical Society*, 470(4):3819–3849.

Buta, R. J., K. Sheth, E. Athanassoula, A. Bosma, J. H. Knapen, E. Laurikainen, H. Salo, D. Elmegreen, L. C. Ho, D. Zaritsky, H. Courtois, J. L. Hinz, J.-C. Muñoz-Mateos, T. Kim, M. W. Regan, D. A. Gadotti, A. o. Gil de Paz, J. Laine, K. Menéndez-Delmestre, S. Comerón, S. Erroz Ferrer, M. Seibert, T. Mizusawa, B. Holwerda, and B. F. Madore
2015. A Classical Morphological Analysis of Galaxies in the Spitzer Survey of Stellar Structure in Galaxies (S4G). *Astrophysical Journal, Supplement*, 217(2):32.

Buta, R. J. and X. Zhang
2009. Pattern Corotation Radii from Potential-Density Phase-Shifts for 153 OSUBGS Sample Galaxies. *Astrophysical Journal, Supplement*, 182(2):559–583.

Canzian, B.
1993. A New Way to Locate Corotation Resonances in Spiral Galaxies. *Astrophysical Journal*, 414:487.

Chandrasekhar, S.
1943. Dynamical Friction. I. General Considerations: the Coefficient of Dynamical Friction. *Astrophysical Journal*, 97:255.

Combes, F. and R. H. Sanders
1981. Formation and properties of persisting stellar bars. *Astronomy and Astrophysics*, 96:164–173.

Comerón, S., B. G. Elmegreen, H. Salo, E. Laurikainen, E. Athanassoula, A. Bosma, J. H. Knapen, D. A. Gadotti, K. Sheth, J. L. Hinz, M. W. Regan, A. Gil de Paz, J. C. Muñoz-Mateos, K. Menéndez-Delmestre, M. Seibert, T. Kim, T. Mizusawa, J. Laine, L. C. Ho, and B. Holwerda
2012. Breaks in Thin and Thick Disks of Edge-on Galaxies Imaged in the Spitzer Survey Stellar Structure in Galaxies (S^4G). *Astrophysical Journal*, 759(2):98.

Comerón, S., H. Salo, E. Laurikainen, J. H. Knapen, R. J. Buta, M. Herrera-Endoqui, J. Laine, B. W. Holwerda, K. Sheth, M. W. Regan, J. L. Hinz, J. C. Muñoz-Mateos, A. Gil de Paz, K. Menéndez-Delmestre, M. Seibert, T. Mizusawa, T. Kim, S. Erroz-Ferrer, D. A. Gadotti, E. Athanassoula, A. Bosma, and L. C. Ho
2014. ARRAKIS: atlas of resonance rings as known in the S^4G. *Astronomy and Astrophysics*, 562:A121.

Contopoulos, G.
1980. How far do bars extend. *Astronomy and Astrophysics*, 81(1-2):198–209.

Contopoulos, G.
1981. The effects of resonances near corotation in barred galaxies. *Astronomy and Astrophysics*, 102(2):265–278.

Corsini, E. M.
2011. Direct measurements of bar pattern speeds. *Memorie della Societa Astronomica Italiana Supplementi*, 18:23.

Corsini, E. M., J. A. L. Aguerri, V. P. Debattista, A. Pizzella, F. D. Barazza, and H. Jerjen
2007. The Bar Pattern Speed of Dwarf Galaxy NGC 4431. *Astrophysical Journal, Letters*, 659(2):L121–L124.

Curtis, H. D.
1918. The Planetary Nebulae. *Publications of Lick Observatory*, 13:55–74.

de Vaucouleurs, G.
1959. Classification and Morphology of External Galaxies. *Handbuch der Physik*, 53:275.

de Vaucouleurs, G.
1975. Southern galaxies. VII. The remarkable lenticular barred galaxy NGC 1291. *Astrophysical Journal, Supplement*, 29:193–218.

Debattista, V. P. and J. A. Sellwood
1998. Dynamical Friction and the Distribution of Dark Matter in Barred Galaxies. *Astrophysical Journal*, 493(1):L5–L8.

Debattista, V. P. and J. A. Sellwood
2000. Constraints from Dynamical Friction on the Dark Matter Content of Barred Galaxies. *Astrophysical Journal*, 543(2):704–721.

Debattista, V. P. and T. B. Williams
2004. Fabry-Perot Absorption-Line Spectroscopy of NGC 7079: Kinematics and Bar Pattern Speed. *Astrophysical Journal*, 605(2):714–724.

Einstein, A.
1916. Die Grundlage der allgemeinen Relativitätstheorie. *Annalen der Physik*, 354(7):769–822.

Elmegreen, B. G. and D. M. Elmegreen
1985. Properties of barred spiral galaxies. *Astrophysical Journal*, 288:438–455.

Elmegreen, B. G. and D. M. Elmegreen
1989. On the Relative Frequency of Flocculent and Grand Design Spiral Structures in Barred Galaxies. *Astrophysical Journal*, 342:677.

Elmegreen, D. M. and B. G. Elmegreen
1995. Inner Two-Arm Symmetry in Spiral Galaxies. *Astrophysical Journal*, 445:591.

Epinat, B., P. Amram, and M. Marcelin
2008. GHASP: an Hα kinematic survey of 203 spiral and irregular galaxies - VII. Revisiting the analysis of Hα data cubes for 97 galaxies. *Monthly Notices of the Royal Astronomical Society*, 390(2):466–504.

Erwin, P., J. E. Beckman, and M. Pohlen
2005. Antitruncation of Disks in Early-Type Barred Galaxies. *Astrophysical Journal, Letters*, 626(2):L81–L84.

Erwin, P., M. Pohlen, and J. E. Beckman
2008. The Outer Disks of Early-Type Galaxies. I. Surface-Brightness Profiles of Barred Galaxies. *Astronomical Journal*, 135(1):20–54.

Eskridge, P. B., J. A. Frogel, R. W. Pogge, A. C. Quillen, A. A. Berlind, R. L. Davies, D. L. DePoy, K. M. Gilbert, M. L. Houdashelt, L. E. Kuchinski, S. V. Ramírez, K. Sellgren, A. Stutz, D. M. Terndrup, and G. P. Tiede
2002. Near-Infrared and Optical Morphology of Spiral Galaxies. *Astrophysical Journal, Supplement*, 143(1):73–111.

Eskridge, P. B., J. A. Frogel, R. W. Pogge, A. C. Quillen, R. L. Davies, D. L. DePoy, M. L. Houdashelt, L. E. Kuchinski, S. V. Ramírez, K. Sellgren, D. M. Terndrup, and G. P. Tiede
2000. The Frequency of Barred Spiral Galaxies in the Near-Infrared. *Astronomical Journal*, 119(2):536–544.

Faber, S. M. and R. E. Jackson
1976. Velocity dispersions and mass-to-light ratios for elliptical galaxies. *Astrophysical Journal*, 204:668–683.

Fathi, K., J. E. Beckman, N. Piñol-Ferrer, O. Hernand ez, I. Martínez-Valpuesta, and C. Carignan
2009. Pattern Speeds of Bars and Spiral Arms from Hα Velocity Fields. *Astrophysical Journal*, 704(2):1657–1675.

Font, J., J. E. Beckman, B. Epinat, K. Fathi, L. Gutiérrez, and O. Hernandez
2011. Resonant Structure in the Disks of Spiral Galaxies, Using Phase Reversals in Streaming Motions from Two-dimensional Hα Fabry-Perot Spectroscopy. *Astrophysical Journal, Letters*, 741(1):L14.

Font, J., J. E. Beckman, I. Martínez-Valpuesta, A. S. Borlaff, P. A. James, S. Díaz-García, B. García-Lorenzo, A. Camps-Fariña, L. Gutiérrez, and P. Amram
2017. Kinematic Clues to Bar Evolution for Galaxies in the Local Universe: Why the Fastest Rotating Bars are Rotating Most Slowly. *Astrophysical Journal*, 835(2):279.

Font, J., J. E. Beckman, M. Querejeta, B. Epinat, P. A. James, J. Blasco-herrera, S. Erroz-Ferrer, and I. Pérez
2014a. Interlocking Resonance Patterns in Galaxy Disks. *Astrophysical Journal, Supplement*, 210:2.

Font, J., J. E. Beckman, J. Zaragoza-Cardiel, K. Fathi, B. Epinat, and P. Amram
2014b. The ratio of pattern speeds in double-barred galaxies. *Monthly Notices of the Royal Astronomical Society*, 444:L85–L89.

Font, J., M. Querejeta, J. E. Beckman, and P. James
2014c. Multiple Pattern Speeds in Disc Galaxies. In *Multi-Spin Galaxies*, E. Iodice and E. M. Corsini, eds., volume 486 of *Astronomical Society of the Pacific Conference Series*, P. 133.

Foster, T. J.
2004. *A rich new approach to determining the structure and dynamics of the Milky Way galaxy*. PhD thesis, University of Alberta (Canada), Canada.

Freeman, K. C.
1970. On the Disks of Spiral and S0 Galaxies. *Astrophysical Journal*, 160:811.

Fujii, M. S., J. Bédorf, J. Baba, and S. Portegies Zwart
2018. The dynamics of stellar discs in live dark-matter haloes. *Monthly Notices of the Royal Astronomical Society*, 477(2):1451–1471.

Gavazzi, R., T. Treu, J. D. Rhodes, L. V. E. Koopmans, A. S. Bolton, S. Burles, R. J. Massey, and L. A. Moustakas
2007. The Sloan Lens ACS Survey. IV. The Mass Density Profile of Early-Type Galaxies out to 100 Effective Radii. *Astrophysical Journal*, 667(1):176–190.

Gerhard, O.
2002. Mass distribution in our Galaxy. *Space Science Reviews*, 100:129–138.

Gerssen, J., K. Kuijken, and M. R. Merrifield
1999. The pattern speed of the bar in NGC 4596. *Monthly Notices of the Royal Astronomical Society*, 306(4):926–930.

Gerssen, J., K. Kuijken, and M. R. Merrifield
2003. Model-independent measurements of bar pattern speeds. *Monthly Notices of the Royal Astronomical Society*, 345(1):261–268.

Gilmore, G. and N. Reid
1983. New light on faint stars - III. Galactic structure towards the South Pole and the Galactic thick disc. *Monthly Notices of the Royal Astronomical Society*, 202:1025–1047.

Gilmore, G. and R. F. G. Wyse
1989. Structure and Evolution of the Milky way Galaxy. In *IAU Colloq. 111: The Use of pulsating stars in fundamental problems of astronomy*, E. G. Schmidt, ed., P. 83.

Goldreich, P. and S. Tremaine
1982. The dynamics of planetary rings. *Annual Review of Astronomy and Astrophysics*, 20:249–283.

Gonzalez, R. A. and J. R. Graham
1996. Tracing the Dynamics of Disk Galaxies with Optical and Infrared Surface Photometry: Color Gradients in M99. *Astrophysical Journal*, 460:651.

Guo, R., S. Mao, E. Athanassoula, H. Li, J. Ge, R. J. Long, M. Merrifield, and K. Masters
2019. SDSS-IV MaNGA: pattern speeds of barred galaxies. *Monthly Notices of the Royal Astronomical Society*, 482(2):1733–1756.

Hackwell, J. A. and F. Schweizer
1983. Infrared mapping and UBVRi photometry of the spiral galaxy NGC 1566. *Astrophysical Journal*, 265:643–647.

Harris, W. E.
1996. A Catalog of Parameters for Globular Clusters in the Milky Way. *Astronomical Journal*, 112:1487.

Herschel, W.
1785. On the Construction of the Heavens. *Philosophical Transactions of the Royal Society of London Series I*, 75:213–266.

Hoyle, F. and J. G. Ireland
1961. Note on the magnetic structure of the galaxy. *Monthly Notices of the Royal Astronomical Society*, 122:35.

Hubble, E.
1929. A Relation between Distance and Radial Velocity among Extra-Galactic Nebulae. *Proceedings of the National Academy of Science*, 15(3):168–173.

Hubble, E. P.
1926. Extragalactic nebulae. *Astrophysical Journal*, 64:321–369.

Hubble, E. P.
1936. *Realm of the Nebulae*.

Hunter, J. H., J., R. Ball, J. M. Huntley, M. N. England , and S. T. Gottesman
1988. Dynamical Models of the Barred Spiral Galaxy NGC 3992. *Astrophysical Journal*, 324:721.

Julian, W. H. and A. Toomre
1966. Non-Axisymmetric Responses of Differentially Rotating Disks of Stars. *Astrophysical Journal*, 146:810.

Kalnajs, A. J.
1978. A Confrontation of Density Wave Theories with Observations. In *Structure and Properties of Nearby Galaxies*, E. M. Berkhuijsen and R. Wielebinski, eds., volume 77 of *IAU Symposium*, P. 113.

Kaspi, S. and H. Netzer
1999. Modeling Variable Emission Lines in Active Galactic Nuclei: Method and Application to NGC 5548. *Astrophysical Journal*, 524(1):71–81.

Kent, S. M.
1987. The Pattern Speed in the SB0 Galaxy NGC 936. *Astronomical Journal*, 93:1062.

Kim, T., K. Sheth, D. A. Gadotti, M. G. Lee, D. Zaritsky, B. G. Elmegreen, E. Athanassoula, A. Bosma, B. Holwerda, L. C. Ho, S. Comerón, J. H. Knapen, J. L. Hinz, J.-C. Muñoz-Mateos, S. Erroz-Ferrer, R. J. Buta, M. Kim, E. Laurikainen, H. Salo, B. F. Madore, J. Laine, K. Menéndez-Delmestre, M. W. Regan, B. de Swardt, A. Gil de Paz, M. Seibert, and T. Mizusawa
2015. The Mass Profile and Shape of Bars in the Spitzer Survey of Stellar Structure in Galaxies (S^4G): Search for an Age Indicator for Bars. *Astrophysical Journal*, 799(1):99.

Knapen, J. H., D. Pérez-Ramírez, and S. Laine
2002. Circumnuclear regions in barred spiral galaxies - II. Relations to host galaxies. *Monthly Notices of the Royal Astronomical Society*, 337(3):808–828.

Kormendy, J.
1981. The structure of barred galaxies. In *Structure and Evolution of Normal Galaxies*, S. M. Fall and D. Lynden-Bell, eds., Pp. 85–110.

Kormendy, J.
1993. Kinematics of extragalactic bulges: evidence that some bulges are really disks. In *Galactic Bulges*, H. Dejonghe and H. J. Habing, eds., volume 153 of *IAU Symposium*, P. 209.

Kormendy, J.
2016. Elliptical Galaxies and Bulges of Disc Galaxies: Summary of Progress and Outstanding Issues. In *Galactic Bulges*, E. Laurikainen, R. Peletier, and D. Gadotti, eds., volume 418 of *Astrophysics and Space Science Library*, P. 431.

Kormendy, J. and D. Richstone
1995. Inward Bound—The Search For Supermassive Black Holes In Galactic Nuclei. *Annual Review of Astronomy and Astrophysics*, 33:581.

Laine, J., E. Laurikainen, and H. Salo
2016. Influence of galaxy stellar mass and observed wavelength on disc breaks in S^4G, NIRS0S, and SDSS data. *Astronomy and Astrophysics*, 596:A25.

Laine, J., E. Laurikainen, H. Salo, S. Comerón, R. J. Buta, D. Zaritsky, E. Athanassoula, A. Bosma, J. C. Muñoz-Mateos, D. A. Gadotti, J. L. Hinz, S. Erroz-Ferrer, A. Gil de Paz, T. Kim, K. Menéndez-Delmestre, T. Mizusawa, M. W. Regan, M. Seibert, and K. Sheth
2014. Morphology and environment of galaxies with disc breaks in the S^4G and NIRS0S. *Monthly Notices of the Royal Astronomical Society*, 441(3):1992–2012.

Lauer, T. R.
1985. Boxy isophotes, discs and dust lanes in elliptical galaxies. *Monthly Notices of the Royal Astronomical Society*, 216:429–438.

Laurikainen, E. and H. Salo
2002. Bar strengths in spiral galaxies estimated from 2MASS images. *Monthly Notices of the Royal Astronomical Society*, 337(3):1118–1138.

Laurikainen, E., H. Salo, E. Athanassoula, A. Bosma, and M. Herrera-Endoqui
2014. Milky Way mass galaxies with X-shaped bulges are not rare in the local Universe. *Monthly Notices of the Royal Astronomical Society*, 444:L80–L84.

Lemaître, G.
1927. Un Univers homogène de masse constante et de rayon croissant rendant compte de la vitesse radiale des nébuleuses extra-galactiques. *Annales de la Société Scientifique de Bruxelles*, 47:49–59.

Lin, C. C. and F. H. Shu
1964. On the Spiral Structure of Disk Galaxies. *Astrophysical Journal*, 140:646.

Lin, C. C. and F. H. Shu
1966. On the Spiral Structure of Disk Galaxies, II. Outline of a Theory of Density Waves. *Proceedings of the National Academy of Science*, 55(2):229–234.

Lin, C. C., C. Yuan, and F. H. Shu
1969. On the Spiral Structure of Disk Galaxies. III. Comparison with Observations. *Astrophysical Journal*, 155:721.

Lindblad, B.
1927. On the state of motion in the galactic system. *Monthly Notices of the Royal Astronomical Society*, 87:553–564.

Lindblad, P. A. B. and H. Kristen
1996. Hydrodynamical simulations of the barred spiral galaxy NGC 1300. Dynamical interpretation of observations. *Astronomy and Astrophysics*, 313:733–749.

López-Corredoira, M., C. Allende Prieto, F. Garzón, H. Wang, C. Liu, and L. Deng
2018. Disk stars in the Milky Way detected beyond 25 kpc from its center. *Astronomy and Astrophysics*, 612:L8.

Lynden-Bell, D. and A. J. Kalnajs
1972. On the generating mechanism of spiral structure. *Monthly Notices of the Royal Astronomical Society*, 157:1.

Lynden-Bell, D. and J. E. Pringle
1974. The evolution of viscous discs and the origin of the nebular variables. *Monthly Notices of the Royal Astronomical Society*, 168:603–637.

Lynden-Bell, D. and R. Wood
1968. The gravo-thermal catastrophe in isothermal spheres and the onset of red-giant structure for stellar systems. *Monthly Notices of the Royal Astronomical Society*, 138:495.

Mandelbaum, R., U. Seljak, G. Kauffmann, C. M. Hirata, and J. Brinkmann
2006. Galaxy halo masses and satellite fractions from galaxy-galaxy lensing in the Sloan Digital Sky Survey: stellar mass, luminosity, morphology and environment dependencies. *Monthly Notices of the Royal Astronomical Society*, 368(2):715–731.

Mark, J. W. K.
1976. On Density Waves in Galaxies. III. Wave Amplification by Stimulated Emission. *Astrophysical Journal*, 205:363–378.

Martínez-García, E. E., R. A. González-Lópezlira, and G. Bruzual-A
2009. Spiral Density Wave Triggering of Star Formation in SA and SAB Galaxies. *Astrophysical Journal*, 694(1):512–545.

Mathewson, D. S., P. C. van der Kruit, and W. N. Brouw
1972. A High Resolution Radio Continuum Survey of M51 and NGC 5195 at 1415 MHz. *Astronomy and Astrophysics*, 17:468.

Meidt, S. E., R. J. Rand, and M. R. Merrifield
2009. Uncovering the Origins of Spiral Structure by Measuring Radial Variation in Pattern Speeds. *Astrophysical Journal*, 702(1):277–290.

Merrifield, M. R. and K. Kuijken
1995. The pattern speed of the bar in NGC 936. *Monthly Notices of the Royal Astronomical Society*, 274(3):933–938.

Miwa, T. and M. Noguchi
1998. Dynamical Properties of Tidally Induced Galactic Bars. *Astrophysical Journal*, 499(1):149–166.

Moons, M. and A. Morbidelli
1995. Secular resonances inside mean-motion commensurabilities: the 4/1, 3/1, 5/2 and 7/3 cases. *Icarus*, 114(1):33–50.

Moore, B., G. Lake, and N. Katz
1998. Morphological Transformation from Galaxy Harassment. *Astrophysical Journal*, 495(1):139–151.

Morgan, W. W.
1958. A Preliminary Classification of the Forms of Galaxies According to Their Stellar Population. *Publications of the Astronomical Society of the Pacific*, 70(415):364.

Oort, J. H.
1927. Observational evidence confirming Lindblad's hypothesis of a rotation of the galactic system. *Bulletin of the Astronomical Institutes of the Netherlands*, 3:275.

Pasha, I. I.
2004. Density-Wave Spiral Theories in the 1960s. I. *arXiv e-prints*, Pp. astro–ph/0406142.

Peletier, R. F., J. Falcón-Barroso, R. Bacon, M. Cappellari, R. L. Davies, P. T. de Zeeuw, E. Emsellem, K. Ganda, D. Krajnović, H. Kuntschner, R. M. McDermid, M. Sarzi, and G. van de Ven
2007. The SAURON project - XI. Stellar populations from absorption-line strength maps of 24 early-type spirals. *Monthly Notices of the Royal Astronomical Society*, 379(2):445–468.

Peng, C. Y., L. C. Ho, C. D. Impey, and H.-W. Rix
2002. Detailed Structural Decomposition of Galaxy Images. *Astronomical Journal*, 124(1):266–293.

Peterson, B. M. and A. Wandel
1999. Keplerian Motion of Broad-Line Region Gas as Evidence for Supermassive Black Holes in Active Galactic Nuclei. *Astrophysical Journal, Letters*, 521(2):L95–L98.

Porco, C. C., E. Baker, J. Barbara, K. Beurle, A. Brahic, J. A. Burns, S. Charnoz, N. Cooper, D. D. Dawson, A. D. Del Genio, T. Denk, L. Dones, U. Dyudina, M. W. Evans, B. Giese, K. Grazier, P. Helfenstein, A. P. Ingersoll, R. A. Jacobson, T. V. Johnson, A. McEwen, C. D. Murray, G. Neukum, W. M. Owen, J. Perry, T. Roatsch, J. Spitale, S. Squyres, P. Thomas, M. Tiscareno, E. Turtle, A. R. Vasavada, J. Veverka, R. Wagner, and R. West
2005. Cassini Imaging Science: Initial Results on Saturn's Rings and Small Satellites. *Science*, 307(5713):1226–1236.

Prialnik, D.
2000. *An Introduction to the Theory of Stellar Structure and Evolution*.

Puerari, I. and H. Dottori
1997. A Morphological Method to Determine Corotation Radii in Spiral Galaxies. *Astrophysical Journal, Letters*, 476(2):L73–L75.

Rafikov, R. R.
2001. The local axisymmetric instability criterion in a thin, rotating, multicomponent disc. *Monthly Notices of the Royal Astronomical Society*, 323(2):445–452.

Rand, R. J.
1993. Density Wave Kinematics and Giant Molecular Association Formation in M51. *Astrophysical Journal*, 410:68.

Rand, R. J. and J. F. Wallin
2004. Pattern Speeds of BIMA SONG Galaxies with Molecule-dominated Interstellar Mediums Using the Tremaine-Weinberg Method. *Astrophysical Journal*, 614(1):142–157.

Rautiainen, P., H. Salo, and R. Buta
2004. Dynamical modelling of the remarkable four-armed barred spiral galaxy ESO 566-24. *Monthly Notices of the Royal Astronomical Society*, 349(3):933–944.

Rautiainen, P., H. Salo, and E. Laurikainen
2005. The Pattern Speeds of 38 Barred Galaxies. *Astrophysical Journal, Letters*, 631(2):L129–L132.

Rautiainen, P., H. Salo, and E. Laurikainen
2008. Model-based pattern speed estimates for 38 barred galaxies. *Monthly Notices of the Royal Astronomical Society*, 388(4):1803–1818.

Rix, H.-W. and J. Bovy
2013. The Milky Way's stellar disk. Mapping and modeling the Galactic disk. *Astronomy and Astrophysics Reviews*, 21:61.

Roberts, W. W.
1969. Large-Scale Shock Formation in Spiral Galaxies and its Implications on Star Formation. *Astrophysical Journal*, 158:123.

Roca-Fàbrega, S., T. Antoja, F. Figueras, O. Valenzuela, M. Romero-Gómez, and B. Pichardo
2014. A novel method to bracket the corotation radius in galaxy discs: vertex deviation maps. *Monthly Notices of the Royal Astronomical Society*, 440(3):1950–1963.

Salak, D., Y. Noma, K. Sorai, Y. Miyamoto, N. Kuno, A. R. Pettitt, H. Kaneko, T. Tanaka, A. Yasuda, S. Kita, Y. Yajima, S. Shibata, N. Nakai, M. Seta, K. Muraoka, M. Kuroda, H. Nakanishi, T. T. Takeuchi, M. Yoda, K. Morokuma-Matsui, Y. Watanabe, N. Matsumoto, N. Oi, H.-A. Pan, A. Kajikawa, Y. Yashima, and R. Komatsuzaki
2019. CO Multi-line Imaging of Nearby Galaxies (COMING). VII. Fourier decomposition of molecular gas velocity fields and bar pattern speed. *Publications of the Astronomical Society of Japan*, P. 17.

Salo, H. and E. Laurikainen
1993. The Interacting System NGC 7753–7752 (Arp 86). II. N-Body Modeling. *Astrophysical Journal*, 410:586.

Salo, H. and E. Laurikainen
2000a. N-body model for M51 - I. Multiple encounter versus single passage? *Monthly Notices of the Royal Astronomical Society*, 319(2):377–392.

Salo, H. and E. Laurikainen
2000b. N-body model for M51 - II. Inner structure. *Monthly Notices of the Royal Astronomical Society*, 319(2):393–413.

Salo, H., E. Laurikainen, J. Laine, S. Comerón, D. A. Gadotti, R. Buta, K. Sheth, D. Zaritsky, L. Ho, J. Knapen, E. Athanassoula, A. Bosma, S. Laine, M. Cisternas, T. Kim, J. C. Muñoz-Mateos, M. Regan, J. L. Hinz, A. Gil de Paz, K. Menendez-Delmestre, T. Mizusawa, S. Erroz-Ferrer, S. E. Meidt, and M. Querejeta
2015. The Spitzer Survey of Stellar Structure in Galaxies (S^4G): Multi-component Decomposition Strategies and Data Release. *Astrophysical Journal, Supplement*, 219(1):4.

Salo, H., P. Rautiainen, R. Buta, G. B. Purcell, M. L. Cobb, D. A. Crocker, and E. Laurikainen
1999. The Structure and Dynamics of the Early-Type Resonance Ring Galaxy IC 4214. II. Models. *Astronomical Journal*, 117(2):792–810.

Sandage, A.
1975. *Classification and Stellar Content of Galaxies Obtained from Direct Photography*, P. 1.

Schödel, R., T. Ott, R. Genzel, R. Hofmann, M. Lehnert, A. Eckart, N. Mouawad, T. Alexander, M. J. Reid, R. Lenzen, M. Hartung, F. Lacombe, D. Rouan, E. Gendron, G. Rousset, A. M. Lagrange, W. Brandner, N. Ageorges, C. Lidman, A. F. M. Moorwood, J. Spyromilio, N. Hubin, and K. M. Menten
2002. A star in a 15.2-year orbit around the supermassive black hole at the centre of the Milky Way. *Nature*, 419(6908):694–696.

Schwarz, M. P.
1981. The response of gas in a galactic disk to bar forcing. *Astrophysical Journal*, 247:77–88.

Schwarz, M. P.
1984. How bar strength and pattern speed affect galactic spiral structure. *Monthly Notices of the Royal Astronomical Society*, 209:93–109.

Schweizer, F.
1976. Photometric studies of spiral structure. I. The disks and arms of six Sb I and Sc I galaxies. *Astrophysical Journal, Supplement*, 31:313–332.

Seigar, M. S., A. Harrington, and P. Treuthardt
2018. Determination of resonance locations in NGC 613 from morphological arguments. *Monthly Notices of the Royal Astronomical Society*, 481(4):5394–5400.

Sempere, M. J., S. Garcia-Burillo, F. Combes, and J. H. Knapen
1995. Determination of the pattern speed in the grand design spiral galaxy NGC 4321. *Astronomy and Astrophysics*, 296:45.

Shapley, H.
1918. Studies based on the colors and magnitudes in stellar clusters. VII. The distances, distribution in space, and dimensions of 69 globular clusters. *Astrophysical Journal*, 48:154–181.

Shu, F. H.
2016. Six Decades of Spiral Density Wave Theory. *Annual Review of Astronomy and Astrophysics*, 54:667–724.

Sierra, A. D., M. S. Seigar, P. Treuthardt, and I. Puerari
2015. Determination of resonance locations in barred spiral galaxies using multiband photometry. *Monthly Notices of the Royal Astronomical Society*, 450(2):1799–1811.

Sparke, L. S. and I. Gallagher, John S.
2000. *Galaxies in the universe : an introduction*.

Thomasson, M. and K. J. Donner
1993. A model of the tidal interaction between M 81 and NGC 3077. *Astronomy and Astrophysics*, 272:153–160.

Toomre, A.
1964. On the gravitational stability of a disk of stars. *Astrophysical Journal*, 139:1217–1238.

Toomre, A.
1981. What amplifies the spirals. In *Structure and Evolution of Normal Galaxies*, S. M. Fall and D. Lynden-Bell, eds., Pp. 111–136.

Toomre, A. and J. Toomre
1972. Galactic Bridges and Tails. *Astrophysical Journal*, 178:623–666.

Tremaine, S. and M. D. Weinberg
1984. A kinematic method for measuring the pattern speed of barred galaxies. *Astrophysical Journal, Letters*, 282:L5–L7.

Treuthardt, P., R. Buta, H. Salo, and E. Laurikainen

2007. The Kinematically Measured Pattern Speeds of NGC 2523 and NGC 4245. *Astronomical Journal*, 134(3):1195–1205.

Tully, R. B. and J. R. Fisher

1977. Reprint of 1977A&A....54..661T. A new method of determining distance to galaxies. *Astronomy and Astrophysics*, 500:105–117.

Vallée, J. P.

2014. Catalog of Observed Tangents to the Spiral Arms in the Milky Way Galaxy. *Astrophysical Journal, Supplement*, 215(1):1.

Visser, H. C. D.

1980. The dynamics of the spiral galaxy M 81. I. Axisymmetric models and the stellar density wave. *Astronomy and Astrophysics*, 88:149–158.

Vorobyov, E. I. and C. Theis

2008. Shape and orientation of stellar velocity ellipsoids in spiral galaxies. *Monthly Notices of the Royal Astronomical Society*, 383(3):817–830.

Vorontsov-Velyaminov, B. A.

1958. Spiral structure and the rotation of galaxies. In *Comparison of the Large-Scale Structure of the Galactic System with that of Other Stellar Systems*, N. G. Roman, ed., volume 5 of *IAU Symposium*, P. 65.

Wada, K.

1994. Gaseous Orbits in a Weak Bar Potential: Bar-Driven Spirals and the Effects of Resonances. *Publications of the Astronomical Society of Japan*, 46:165–172.

Wada, K.

2004. Fueling Gas to the Central Region of Galaxies. In *Coevolution of Black Holes and Galaxies*, L. C. Ho, ed., P. 186.

Watkins, A. E., J. Laine, S. Comerón, J. Janz, and H. Salo

2019. Varied origins of up-bending breaks in galaxy disks. *Astronomy and Astrophysics*, 625:A36.

Wright, T.

1750. *An original theory or new hypothesis of the universe : founded upon general phaenomena of the visible creation; and particularly the Via the laws of nature, and solving by mathematical principles : the Lactea ...compris'd in nine familiar letters from the author to his friendand : illustrated with upward of thirty graven and mezzotinto plates ...*

Yuan, C. and P. Grosbol

1981. Surface photometry of spiral galaxies. I - Theoretical color variation and surface brightness across spiral arms. *Astrophysical Journal*, 243:432–444.

Zasowski, G., R. L. Beaton, K. K. Hamm, S. R. Majewski, B. Babler, R. A. Benjamin, E. Churchwell, M. Meade, R. J. Patterson, C. Watson, and B. A. Whitney
2013. Open Clusters in the Milky Way Outer Disk: Newly Discovered and Unstudied Clusters in the Spitzer GLIMPSE-360, CYG-X, and SMOG Surveys. *Astronomical Journal*, 146(3):64.

Zhang, X. and R. J. Buta
2007. The Potential-Density Phase-Shift Method for Determining the Corotation Radii in Spiral and Barred Galaxies. *Astronomical Journal*, 133(6):2584–2606.

Zimmer, P., R. J. Rand, and J. T. McGraw
2004. The Pattern Speeds of M51, M83, and NGC 6946 Using CO and the Tremaine-Weinberg Method. *Astrophysical Journal*, 607(1):285–293.